NARROW-BAND PASSIVE SYSTEMS THEORY WITH APPLICATIONS TO POSITIONING AND NAVIGATION

JOSÉ MANUEL FONSECA DE MOURA

TECHNICAL REPORT 490
April 28, 1976

MASSACHUSETTS INSTITUTE OF TECHNOLOGY
RESEARCH LABORATORY OF ELECTRONICS
CAMBRIDGE, MASSACHUSETTS 02139

The Research Laboratory of Electronics is an interdepartmental laboratory in which faculty members and graduate students from numerous academic departments conduct research.

The research reported in this document was made possible in part by support extended the Massachusetts Institute of Technology, Research Laboratory of Electronics, by the JOINT SERVICES ELECTRONICS PROGRAM (U.S. Army, U.S. Navy, and U.S. Air Force) under Contract No. DAAB07-75-C-1346.

Requestors having DOD contracts or grants may apply for copies of technical reports to the Defense Documentation Center, Cameron Station, Alexandria, Virginia 22314. Copies can also be obtained from the Document Room, 36-412, Research Laboratory of Electronics, Massachusetts Institute of Technology, Cambridge, Massachusetts 02139.

UNCLASSIFIED

SECURITY CLASSIFICATION OF THIS PAGE (When Data Entered)

REPORT DOCUMENTATION PAGE		READ INSTRUCTIONS BEFORE COMPLETING FORM
1. REPORT NUMBER	2. GOVT ACCESSION NO.	3. RECIPIENT'S CATALOG NUMBER
4. TITLE (and Subtitle) NARROW-BAND PASSIVE SYSTEMS THEORY WITH APPLICATIONS TO POSITIONING AND NAVIGATION		5. TYPE OF REPORT & PERIOD COVERED Technical Report 6. PERFORMING ORG. REPORT NUMBER 490
7. AUTHOR(s) José Manuel Fonseca de Moura		8. CONTRACT OR GRANT NUMBER(s) DAAB07-75-C-1346
9. PERFORMING ORGANIZATION NAME AND ADDRESS Research Laboratory of Electronics Massachusetts Institute of Technology Cambridge, Massachusetts 02139		10. PROGRAM ELEMENT, PROJECT, TASK AREA & WORK UNIT NUMBERS C8-5-04533-01-C-8-CA C8-5-04534-01-C-8-CA
11. CONTROLLING OFFICE NAME AND ADDRESS Department of the Army Headquarters U.S. Army Electronics Command Fort Monmouth, New Jersey 07703		12. REPORT DATE April 28, 1976 13. NUMBER OF PAGES 214
14. MONITORING AGENCY NAME & ADDRESS(if different from Controlling Office) U.S. Army Electronics Technology and Devices Laboratories Fort Monmouth, New Jersey 07703		15. SECURITY CLASS. (of this report) Unclassified 15a. DECLASSIFICATION/DOWNGRADING SCHEDULE

16. DISTRIBUTION STATEMENT (of this Report)

Approved for public release; distribution unlimited

17. DISTRIBUTION STATEMENT (of the abstract entered in Block 20, if different from Report)

18. SUPPLEMENTARY NOTES

19. KEY WORDS (Continue on reverse side if necessary and identify by block number)

Adaptive array processing
Passive sonar
Source location
Narrow-band tracking
Positioning and navigation

20. ABSTRACT (Continue on reverse side if necessary and identify by block number)

See other side

DD FORM 1 JAN 73 1473 EDITION OF 1 NOV 65 IS OBSOLETE
S/N 0102-014-6601

UNCLASSIFIED

SECURITY CLASSIFICATION OF THIS PAGE (When Data Entered)

20. ABSTRACT

The passive tracking problem with narrow-band and linear constraints on geometry and motion is considered.

In Part I a model is developed which exhibits explicitly the nonhomogeneous received wave field structure induced by the spatial baseline (observer's array) and/or temporal diversity (source motion). This model encompasses the basic phenomena of many practical situations, and is sufficiently simple to be useful in analytical studies. The fundamental question of global parameter identifiability is pursued, with emphasis on passive ranging. The structure and global and local performance of the optimal and suboptimal receivers is examined and, by considering two limiting geometries (distant and close observer), analytical intuitively pleasing expressions are derived which bound the mean-square performance. The issues of spatial/temporal factorability and coupling are investigated, with the focus on the implications of processing complexity and identifiability nonsingularity.

In Part II a practical hybrid solution to the passive tracking problem is developed, and a compromise is achieved between global parameter identifiability and receiver complexity. The behavior of the hybrid algorithm and its sensitivity to the underlying model assumptions of linear path perturbations are analyzed. The theory of passive tracking is applied to positioning in such situations as air traffic control, underwater acoustics, and navigation (orbiting and geostationary satellites). Tradeoffs among attainable accuracy, geometry, and statistical parameters are discussed. Finally, Monte Carlo simulations are presented, showing the existence of regions where the theoretical and simulated results converge.

MASSACHUSETTS INSTITUTE OF TECHNOLOGY

RESEARCH LABORATORY OF ELECTRONICS

Technical Report 490 April 28, 1976

NARROW-BAND PASSIVE SYSTEMS THEORY WITH APPLICATIONS TO POSITIONING AND NAVIGATION

José Manuel Fonseca de Moura

Submitted to the Department of Electrical Engineering and Computer Science at the Massachusetts Institute of Technology, April 7, 1975, in partial fulfillment of the requirements for the degree of Doctor of Science.

(Manuscript received May 15, 1975)

ABSTRACT

The passive tracking problem with narrow-band and linear constraints on geometry and motion is considered.

In Part I a model is developed which exhibits explicitly the nonhomogeneous received wave field structure induced by the spatial baseline (observer's array) and/or temporal diversity (source motion). This model encompasses the basic phenomena of many practical situations, and is sufficiently simple to be useful in analytical studies. The fundamental question of global parameter identifiability is pursued, with emphasis on passive ranging. The structure and global and local performance of the optimal and suboptimal receivers is examined and, by considering two limiting geometries (distant and close observer), analytical intuitively pleasing expressions are derived which bound the mean-square performance. The issues of spatial/temporal factorability and coupling are investigated, with the focus on the implications of processing complexity and identifiability nonsingularity.

In Part II a practical hybrid solution to the passive tracking problem is developed, and a compromise is achieved between global parameter identifiability and receiver complexity. The behavior of the hybrid algorithm and its sensitivity to the underlying model assumptions of linear path perturbations are analyzed. The theory of passive tracking is applied to positioning in such situations as air traffic control, underwater acoustics, and navigation (orbiting and geostationary satellites). Tradeoffs among attainable accuracy, geometry, and statistical parameters are discussed. Finally, Monte Carlo simulations are presented, showing the existence of regions where the theoretical and simulated results converge.

TABLE OF CONTENTS

Part I. GLOBAL ACQUISITION via MAXIMUM-LIKELIHOOD TECHNIQUES

CONTENTS

CONTENTS

CONTENTS

Part I. Global Acquisition via Maximum-Likelihood Techniques

I. INTRODUCTION

Passive situations that do not involve the use of active radar or sonar equipment arise in a variety of fields: oceanography (locating drifting buoys),[1-3] meteorology (tracking radiosondes or balloon-borne devices),[4-6] passive sonar (positioning submersibles),[7] navigation (obtaining position fixes),[8-10] radio astronomy (sensing natural radiation),[11] and so forth.

In this report we are concerned with analysis and design of receivers for these applications where a moving or a stationary source has to be located from noisy observations of its signature.

1.1 POSITIONING AND NAVIGATION

In such problems we are interested in determining the relative source/receiver geometry and in finding the ultimate geographical location of both source and receiver from a priori knowledge of the absolute position of either one. We classify passive tracking as navigational or positioning problems according to whether the location of the receiver or of the source is to be determined.

Figure 1 shows some typical navigational configurations. The basic characteristic in (a) and (b) is the spatial separation or baseline at the source (beacons B_1 to B_N) or at the receiver. In (c) and (d) this separation is synthetically generated in time by the motions of the source and/or the receiver. In (a) and (b) the configuration is stationary, unchanging significantly during the time interval of observation. The navigational

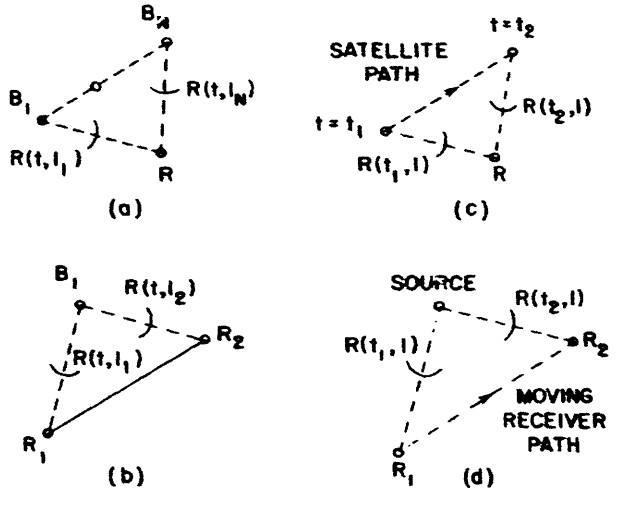

Fig. 1. Typical navigational configurations: (a) extended source, (b) extended receiver, (c) moving source, (d) moving receiver.

problem is solved from the modifications induced on the signals by the overall spatial diversity. In (c) and (d) the signal is modulated by the relative dynamics. In general, because of the nonnegligible source and/or receiver spatial extent and the relative dynamics, we have a coupled spatial and temporal diversity signal structure.

To each navigational geometry there corresponds a twin positioning geometry, where a stationary or moving receiver tracks a stationary or moving source. Given the dualism, for the most part we shall restrict our discussion to positioning configurations. We shall concentrate on the fundamental aspects that are common to all problems: source/receiver parameter identifiability, optimal and suboptimal receiver design, and performance analysis.

1.2 MODEL

Figure 2 illustrates the passive tracking problem in a sonar context. A moving source (MS) emits some kind of radiation (source signature) which propagates through the surrounding medium and is sensed by the receiving devices, hereafter called sensors or array elements.

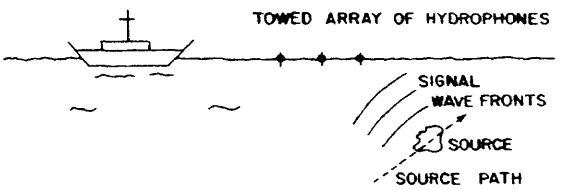

Fig. 2. Passive sonar.

The source signature is either random or deterministic in nature, and depends on both time and space. The global geometry and the relative source/receiver dynamics affect the spatial and temporal field distribution characteristics, inducing modulations on the spatial and temporal signal structure, as reflected at distinct points in space and instants in time by differences in arrival times (delays), measured frequency content (Doppler modulation), and signal strength (spherical spreading, attenuation). If the source signature is structurally known, the passive tracking relates to a stochastic decision upon the source energy distribution function, sensed by the receiver, on a space/time domain, or on its Fourier dual, a wave number/frequency space.

There are two modeling issues: The first involves the wave field's structure; the second concerns the global geometry and the relative dynamics.

Our study is restricted to a simple class of random wave fields, in which narrowband signals multiplied by a Rayleigh-Gaussian random parameter are observed, imbedded in an additive, spatially homogeneous, temporally white Gaussian noise process. The Rayleigh-Gaussian parameter, besides propagation losses and other model inaccuracies, reflects the fundamental constraint of lack of absolute phase reference.

As a consequence, passive tracking is achieved from the higher order phase modulations and not from the absolute phase reference (travel time delay).

We assume a planar geometry with the following linear constraints:

a. The receiving aperture is either omnidirectional or a linear structure.

b. The source/receiver dynamics is either stationary (with no relative motions) or linear; for example, the source follows a deterministic constant-speed linear path, as displayed in Fig. 3. In Part II, Section V, we discuss a more realistic model, with this nominal linear path disturbed by random accelerations.

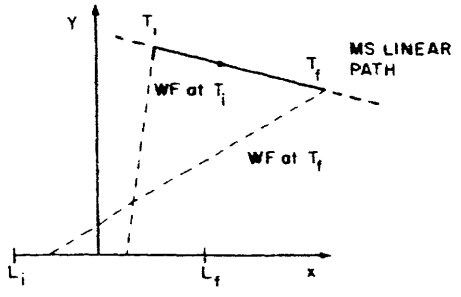

Fig. 3.
Passive tracking global geometry.

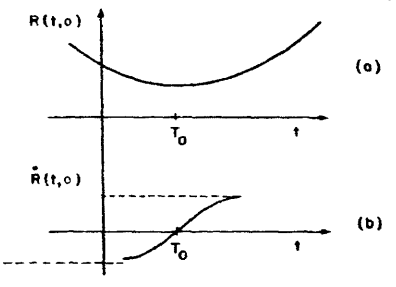

Fig. 4.
Doppler modulations induced on the temporal signal structure.

With these assumptions the resulting wave field distribution exhibits in time and space a "narrow-band" modulated structure, and thus is temporally nonstationary and spatially inhomogeneous. In Fig. 3, the distance between the source and the linear array's geometric center assumes the parabolic form of Fig. 4a, thereby inducing the time-variant Doppler modulation indicated in Fig. 4b. At point T_o of the stationary Doppler modulation (closest point of approach) the line defined by the array's geometric center and the source is normal to the path. Many practical positioning and navigational techniques are based on this elementary observation.

Although the ideal tracking system would use all available information conveyed by the received wave fields, we concentrate our analysis on the phase modulations of the narrow-band signals. In particular, we ignore the observed changes in the signal strength occurring either across the extended receiving aperture or during the finite time observation interval. These are of practical significance only, for example, when the total array dimensions are much larger than the source/receiver separation and hence represent higher order corrections that will not be pursued here. The passive tracking reduces then to a (nonlinear) phase demodulation problem.

1.3 RELATION TO OTHER WORK ON PASSIVE TRACKING

Narrow-band passive tracking has received considerable attention.[7, 12, 13] In most

of the studies three important simplifying assumptions are made.

S1. Planar wave fronts: The incoming wave fronts are assumed planar, with no curvature at global or local levels.

S2. Decoupling: The spatial and temporal aspects are decoupled.

S3. Finite parameter context: The relative source/receiver dynamics is stationary or deterministic.

Under these assumptions, the problem reduces to a "bearings only" situation, wherein the observable source/receiver parameter is the bearing angle and/or the source (radial) velocity. Ranging is accomplished either by an auxiliary active system or by ad hoc procedures such as simple triangulation or Doppler counting.

To our knowledge, only recently[14,15] has some preliminary analytical work with the (spatial) curvature of the wave fronts been reported, and inhomogeneous fields have received scant attention in other applied areas. An exception is in optics[16] where quadratic approximations to the wave front curvature are usually made in Fresnel diffraction studies. Also, the measurement of the nonlinear modulations of the spatial structure of the signals is emerging as a means of exploiting the wave front curvature in seismic profiling.[17,18] Another area is in wave theory where a mixture of plane and nonhomogeneous waves is considered when the distribution of a field scattered by a rough surface is to be found.[19]

We have previously studied passive narrow-band tracking when only S1 is assumed.[20,21] The motions were modeled by a stochastic finite-dimensional dynamical system. A spatial/time integrated approach, with planar wave front structure, was developed based on first-order approximations to the infinite-dimensional filter. Analysis substantiated by Monte Carlo simulations showed that the filter only tracked local dynamics, and lacked global range observability.

We shall concentrate on the fundamental issue of identifying the global range and the remaining source parameters. The model incorporates explicitly the spatially inhomogeneous, and/or the temporally nonstationary character of the wave fields (spatial and temporal curvature). The absence of the hypothesis of S1 is the essential underlying characteristic of the present study.

In Part I, Sections II-IV we assume S3, that is, classes of stationary or deterministic motions, with the passive tracking fitting a finite parameter estimation problem. In Sections II and III, S2 is naturally imbedded in the formulation, by restricting the analysis to stationary geometries (Sec. II) where no significant temporal diversity occurs, or to point sources and omnidirectional sensors (Sec. III) where no meaningful spatial diversity is available. In Section IV we consider spatially extended receivers and moving sources, focusing on the implications of space/time factorability and space/time coupling.

In Part II, Section V, we generalize the class of motions to include dynamics generated by a finite-dimensional stochastic system. We study a "hybrid" practical solution to the problem resulting from a compromise between the two conflicting requirements

of global identifiability of the relative source/receiver geometry and minimization of the receiver's complexity.

In Section VI we discuss applications of the theory to three problems of practical significance: (i) precision landing in air traffic control; (ii) underwater acoustic positioning; and (iii) navigation by passive means, with orbiting and geostationary satellites. We also present the results of Monte Carlo simulation studies.

We review our main conclusions in Section VII and also expand on possible generalizations and extensions of the present work.

II. SYNTHETIC ARRAY WITH STATIONARY SOURCE (SASS)

In this section we study a class of narrow-band passive tracking systems arising in two extreme situations of practical significance. In the first, a stationary array detects and estimates the location of a stationary source. In the second, a moving omnidirectional observer that generates a synthetic array tracks a stationary source. We refer to both as Synthetic Array with Stationary Source (SASS). We consider the simplest estimation hierarchy, that of a finite parameter estimation model. In describing the model we emphasize the space/time geometric dualism of both problems and establish in which sense they are equivalent. We present a practical implementation to the maximum-likelihood receiver and analyze the generalized ambiguity function characterizing the processor's fundamental structure. Finally, we study the error constraints on this receiver, derive performance bounds, and discuss threshold effects.

2.1 MODEL GEOMETRY

We assume a planar geometry (Fig. 5) and a point source radiating narrow-band

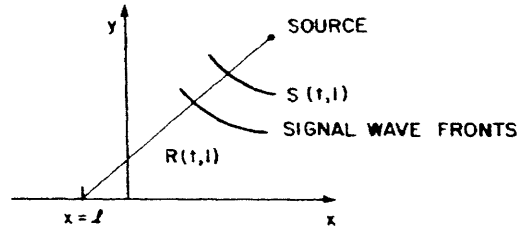

Fig. 5. Planar geometry for a stationary source.

signals, which at time t and point ℓ in space are given by

$$S(t, \ell) = \sqrt{2}\ \mathrm{Re}\left\{\tilde{s}(t, \ell)\ \exp j\omega_c t\right\}. \tag{1}$$

The wave fronts at the receiving aperture are

$$r(t, \ell) = \sqrt{2}\ \mathrm{Re}\left\{\tilde{r}(t, \ell)\ \exp j\omega_c t\right\} \tag{2a}$$

with

$$\tilde{r}(t, \ell) = \tilde{s}(t, \ell) + \tilde{w}(t, \ell). \tag{2b}$$

The signal complex envelope is

$$\tilde{s}(t, \ell) = \left(\frac{E_r}{LT}\right)^{1/2} \tilde{b}\ \exp\left[j\,\frac{2\pi}{\lambda}\,R(t, \ell)\right], \tag{2c}$$

where E_r = total received energy during the observation interval $[-T/2, T/2]$, and by an array of dimension parameter L; $R(t, \ell)$ = distance (range) at time t from the source

to the array element at location ℓ; $\lambda = \frac{2\pi f}{c} = \frac{\omega_c}{c}$ = wavelength, and $\tilde{b} = b \exp(j\psi)$. Here b is a Rayleigh-distributed random variable and ψ is uniformly distributed in $[0, 2\pi]$. We note that $\tilde{b}$ is a complex Gaussian random variable,

$$E|\tilde{b}| = 0 \tag{3a}$$

$$E|\tilde{b}|^2 = 2\sigma_b^2 \tag{3b}$$

accounting for model inaccuracies that, for example, are due to variations on the radiated signal power about some nominal value, fading in the transmission medium, etc. More important from a structural point of view, the unknown phase ψ represents lack of knowledge of the absolute phase (incoherent receiver). This is a fundamental constraint, modeling the fact that global range estimation is achieved from the modulation induced on the signal structure, not from the absolute phase reference.

The complex noise $\tilde{w}(t, \ell)$ is assumed spatially homogeneous and temporally wideband (white) Gaussian, with spectral height N_o.

2.1.1 Stationary Array/Stationary Source

In this case the point stationary source is tracked by a linear stationary array, as shown in Fig. 6. The linear array is oriented along the x axis and the source parameter vector is $A = \begin{bmatrix} R_o \\ \sin\theta \end{bmatrix}$.

The choice of $\sin\theta$ over the angle parameter itself corresponds to a wave number type of dependence for the space/time processing techniques. This removes from the model the ambiguity characteristic of a linear array, that it can only solve for $\theta \in \left[-\frac{\pi}{2}, \frac{\pi}{2}\right]$. This is immediately apparent from Eq. 4. Nevertheless, we refer to this parameter as the bearing angle or bearing information.

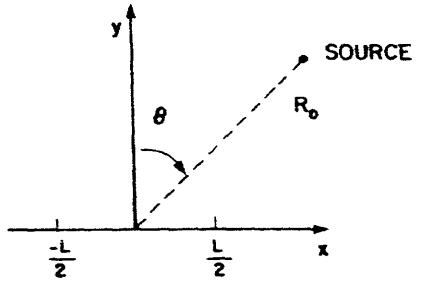

Fig. 6.
Stationary Array/Stationary Source geometry.

The range function at the array location ℓ is

$$R(t, \ell) = \{R_o^2 + \ell^2 - 2\ell R_o \sin\theta\}^{1/2}, \qquad \ell \in [-L/2, L/2],\ t \in [-T/2, T_2]. \tag{4}$$

We observe from Eq. 4 that the source parameters are imbedded in the spherical curvature of the incoming wave fronts, as observed across the array (targets in the near field).

2.1.2 Moving Array/Stationary Source (Sometimes Referred to in the Sequel as MASS)

In this problem a moving omnidirectional sensor locates a stationary source. We assume that the observer motion is perfectly known with respect to a rigid framework,

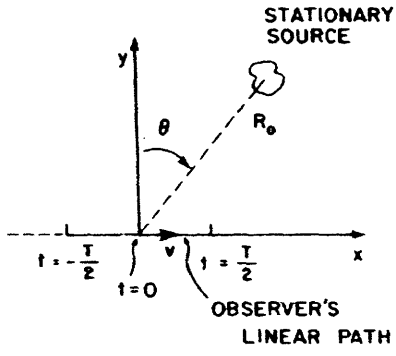

Fig. 7.
Moving Array/Stationary Source configuration.

and is constrained to a linear path with constant speed v. Figure 7 shows the parametrization to be used.

As in the preceding case, the source parameter vector is $A = \begin{bmatrix} R_o \\ \sin\theta \end{bmatrix}$. At time t, the range is

$$R(t) = \{R_o^2 + v^2t^2 - 2vtR_o \sin\theta_o\}^{1/2}, \quad t \in [-T/2, T/2],\ \ell \in [-L/2, L/2]. \tag{5}$$

Equation 5 represents the range function in terms of the source parameters at the midpoint of the observation interval. This introduces no a priori reference location assumptions, and allows further algebraic simplification of the final results. Note that we have assumed that the omnidirectional sensor is a nonlinear array with dimension parameter L.

Identification of the length ℓ with vt in Eqs. 4 and 5 emphasizes the theoretical similarity underlying the measurement of the source parameters in both applications. The quantitative results for one problem are immediately translated into the other's, by substituting L for vT or vice versa. In the sequel we shall let

$$Z = \frac{L}{2} \quad \text{or} \quad Z = \frac{vT}{2} \tag{6}$$

and define the spatial variable

$$x = \ell \quad \text{or} \quad x = vt,$$

depending on the specific application.

The mathematical equivalence of the two situations stresses their space/time dualism. In the stationary array/stationary source context the spherical curvature of the incoming wave fronts induces a nonlinear spatial modulation on the signal, which is measured by the spatially extended linear array. With the moving omnidirectional configuration that we have just described, the range and angle information are conveyed by the nonlinear temporal modulations induced on the signal structure by the relative dynamics (see Fig. 8). This can be contrasted with a synthetic aperture radar (SAR),[22] which is

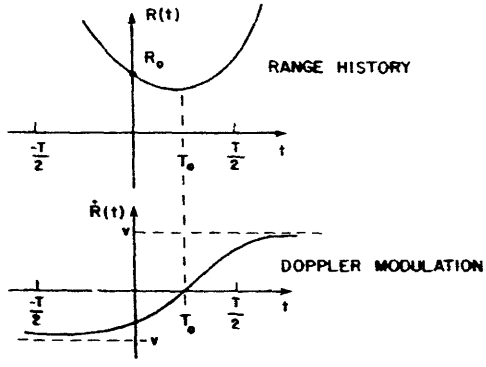

Fig. 8.
Modulations induced on the temporal signal structure.

an airborne system following a prescribed path (observer's motion constraints) and carrying the scanning beam that illuminates the terrain. The observer's motion has the net effect of generating a longer effective baseline array. The reflected echo arrives at the SAR receiver phase modulated by the relative motion. These modulations give to the two-dimensional signal a structure similar to a frequency-modulated signal, compressing it in the angle direction (referred to as azimuth). SAR recovers the range from an active modulation, while the azimuth is estimated from the "passive" modulations induced by the relative motions. The SASS problem with the omnidirectional sensor represents the other extreme where no "active" range measurement occurs. In other words, the global target parameters are to be reconstructed solely from the modulations induced by the relative motions.

The range phase, Eqs. 5 or 6, can be approximated by truncated Taylor's series expansions. For targets in the far field, known as the Fraunhofer zone, a linear

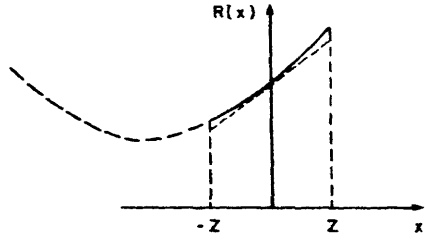

Fig. 9.
Source in the far field (linear approximation).

expansion is valid (see Fig. 9) and the phase is

$$R(x) = \left(R_o^2 + x^2 - 2xR_o \sin\theta\right)^{1/2} \approx R_o - x \sin\theta, \qquad x \in [-Z, +Z]. \tag{7}$$

Given the incoherent phase model assumed, the wave fronts are practically planar at the receiver front end and with lack of any phase reference they convey no range information.

For targets in the so-called Fresnel zone a second-order expansion is appropriate (Fig. 10), which leads to

$$R(x) \approx R_o - x \sin\theta + \frac{(x \cos\theta)^2}{2R_o}, \qquad x \in [-Z, +Z]. \tag{8}$$

The range may now be observed from the second-order modulations induced on the spatial/temporal signal structure. A suboptimal estimation algorithm may be developed

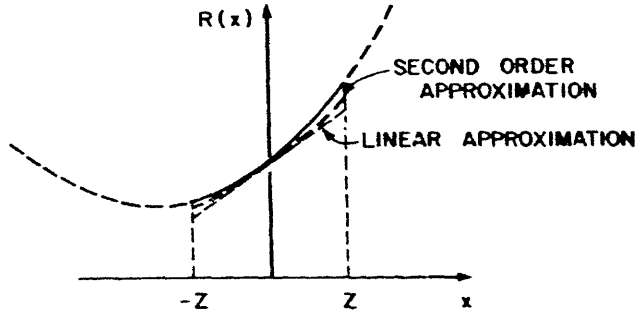

Fig. 10. Source in the Fresnel zone (quadratic approximation).

by first tracking the Doppler modulation and the Doppler rate by means of phase-locked loops, and then performing the nonlinear transformation

$$\sin\theta = -\dot{R}_o \tag{9a}$$

$$R_o = \frac{1 - \dot{R}_o^2}{\ddot{R}_o}, \tag{9b}$$

where

$$(i) \quad R_o = \left.\frac{d^i R(x)}{dx^i}\right|_{x=0}. \tag{9c}$$

We conclude that the identification of the source/receiver separation (range) requires synthesis of the extended apertures measuring the higher order effects induced on the signal structure.

2.2 RECEIVER DESIGN

Under the white and Gaussian assumptions on the noise and Rayleigh parameter statistics, the optimum receiver for the parameter estimation problem that we have described is a maximum-likelihood (ML) processor that is essentially a matched filter followed by an envelope detector (see Van Trees[23,24]). The filter maximizes a monotonic function of the ML-function (its natural logarithm) on the parameter space. The log ML-function[25] is

$$\ln \Lambda_1(A) = \frac{1}{N_o} \frac{\bar{E}_r/N_o}{1 + \frac{\bar{E}_r}{N_o}} \left|\tilde{L}(\bar{A})\right|^2, \tag{10a}$$

where A is the parameter vector,

$$\bar{E}_r = \left(2\sigma_b^2\right) E_r = \text{average received energy,}$$

and

$$\left|\tilde{L}(\bar{A})\right|^2 = \left| \int_{-T/2}^{T/2} dt \int_{-L/2}^{L/2} dr\, \tilde{r}(t, \ell)\, \tilde{s}^*(t, \ell, \bar{A}) \right|^2. \tag{10b}$$

Notation

1. The inner product in Eq. 10b is abbreviated

$$\left|\tilde{L}(\bar{A})\right|^2 = \left|\langle \tilde{r}, \tilde{s}(\bar{A}) \rangle\right|^2. \tag{10c}$$

2. The star stands for complex conjugation.

3. To avoid cumbersome expressions, we do not always show explicitly the functional dependence of the several quantities on all variables and/or source parameters, exhibiting only those of most concern in the specific argument; for example, the signal will generally be represented by $\tilde{s}(t)$ or $\tilde{s}(t, \ell)$, although on occasion we use $\tilde{s}(t, \ell, A)$.

The ML estimator is unrealizable in practice, since it requires the (stochastic) maximization of $\left|\tilde{L}(\bar{A})\right|^2$ over the (continuous) parameter space Ω. A practical suboptimal receiver can be constructed, however, by exploiting the signal autocorrelation function and the noise statistics.

Substituting the value of the received signal given by Eq. 2 in the expression for the log ML-function, we obtain

$$\left|\tilde{L}(\bar{A})\right|^2 = \left|\langle \tilde{s}(A), \tilde{s}(\bar{A}) \rangle + \langle \tilde{w}, \tilde{s}(\bar{A}) \rangle\right|^2, \tag{10d}$$

where A and $\bar{A}$ represent the actual and scanning parameter values.

In the absence of additive measurement noise, the output of the ML receiver is

$$|\tilde{L}(\bar{A})|^2 = |\langle \tilde{s}(A), \tilde{s}(\bar{A})\rangle|^2 = |\psi_s(A, \bar{A})|^2 = \phi_s(A, \bar{A}). \tag{11}$$

This is a scaled version of the so-called generalized ambiguity function, which will be discussed soon. The noise component in Eq. 10d, $\tilde{w}(\bar{A}) = \langle \tilde{w}, \tilde{s}(\bar{A})\rangle$, is a Gaussian complex random variable with zero mean and variance N_o.

At two scanning points A_1, $A_2 \in \Omega$

$$E[(\tilde{L}(A_1) - \psi_s(A, A_1))(\tilde{L}(A_2) - \psi_s(A, A_2))^*] = E[\tilde{w}(A_1)\,\tilde{w}^*(A_2)] = \psi_s(A_1, A_2). \tag{12}$$

This expression shows that since A_i is scanned over Ω, the noise samples at the output of the matched filter exhibit a crosscorrelation given in terms of the signal autocorrelation function. Because this function essentially has a finite extent, which will be determined in the sequel, we define a coherence or correlation distance in Ω. Points whose separation is greater than this distance lead to uncorrelated noise components $\tilde{w}(A_i)$ at the output of the ML processor. This suggests a two-step implementation for the ML algorithm. The first substitutes the continuous by a discretized search, where the scanned points are separated by the coherence distance. The region of interest is divided in cells (whose form and number M is to be determined subsequently), and in each one we assume that the parameter vector takes only a fixed value (e.g., the center of the cell). With this discrete structure for Ω, we perform a crude maximization of the log ML-function, by computing it at all grid vertices, and choosing the point at which it is maximum. The receiver performs a "largest of" M-ary hypothesis decision with uncorrelated signals; at this stage, it has a two-dimensional bank of matched filters followed by square envelope detectors. Figure 11 illustrates the "largest of" receiver.

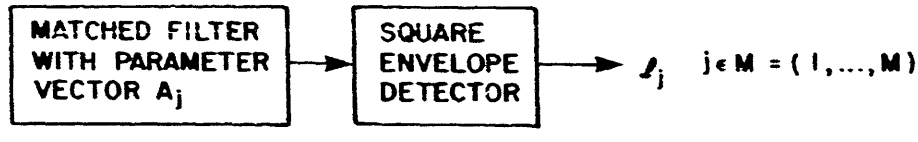

Fig. 11. Coarse search ML algorithm.

The coarse search returns a crude estimate $\tilde{\lambda}_{m\ell} = A_i$ for which $\ell_i = \max_{j \in M} \ell_j$ (see Fig. 11).

In the second step the mechanism accomplishes a local maximization of the log ML-function about $\tilde{A}_{m\ell}$. It can be done by a finer search procedure or by any other method, e.g., a steepest-descent. The approach in two steps to the ML receiver was first taken by Woodward[26] in the context of (active) radar range measurements, and the technique is referred to in the literature of frequency estimation as frequency-shift keying (FSK).

2.3 GENERALIZED AMBIGUITY FUNCTION

We have seen that the statistical behavior of the ML receiver is determined by $\phi_s(A,\bar{A})$. We now give some preliminary definitions.

Definition 1. The signal autocorrelation function is

$$\psi(A,\bar{A}) = \langle \tilde{s}_n(A), \tilde{s}_n(\bar{A}) \rangle, \tag{13a}$$

where $\tilde{s}_n(A)$ stands for the signal normalized version

$$\tilde{s}_n(A) = \frac{1}{\sqrt{LT}} \exp\left\{ j \frac{2\pi}{\lambda} [t - R(t,\ell,A)] \right\}, \quad t \in \left[-\frac{T}{2}, \frac{T}{2} \right], \ \ell \in \left[-\frac{L}{2}, \frac{L}{2} \right]. \tag{13b}$$

Definition 2. The generalized ambiguity function (GAF) is

$$\phi(A,\bar{A}) = |\psi(A,\bar{A})|^2. \tag{13c}$$

Substitution of Eq. 13b in Definition 2 leads to

$$\phi(A,\bar{A}) = \left| \frac{1}{LT} \int_{-T/2}^{T/2} dt \int_{-L/2}^{L/2} d\ell \exp\left[j \frac{2\pi}{\lambda} \Delta R(t,\ell,A,\bar{A}) \right] \right|^2, \tag{13d}$$

where the range phase difference is

$$\Delta R(t,\ell,A,\bar{A}) \triangleq R(t,\ell,A) - R(t.\ell,\bar{A}). \tag{13e}$$

We observe the properties

PROPERTY 1. $\phi(A,A) = 1$.

PROPERTY 2. $\phi(A,\bar{A}) \leq \phi(A,A)$.

By applying these definitions to the SASS context, and working with the general variable x, we find that the GAF is

$$\phi(A,\bar{A}) = \left| \frac{1}{2Z} \int_{-Z}^{Z} dx \exp\left[j \frac{2\pi}{\lambda} \Delta R(x,A,\bar{A}) \right] \right|^2 \tag{14}$$

with Z defined in (6), and the range phase difference given by

$$\Delta R(x,A,\bar{A}) = \left(R_o^2 + x^2 - 2xR_o \sin\theta \right)^{1/2} - \left(\bar{R}_o^2 + x^2 - 2x\bar{R}_o \overline{\sin\theta} \right)^{1/2}. \tag{15}$$

Equation 14 can be renormalized:

$$\phi(A,\bar{A}) = \left| \frac{1}{2} \int_{-1}^{1} dz \exp j \frac{2\pi Z}{\lambda} \left[\left(r_o^2 + z^2 - 2zr_o \sin\theta \right)^{1/2} - \left(\bar{r}_o^2 + z^2 - 2z\bar{r}_o \overline{\sin\theta} \right) \right] \right|^2,$$

where $z = \frac{x}{Z}$ and $r_o = \frac{R_o}{Z}$. Since the GAF plays an important role in evaluating the

ML receiver's ability to locate the source, it is important to have a clear idea of its structure. From active radar system theory we know that an impulsive ambiguity, i.e., a narrow spike at the source location, is a desirable pattern. This idealized ambiguity is physically unrealizable because of the volume invariance of the time frequency radar ambiguity function, but it suggests an optimal limiting form to look for when designing the radar modulating signal.

In the passive problem, we have no control over the signal design, since it is radiated by the source. Our task is to analyze the GAF structure, in order to quantify the receiver's capability to locate the target.

We observe that the GAF is not a function of the vector difference $A-\bar{A}$ but also depends on the actual source parameter values. This contrasts with Woodward's radar frequency-time ambiguity function, but is similar to the dependence of the ambiguity function associated with the problem of echo-locating, high-velocity, accelerating targets with active systems.[27]

This report does not deal with the important questions of designing the array geometry and weighting pattern. We restrict the analysis to linear structures with uniform shading, addressing the basic questions of source parameter identifiability and ultimate performance bounds for the least complex situation of practical significance, that of spatially homogeneous and temporally white background noise. In the presence of directional noise sources higher order array processing techniques may be required, which shape the array beam pattern to the statistical environment and provide for null cancellations at the wave number space direction of the noise interference, at the cost of undesirable sidelobes and/or deterioration in performance in the presence of the white background noise alone. We shall not pursue here these high-resolution array processing techniques, since they represent second-order complications in the problem, but refer the reader to Baggeroer[28] and Van Trees,[29] who deal with these methods in the "bearings only" context.

Figure 12 presents three-dimensional and contour plots of the GAF for typical values of the parameters. The function exhibits a main peak centered at the source location, whose contours are essentially ellipses, and some subsidiary structure outside the main lobe. In the absence of the additive observation white noise the output of the filters is a point on this curve, and the maximum-likelihood (ML) estimates are the parameters for the matched filter whose output leads to the absolute maximum of the function. In the presence of measurement disturbances, the noise contribution at the filter output may lead to an absolute maximum that is in error. In order to quantify the statistics of these errors, we need a better quantitative understanding of the GAF. We need to know the dimensions of its main lobe and the size of any secondary peak in the subsidiary GAF structure, i.e., outside the main lobe. Both graphical and analytical techniques will be used.

In Appendix A we do an approximate analysis of the GAF by assuming polynomial approximations to the phase range difference. We also derive bounds on the rate of

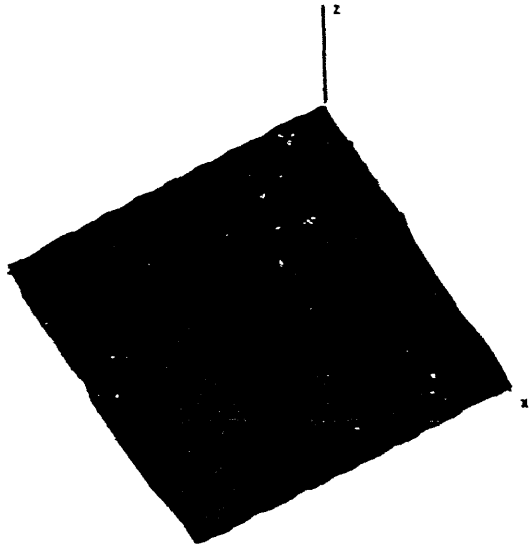

(a)

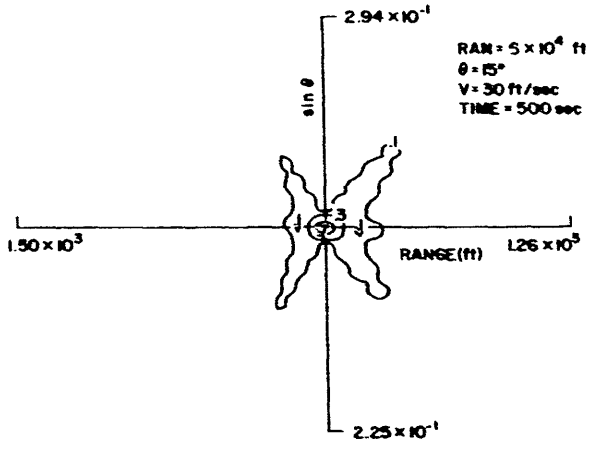

(b)

Fig. 12. (a) Three-dimensional range/angle ambiguity structure (X=1/4).
(b) Contour range/angle ambiguity structure (X=1/4).

falloff of the ambiguity structure for these approximations and for the general expression. We restrict our attention to the main results therein, and combine them with a pictorial representation of the GAF for several values of the important parameters, to obtain a complete qualitative and quantitative evaluation of the GAF.

2.3.1 Approximate Analysis of the Generalized Ambiguity Function (GAF)

In Appendix A we approximate the range phase difference by a polynomial expansion

$$\Delta R(x, A, \bar{A}) \approx \sum_{i=0}^{n} \Delta_i x^i, \tag{16a}$$

where we define

$$\Delta_i \triangleq \frac{1}{i!} \Delta R_o^{(i)} = \frac{1}{i!} \left[\frac{d^i R(x, A)}{dx^i} - \frac{d^i R(x, \bar{A})}{dx^i} \right]_{x=0}. \tag{16b}$$

For a linearized expansion the GAF has a sinc^2 structure

$$\phi(A, \tilde{A}) \approx \text{sinc}^2 \left[\frac{2\pi}{\lambda} \Delta(\sin\theta)\, Z \right] = \left| \frac{\sin \frac{2\pi}{\lambda} \Delta(\sin\theta)\, Z}{\frac{2\pi}{\lambda} \Delta(\sin\theta)\, Z} \right|^2 \tag{17}$$

as illustrated in Fig. 13. As we depart from the origin, the maxima decrease monotonically along the angle parameter axis with the second maximum reduced to approximately 4.5% of the value at the origin.

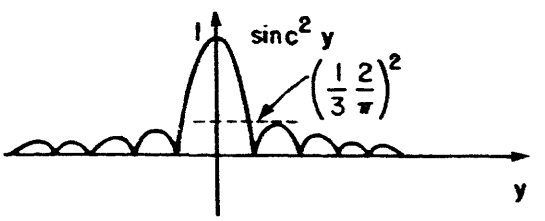

Fig. 13. Linearized ambiguity sinc structure.

The ambiguity pattern is constant along the range parameter axis, and the linearized GAF presents no range focusing ability. This is not surprising, since the range is estimated from the higher order modulations induced on the signal structure by the waveform curvature, and not from the absolute phase reference. In analogy to optics, this amounts to saying that for targets at the Fraunhofer zone the incoming waveforms are planar at the observer site, with no information on the range conveyed to the passive receiver. The bearing is measured from the linear delays recorded either across the array or by the moving observer along its linear path. For a quadratic approximation

and along the radial line $\Delta\dot{R}_o = 0 \Longrightarrow \Delta(\sin\theta) = 0$, the ambiguity function is approximated by

$$\phi(A,\bar{A}) = \left|\frac{1}{\Sigma}\mathcal{F}(\Sigma)\right|^2, \tag{18a}$$

where

$$\Sigma = \left(\frac{\pi}{\lambda}\Delta\left(\frac{\cos^2\theta}{R_o}\right)\right)^{1/2} Z \tag{18b}$$

and $\mathcal{F}(\cdot)$ is the (exponential) Fresnel integral, whose graph in the complex plane gives the cornu spiral (Fig. 14). The ambiguity function along the radial-acceleration axis, parameter $\Delta\ddot{R}_o$, is shown in Fig. 15. The first minimum occurs at $\Sigma_m \cong 1.9$, and the second local maximum at $\Sigma_{2M} \approx 2.26$, where $\phi(A,\bar{A}) \approx .132$; i.e., it is reduced to

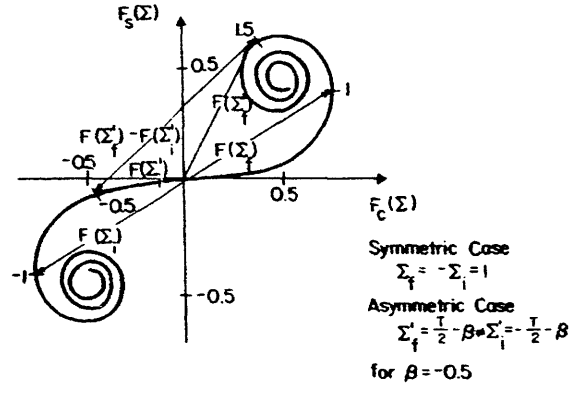

Fig. 14.
Cornu spiral.

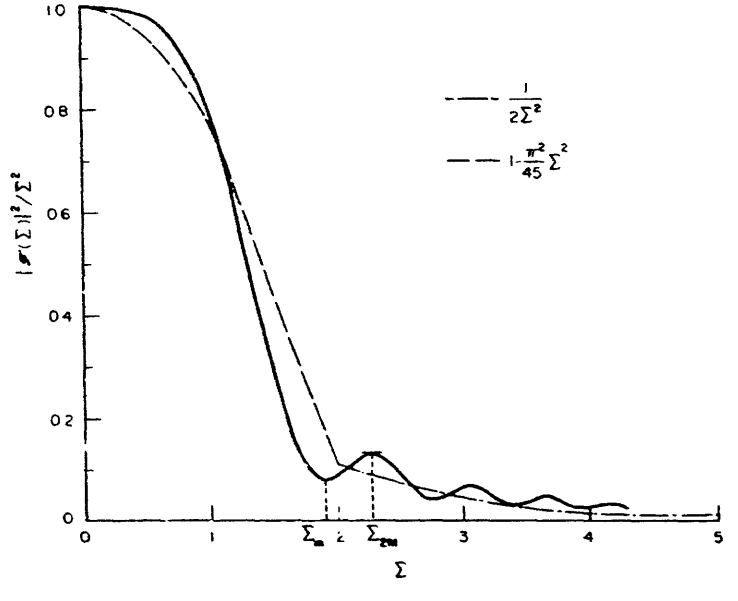

Fig. 15.
Quadratic (Fresnel) ambiguity structure with local and asymptotic approximations.

approximately 13% of its maximum value 1, at the origin. By establishing the equivalence of the signal correlation function $\psi(A, \bar{A}) = \frac{1}{\Sigma} \mathcal{F}(\Sigma)$ and a certain confluent hypergeometric function, we apply known developments[30] in Appendix A to obtain local expansions (about $\Sigma = 0$; Eq. A.19) and asymptotic (large Σ; Eq. A. 20) expansions. From the latter we find that the ambiguity function falls off along the radial-acceleration line as $\phi(A, \bar{A}) \approx \frac{1}{2\Sigma^2}$.

For the general quadratic phase approximation the GAF is

$$\phi(A, \bar{A}) \cong \left| \frac{1}{\Delta\Sigma} \left[\mathcal{F}(\Sigma_f) - \mathcal{F}(\Sigma_i) \right] \right|^2, \tag{19}$$

where $\Delta\Sigma = \Sigma_f - \Sigma_i$, with $\Sigma_f = \sqrt{\Delta_2} \left(Z + \frac{\Delta_1}{2\Delta_2} \right)$, and $\Sigma_i = \sqrt{\Delta_2} \left(-Z + \frac{\Delta_1}{2\Delta_2} \right)$.

In terms of the cornu spiral representation of the Fresnel integral, $\mathcal{F}(\Sigma_f) - \mathcal{F}(\Sigma_i)$ is a running vector based on the spiral, i.e., with both end points on the curve (for a specific example see Fig. 14). The ambiguity function is given by the modulus squared of this vector, divided by the square of the distance of the arguments $\Sigma_f - \Sigma_i$.

2.3.2 General Case

We now study graphically the structure of the GAF as given by the exact expression (14).

We presented in Fig. 12 three-dimensional and contour plots of the GAF for source parameters given by

$$A_a = \begin{bmatrix} R_{o_a} \\ \sin \theta_a \end{bmatrix} = \begin{bmatrix} .6 \times 10^5 \text{ ft} \\ \sin 15^\circ \end{bmatrix}$$

with the geometric parameter $X = \frac{Z}{R_o} = \frac{1}{4}$. The line of sight for the three-dimensional graph is given by the angles θ and ϕ illustrated in Fig. 16. For Fig. 12a these parameters are $\theta = 150^\circ$, $\phi = 210^\circ$; that is, the GAF is viewed from behind and below.

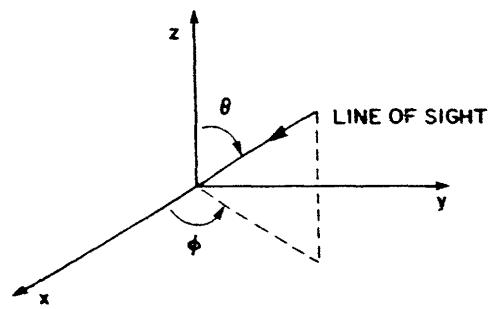

Fig. 16. Line-of-sight definition for three-dimensional graphs.

Figures 17 and 18 show the ambiguity structure for a smaller value of the geometric parameter, $X = \frac{1}{40}$. Reducing X (smaller array or shorter observation interval, or equivalently for the same synthetic aperture, larger range), results in a flatter main lobe with a larger ridge. This means that whenever all other conditions are identical (e.g., source/receiver separation, signal-to-noise ratio) the simultaneous range and angle focusing requires larger synthetic arrays, as we would expect. In the sequel we shall quantify these statements.

Finally, Fig. 19 displays the ambiguity pattern for a large value of X, X = 6, referred to as the close observer configuration. It shows the asymptotic behavior of the GAF as the (synthetic) array length grows compared with the source/receiver separation.

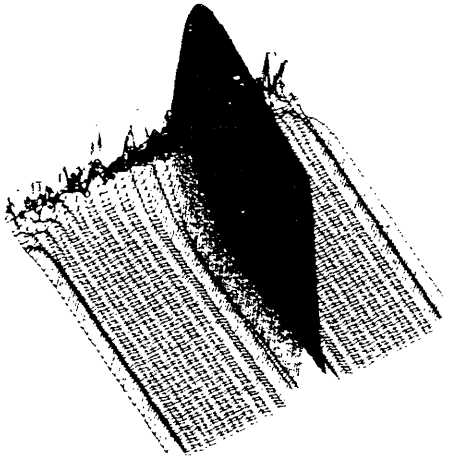

Fig. 17.
Three-dimensional range/angle ambiguity structure (X=1/40).

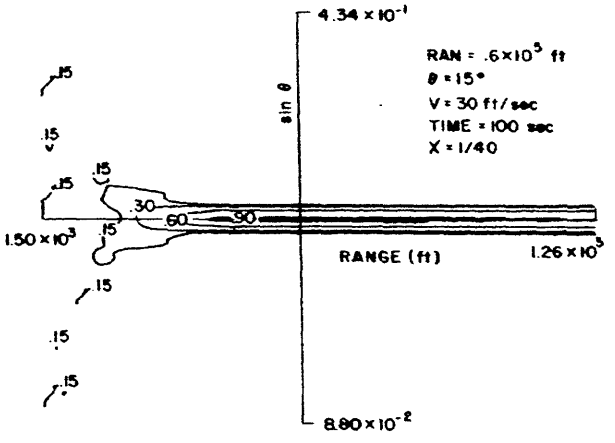

Fig. 18.
Contour range/angle ambiguity structure (X=1/40).

We note the scale changes in the different figures. Along the sin θ axis the ambiguity function has been scanned at points whose positions were determined by the sinc^2 structure of Eq. 17; i.e., the elementary interval between scanning points was

$$\Delta(\sin\theta) \approx \frac{1}{n}\frac{\lambda}{2L}, \quad n \text{ some integer} \geq 2.$$

Along the range axis the scale is essentially the same as in Figs. 12b and 18, but has changed drastically as shown in Fig. 19, reflecting the sharper lobe for large parameter X.

The graphs display the peaked structure of the GAF, and also show that outside the

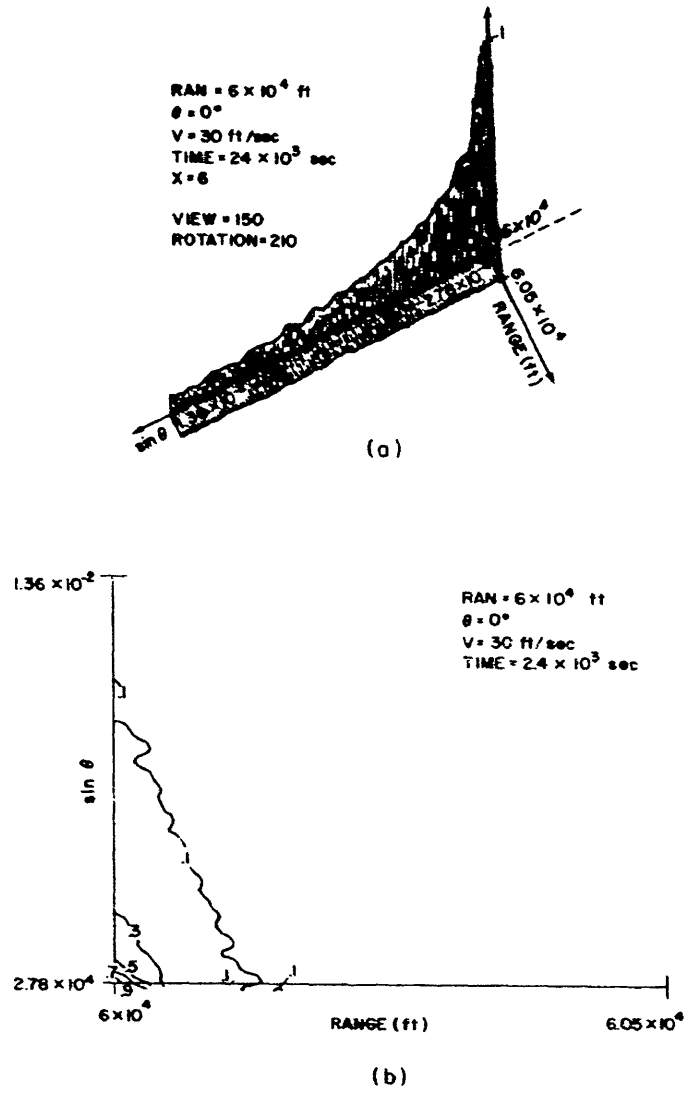

Fig. 19. Range/angle ambiguity structure (X = 6). (a) three-dimensional structure, (b) contour.

main lobe the secondary peaks are negligible.

Both local and asymptotic analyses can be pursued in much the same terms. The local analysis determines the GAF main lobe structure; the asymptotic analysis studies the GAF rate of falloff.

From the figure we see that the equal height contours on the main lobe are approximately ellipses. Since for higher dimensions this generalizes to ellipsoids, we refer to it as the GAF main lobe ellipsoidal structure. Given the ellipsoidal structure, the dimensions of the main lobe are determined from a second-order analysis of the GAF on the parameter space Ω, i.e., on the errors on the parameters. That is done in connection with our discussion of the performance of the ML receiver. The

second-order analysis should not be confused with the second-order analysis carried out in Appendix A, which is in the time variable.

The bounds on the subsidiary ambiguity pattern are derived in Appendix A by application of the method of stationary phase, and are summarized by Eqs. A.38, A.40, and A.41. The bounds at each point

$$\bar{A} = \begin{bmatrix} \bar{R}_o \\ \overline{\sin\theta} \end{bmatrix}$$

of the parameter space Ω depend on the behavior of the range phase difference at that point in the observation interval $[-Z, Z]$, that is, on the order n of the first nonzero derivative of the range phase difference in x, $x \in [-Z, Z]$. If n is even,

$$\phi(A, \bar{A}) \sim \left[\frac{1}{Z} \frac{\Gamma(1/n)}{\sqrt[n]{\frac{2\pi}{\lambda} \overset{(n)}{\Delta R}(x_o)/n!}} \right]^2 . \tag{20a}$$

If n is odd >1,

$$\phi(A, \bar{A}) \sim \left[\frac{1}{Z} \frac{\Gamma(1/n) \cos\frac{\pi}{2n}}{\sqrt[n]{\frac{2\pi}{\lambda} \overset{(n)}{\Delta R}(x_o)/n!}} \right]^2 , \tag{20b}$$

where $x_o[-Z, Z]$ is the point where the lower order derivatives vanish at $\bar{A} \in \Omega$. For n = 1

$$\phi(A, \bar{A}) \sim < \left[\frac{1}{2Z \frac{2\pi}{\lambda}} \left(\frac{1}{|\dot{\Delta R}(Z)|} + \frac{1}{|\dot{\Delta R}(-Z)|} \right) \right]^2 . \tag{20c}$$

Equations 20 exhibit the decaying of the ambiguity pattern in terms of the inverse of a certain power of the errors of the least order nonvanishing derivative at x_o; that is, in terms of $\left(\overset{(n)}{\Delta R} \right)^{-2/n}$. We refer to this rate of decay as the GAF hyperbolic rate of falloff. For the problem at hand, and except for degenerate condition (end-fire), n = 1 or n = 2.

To summarize briefly, we have now analyzed the ambiguity pattern for the SASS problem with narrow-band passive signals. For targets in the far field no range focusing is possible, and the stationary array/stationary source problem reduces to the classical passive bearing measurement problem. The moving omnidirectional sensor with stationary array compares conceptually with the "passive" azimuth measurement in SAR systems. The ambiguity function has a sinc^2 structure that is constant along the range axis. For targets in the Fresnel zone (quadratic approximation) or in the near field, the ambiguity structure is concentrated on a main lobe, and no significant sidelobes arise. By a bounding procedure, coupled with the pictorial representation of the GAF, we have concluded that the limiting behavior of the GAF for large parameter errors is essentially

negligible. We can then extrapolate the graphic displays to the whole parameter space by assuming that the ambiguity function is concentrated in its main lobe and is zero in the remaining space.

2.4 PERFORMANCE ANALYSIS

We have described a practical two-stage implementation for the maximum-likelihood (ML) receiver. In the first stage the parameter space is discretized by a grid. The algorithm performs a coarse search, aiming at the grid point that is closest to the actual parameter values. In the second stage a finer search about the previous value returns the approximate ML estimate. In other words, the maximization of the ML-function is accomplished by a global step, performing a multiple hypothesis decision ("largest of" receiver[31]), which chooses a cell from the assumed discrete grid, followed by a local step, maximizing the ML-function (or equivalently its logarithm) on the chosen cell of the parameter space.

We now discuss the estimation errors induced by the algorithm for this implementation and find bounds constraining its performance.

Let A_j represent the j^{th} component of the source parameter vector A. From the previous description, the mean-square error on the estimate $A_{jm\ell}$ will be

$$E\left(A_{j_\epsilon}^2\right) \triangleq E\left[(A_j - A_{jm\ell})^2\right] = E\left(A_{j_\epsilon}^2 \mid \epsilon\right) \Pr(\epsilon) + E\left(A_{j_\epsilon}^2 \mid \epsilon^c\right)(1-\Pr(\epsilon)), \tag{21}$$

where ϵ is the event that a decision error or diversion occurred, i.e., that the wrong grid interval was chosen by the "largest of" receiver; ϵ^c is the complement of ϵ, i.e., the event that no diversion occurred and the correct cell has been chosen on the first step; and $\Pr(\epsilon)$ is the probability of the event ϵ.

The computation of the various quantities in Eq. 21 depends on the design and dimension of the grid discretizing the parameter space. Given the ellipsoidal structure of the ambiguity function, we assume an ellipsoidal mode grid, i.e., that the grid cell blocks are approximately ellipsoids. The size of these elementary cells is determined from the dimensions of the GAF main lobe. Retention of up to second-order terms in its Taylor's series expansion about the actual source parameter value A_a leads to

$$\phi(A, A_a) \cong \phi(A_a, A_a) + \left[\nabla_A \phi(A, A_a)\Big|_{A=A_a}\right]^T \Delta A + \frac{1}{2} \sum_{i,j} \left.\frac{\partial^2 \phi(A, A_a)}{\partial A_i \partial A_j}\right|_{A=A_a} \Delta A_i \Delta A_j,$$

where

$$\Delta A = A - A_a = \begin{bmatrix} \text{---} \\ A_j - A_{ja} \\ \text{---} \end{bmatrix}$$

and $\nabla_A = \text{grad}_A$. Since $\phi(A_a, A_a) = 1$, and by direct substitution

$$\nabla_A \phi(A, A_a)\Big|_{A=A_a} = 0, \tag{22}$$

the GAF is approximated by

$$\phi(A, A_a) \cong 1 - \Delta A^T \mathcal{M}\, \Delta A \tag{23}$$

where we used the following definition.

Definition 3. The mean-square spread matrix (MSSM) $\mathcal{M}$ is given by

$$\mathcal{M} = -\frac{1}{2}\left[\frac{\partial^2 \phi(A, A_a)}{\partial A_i A_j}\Big|_{A=A_a}\right]_{i,j}.$$

Given the quadratic approximation (23), we note that the spread matrix quantifies the extension of the main lobe of the GAF, thereby determining the coherence distance of the noise samples previously referred to. Let $Q(\Delta A) = \Delta A^T \mathcal{M}\, \Delta A$. Then

$$\phi(A, A_a) \cong 1 - Q(\Delta A). \tag{24}$$

The ambiguity function will have a stationary point that is a maximum at $A = A_a$ when, besides (22), we also have $\mathcal{M} > 0$, i.e., whenever $Q(\Delta A)$ is a positive-definite quadratic form. Since the ambiguity function by definition is $\phi(A, A_a) \geq 0$, we see from Eq. 24 that its first minimum occurs approximately when

$$Q(\Delta A) = 1. \tag{25}$$

Equation 25 gives the dimensions of the ellipsoid defining the elementary cell of the discrete grid, whose form and size are determined by $\mathcal{M}$, in particular, by its eigenvalues and eigenvectors. As we shall see, this matrix also plays an important role in the Cramer-Rao performance analysis.

The exact computation of Eq. 21 is difficult in general. First, we resort to the calculation of bounds for the mean-square error. A well-known and general bound results from the Cramer-Rao inequality.[24] We return then to the definition of the mean-square error and evaluate directly an approximation bounding the right-hand side of expression (23). Finally, we discuss the conditions under which the estimation algorithm is efficient; that is, when is its performance accurately predicted by the Cramer-Rao bounds, or when and where do threshold effects occur with the processor's expected performance deteriorating faster than predicted by the Cramer-Rao bounds.

2.4.1 Cramer-Rao Performance Analysis

It is well known that if $\Lambda_\epsilon = \left[\sigma_{ij}^2\right]$ is the error covariance matrix of the parameter estimates, then

$$\Lambda_\epsilon \geq J^{-1}, \tag{26}$$

where J is the Fisher information matrix (FIM). For the general signal model described earlier, FIM is given[24] by

$$J = [J_{ij}] = -E\left[\frac{\partial^2 \ln \Lambda_l(A)}{\partial A_i \partial A_j}\right]. \tag{27a}$$

Under general regularity conditions, which are satisfied by this problem, we can interchange the partial derivatives with the expectation operator. Doing this, and replacing the log ML-function, as given by Eq. 10a, we get

$$J_{ij} = -\frac{1}{2} G' \left.\frac{\partial^2 \phi(A, A_a)}{\partial A_i \partial A_j}\right|_{A=A_a}, \tag{27b}$$

where G' is a multiplicative gain

$$G' = 2\,\frac{\bar{E}_R}{N_o}\,\frac{\bar{E}_R}{N_o + \bar{E}_r}. \tag{27c}$$

Recalling the matrix $\mathcal{M}$ defining the ellipsoidal structure of the GAF main lobe, we rewrite FIM as

$$J = G'\mathcal{M}. \tag{28}$$

The spread matrix $\mathcal{M}$ is computed in Appendix B, where closed-form expressions are presented. Apart from scaling factors (Eq. B.15), the elements of $\mathcal{M}$ are only

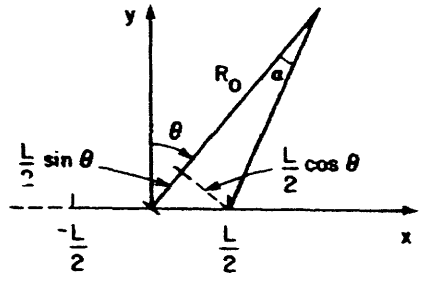

Fig. 20.
Geometric interpretation of parameter X.

functionally dependent on the bearing angle θ and the geometric parameter $X = Z/R_o$. From Fig. 20 we obtain

$$\tan\alpha = \frac{X\cos\theta}{1 - X\sin\theta},$$

i.e., X relates directly to the angle α spanned by the receiver at the source location R_o. For a broadside geometry $\theta = 0$ and $\tan\alpha = X$.

As in the delay/Doppler radar, the elements of $\mathcal{M}$ are additively given by two terms (see Eqs. B.2, B.3, B.4). With active radar, and except in multitone applications, the elements of $\mathcal{M}$ can usually be made zero by convenient choice of time origin and carrier

frequency.[32] With the passive problem, and inspecting Eqs. B.8 through B.14, only for a broadside geometry, $\theta = 0°$, do we find that

$$\mathcal{M}_{1 \sin\theta} = 0 \tag{29}$$

is the first moment centralized.

In order to obtain a more intuitive quantitative description for the Cramer-Rao bounds, we carry out a local analysis by a Taylor's series expansion of Eqs. B.2 through B.14. Then we study their asymptotic behavior as the array length increases without bound. Finally, we plot the Cramer-Rao bounds as computed exactly with a digital computer, and compare these results with the local and asymptotic expressions.

a. Short Observation Interval Analysis of the Cramer-Rao Bounds

In most applications, we face the fact that the geometric parameter X will be small. As long as $X = \frac{L}{2R_o}$ or $X = \frac{vT}{2R_o} < 1$ a Taylor's series analysis is valid, and leads to meaningful results. Accordingly, we consider this approach.

Truncation after the first nonzero term leads to

$$\mathcal{M} \simeq \left(\frac{2\pi}{\lambda}\right)^2 \left[\begin{array}{c|c} \frac{\cos^4\theta X^4}{45} & R_o \frac{11 \sin\theta \cos^2\theta X^4}{45} \\ \hline = & R_o^2 \frac{X^2}{3} \end{array}\right]. \tag{30a}$$

Similar expressions for the diagonal elements of $\mathcal{M}$, for the short observation interval analysis, with a different model, have also been found previously.[14, 15]

For the Cramer-Rao bounds we are also interested in the inverse matrix

$$\mathcal{M}^{-1} \simeq \left(\frac{\lambda}{2\pi}\right)^2 \left[\begin{array}{c|c} \frac{45}{\cos^4\theta X^4} & -\frac{33 \sin\theta}{R_o \cos^2\theta X^2} \\ \hline = & \frac{3}{R_o^2} \frac{1}{X^2} \end{array}\right]. \tag{30b}$$

The determinant is

$$\det \mathcal{M} \simeq \left(\frac{2\pi}{\lambda}\right)^4 \frac{R_o^2 \cos^4\theta X^6}{3^3 \times 5} \left[1 + \frac{3}{5 \times 7}(-11 \cos^2\theta + 29 \sin^2\theta) X^2\right]. \tag{30c}$$

We remark that in the expression of det $\mathcal{M}$ the coefficient of X^8 has been computed by using the higher order terms contributing to it, but not shown in Eq. 30a.

The eigenvalues and eigenvectors of $\mathcal{M}$ up to first order are

$$\lambda_{R_o} \approx \left(\frac{2\pi}{\lambda}\right)^2 \frac{\cos^4\theta X^4}{45} \qquad e_{R_o} \approx \begin{bmatrix} 1 \\ 0 \end{bmatrix} \tag{31a}$$

$$\lambda_{\sin\theta} \approx \left(\frac{2\pi}{\lambda}\right)^2 \frac{R_o^2 X^2}{3} \qquad e_{\sin\theta} \approx \begin{bmatrix} 0 \\ 1 \end{bmatrix} \tag{31b}$$

The Cramer-Rao bounds are obtained by readjusting $\mathcal{M}^{-1}$ by a gain. From Eqs. 26 and 28 we obtain

$$\Lambda_\epsilon = \left[\begin{array}{c|c} \Lambda_{R_o} & \Lambda_{R_o \sin\theta} \\ \hline = & \Lambda_{\sin\theta} \end{array}\right] \geq G'^{-1}\mathcal{M}^{-1}. \tag{32}$$

The standard deviations are

$$\sigma_{R_o} = \Lambda_{R_o}^{1/2} \geq \left[\frac{1}{\frac{2\bar{E}_R}{N_o}\frac{\bar{E}_R}{N_o+\bar{E}_R}}\left(\frac{\lambda}{2\pi}\right)^2\right]^{1/2} 3\sqrt{5}\,\frac{1}{\cos^2\theta X^2} \tag{33a}$$

$$\sigma_{\sin\theta} = \Lambda_{\sin\theta}^{1/2} \geq \left[\frac{1}{\frac{2\bar{E}_r}{N_o}\frac{\bar{E}_R}{N_o+\bar{E}_R}}\left(\frac{\lambda}{2\pi}\right)^2\right]^{1/2} \frac{\sqrt{3}}{R_o}\frac{1}{X}. \tag{33b}$$

Recall that

$$\bar{E}_R = \text{average received energy} = P_n TL\left(2\sigma_b^2\right), \tag{33c}$$

where we renormalized the received power as

$$P_n = \frac{P}{\left(\frac{R_o}{R_o^r}\right)^2} \tag{33d}$$

with R_o^r standing for the nominal range of operation for which the system has been designed.

The bracketed term in Eqs. 33a and 33b can be rearranged as

$$G^{-1/2} = \left[1 + \frac{N_o}{P_n\left(2\sigma_b^2\right)}\frac{1}{LT}\right]^{1/2} \frac{1}{\sqrt{\frac{2P}{N_o}\left(2\sigma_b^2\right)\left(\frac{2\pi}{\lambda}\right)^2}}\,\frac{R_o}{R_o^r}\frac{1}{\sqrt{LT}}. \tag{34a}$$

Define

$$SNR_{eq} = \frac{2P\left(2\sigma_b^2\right)}{N_o}\left(\frac{2\pi}{\lambda}\right)^2 \tag{34b}$$

$$SNR_{eff} = \frac{SNR_{eq}}{\left(R_o/R_o^r\right)^2} \tag{34c}$$

$$a = \left[1 + \frac{N_o}{2P_n\sigma_b^2}\frac{1}{LT}\right]^{1/2}. \tag{34d}$$

SNR_{eq} is an equivalent signal-to-noise ratio taking into account the channel Rayleigh fading (factor $2\sigma_b^2$) and the effect of the modulation index

$$\beta = \frac{2\pi}{\lambda}. \tag{34e}$$

SNR_{eff} is the effective signal-to-noise ratio at the receiver level, after normalizing the emitted power with the inverse of the squared distance to take into account the spherical spreading of the propagating signals.

The gain can now be rewritten as

$$G^{-1/2} = \frac{a}{(SNR_{eff})^{1/2}}\frac{1}{\sqrt{LT}}, \tag{35}$$

and the standard deviations as

$$\sigma_{R_o} \geq \frac{a}{(SNR_{eff}LT)^{1/2}}\frac{3\sqrt{5}}{\cos^2\theta X^2} = \frac{1}{(SNR_{eff}LT)^{1/2}}\, g_{R_o}(\theta, X) \tag{36a}$$

$$\sigma_{\sin\theta} \geq \frac{a}{(SNR_{eff}LT)^{1/2}}\frac{\sqrt{3}}{R_o X} = \frac{1}{(SNR_{eff}LT)^{1/2}}\, g_{\theta}(R_o, X). \tag{36b}$$

These expressions are separated into two factors. The first is due to power-level considerations, and involves detailed model specifications. The second reflects how the modulations induced on the signal spatial/temporal structure affect the performance. The bearing estimation is fundamentally dependent on linear effects such as linear delay across the array or observed Doppler modulation. The range performance deteriorates with X^{-2}, since the range focusing is achieved from the second-order effects, such as the spherical curvature of the incoming wave fronts (stationary array/stationary source) or the chirp modulations induced on the signal temporal structure by the relative dynamics (moving omnidirectional sensor with stationary source). We also note

that σ_{R_o} increases monotonically as we go from broadside to end-fire, as a consequence of a reduction on the effective array length. The angle estimation grows worse as the source/receiver separation increases.

Finally, the crosscorrelation between the errors on the parameter estimates, as predicted by the Cramer-Rao inequality, is

$$\rho_{R_o, \sin\theta} \cong \frac{\mathcal{M}^{-1}_{12}}{\left(\mathcal{M}^{-1}_{11}\mathcal{M}^{-1}_{22}\right)^{1/2}} \cong -\frac{11 \sin\theta X}{\sqrt{15}}. \tag{37}$$

For small X the errors are almost uncorrelated. A similar conclusion follows from the eigenvalues of $\mathcal{M}$, as given by (31a) and (31b). Up to truncation to the lowest non-zero power of X the estimation problem is essentially uncoupled.

b. Asymptotic Behavior of the Cramer-Rao Bounds

In Appendix C we study the asymptotic behavior of the elements $\mathcal{M}_{ij}$ as the geometric parameter

$$X = \frac{Z}{R_o} \to \infty \tag{38a}$$

or equivalently

$$Y = \frac{R_o}{Z} \to 0. \tag{38b}$$

We stress that the analysis considers only the phase information, neglecting amplitude attenuation effects across the observing array.

We summarize here the main results.

$$\mathcal{M} \sim \left(\frac{2\pi}{\lambda}\right)^2 \left[\begin{array}{c|c} \sin^2\theta + \cos\theta \cos 2\theta \frac{\pi}{2} Y & = \\ \hline R_o\left(-\sin\theta + \frac{\pi}{2}\sin 2\theta\, Y\right) & R_o^2\left(1 - \frac{\cos 2\theta}{\cos\theta}\frac{\pi}{2} Y\right) \end{array}\right] \tag{39a}$$

$$\det \mathcal{M} \sim \left(\frac{2\pi}{\lambda}\right)^4 R_o^2 \frac{\pi}{2} \frac{Y}{\cos\theta} \tag{39b}$$

$$\mathcal{M}^{-1} \sim \left(\frac{\lambda}{2\pi}\right)^2 \left[\begin{array}{c|c} \frac{2}{\pi}\frac{\cos\theta}{Y} - \cos 2\theta & \frac{\sin 2\theta}{R_o}\left(\frac{1}{\pi Y} - \cos\theta\right) \\ \hline = & \frac{1}{R_o^2}\left(\frac{2}{\pi}\frac{\cos\theta \sin^2\theta}{Y} + \cos^2\theta \cos 2\theta\right) \end{array}\right] \tag{39c}$$

The Cramer-Rao bounds are obtained by scaling $\mathcal{M}$ with the signal energy-to-noise ratio gain G given by Eq. 35.

If the estimation problem reduces to a single range parameter estimation, with the other parameter assumed known a priori, the standard deviations are given by

$$\sigma_{R_o} \sim G^{-1/2} \frac{1}{\sin^2\theta} \quad \text{(bearing known)} \tag{40a}$$

or

$$\sigma_{\sin\theta} \sim G^{-1/2} \frac{1}{R_o} \quad \text{(range known)}. \tag{40b}$$

Because

$$G^{-1/2} \xrightarrow[L\to\infty]{} 0 \tag{41a}$$

we obtain

$$\sigma_{R_o} \xrightarrow[L\to\infty]{} 0 \tag{41b}$$

or

$$\sigma_{\sin\theta} \xrightarrow[L\to\infty]{} 0. \tag{41c}$$

This reflects the unrealistic assumption of an array with infinite gain. For large but finite array gain L, the individual parameter performances depend on the relative source/receiver geometry, as illustrated in Fig. 21. Both curves present an intuitively

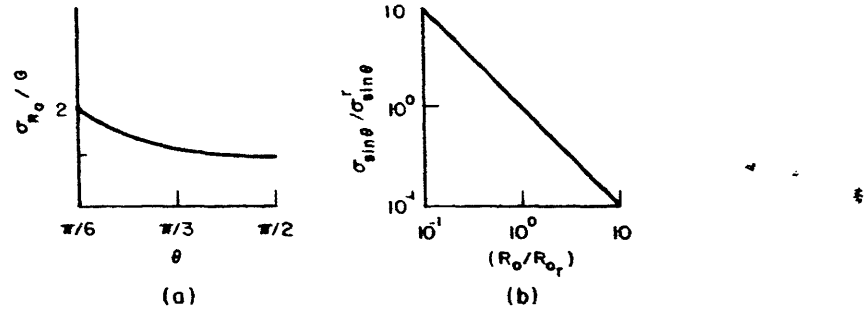

Fig. 21. Asymptotic behavior of single mean-square spread matrix SASS parameter.

satisfying behavior. As the geometry progresses from broadside to end-fire, and when the effective array length is larger than the source/array center separation R_o, the performance of the single range parameter estimation problem improves. Similarly,

expression (40b) or Fig. 21b says that the single parameter angle performance for large arrays is determined by the source/receiver separation.

We consider now the full SASS problem. The mean-square range and bearing asymptotic spread functions

$$f_{R_o}(Y,\theta) = \frac{2}{\pi}\frac{\cos\theta}{Y} - \cos 2\theta \tag{42a}$$

$$f_{\theta}(Y,\theta) = \frac{1}{R_o^2}\left[\frac{2}{\pi}\frac{\cos\theta \sin^2\theta}{Y} + \cos^2\theta \cos 2\theta\right] \tag{42b}$$

are studied analytically in Appendix C and also displayed in Figs. 22 and 23 where

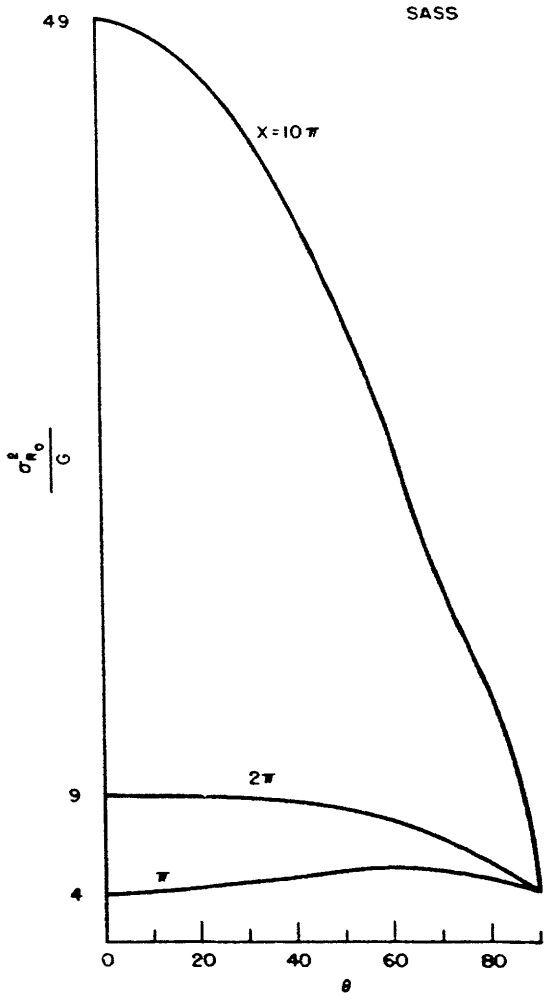

Fig. 22.
Asymptotic behavior of mean-square spread matrix range parameter (SASS).

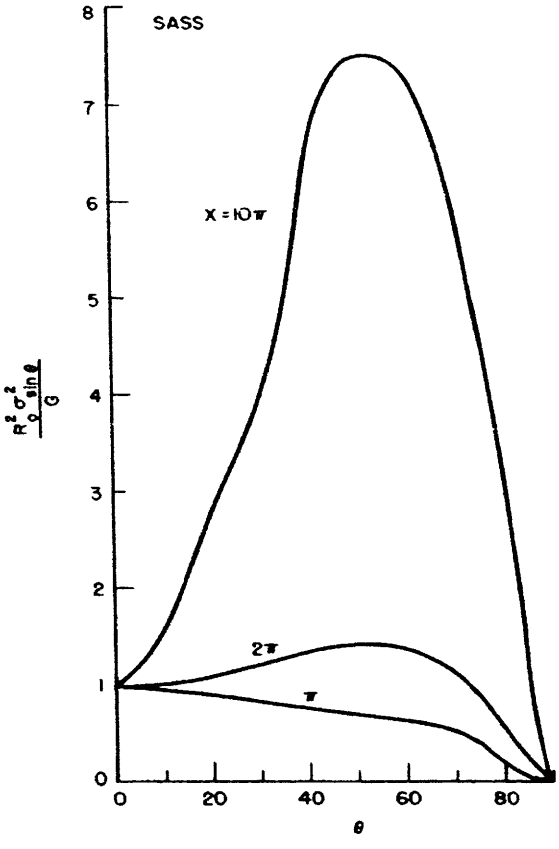

Fig. 23.
Asymptotic behavior of mean-square spread matrix angle parameter (SASS).

it is seen that for large effective array length the receiver's behavior is highly sensitive to the relative geometry of the problem. This is due to the high correlation between the errors in the estimates. The crosscorrelation for $\theta \neq 0, \frac{\pi}{2}$,

$$\rho^2_{R_o, \sin\theta} \sim \frac{\sin^2\theta - 2\frac{\pi}{2} Y \sin\theta \sin 2\theta}{\sin^2\theta + \frac{\pi}{2} Y \frac{\cos^2 2\theta}{\cos\theta}} \cong 1 - \frac{\pi}{2} Y \frac{1}{\sin^2\theta \cos\theta} \xrightarrow[Y \to 0]{} 1, \tag{43}$$

tends asymptotically to 1 (perfect correlation), and $\mathcal{M}$ becomes singular as Y goes to zero. For small nonzero Y, the behavior is highly dependent on the geometry as illustrated in Fig. 24.

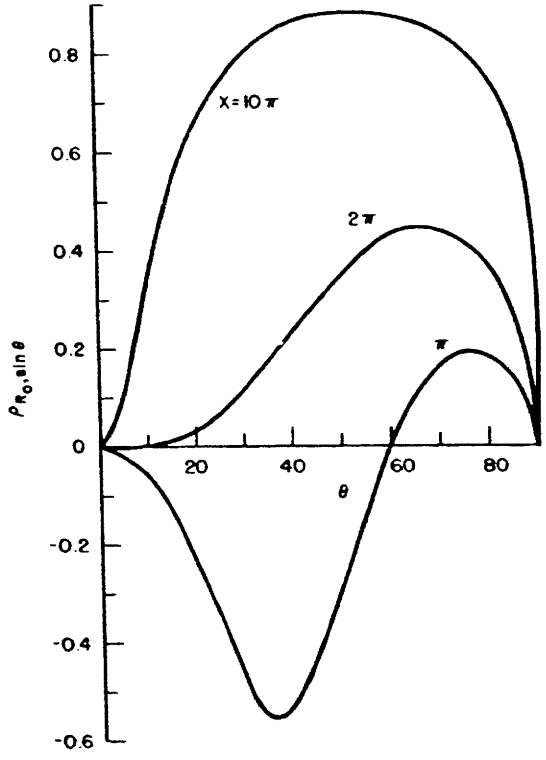

Fig. 24. Asymptotic behavior of crosscorrelation for SASS parameters.

The asymptotic behavior of the mean-square performance bounds is obtained by scaling the diagonal elements of $\mathcal{M}^{-1}$ in Eq. 39c. We obtain

$$\sigma^2_{R_o} \sim G^{-1} f_{R_o}(Y, \theta) = G^{-1}\left[\frac{2}{\pi}\frac{\cos\theta}{Y} - \cos 2\theta\right] \tag{44a}$$

$$\sigma^2_{\sin\theta} \sim G^{-1} f_{\theta}(Y, \theta) = G^{-1} \frac{1}{R_o^2}\left[\frac{2}{\pi}\frac{\cos\theta \sin^2\theta}{Y} + \cos^2\theta \cos 2\theta\right]. \tag{44b}$$

As the array length increases

$$\sigma^2_{R_o} \to \sigma^2_{R_{o_\infty}} = \frac{a^2}{(SNR_{eff}T)} \frac{2}{\pi} \frac{\cos\theta}{R_o} \tag{45a}$$

$$\sigma^2_{\sin\theta} \to \sigma^2_{\sin\theta_\infty} = \frac{a^2}{(SNR_{eff}T)} \frac{2}{\pi} \frac{\cos\theta}{R_o} \frac{\sin^2\theta}{R_o^2} \tag{45b}$$

with the relation

$$\left(\frac{\sigma_{R_{o_\infty}}}{R_o}\right)^2 = \left(\frac{\sigma_{\sin\theta_\infty}}{\sin\theta}\right)^2 . \tag{45c}$$

For large values of X, the range and bearing performances approach the finite asymptotic values (45a) and (45b). But the estimation problem is highly sensitive, since in the limit as $X \to \infty$, the spread matrix becomes singular. The asymptotic values (45a) and (45b) combine this highly sensitive behavior with the unrealistic assumption of an array with unbounded gain. In order to retain the simultaneous identifiability of both range and bearing, we need at least the first-order terms in Y.

An intuitive explanation for this behavior is obtained by analyzing the range phase history for the ∞-observation interval. Rewrite the range phase as

$$R(\ell) = \left\{(\ell - R_o \sin\theta)^2 + R_o^2 \cos^2\theta\right\}^{1/2}, \qquad \ell \in \left[-\frac{L}{2}, \frac{L}{2}\right]$$

and define the range phase information content on the observations as the graph of the range phase

$$R_L = \left\{R(\ell) = \left\{(\ell - R_o \sin\theta)^2 + R_o^2 \cos^2\theta\right\}^{1/2}, \quad \ell \in \left[-\frac{L}{2}, \frac{L}{2}\right]\right\} .$$

Set

$$R_Z = \left\{R(z) = \left\{z^2 + R_o^2 \cos^2\theta\right\}^{1/2}, \quad z \in [-Z, +Z]\right\}.$$

For $Z = \frac{L}{2} - R_o \sin\theta$ we have $R_L = R_Z$; when $L \to \infty \Longrightarrow Z \to \infty$, and we obtain the isomorphism of the two information contents $\lim_{L\to\infty} R_L = R_{Z=\infty}$. But $R_{Z=\infty}$ is completely determined by a single parameter, the distance $R_o \cos\theta$ from the source to the linear observer, and so, for an infinitely large array, this is the identifiable parameter.

c. Very Long Baseline Staved Array

In radio and radar astronomy it is well known that Very Long Baseline Interferometry (VLBI) achieves high angular resolution by using two or more widely separated radio telescopes.[33] The quantity that is measured by VLBI techniques is simply a differential delay the difference between the times of propagation from the source to two or more

separated receiving sites. A complete analysis of the techniques for estimating this differential delay from the data recorded simultaneously at several receiving stations, and the accuracy attained, has been given by Hinteregger[34] and Rogers.[35] With natural radio sources the attainable accuracy within each fringe of ambiguity is inversely proportional to the carrier frequency and the available signal-to-noise ratio. The VLBI concept has also been applied with coherent sources, i.e., sources whose emitted signals are slowly varying sinusoidals such as the artificial radio transmitters used with the Apollo Lunar Surface Experiment Package (ALSEP) that were developed for tracking the lunar rover vehicle.[33,11]

With these VLBI techniques the source is assumed at infinity ("distant" observer). We now study performance bounds for a simple geometry wherein a very long baseline observer is generated by linear arrays located at distant sites, with simultaneous measurement of the angle and range source parameters. The essential distinction with the VLB interferometry is that now we analyze the possibility of measuring the source/receiver separation from the phase modulations, by assuming that the source is within the observer's finite geometry. This will be made precise subsequently.

Figure 25 illustrates a linear observer composed of three widely separated short collinear arrays placed far apart. We derive the Cramer-Rao performance bounds for the range and bearing parameters, under suitable assumptions made explicit below. In

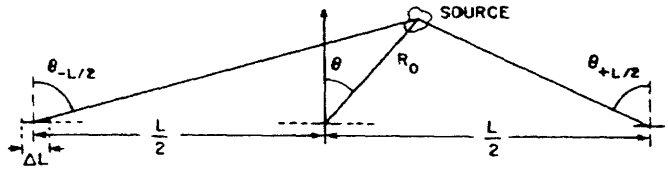

Fig. 25. Long baseline (three-element) staved linear array.

Appendix C for $R_o \gg \Delta L$ we linearize the range phase function across each individual stave about its geometric center. For $R_o \ll L$ we approximate $\sin(\theta_{\pm L/2})$ by the arc. With these simplifications the Cramer-Rao bounds (Eqs. C.44 and C.45) of Appendix C are

$$\sigma_{\sin\theta} \approx \frac{a}{(SNR_{eff})^{1/2}} \frac{1}{(\Delta LT)^{1/2}} \sqrt{\frac{3}{2}} \frac{1}{\pi} \left(\frac{1}{\Delta L/\lambda}\right) \tag{46a}$$

and

$$\sigma_{R_o} \approx \sigma_{\sin\theta} \tan^2\theta_{L/2} R_o. \tag{46b}$$

These expressions illustrate the performance achieved by triangulation with a linear scheme, when the assumed simplifications hold. We conclude that the angle performance

is determined from the central element, while the range observation is accomplished by triangulation with the end point elements. Finally, from Eqs. 46 we see that the performance deteriorates monotonically with the viewing angle $\theta_{L/2}$:

$$\sigma_{R_o} \xrightarrow[\theta_{\frac{L}{2}} \to \frac{\pi}{2}]{} \infty. \tag{46c}$$

d. Graphical Representation of the Cramer-Rao Bounds

We evaluate in a digital computer the exact closed-form expressions (B. 8)-(B. 14) in Appendix B of the elements of the inverse mean-square spread matrix $\mathcal{M}^{-1}$, and the Cramer-Rao bounds obtained after normalizing them by the gain G.

The nominal conditions that are assumed are

$R_o = R_o^r = 6 \times 10^4$ ft

$\theta = 15°$

$\lambda = 50$ ft

$\beta = \frac{2\pi}{\lambda}$ = modulation index

$SNR = P/N_o = -3$ dB

$2\sigma_b^2 = 1$

T = 250 sec for the stationary array/stationary source

L = 250 ft, v = 30 ft/sec for the moving omnidirectional sensor with stationary source.

In Fig. 26 we represent the diagonal elements of $\mathcal{M}^{-1}$ normalized by the square of the modulation index

$$\tilde{\mathcal{M}}^{-1}_{ii} = \frac{\mathcal{M}^{-1}_{ii}}{(\lambda/2\pi)^2}, \qquad i = R_o, \sin\theta$$

and the crosscorrelation $\rho_{R_o, \sin\theta}$ as a function of the geometric parameter X.

We observe the quadratic (convex cup) behavior of the range and bearing mean-square spreads. This is the result of two different phenomena. For small X (distant observer) the main lobe is spread out and flat at the origin (source location) with corresponding large inverses of the second-order derivatives of the GAF. When X increases it becomes sharper, but the crosscorrelation also decreases monotonically to -1 with a shearing of the main lobe. As a consequence, the spread functions bottom down at a value of X between 6 and 7, and then increase monotonically. Figure 26 also displays the local and asymptotic tangents to which the spread functions converge; these were

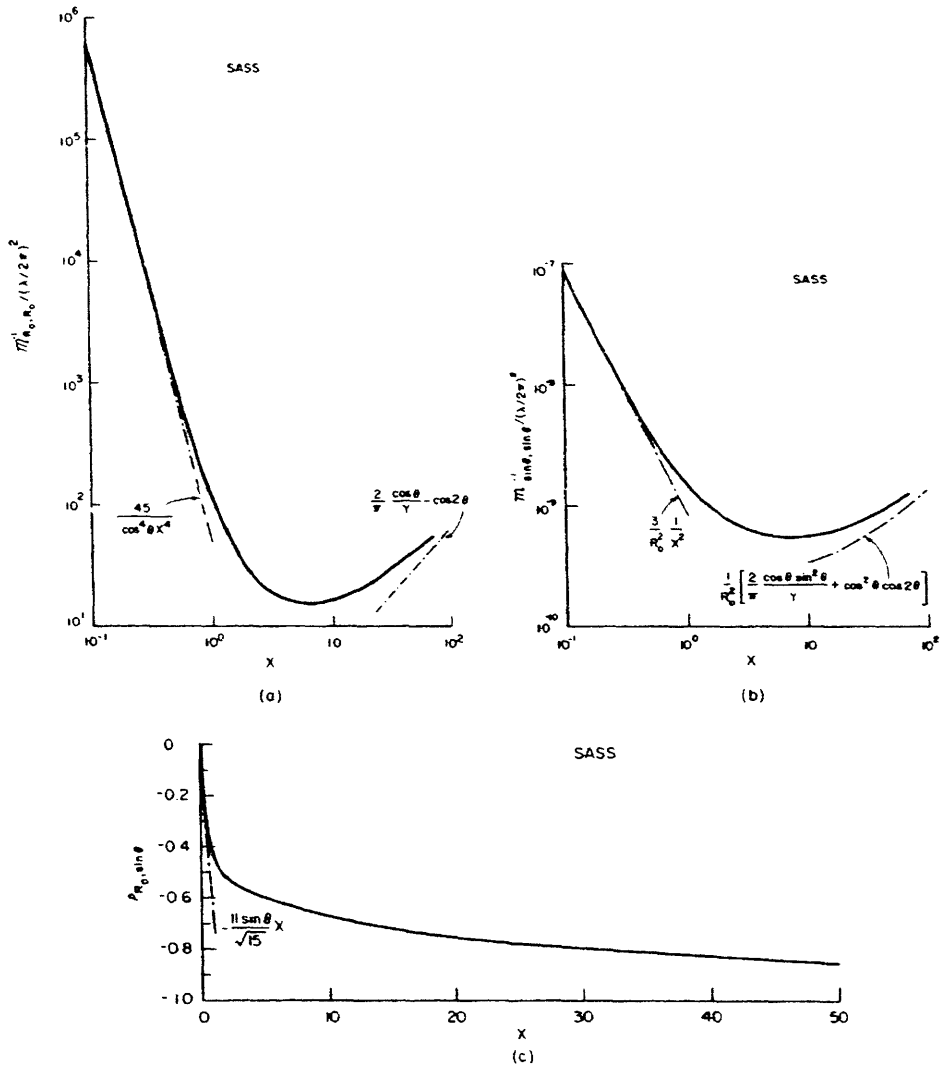

Fig. 26. (a) Inverse range mean-square spread vs X.
(b) Inverse angle mean-square spread vs X.
(c) Range/angle crosscorrelation vs X.

derived in sections 2.4.1a and 2.4.1b.

Figure 27a and 27b shows the range and bearing standard deviations predicted by the Cramer-Rao bounds when the parameter X varies. These curves are a consequence of associating to the geometric effects displayed in Fig. 26a and 26b the energy-to-noise ratio gain, which increases with X and leads to an overall steady improvement in the predicted accuracy, as we would expect. But we stress that sensitivity problems arise for large X, since the estimation errors become highly correlated, as shown by the right ends of Fig. 26c, or as predicted by the analytical results of the asymptotic analysis.

Finally, Fig. 27c illustrates the behavior of σ_{R_o} as a function of the bearing angle θ for a small value of X, namely $X = \frac{1}{2}$. The performance deteriorates when the geometry progresses from broadside to end-fire, as concluded from the local analysis.

2.4.2 Global Performance

The Cramer-Rao bounds that have just been studied place theoretical limitations on the accuracy of the source parameter estimates. We shall analyze how these bounds compare with the mean-square errors in the algorithm implementing the ML estimation, by working directly with Eq. 21.

From physical considerations, dependent upon the particular application, we delimit the parameter space region of interest, Ω, to the two-dimensional rectangle

$$\Omega = \bigtimes_{i=1}^{2} \left[A_{j_m}, A_{j_M}\right] = \left[R_{o_m}, R_{o_M}\right] \times \left[\sin\theta_m, \sin\theta_M\right]. \tag{47}$$

By designing the elementary cell of the grid discretizing Ω on the coarse search step as the ellipsoid defined by the quadratic form (Eq. 25) $Q(\Delta A) = (\Delta A)^T \mathcal{M} (\Delta A) = 1$, it follows, from the negligible sidelobe structure of the ambiguity function (see sec. 2.3), that the signals evaluated at points in different cells are uncorrelated. These considerations justify modeling the coarse search as an M-ary hypothesis decision testing problem with orthogonal signals transmitted over a Rayleigh channel.

Under the hypothesis H_n, $n = 1, \ldots, M$ the received waveform is

$$H_n = \tilde{r}_n(t) = \sqrt{2}\ \mathrm{Re}\left\{\left[\left(\frac{\tilde{E}_r}{LT}\right)^{1/2} \tilde{b} \exp j\frac{2\pi}{\lambda}\left(R_{o_n}^2 + x^2 + 2xR_{o_n}\sin\theta_n\right)^{1/2} + \tilde{w}(x)\right] \exp(-j\omega_c x)\right\} \quad n \in M = \{1, \ldots, M\}$$

with

M = total number of cells of Ω

$A_n = \begin{bmatrix} R_{o_n} \\ \sin\theta_n \end{bmatrix}$ = center coordinates of each cell

$\tilde{w}(x)$ = complex "white" Gaussian noise with double spectral height N_o.

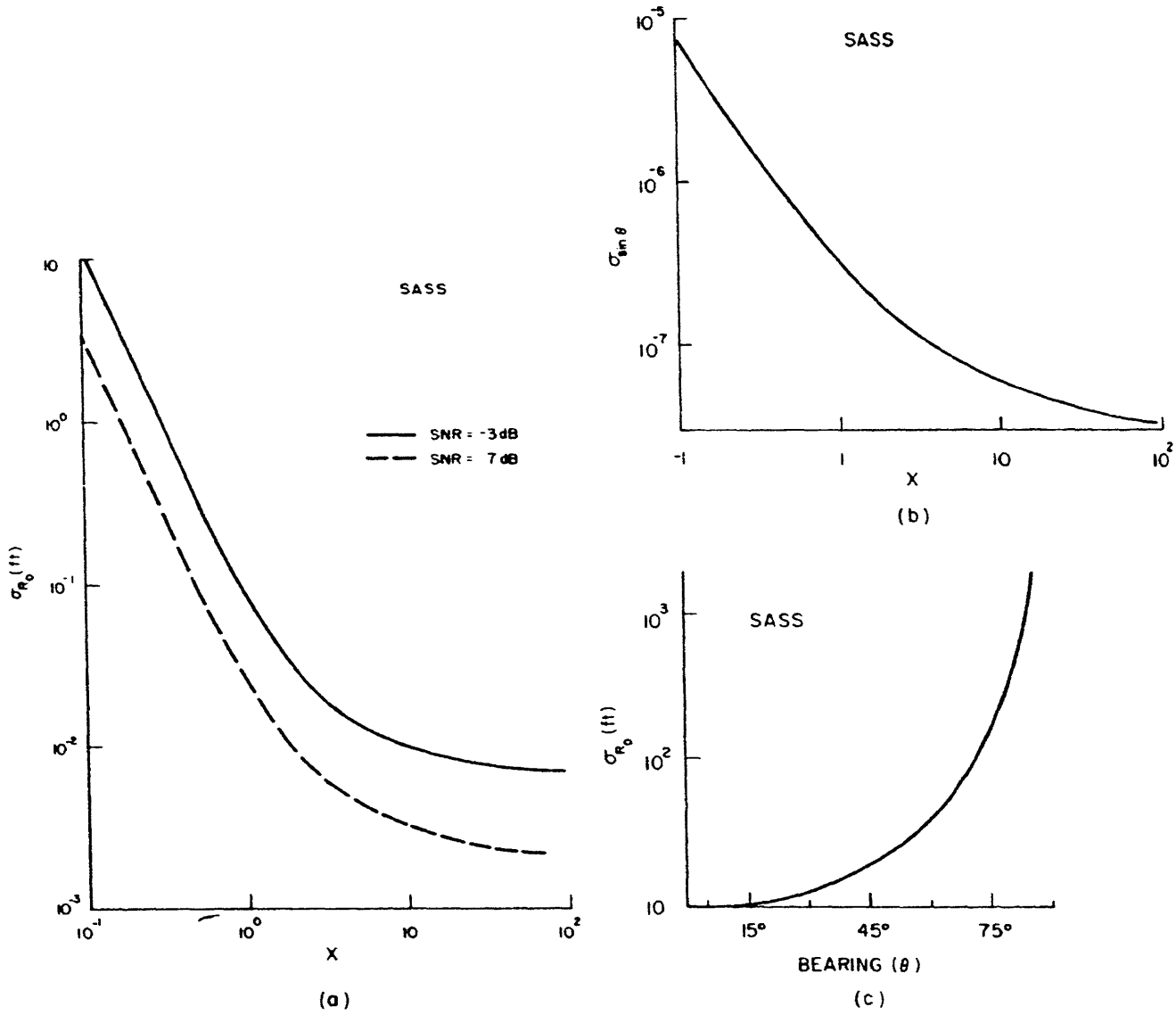

Fig. 27. (a) Range standard deviation vs X.
(b) Angle standard deviation vs X.
(c) Range standard deviation vs bearing angle.

The hypotheses are a priori equally probable, since no further knowledge of the source parameters is assumed, apart from the overall dimensions of Ω.

The first step of the estimation algorithm is then a "largest of" receiver choosing the largest ℓ_m of the sufficient statistics

$$\ell_n = |\tilde{L}_n|^2 = |\langle \tilde{r}(t), \tilde{s}(t, \ell, A_n)\rangle|^2, \quad n \in M$$

and identifying the ML estimate $\tilde{A}_{m\ell} = A_m$.

We proceed with the computation of each quantity in Eq. 21.

a. $E\left(A_{j\epsilon}^2 | \epsilon\right)$

$$E\left(A_{j\epsilon}^2 | \epsilon\right) \triangleq E\left[(A_j - A_{jm\ell})^2 | \epsilon\right]$$

$$= E\left\{\left[(A_j - \bar{A}_j) - (A_{jm\ell} - \bar{A}_j)\right]^2 | \epsilon\right\}$$

$$= E[(A_j - \bar{A}_j)^2 | \epsilon] + E[(A_{jm\ell} - \bar{A}_j)^2 | \epsilon] - 2E[(A_j - \bar{A}_j)(A_{jm\ell} - \bar{A}_j) | \epsilon], \tag{48a}$$

where

$$\bar{A}_j = E(A_j | \epsilon) = E(A_{jm\ell} | \epsilon) = \frac{A_{jM} - A_{jm}}{2} \triangleq \frac{\Delta_M A_j}{2}.$$

The ML estimates have a MAP interpretation, that they coincide with the maximum a posteriori estimates when the parameters' a priori distribution is uniform in Ω. For the purpose of computing the mean-square error when a diversion occurs, we use this MAP interpretation, and model A_j as uniformly distributed in $[A_{jm}, A_{jM}]$, $j = 1, 2$.

The second equality follows because, by the original orthogonal signals assumption, if a diversion had occurred, it is equally likely to have been decided upon any one of the wrong cells. From this we also conclude that the last term in Eq. 48a is zero. The two other terms will be bounded by

$$E[(A_j - \bar{A}_j)^2 | \epsilon] = E[(A_{jm\ell} - \bar{A}_j)^2 | \epsilon] \leq \frac{(A_{jM} - A_{jm})^2}{12} \quad \frac{\Delta_M A_j^2}{12},$$

where we have neglected the influence of diversions carrying no error on the A_j parameter. It follows that

$$E\left(A_{j\epsilon}^2 | \epsilon\right) \geq 2\sigma_{A_j}^2 = \frac{(A_{jM} - A_{jm})^2}{6} = \frac{\Delta_M A_j^2}{6}. \tag{48b}$$

b. Probability of a Diversion

The probability of a diversion is the probability of error of an M-ary decision with

orthogonal signals transmitted over a Rayleigh channel. Several authors have studied this probability of error for M-ary signaling over fading channels (see Pierce;[36] for additional references see Van Trees[24]). The exact expression is

$$Pr(\epsilon) = \sum_{i=1}^{M} \binom{M-1}{n} \frac{(-1)^{n+1}}{n+1+n\beta}, \tag{49a}$$

where

$$\beta = \frac{\bar{E}_R}{N_o} = \frac{2\sigma_b^2 E_t}{N_o}. \tag{49b}$$

Equation 49a is an alternating series of large terms posing numerical problems in a digital computer. Sussman[37] has derived more convenient equivalent expressions and several approximations displaying the functional dependence of $Pr(\epsilon)$ on the several parameters. In particular,

$$Pr(\epsilon) = 1 - \frac{\Gamma\left(1 + \frac{1}{\beta+1}\right)\Gamma(M)}{\Gamma\left(M + \frac{1}{\beta+1}\right)},$$

where Γ is the gamma function.

For $\beta \gg 1$ a truncated Taylor's series expansion approximates the probability of a diversion by

$$Pr(\epsilon) \approx \frac{1}{\beta}[\psi(M) + \gamma], \tag{50a}$$

where $\psi(M)$ is the digamma or psi function,[30] defined as

$$\psi(z) = \frac{d}{dz} \ln \Gamma(z) = \frac{\Gamma'(z)}{\Gamma(z)},$$

and γ is Euler's constant $\gamma = 0.5772156649$.

From the asymptotic expansion for $\psi(z)$,

$$\psi(z) \sim \ln z - \frac{1}{2z} - \frac{1}{12z^2} + \frac{1}{120z^4} - \frac{1}{252z^6} + \ldots,$$

we get approximately

$$Pr(\epsilon) \approx \frac{1}{\beta}\left[\ln M - \frac{1}{2M} + \gamma\right], \tag{50b}$$

with an error smaller than $1/12M^2$.

Another useful expression follows from

$$\psi(M) = -\gamma + \sum_{k=1}^{M-1} k^{-1},$$

and it leads to

$$Pr(\epsilon) \approx \frac{1}{\beta} \sum_{k=1}^{M-1} k^{-1}.$$

Figure 28 compares the probability of a diversion, as computed from the exact and the approximate expressions, as a function of the energy-to-noise ratio β (Fig. 28a), and having M as a parameter (Fig. 28b). The curves demonstrate good agreement between both expressions for sufficiently large energy-to-noise ratio parameter values.

c. $E\left(A_{j\epsilon}^2 \mid \epsilon^c\right)$

This quantity represents the mean-square error when no diversion occurs, and the coarse search leads to the correct cell in the Ω region of the parameter space. The fine search proceeds within the main lobe, and this local mean-square error will depend on the quantitative description of the GAF near the origin.

We note that for a rectangular grid aligned with the coordinate axis we have

$$0 \leq E\left(A_{j\epsilon}^2 \mid \epsilon^c\right) \leq \frac{(A_{jM} - A_{jm})^2}{M_j}, \tag{51}$$

where M_j is the number of subintervals into which the A_j axis is divided by the grid.

As the geometric parameter X increases, we note a shearing effect on the main lobe, with the grid tilting over both axes, so that the high bound in Eq. 51 does not hold. Alternatively, working with a quadratic description for the main lobe, as given by Eq. 24, it is plausible to approximate the local mean-square error by the Cramer-Rao bounds computed in section 2.4.1; i.e., we assume that $E\left(A_{j\epsilon}^2 \mid \epsilon^c\right) \approx \sigma_{jj}^2$, with σ_{jj} given by Eq. 33.

In summary, the total mean-square error is decomposed on a global and a local component

$$\sigma_{tot_j}^2 = E\left(A_j^2\right) \simeq \sigma_{gl_j}^2 + \sigma_{loc_j}^2, \tag{52a}$$

where

$$\sigma_{gl_j}^2 \approx \frac{\Delta_M A_j^2}{6} Pr(\epsilon) \tag{52b}$$

$$\sigma_{loc_j}^2 = \sigma_{jj}^2 [1 - Pr(\epsilon)]. \tag{52c}$$

d. Performance Graphical Analysis

The nominal values here are those assumed when studying numerically the Cramer-Rao bounds at the beginning of section 2.4.1b. Furthermore, we take

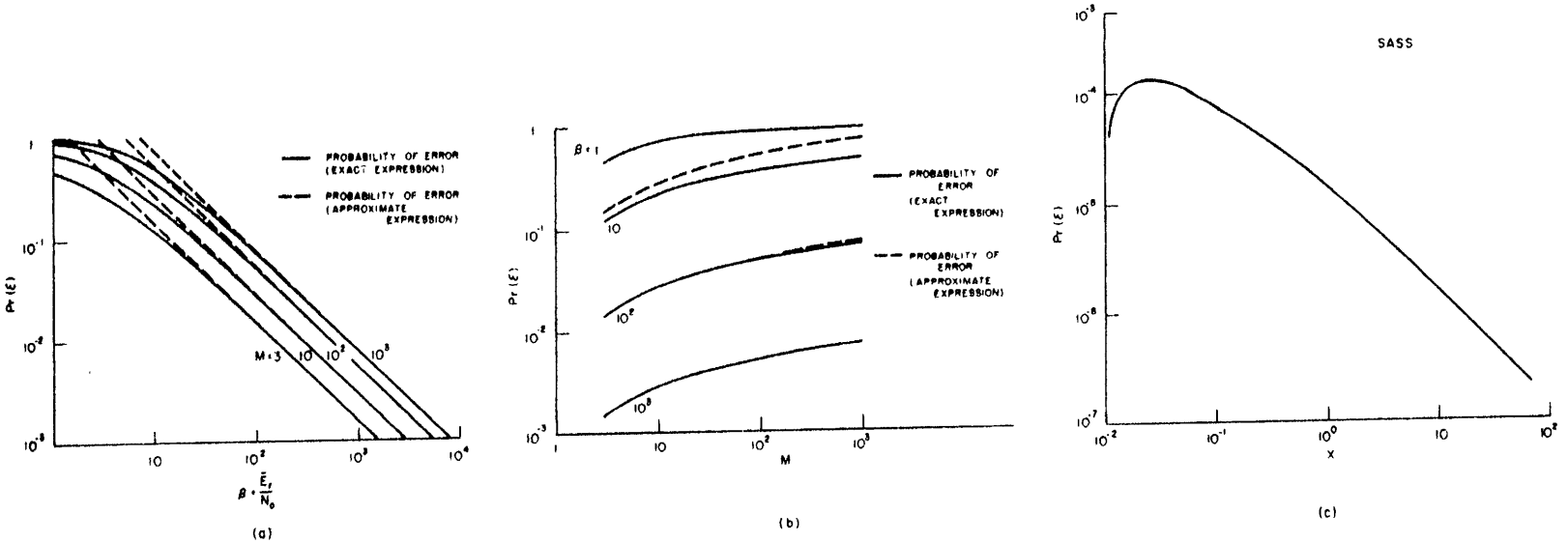

Fig. 28. (a) Probability of diversion vs signal energy-to-noise ratio.
(b) Probability of diversion vs total number of cells.
(c) Probability of diversion vs X.

$$V_\Omega = \Delta_M R_o \times \Delta_M \sin\theta,$$

with $\Delta_M R_o = R_{o_M} - R_{o_m} = 10\ R_o$, $\Delta_M \theta = \theta_M - \theta_m \tilde{=} 5^o$. We start by analyzing the dependence of the probability of error and the total number of grid cells on the geometric parameter X.

We have

$$M = \frac{V_\Omega}{V_a}, \tag{53}$$

where

$$V_\Omega = \text{volume of } \Omega = \prod_{j=1}^{2} \Delta_M A_j = \Delta_M R_o \times \Delta_M \sin\theta$$

V_a = volume of elementary cell.

For a fixed V_Ω the total number M decreases with V_a. The volume of the elementary cell depends on the eigenvalues and eigenvectors of $\mathcal{M}^{-1}$ which determines the form and dimensions of the cell. In particular, we have

$$V_a = k \prod_{i=1}^{2} \lambda_i^{-1/2} = k(\det \mathcal{M})^{-1/2}, \tag{54}$$

where

λ_i = eigenvalues of $\mathcal{M}$ given by Eqs. 31a and 31b

$\det \mathcal{M}$ = determinant of $\mathcal{M}$.

k = constant dependent on the specific form assumed for a.

For the elementary ellipsoid,

$$Q(\Delta A) = \Delta A^T \mathcal{M} \Delta A = \sum_{j=1}^{2} \frac{(\Delta A_j)^2}{\left(\frac{1}{\sqrt{\lambda_j}}\right)^2} = 1,$$

we have $k = k_\ell = \pi$. For the rectangular parallelepiped circumscribing this ellipsoid $k = k_\rho = 4$. The total number of cells is then

$$M = \frac{V_\Omega}{k} (\det \mathcal{M})^{1/2}. \tag{55}$$

In Fig. 29a we show $\det \mathcal{M}$ as a function of X and the local and asymptotic approximations. The convex cap behavior has essentially the physical interpretation already noted, that for small X the main lobe is flat at the origin and well spread out, while for large X

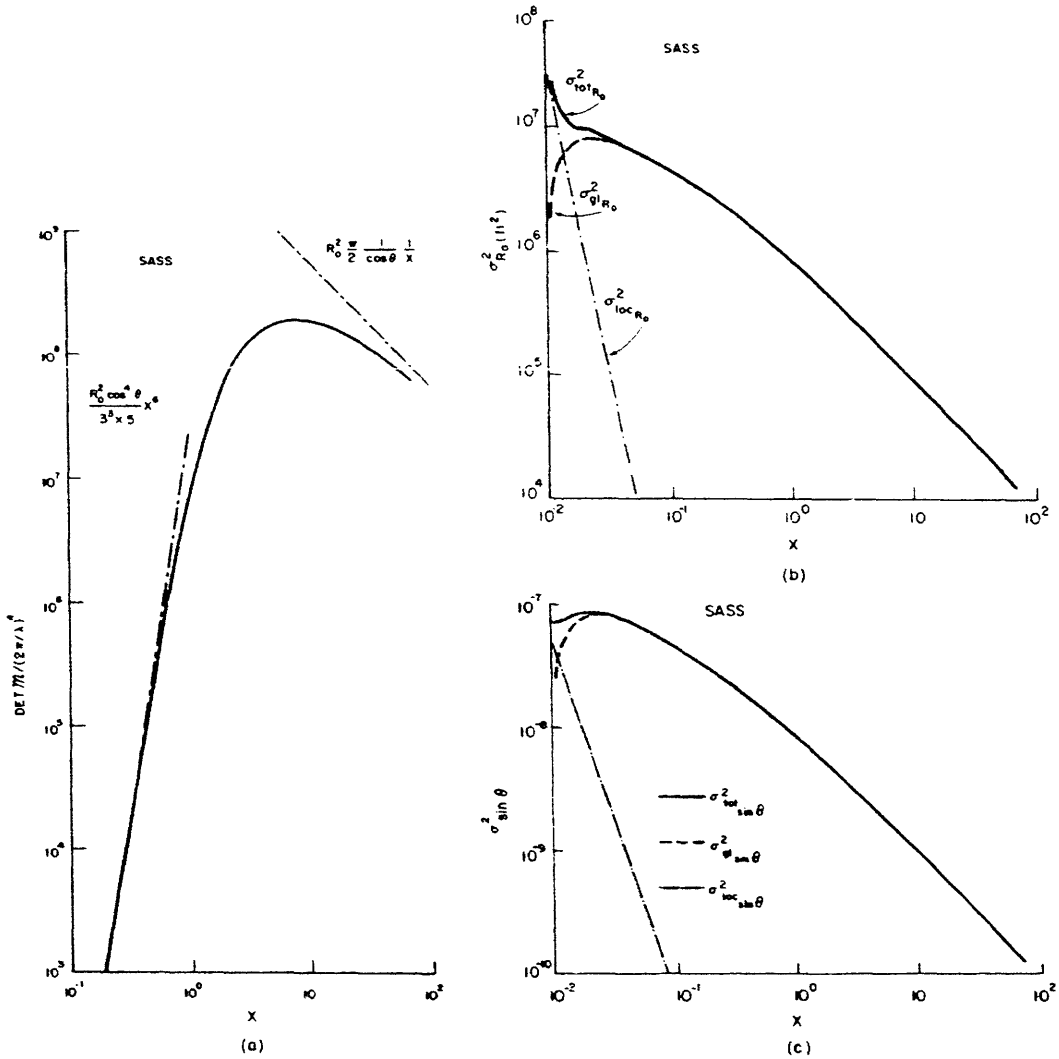

Fig. 29. (a) Determinant of $\mathcal{M}$ vs X.
(b) Total range mean-square error vs X.
(c) Total angle mean-square error vs X.

it approaches a sheared rectangular type format.

The total number M presents a similar dependence on X. We observe the large computational work involved when actually implementing the ML receiver, because of the large number of grid cells.

In Fig. 28c we showed the evolution of the probability of error with X. As X increases, M not only changes according to the cap behavior of Fig. 29a bu. the signal energy-to-noise ratio also increases. Since for very small X the main lobe spreads over all the Ω space, the grid reduces to one cell and the probability of error vanishes. As X increases, M eventually gets larger than 1. Initially this dominates the corresponding increase of $\beta = \bar{E}_r/N_o$, and the probability of error changes drastically to a maximum value, after which it decreases monotonically as a ln X/X law. Estimates on the value of M can be obtained from the local and asymptotic expressions for det $\mathcal{M}$. Specifically, for small X we have

$$M \sim M_{loc} \cong M_{\Omega} \frac{1}{3\sqrt{15}} R_o \cos^2\theta X^3 \tag{56a}$$

and for large X we have

$$M \sim M_{asymp} \cong M_{\Omega} \left(\frac{\pi}{2}\right)^{1/2} R_o \frac{1}{(X \cos\theta)^{1/2}}, \tag{56b}$$

where

$$M_{\Omega} = \frac{V_{\Omega}}{k} \left(\frac{2\pi}{\lambda}\right)^2 = \frac{\Delta_M R_o \Delta_M \sin\theta}{k} \left(\frac{2\pi}{\lambda}\right)^2. \tag{56c}$$

These expressions exhibit the rate of growth of M with the several parameters specifying the model and the geometry, and reflect the elementary cell's volume dependence on the source parameters.

Figure 29b and 29c shows the behavior as a function of X of the total, as well as the global and local components of the performance bounds. $\sigma^2_{loc_j}$ follows essentially the Cramer-Rao bounds, while $\sigma^2_{gl_j}$ reflects the behavior of $Pr(\epsilon)$ with X. We note that for small X, the local errors dominate the global ones, since the probability of error is practically zero because of the wide spread of the main lobe. After a transitional value, X_{tr}, between .02 and .04, the algorithm mean-square performance is essentially dominated by the global errors. These threshold effects will now be discussed in more detail.

2.4.3 Limiting Behavior of the ML Algorithm for Large Signal-to-Noise Ratio and with the Total Number of Independent Observations

Figure 29b and 29c exhibits a well-defined threshold on the processor's performance. For $X < X_{tr}$ the system behaves as predicted by the Cramer-Rao bounds. For $X > X_{tr}$

the global errors dominate the algorithm behavior, and the performance departs significantly from that predicted by the Cramer-Rao bounds. For high signal energy-to-noise ratio and with $\Pr(\epsilon) \ll 1$, the ratio of the two mean-square error components leads to

$$\delta = \frac{\sigma^2_{gl_j}}{\sigma^2_{loc_j}} \approx \frac{\frac{(\Delta_M A_j)^2}{6}\left[\ln M - \frac{1}{2M} + \gamma\right]}{\left(\frac{\lambda}{2\pi}\right)^2 f_j(A,X)}, \tag{57}$$

where f_j represents the dependence on A and X of the diagonal elements of $\mathcal{M}^{-1}$. This expression shows that for high signal energy-to-noise ratio δ is practically independent of the signal-to-noise ratio.

Depending on the several parameters, and as shown in Fig. 29b and 29c, δ may be greater or smaller than 1, with the expected performance dominated by the global or the local errors. When $\delta > 1$, no matter how large we make the signal-to-noise ratio, the mean-square error performance does not approach the Cramer-Rao bounds. This inherent suboptimality is characteristic of the way the ML algorithm is implemented, that is, in the two-step procedure.

We shall comment in section 3.4.5 that it is easy to prove that the ML estimates are still asymptotically efficient in the signal-to-noise ratio sense.

In practice, this is not a major issue and can be circumvented by means of independent measurements. In actual applications the channel characteristics have a finite coherence time, and so multiple independent measurements are available. For N independent measurements with

$$\tilde{r}_i(t) = \sqrt{2}\ \mathrm{Re}\left\{\left[\tilde{b}_i \tilde{s}(t) + \tilde{w}_i(t)\right]\exp(-j\omega_c t)\right\} \quad i = 1, \ldots N, \tag{58}$$

where the $\tilde{b}_i$ are independent, identically distributed, complex Gaussian random variables, the first step of the algorithm can be modeled as a multiple hypothesis testing with diversity, i.e., an M-ary decision with orthogonal observations transmitted over N Rayleigh channels. For high signal energy-to-noise ratio,[31,24] the probability of error can be approximated by

$$\Pr(\epsilon) = M\left(\frac{1}{\pi N}\right)^{1/2} \frac{(1+\bar{E}_r/N_o)^N}{\frac{\bar{E}_r}{N_o}\left(1+\frac{2\bar{E}_r}{N_o}\right)^{2N-1}}.$$

The Cramer-Rao bounds are given by expressions equivalent to those derived before, provided we normalize the signal energy-to-noise ratio by a factor of N. For $N \geq 2$, it follows that $\lim_{SNR\to\infty} \delta = 0$ or $\lim_{N\to\infty} \delta = 0$, i.e., that the estimates are asymptotically efficient in both signal-to-noise and classical senses (large N).

III. STATIONARY (OMNIDIRECTIONAL) ARRAY WITH MOVING SOURCE ($SAMS_o$)

We have studied in detail tracking stationary sources with linear observers. The problem reduced to the estimation of two parameters, range and bearing, from narrow-band passive signals.

Now we shall enlarge the class of passive tracking problems to include nonstationary sources. In order to resolve the fundamental issues, we restrict the source dynamics to be deterministic and linear. For simplicity, we assume a stationary and omnidirectional receiver. In Section IV we shall lift this restriction and point out the essential features in a general tracking problem. We shall see there how these relate to and include the features dealt with here.

First, we establish the model and discuss the constraints imposed on the problem. Next, we design the receiver. Then we analyze the receiver structure and study its error performance. The essential aspects of the theory (maximum-likelihood) follow the details described in Section II. We shall refer to the general results and proceed to their application to the present problem.

3.1 MODEL

As in the previous section the geometry is planar and the signals are narrow-band. Equations 1, 2, and 3 describe in detail the assumed signal structure.

The functional form of the range function depends on the class of motions and parametrization chosen. We assume that the source moves along a deterministic linear path with constant speed v, as illustrated in Fig. 30.

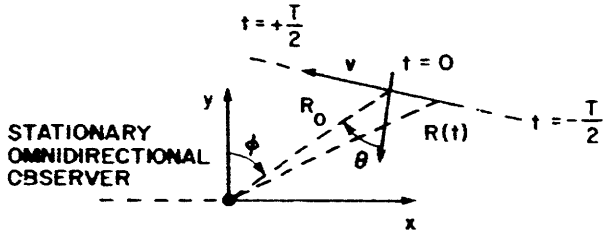

Fig. 30. Stationary Array/Moving Source.

The observer is stationary and has no bearing discrimination capabilities of its own; it is either a short baseline linear array, or an omnidirectional nonlinear array with dimension L. With this geometry the estimation problem is reduced to a three-parameter estimation where

$$R(t, \ell) = \{R_o^2 + v^2 t^2 - 2vtR_o \sin\theta\}^{1/2}, \qquad t \in \left[-\frac{T}{2}, \frac{T}{2}\right] \tag{59a}$$

with the parameter vector

$$A = \begin{bmatrix} R_o \\ v \\ \sin\theta \end{bmatrix}. \tag{59b}$$

Comparing this problem with SASS we have, in addition to the range and angle parameters, the source speed v, an unknown, to be estimated. We remark also that the problem as described is unrealistic from a practical point of view, since the angle ϕ in Fig. 30 is not uniquely specified, and the geometry rotates about the observer location on the plane defined by the source linear motion and the sensor. To solve this ambiguity, the observer needs its own angle discrimination. This will be considered in Section IV.

Equation 59a shows that for $SAMS_o$ the required information to describe the range function in the entire observation interval is conveyed by three parameters. Conversely, $SAMS_o$ represents the problem where the range function (the three source parameters) is reconstructed solely from the temporal modulations induced by the relative dynamics.

By a Taylor's series expansion, we approximate Eq. 59a:

$$R(t, \ell) \cong R_o - (v \sin\theta)t - \frac{v^2\cos^2\theta}{R_o}\frac{t^2}{2!} + 3\frac{v^2\cos^2\theta}{R_o}\frac{v\sin\theta}{R_o}\frac{t^3}{3!} + \ldots \tag{60}$$

Since the signal model assumes no knowledge of the absolute phase, the information on the source parameters is on the modulations induced on the temporal signal structure. For small observation intervals a linearized approximation is valid, and the observer measures the source downrange velocity component. This finds practical applications in navigation, with radiolocation systems, such as Loran, Decca, or Omega, utilizing phase information to measure velocity. This velocity determination has also found increased use when tracking remote platforms such as dropsonders, balloons measuring wind, drifting buoys for collecting oceanographic data (e. g., ocean currents). A receiver is installed on the moving platform and the radio navigation information is retransmitted to the base station, which determines the velocity (downrange) from the recorded incremental motion.

By further enlarging the observation interval, the second- (radial acceleration) and third-order effects can be measured. Since the transformation of coordinates defined by

$$\dot{R}_o = -v \sin\theta$$

$$\ddot{R}_o = \frac{v^2\cos^2\theta}{R_o}$$

$$\dddot{R}_o = 3\frac{v^2\cos^2\theta}{R_o}\frac{v\sin\theta}{R_o}$$

has a nonzero Jacobian

$$\frac{\partial(\dot{R}_o, \ddot{R}_o, \dddot{R}_o)}{\partial(R_o, v, \sin\theta)} = \frac{6v^5}{R_o^4}\cos^2\theta\sin\theta,$$

except for broadside ($\theta = 0$), end-fire ($\theta = \pi/2$), or stationary target/receiver ($v = 0$) configurations, we conclude that third-order effects are sufficient for local specification of the source position and dynamics (Implicit Function theorem). That the Jacobian is zero for specific geometries, may serve as a warning about possible difficulties for these configurations. Whenever the Jacobian is nonzero, we have

$$R_o = -\frac{3\ddot{R}_o\dot{R}_o}{\dddot{R}_o} = 3\left|\frac{\dot{R}_o\ddot{R}_o}{\dddot{R}_o}\right| \tag{61a}$$

$$v = \dot{R}_o\left[1 - \frac{3\ddot{R}_o^2}{\dot{R}_o\dddot{R}_o}\right]^{1/2} = \dot{R}_o\left[1 + \frac{3\ddot{R}_o^2}{|\dot{R}_o\dddot{R}_o|}\right]^{1/2} \tag{61b}$$

$$\sin\theta = -\frac{1}{\left[1 + \dfrac{3\ddot{R}_o^2}{|\dot{R}_o\dddot{R}_o|}\right]^{1/2}} \tag{61c}$$

and, besides an indetermination on the signal of v or $\sin\theta$, we have global parameter identifiability; therefore, we assume $v > 0$.

3.2 RECEIVER DESIGN

We apply the maximum-likelihood techniques previously described. The receiver is a matched filter followed by an envelope detector. The log ML-function is given by Eq. 10a, but now the parameter vector is the three-dimensional vector of Eq. 59b. We have a three-dimensional stochastic maximization that will be accomplished via the two-step mechanization discussed in Section II. The receiver is equivalent to a three-dimensional bank of matched filters followed by square envelope detectors. We look essentially for the network cell maximizing the signal-to-noise ratio. A local tune-up on the source parameters follows the coarse search accomplished in the first step.

3.3 GENERALIZED AMBIGUITY FUNCTION (GAF)

The signal autocorrelation and the generalized ambiguity functions were given in Definitions 1 and 2, and Eqs. 13. The range phase difference now is

$$\Delta R(t, A, \bar{A}) = \frac{2\pi}{\lambda} \left\{ \left[R_o^2 + v^2 t^2 - 2vtR_o \sin\theta \right]^{1/2} - \left[\bar{R}_o^2 + \bar{v}^2 t^2 - 2\bar{v}t\bar{R}_o \overline{\sin\theta} \right]^{1/2} \right\}. \qquad (62)$$

As discussed previously, the receiver's ability to locate the source is intrinsically connected to the GAF structure. Two main points have to be investigated, the form and dimensions of the main lobe designing the grid discretizing the parameter space, and the sidelobe structure resulting from significant secondary maxima of the GAF.

The first point, which is that of the main lobe, essentially requires a local analysis on the parameter space; that is, the GAF is expanded in a truncated Taylor's series. Graphical analysis confirms that a second-order expansion on the parameter errors accurately describes the structure of the main lobe. The second point is made through an asymptotic analysis studying the GAF rate of falloff and bounding the GAF structure as the parameter errors increase. We have then two descriptions of the GAF, each of which is valid in a certain region of the parameter space. By graphical analysis, we may conclude that these descriptions essentially account for all the significant structure of the ambiguity function.

Before proceeding, in analogy with Section II, we consider first an approximate expression for the GAF that is obtained when the third-order polynomial approximation (Eq. 60) is valid.

3.3.1 Polynomial Approximations to the Range Phase Difference

In Appendix A we analyze the ambiguity function when the range is approximated by a third-order polynomial, as in Eq. 60. The results are naturally interpreted using the coefficients of Eq. 60 which represent, as seen before, the mismatch on the Doppler modulation, radial acceleration, and third-order time derivative of the range. Since the source parameters may be recovered from these (see Eqs. 61), we concentrate the discussion in terms of the range time derivatives.

Given the form of the GAF along the parameter axis, we give the following definition.

Definition 4. The sinc^2 function of the n^{th} order is given by

$$\text{sinc}_n^2(\Sigma) = \left| \frac{1}{2\Sigma} \int_{-\Sigma}^{\Sigma} \exp j\tau^n \, d\tau \right|^2 . \qquad (63a)$$

It is easily seen that

$$\text{sinc}_n^2(\Sigma) = \left| \frac{1}{\Sigma} \int_0^{\Sigma} \cos \tau^n \, d\tau \right|^2 ; \quad n \text{ odd}. \qquad (63b)$$

$$\text{sinc}_n^2(\Sigma) = \left| \frac{1}{\Sigma} \int_0^{\Sigma} \exp j\tau^n \, d\tau \right|^2 ; \quad n \text{ even}. \qquad (63c)$$

Along the parameter axis the ambiguity function is given by these sinc_n^2 functions. Specifically, along the Doppler axis it is the usual sinc^2 function (see Fig. 13). For the

radial-acceleration parameter the GAF is sinc_2^2 which relates to the Fresnel integrals. Finally, along the third-order time derivative parameter axis the GAF is

$$\text{sinc}_3^2 = \left| \frac{1}{\Sigma} \int_0^{\Sigma} \cos \tau^3 \, d\tau \right|^2 . \tag{64}$$

The integral in Eq. 64 is represented in Fig. 31a, with the limit for large Σ being given in terms of the value at zero of an Airy function,

$$\lim_{\Sigma \to \infty} \int_0^{\Sigma} \cos \tau^3 \, d\tau = \frac{\pi \text{Ai}(0)}{3^{1/3}} = \frac{\pi}{3\Gamma\left(\frac{2}{3}\right)} \approx .765. \tag{65}$$

Figure 31b represents sinc_3^2 and Fig. 31c compares the first three sinc^2 functions. We observe that for larger n, sinc_n^2 is flatter near the origin, as would be expected, with the main lobe approaching a rectangle window type. Outside this main lobe we observe ripples that are more significant, but also die out faster as the order of the function increases. The rippling behavior is intuitively related to the overshooting of the integrals (Gibb's phenomena, see Fig. 31c). The smoother behavior for the higher order sinc_n^2 relates directly to the cancellation of the integral, because of the highly oscillatory character of the exponential function, and is the naive reason for studying these integrals by the method of stationary phase (MSP) (see Appendix A).

For sinc_3^2 the first minimum occurs approximately at $\Sigma_m \approx 1.72$, with $\text{sinc}_3^2(\Sigma_M) \approx .1449$, and the largest secondary maximum is the first one outside the main lobe at $\Sigma_{M_2} \approx .196$, with $\text{sinc}_3^2(\Sigma_{M_2}) \approx .184$. That is, the function is reduced to approximately 18.4% of its maximum at the origin.

In Appendix A, and by a change of variable, we arrive at the signal autocorrelation function for the general third-order polynomial range approximation

$$\psi(A, \bar{A}) = \frac{1}{\Delta\Sigma} \int_{\Sigma_i}^{\Sigma_f} \exp j\omega\tau \exp j\tau^3 \, d\tau$$

with

$$\omega = \frac{1}{\Delta_3^{1/3}} \left(\Delta_1 - \frac{\Delta_2^2}{3\Delta_3} \right)$$

$$\Delta\Sigma = \Sigma_f - \Sigma_i = \Delta_3^{1/3} \left[\frac{T}{2} + \frac{1}{3} \frac{\Delta_2}{\Delta_3} \right] - \Delta_3^{1/3} \left[-\frac{T}{2} + \frac{1}{3} \frac{\Delta_2}{\Delta_3} \right] = \Delta_3^{1/3} T.$$

We shall not display this function graphically here, since we shall present graphs of the exact ambiguity structure later. We turn instead to its asymptotic behavior. For

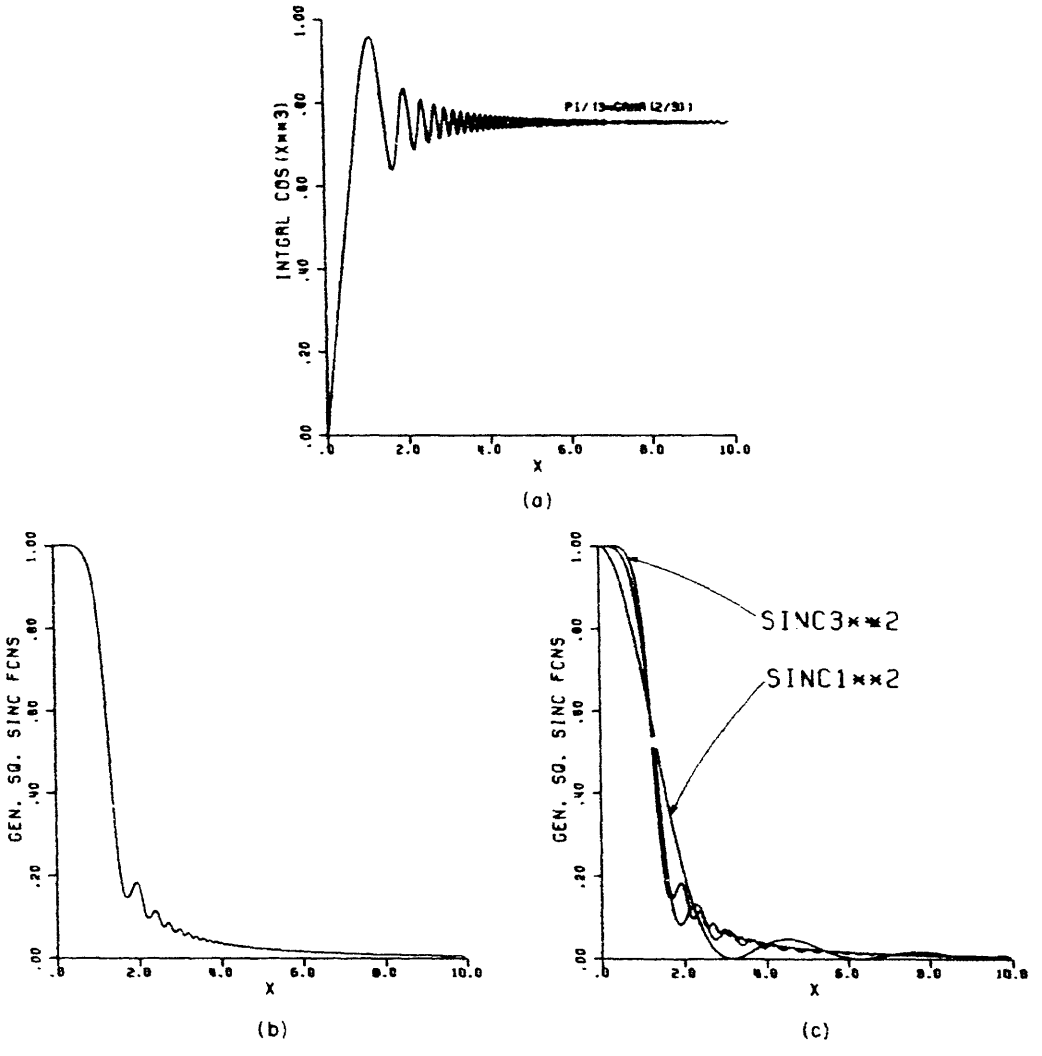

Fig. 31. (a) Integral of cos X^3 vs integration interval.
(b) Generalized third-order sinc^2 function.
(c) Generalized sinc^2 functions up to third order.

large observation intervals the signal autocorrelation function may be written in terms of an Airy function (see Appendix A). We have

$$\psi(A, \bar{A}) \sim \frac{\pi}{3^{1/3}} \frac{1}{\Sigma} \text{Ai}\left(\pm \frac{\omega}{3^{1/3}}\right).$$

Using the asymptotic expansions for the Airy functions shown in Appendix A, for large ω we have

$$\psi(A, \bar{A}) \sim \frac{\pi}{2 \times 3^{1/3}} \frac{1}{\Sigma} \left(\pi^2 \frac{\omega}{3^{1/3}}\right)^{-1/4} e^{-\xi} \left(1 - \frac{5}{72} \xi^{-1}\right) \tag{66a}$$

if $\omega > 0$, and

$$\psi(A, \bar{A}) \sim \frac{\pi}{2 \times 3^{1/3}} \frac{1}{\Sigma} \left(\pi^2 \frac{\omega}{3^{1/3}} \right)^{-1/4} \left[\sin\left(\xi + \frac{\pi}{4}\right) - \cos\left(\xi + \frac{\pi}{4}\right) \frac{5}{72} \xi^{-1} \right] \qquad (66b)$$

if $\omega < 0$, where $\xi = \frac{2}{3}\left(\frac{\omega}{3^{1/3}}\right)^{3/2}$ and $\Sigma = \Delta_3^{1/3} \frac{T}{2}$.

Equations 66 show that for large parameter errors the ambiguity function decreases with the inverse of a certain power of Σ and ω, and hence of the mismatch on the range derivative parameters.

3.3.2 General Case

The generalized ambiguity function, given by Eqs. 13 and 14, is studied graphically for the $SAMS_o$ context in Figs. 32, 33, and 34 (see also Fig. 12a and 12b). The source actual parameters are assumed fixed:

$$A_a = \begin{bmatrix} R_{o_a} \\ v_a \\ \sin\theta_a \end{bmatrix} = \begin{bmatrix} .6 \times 10^5 \text{ ft} \\ 30 \text{ ft/sec} \\ \sin 15° \end{bmatrix}.$$

Figures 32a and 33b are three-dimensional plots of the GAF on the coordinate planes. The line of sight is given by the angles θ and ϕ illustrated in Fig. 16. In particular, for these figures $\theta = 150°$ and $\phi = 210°$. That is, the GAF is viewed from below and behind. Figures 12b, 32b, and 33b show the corresponding contour plots. In Fig. 33b the shearing of the ambiguity function is like what occurs with chirp (linear frequency-modulated) cw radars. The value of the geometric parameter is $X = \frac{vT}{2R_o} = \frac{1}{8}$. Figure 34a and 34b shows the ambiguity function on the range/velocity plane for a smaller value, $X = 1/16$ as seen from two different viewing angles. Figure 34c is the corresponding contour plot. In Section II we presented several three-dimensional and contour plots of the GAF on the range/sin θ plane for different values of X. We shall not repeat them here.

From these graphs we conclude qualitatively that the ambiguity function has a main lobe, centered at the source geographical position at $t = 0$ (midpoint of the observation interval) and negligible subsidiary peaks that will be ignored in the subsequent error analysis. We recall that the generalized ambiguity function is the output of the ML receiver in the absence of noise. Its peaked structure shows the model global identifiability, and hence that it is possible to estimate globally and simultaneously all of the source parameters from the array measurements.

Figures 12b, 32b, and 33b show the main lobe equal height contours on the three coordinate planes as approximate ellipses; this suggests that the three-dimensional

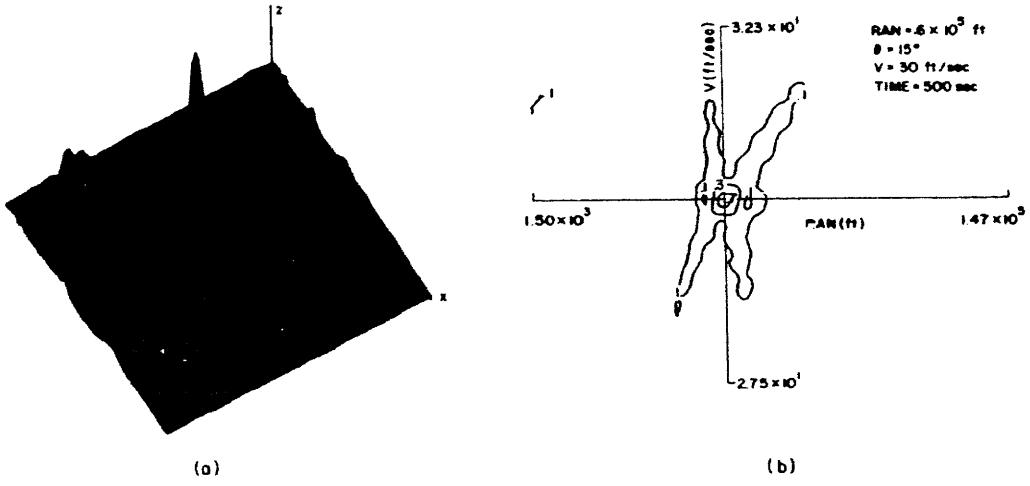

Fig. 32. (a) Three-dimensional range/velocity ambiguity structure (X=1/8).
(b) Contour range/velocity ambiguity structure (X=1/8).

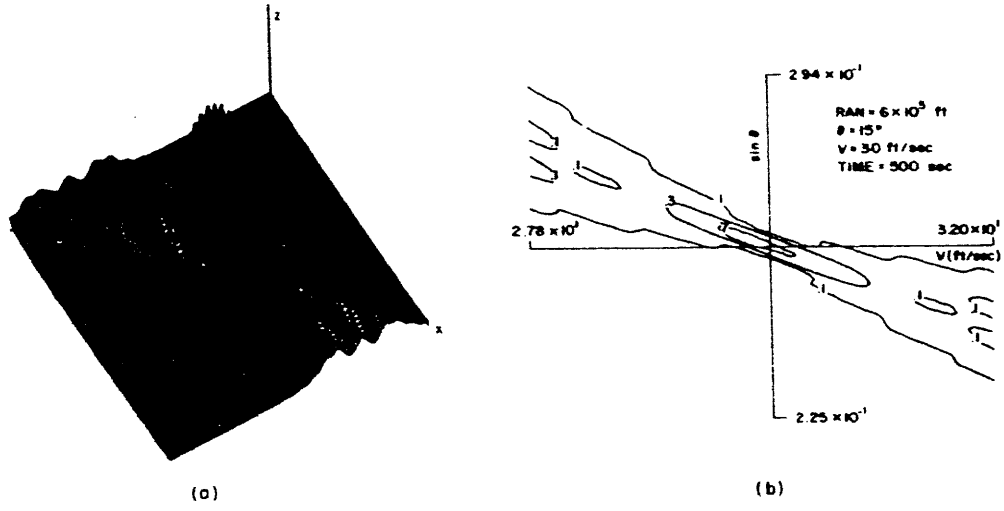

Fig. 33. (a) Three-dimensional velocity/angle ambiguity structure (X=1/8).
(b) Contour velocity/angle ambiguity structure (X=1/8).

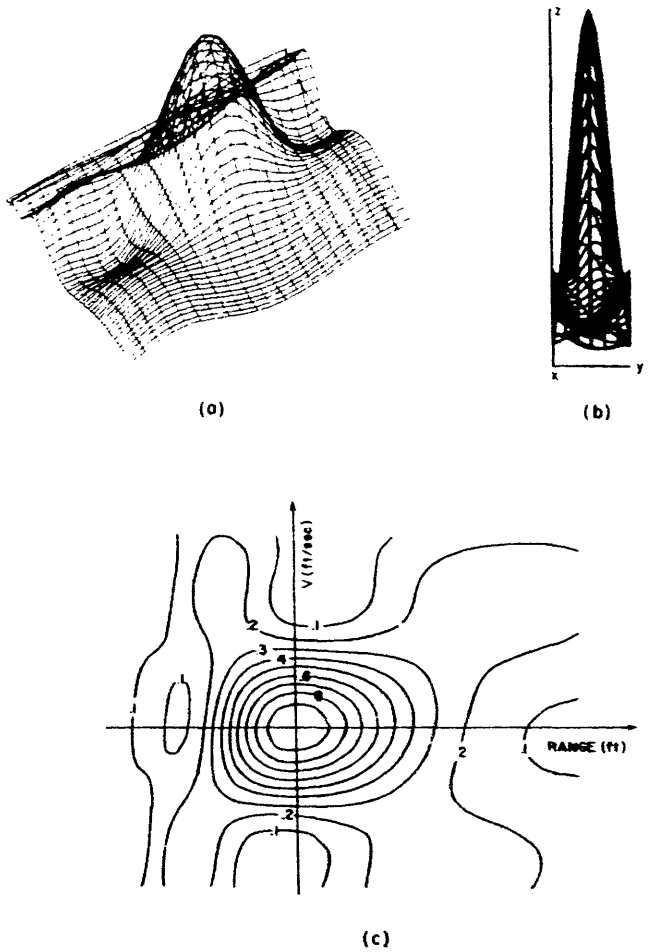

Fig. 34. (a) Three-dimensional range/velocity ambiguity structure (X=1/16).
(b) Three-dimensional range/velocity ambiguity structure (X=1/16).
(c) Contour range/velocity ambiguity structure (X=1/16).

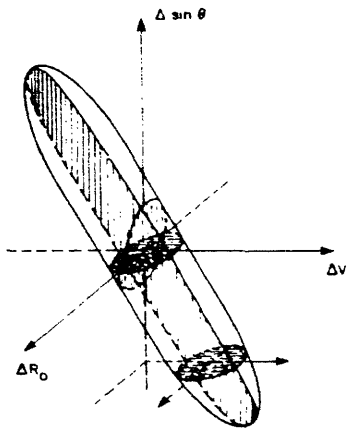

Fig. 35.
Main lobe ellipsoidal structure.

equal height contours of the main lobe are roughly ellipsoids. This was confirmed by looking at the equal height contour plots of the GAF main lobe on planes parallel to the coordinate axes planes. In Fig. 35 we show one of these ellipsoids generated from the corresponding intersections (ellipses) on the coordinate axes planes.

This main lobe configuration will be referred to as ellipsoidal structure. As we shall see, it plays an important role in performance studies, since it determines the form and dimension of the elementary cells of the grid used in the first step of the algorithm implementing the ML estimation.

Finally, we shall comment on the rate of fall of the secondary GAF structure, in order to find how large the secondary main lobes of the GAF are, how they fall off as we get farther away from the source location in the parameter space, and what is the asymptotic behavior of this secondary structure as the observation interval is increased.

In Appendix A we resort to the method of stationary phase (MSP) to find the asymptotic behavior of the GAF and to bound its secondary structure. We find that at each point of the parameter space Ω these bounds depend on the value of the first nonzero range phase difference derivatives in the observation interval. For the actual form of these bounds, refer to Eqs. A.40 and A.41. These equations show that the ambiguity structure decreases hyperbolically with the square of the n^{th} root of the n^{th} range phase difference derivative (which is the first derivative evaluated at that point of the parameter space which does not vanish in the whole observation interval). This asymptotic structure also decreases with $(T/2)^{-2}$.

We keep referring to this structure of the ambiguity function because it plays an essential role in the global parameter observability, and in the mean-square performance bounds. We normalize our nomenclature.

1. Main lobe ellipsoidal structure stands for a GAF that exhibits a main lobe well approximated by a quadratic expansion on Ω.

2. Secondary negligible structure means that the GAF is negligible outside its main lobe.

3. Hyperbolic secondary structure refers to the GAF decay with the inverse of a certain power of the parameter errors on Ω.

The evolution of the form and dimensions of the main lobe as we increase the observation interval will be quantified later when we study the asymptotic performance of the mechanization of the ML algorithm.

3.4 PERFORMANCE ANALYSIS

We analyze the mean-square error performance of the two-step algorithm mechanizing the ML estimation of the source parameter vector $A = \begin{bmatrix} R_o \\ v \\ \sin\theta \end{bmatrix}$. The total mean-square error of the component A_j is decomposed in two terms. The first, referred to as the global mean-square error $\sigma^2_{gl_j}$, results from decision errors or diversions. The

second, the local mean-square error $\sigma^2_{loc_j}$, depends on the flatness of the main lobe, and is estimated from the Cramer-Rao bounds.

Because of the main lobe ellipsoidal structure, and the negligible secondary structure, the assumptions behind the derivation of the mean-square error expressions in Section II still hold. In particular, the GAF can be approximated by a second-order expansion about the actual source parameter values, with the result expressed in terms of the mean-square spread matrix $\mathcal{M}$; and the first step of the ML algorithm modeled as an M-ary decision problem with orthogonal signals over a Rayleigh channel. Again, the total number M of hypotheses depends on the a priori region of interest Ω in the parameter space and on the matrix $\mathcal{M}$, namely on its eigenvalues and eigenvectors.

These circumstances underline the importance of the mean-square spread matrix $\mathcal{M}$. In Appendix B we compute this matrix and arrive at closed-form expressions for its elements. Given its unappealing complexity, we first present a local analysis based on truncated Taylor's series when the geometric parameter $X = vT/2R_o$ is small.

3.4.1 Short Observation Interval Analysis (Distant Observer)

a. Full $SAMS_o$ Problem

In many situations of practical significance the geometric parameter $X = \frac{vT}{2R_o} < 1$; that is, the geometry corresponds to a distant observer type. With this condition, a truncated Taylor's series analysis can be pursued, and it leads to meaningful results. Accordingly, we consider this approach.

The range phase is approximated by an n^{th}-order polynomial

$$R(t, A) = \left[R_o^2 + v^2t^2 - 2vtR_o \sin\theta\right]^{1/2} \cong \sum_{i=0}^{n} {}^{(i)}R_o \frac{t^i}{i!}, \tag{67}$$

where ${}^{(i)}R_o = \frac{d^i}{dt^i} R(t, A)\Big|_{t=0}$.

In the sequel we are interested in the matrix $\mathcal{M}$, its inverse, its classical adjoint $\tilde{\mathcal{M}} = (\det \mathcal{M})\mathcal{M}^{-1}$, and its determinant. As it turns out, the first nonzero coefficient of the Taylor's series of $\det \mathcal{M}$ is the coefficient of the 12^{th} power in X. In order to get its correct expression, it is required that we keep terms at least up to sixth order in the development of Eq. 67.

We present merely the results of the local analysis. Part of the algebraic manipulations were carried out with the use of MACSYMA, a symbol-manipulating system at Project MAC, M.I.T. For the sake of brevity and intuition, we display only the leading term of the Taylor's series expansion for each element (i.e., its first nonzero term). Higher order terms have to be included in actual computations (e.g., computing $\det \mathcal{M}$

or $\mathcal{M}^{-1}$ from $\mathcal{M}$) so that we preserve the nonsingular character of $\mathcal{M}$.

$$\mathcal{M} = \left(\frac{2\pi}{\lambda}\right)^2 \begin{bmatrix} \frac{\cos^4\theta X^4}{3^2 \times 5} & \frac{R_o}{v}\frac{(11\sin^2\theta - 2)\cos^2\theta X^4}{3^2 \times 5} & R_o \frac{11\sin\theta\cos^2\theta X^4}{3^2 \times 5} \\ = & \frac{R_o^2}{v^2}\frac{\sin^2\theta X^2}{3} & \frac{R_o^2}{v}\frac{\sin^2\theta X^2}{3} \\ = & = & R_o^2\frac{X^2}{3} \end{bmatrix} \tag{68a}$$

$$\tilde{\mathcal{M}} = \text{Adj}\,\mathcal{M} = \left(\frac{2\pi}{\lambda}\right)^4 \frac{\cos^2\theta X^6}{3^3 \times 5} \begin{bmatrix} \frac{R_o^4}{v^2}\frac{4}{\cos^2\theta} & \frac{R_o^3}{v}2 & -\frac{R_o^3}{v^2}2\sin\theta \\ = & R_o^2\cos^2\theta & -\frac{R_o^2}{v}\sin\theta\cos^2\theta \\ = & = & \frac{R_o^2}{v^2}\sin^2\theta\cos^2\theta \end{bmatrix} \tag{68b}$$

$$\mathcal{M}^{-1} = \left(\frac{\lambda}{2\pi}\right)^2 \frac{5^2 \times 7}{X^6} \begin{bmatrix} \frac{1}{\sin^2\theta\cos^4\theta} & \frac{v}{R_o}\frac{1}{2\sin^2\theta\cos^2\theta} & -\frac{1}{R_o}\frac{1}{2\sin\theta\cos^2\theta} \\ = & \frac{v^2}{R_o^2}\frac{1}{4\sin^2\theta} & -\frac{v}{R_o^2}\frac{1}{4\sin\theta} \\ = & = & \frac{1}{R_o^2}\frac{1}{4} \end{bmatrix} \tag{68c}$$

$$\det \mathcal{M} = \left(\frac{2\pi}{\lambda}\right)^6 \frac{R_o^4}{v^2}\frac{4\sin^2\theta\cos^4\theta X^{12}}{3^3 \times 5^3 \times 7}. \tag{68d}$$

The Cramer-Rao bounds are obtained by normalizing the mean-square spread matrix by the gain G given by Eqs. 34. The standard deviations for the error parameters and for the local analysis results are

$$\sigma_{R_o} = \frac{a}{(SNR_{eff}LT)^{1/2}} \frac{5\sqrt{7}}{\sin\theta \cos^2\theta} \frac{1}{X^3} \tag{69a}$$

$$\sigma_v = \frac{a}{(SNR_{eff}LT)^{1/2}} \frac{5\sqrt{7}}{2} \frac{v}{R_o \sin\theta} \frac{1}{X^3} \tag{69b}$$

$$\sigma_{\sin\theta} = \frac{a}{(SNR_{eff}LT)^{1/2}} \frac{5\sqrt{7}}{2} \frac{1}{R_o} \frac{1}{X^3}, \tag{69c}$$

where we recall that $X = vT/2R_o$ and SNR_{eff} and a are given in Eqs. 34. The source/receiver geometry affects the performance in two distinct ways, which we have separated in expressions (69). On the one hand, it renormalizes the received energy. In particular, for the same emitted power and quality of sensors the standard deviation performance deteriorates with the inverse of the source/receiver separation. On the other hand, the performance bounds are directly affected by the actual source parameters and length of the observations, since they determine the spread out of the GAF main lobe, measured by the matrix $\mathcal{M}$. We shall concentrate the discussion on the last effects.

We note the third-order dependence of the standard deviations on the geometric parameter X. This relates intuitively to the fact that the simultaneous estimation of all three source parameters requires at least the observation of third-order time modulation effects.

The range standard deviation bound, given in Eq. 69a has two stationary points at $\sin\theta = \pm \frac{1}{\sqrt{3}}$, for which $\theta = \theta_{min} \approx 35.26° \left(\text{mod}\,\frac{\pi}{2}\right)$. Its second derivative with respect to $\sin\theta$ is positive for $\sin\theta \in [-1, 1]$; it is a convex cup function of $\sin\theta$. This cup behavior reflects the dependence of the range performance on both the downrange and crossrange velocity components given by $v_s = v\sin\theta$ and $v_c = v\cos\theta$ which vanish for broadside and end-fire geometry. We conclude that the range performance standard deviation for the distant observer geometry (or equivalently short observation interval analysis) presents a minimum at $\theta_{min} \approx 35°$ and deteriorates monotonically as we approach both broadside and end-fire geometry. While this last behavior just reflects the dependence of the range performance on the effective array length, which vanishes for end-fire geometry, the former is a new phenomenon that is characteristic of the $SAMS_o$ problem and does not appear with the SASS configurations.

The velocity standard deviation σ_v has a hyperbolic dependence on $\sin\theta$, increasing drastically for $\theta \approx 0°$ (broadside or closest approach geometry). The bearing performance exhibits a hyperbolic dependence on the source/receiver separation and is practically independent of θ.

From Eqs. 69 we obtain the relations

$$\left(\cos^2\theta \frac{\sigma_{R_o}}{R_o}\right) \approx \frac{\sigma_v}{v} \approx \frac{\sigma_{\sin\theta}}{\sin\theta} \tag{70}$$

that reflect the tradeoffs in the performance errors as we vary the geometric parameters.

We indicate by superscript r the reference or nominal values assumed when designing the receiver to meet a prespecified performance. In actual system operation, when the source parameters are different from those assumed at the design stage (for example, for the range parameter and with all other quantities assumed equal) the performance changes according to

$$\frac{\sigma_{R_o}}{\sigma_{R_o^r}} \approx \left(\frac{T^r}{T}\right)^{7/2} \left(\frac{R_o}{R_o^r}\right)^4. \tag{71a}$$

To match the desired Cramer-Rao nominal performance, the observation durations should be adjusted to

$$T \approx T^r \left(\frac{R_o}{R_o^r}\right)^{8/7}. \tag{71b}$$

We show in Fig. 36 a sketch of geometry in which the Cramer-Rao performance is

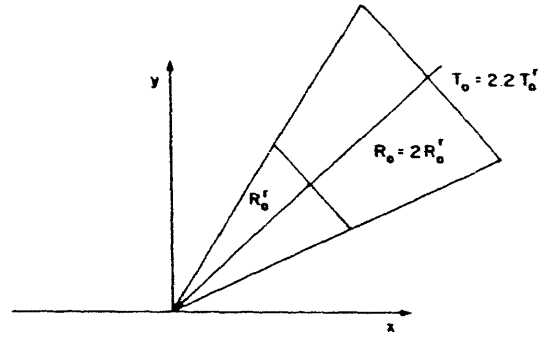

Fig. 36. Cramer-Rao bound equivalent range performance geometry.

practically equivalent. The crosscorrelations of the parameter error, defined as

$$\rho_{ij} = \frac{(\mathcal{M}^{-1})_{ij}}{\left[(\mathcal{M}^{-1})_{ii}(\mathcal{M}^{-1})_{jj}\right]^{1/2}}, \tag{72}$$

from Eq. 68c, are given by

$$\rho_{R_o, v} \approx 1 - a_{R_o, v}(\theta)\, X^2 \tag{73}$$

$$\rho_{R_o, \sin\theta} \approx 1 - a_{R_o, \sin\theta}(\theta)\, X^2 \tag{74}$$

$$\rho_{\sin\theta, v} \approx -1 + a_{v, \sin\theta}(\theta)\, X^2, \tag{75}$$

where $a_{ij}(\theta)$, $i, j = R_o, v, \sin\theta$ are suitable expressions in $\sin\theta$. These results show that the parameter errors are highly correlated up to second-order effects. In order to have a nonsingular estimation problem, i.e.,

$$\rho_{ij} < 1, \qquad i, j \in \{R_o, v, \sin\theta\}, \tag{76}$$

we need a significant value for X. This point will be discussed further when we plot the Cramer-Rao bounds.

Before proceeding, we analyze the spread matrix and the Cramer-Rao performance bounds when we assume that one of the source parameters is known a priori. This may be the case either because it has been determined by some other means or because it represents a higher order of complexity, which happens with the velocity parameter in the Moving (Omnidirectional) Array with Stationary Source (MASS) context, or simply because its incorporation in the estimation problem makes no physical sense (e.g., source speed in SASS). This analysis will shed light on the effects of the geometry, the higher order modulations, and the coupling between the parameter errors on the $SAMS_o$ receiver performance. Besides this, each of the situations that will be described has its own practical significance that warrants further consideration.

The spread matrix is obtained by deletion of the corresponding line and column in the three-dimensional result. We also present the inverse $\mathcal{A}^{-1}$ and other useful parameters.

b. Range/Angle Estimation (SASS)

These applications have been considered in detail in Section II. Knowledge of the vehicle's own speed and/or the total array length makes the range focusing and the angle measurement achievable from the linear and quadratic effects with a corresponding range performance gain of one order of magnitude of X. Furthermore, for broadside geometry and small parameter X, the errors on the parameter estimates are essentially decoupled.

c. Range/Velocity Estimation – Application to Navigation

In this problem the bearing angle is assumed to be known. This might occur in

some navigational applications, or when tracking satellites transmitting narrow-band signals. The latter is illustrated in Fig. 37. The array on Earth observes the satellite

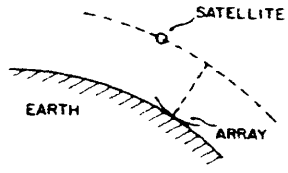

Fig. 37.
Satellite tracking geometry.

passing abeam. The duration of the observations is determined by the strength of the emitted signal and the receiving array gain. Physically speaking, we assume that the observations are symmetric about the rising angle (closest approach), determined, for example, from the position and the orientation of the stationary observer. The essence of the application is that the moving source follows a path that is prescribed or known a priori, the only unknowns being the source/receiver separation and the relative speed.

The results for this problem parallel those for the range/angle estimation (SASS or MASS) after rescaling the involved quantities.

The parameter vector is $A = \begin{bmatrix} R_o \\ v \end{bmatrix}$ and the (local) approximate expressions are

$$\mathcal{M}_{R_o, v} \approx \left(\frac{2\pi}{\lambda}\right)^2 \left[\begin{array}{c|c} \frac{\cos^4\theta X^4}{45} & \frac{R_o}{v}\,\frac{(11\sin^2\theta - 2)\cos^2\theta}{45}\,X^4 \\ \hline = & \frac{R_o^2}{v^2}\,\frac{\sin^2\theta}{3}\,X^2 \end{array}\right] \tag{77a}$$

$$\mathcal{M}^{-1}_{R_o, v} \cong \left(\frac{\lambda}{2\pi}\right)^2 \left[\begin{array}{c|c} \frac{45}{\cos^4\theta X^4} & -\frac{v}{R_o}\,\frac{3\,(11\sin^2\theta - 2)}{\sin^2\theta\cos^2\theta X^2} \\ \hline = & \frac{v^2}{R_o^2}\,\frac{3}{\sin^2\theta X^2} \end{array}\right] \tag{77b}$$

$$\det \mathcal{M}_{R_o, v} \cong \left(\frac{2\pi}{\lambda}\right)^6 \frac{R_o^2}{v^2}\,\frac{\sin^2\theta\cos^4\theta}{135}\,X^6. \tag{77c}$$

The degree of coupling is specified by the crosscorrelation, which is

$$\rho_{R_o, v} \cong -\frac{(11\sin^2\theta - 2)X}{\sqrt{15}\sin\theta}. \tag{78}$$

The eigenvalues and eigenvectors up to truncation are

$$\lambda_{R_o} \cong \left(\frac{2\pi}{\lambda}\right)^2 \frac{\cos^4\theta X^4}{45}, \quad e_{R_o} \cong \begin{bmatrix} 1 \\ 0 \end{bmatrix} \tag{79a}$$

$$\lambda_v \cong \left(\frac{2\pi}{\lambda}\right)^2 \left(\frac{R_o}{v}\right)^2 \frac{\sin^2\theta X^2}{3}, \quad e_v \cong \begin{bmatrix} 0 \\ 1 \end{bmatrix}. \tag{79b}$$

As with SASS, the range is focused from the chirp (second-order) effects, while the source velocity is measured from the linear modulations on the signal structure. We note that the velocity standard deviation increases monotonically as the geometry approaches broadside. This is intuitively clear: for broadside geometry the linear effects are minimum, and the velocity is measured from zero Doppler effects.

d. Velocity/Angle Estimates

In this application we assume that the range is known by means of active range measurement. The analysis brings up one of the major difficulties underlining the $SAMS_o$ estimation problem, the high correlation between the errors in the velocity and angle estimates.

The parameter vector is $A = \begin{bmatrix} v \\ \sin\theta \end{bmatrix}$ and the quantities of interest are given approximately by

$$\mathcal{M}_{v,\sin\theta} \cong \left(\frac{2\pi}{\lambda}\right)^2 \left[\begin{array}{c|c} \frac{R_o^2}{v^2}\left[\frac{\sin^2\theta}{3}X^2 + \frac{\cos^2\theta\,(4-31\sin^2\theta)\,X^4}{45}\right] & \frac{R_o^2}{v}\left[\frac{\sin\theta X^2}{3} + \frac{X^4\sin\theta\,(9\sin^2\theta - 22\cos^2\theta)}{45}\right] \\ \hline = & R_o^2\left[\frac{X^2}{3} + \frac{(31\sin^2\theta - 9)}{45}X^4\right] \end{array}\right] \tag{80a}$$

$$\mathcal{M}^{-1}_{v,\sin\theta} \cong \left(\frac{\lambda}{2\pi}\right)^2 \left[\begin{array}{c|c} \frac{v^2}{R_o^2}\frac{45}{4X^4} & -\frac{v}{R_o^2}\frac{45\sin\theta}{4X^4} \\ \hline & \frac{1}{R_o^2}\frac{45\sin^2\theta}{4X^4} \end{array}\right] \tag{80b}$$

$$\det \mathcal{M}_{v,\sin\theta} \cong \left(\frac{2\pi}{\lambda}\right)^4 \frac{R_o^4}{v^2}\frac{4X^6}{135}. \tag{80c}$$

We stress that the velocity and the angle mean-square errors, calculated from the

diagonal elements of $\mathcal{M}^{-1}$, depend on the 4th power of X^{-1}, as compared with SASS or the previous applications, where they were a function of X^{-2}. One of the eigenvalues is

$$\lambda_s = \left(\frac{2\pi}{\lambda}\right)^2 \frac{R_o^2 X^2}{3}\left(\frac{\sin^2\theta}{v^2} + 1\right)$$

with eigenvector

$$e_s \approx \frac{1}{\sqrt{2}}\begin{bmatrix}1\\1\end{bmatrix}$$

oriented along the downrange velocity component $v_s = v \sin\theta$. The other eigenvalue of order X^4 corresponds to the eigenvector along the crossrange velocity component $v_c = v \cos\theta$. The crosscorrelation between the parameter errors is $\rho_{v,\sin\theta} \approx -1 + a_{v,\sin\theta}(\theta)\, X^2$, which underlines the coupling between the errors on the velocity and angle estimates.

3.4.2 Long Observation Interval Analysis (Close Observer)

We analyze briefly the asymptotic behavior of the Cramer-Rao bounds as the geometric parameter X is increased, or equivalently as

$$Y = X^{-1} = \frac{2R_o}{vT} \to 0.$$

The expressions for the asymptotic behavior of $\mathcal{M}^{-1}$ are presented in Appendix C. After normalizing by G^{-1} we obtain the asymptotic standard deviations predicted by the Cramer-Rao bounds:

$$\sigma_{R_o} \approx \sigma_{R_{o_\infty}} = G^{-1/2}\left(\frac{2\cos\theta}{\pi Y}\right)^{1/2} = \frac{a}{(\pi SNR_{eff} L)^{1/2}}\left(\frac{v\cos\theta}{R_o}\right)^{1/2} \tag{81a}$$

$$\sigma_v \approx \sigma_{v_\infty} = G^{-1/2}\sqrt{12}\,\frac{v}{R_o}\,Y = \frac{a\sqrt{12}}{(\pi SNR_{eff} L)^{1/2}}\,\frac{2R_o}{vT^{3/2}} \tag{81b}$$

$$\sigma_{\sin\theta} \approx \sigma_{\sin\theta_\infty} = \left(\frac{\sigma_{R_{o_\infty}}}{R_o}\right)\sin\theta. \tag{81c}$$

As with SASS, the range and bearing performance decrease monotonically to nonzero lower bounds, while the velocity bound vanishes. The errors in the velocity estimates are asymptotically uncorrelated to the other parameter errors; that is, for large geometric parameter X the velocity estimation uncouples from the bearing and range estimation. This is intuitively clear; for a large observation interval the problem tends to the Doppler configuration illustrated in Fig. 38, for which the ambiguity function is

given by

$$\phi(A, \bar{A}) \sim \text{sinc}^2 \left[\frac{2\pi}{\lambda} \Delta v \, \frac{T}{2} \right] \tilde{\phi}(\Delta R, \Delta \sin\theta, A). \tag{82}$$

That is, the ambiguity structure is essentially decoupled in the velocity parameter.

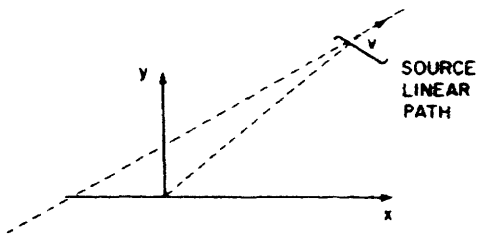

Fig. 38.
Doppler configuration.

Just as with SASS, the errors in the two other parameters are asymptotically perfectly correlated, and involve sensitivity problems like the ones discussed in Section II.

3.4.3 Graphical Display of the Cramer-Rao Bounds

We return to the closed-form expressions for $\mathcal{M}^{-1}$ (see Appendix B) and to the Cramer-Rao bounds obtained from the diagonal elements of $\mathcal{M}^{-1}$, after normalization by the gain G^{-1}.

The nominal conditions, unless otherwise specified, are assumed to be

SNR = emitted signal-to-noise ratio = .5 = -3 dB

$R_o^r = 6 \times 10^4$ ft

$\lambda = 50$ ft

$v = 30$ ft/sec

$\theta = 15°$

$L = 250$ ft

$\sigma_b^2 = .5.$

Figure 39 shows as functions of X the diagonal elements of $\mathcal{M}^{-1}$ normalized by the squared inverse of the modulation index $\beta = 2\pi/\lambda$, with the local and asymptotic tangents arrived at by truncated Taylor's series expansions. The convex cup behavior of $\mathcal{M}^{-1}_{R_o}$ and $\mathcal{M}^{-1}_{\sin\theta}$ is due to the phenomena analyzed in Section II: for small X, the lobe is well spread over Ω with consequent small second-order derivatives of the GAF at the source location; for large X, the main lobe approaches a rectangular type of window in the range/bearing subspace. The inverse velocity spread $\mathcal{M}^{-1}_{v}$ is monotonically decreasing, evolving from the local to the asymptotic tangent.

Figure 40 shows as a function of X the crosscorrelation between the errors in the estimates for the several parameters. For small X the errors are highly correlated.

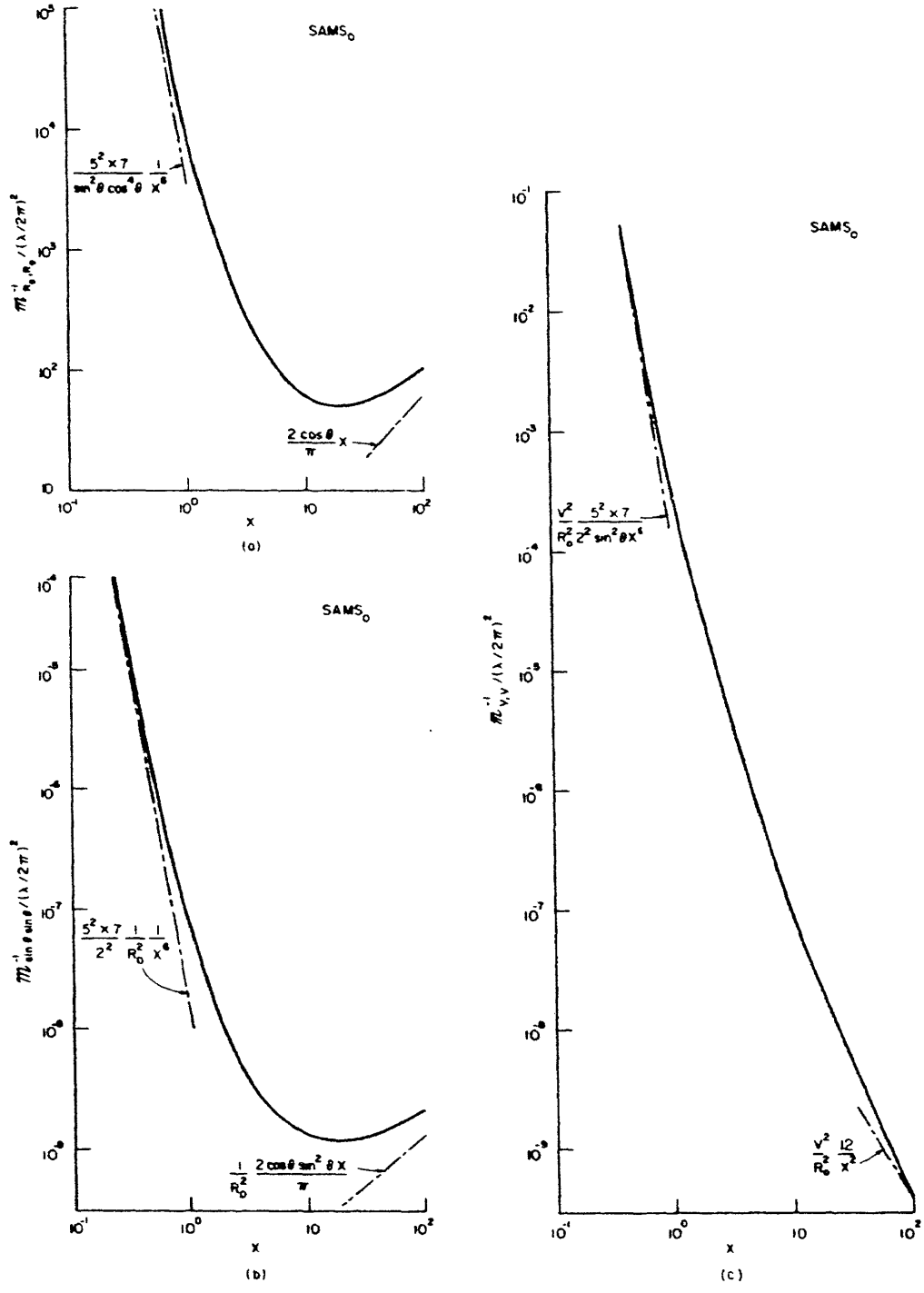

Fig. 39. (a) Range mean-square spread vs X.
(b) Angle mean-square spread vs X.
(c) Speed mean-square spread vs X.

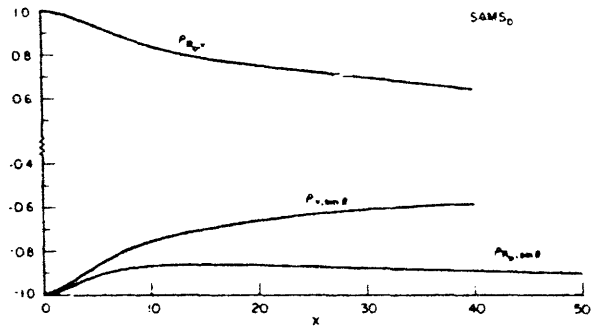

Fig. 40. Crosscorrelation vs X.

As X increases $\rho_{R_o, v}$ and $\rho_{v, \sin\theta}$ decrease monotonically [evolution to Doppler configuration (Fig. 38)], while $\rho_{R_o, \sin\theta}$ decreases first (reflecting reduction in correlation as higher order effects are measured) to increase again for large X (rectangular type of ambiguity function in the $R_o/\sin\theta$ subspace).

For small values of the geometric parameter X (valid local analysis), Figs. 41-43 illustrate the dependence of the Cramer-Rao bounds on the source parameters and the geometry. Figure 41 shows the behavior of σ_{R_o} as a function of θ. It displays the

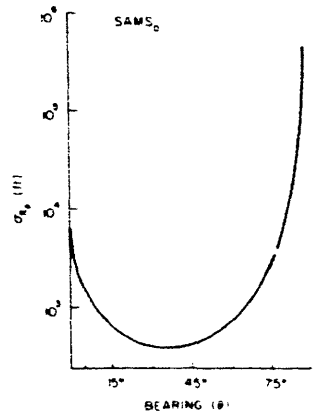

Fig. 41.
Range Cramer-Rao bound vs bearing.

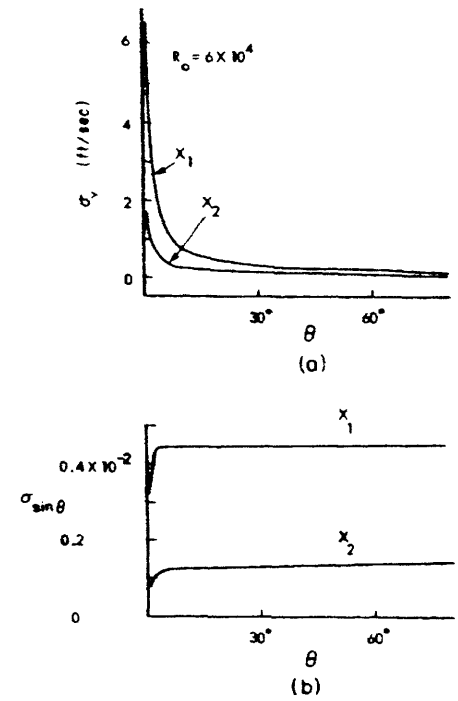

Fig. 42.
(a) Speed and (b) angle Cramer-Rao bound vs bearing.

convex cup behavior referred to in the local analysis of the bound, and reflects the strong coupling between the errors in the angle and velocity estimates (skewed error ellipsoids) that are propagated to the range errors. A maximum range performance is obtained for a geometry with $\theta \approx 35°$, as predicted by the local analysis. This performance deteriorates monotonically, as the geometry approaches either broadside (large errors in the velocity parameter) or end-fire (reduction of effective array length) conditions.

Figure 42 shows the velocity and sin θ performance as a function of bearing. The predicted behavior is confirmed: σ_v increases sharply at broadside (vanishing downrange velocity) and decreases monotonically as we approach end-fire (downrange velocity component is the source speed). The bearing performance is practically invariant to the actual bearing angle.

Figure 43a shows the dependence of the range performance on the absolute value of R_o, as we increase the observation interval proportionately, so that the geometric parameter X is kept constant. The deterioration in performance is essentially due to the signal-power dependence on the normalized inverse of the range squared.

Figure 43b presents the crosscorrelation between the errors in the several parameters as a function of θ with X as a parameter. The strong coupling already noted is displayed, which for small X is one order of magnitude stronger for $\rho_{v,\ \sin\theta}$. The curves for $\rho_{R_o v}$ and $\rho_{R_o \sin\theta}$ should be compared with the corresponding values obtained with the two-parameter estimation problem; the third parameter, either velocity or bearing, is assumed known. It is immediately apparent that the presence of the third parameter in the full $SAMS_o$ introduces a strong coupling between errors.

3.4.4 Global Performance

As we have already discussed, the total mean-square error for the mechanization of the ML algorithm in two stages, $\sigma^2_{tot_j}$, is given approximately (Eqs. 52) by local $\sigma^2_{loc_j}$ and global $\sigma^2_{gl_j}$ components. We shall analyze the dependence of these quantities on the several parameters. In the graphical representations we assume, unless otherwise stated, the nominal conditions previously given. We also assume that the a priori region Ω of interest in the parameter space is

$$\Omega = \begin{cases} \Delta_M R_o = R_{o_M} - R_{o_m} = 6 \times 10^5 \text{ ft} \\ \Delta_M v = v_M - v_m = 3 \text{ ft/sec} \\ \Delta_M \theta = \theta_M - \theta_m = 5° \end{cases}$$

and that the signal-to-noise ratio is SNR = 0 dB.

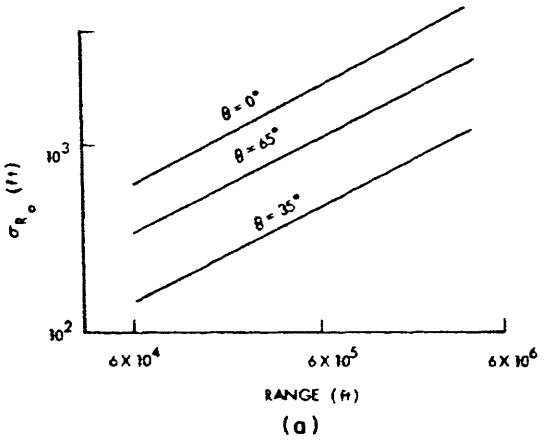

(a)

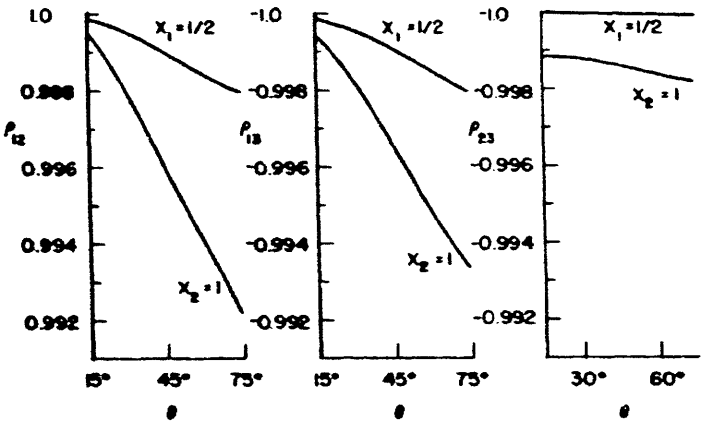

(b)

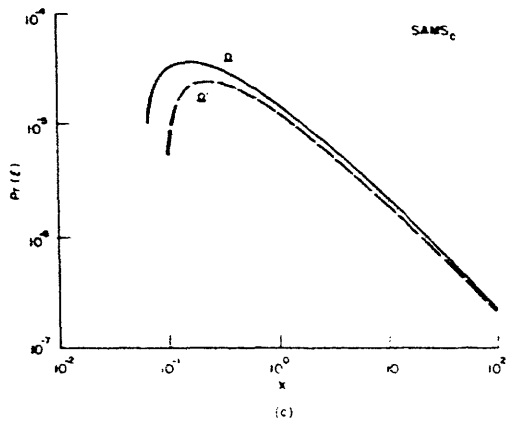

(c)

Fig. 43. (a) Range Cramer-Rao bound vs range (X=constant).
(b) Crosscorrelation vs bearing.
(c) Probability of a diversion X.

a. Probability of Error and Total Number of Grid Cells

We begin by discussing $Pr(\epsilon)$ and M. In Section II several expressions were presented for the probability of a diversion. For the high signal energy-to-noise ratio situation it is approximated by Eq. 50b. The total number of grid cells is given by $M = V_\Omega / V_a$, where the volume of the elementary cell is the product of the square root of the eigenvalues of $\mathcal{M}^{-1}$ after normalization by a factor dependent on the specific form assumed for the elementary cell. An analytic expression for the eigenvalues of $\mathcal{M}^{-1}$ is difficult to obtain, since it would involve the roots of a third-order polynomial. We observe, however, that the product of the eigenvalues is an invariant characteristic of a linear transformation, its determinant, leading to $M = \frac{V_\Omega}{k} (\det \mathcal{M})^{1/2}$. For the distant observer geometry (local analysis)

$$M_{loc} \approx \frac{V_\Omega}{k} \left(\frac{2\pi}{\lambda}\right)^3 \frac{R_o^2}{v} \frac{2 \sin\theta \cos^2\theta X^6}{3 \times 5 \times \sqrt{3 \times 5 \times 7}}. \tag{83a}$$

For the close observer geometry (asymptotic analysis)

$$M_{asympt} \approx \frac{V_\Omega}{k} \left(\frac{2\pi}{\lambda}\right)^3 \frac{R_o^2}{v} \frac{1}{2} \left(\frac{\pi}{6 \cos\theta Y}\right)^{1/2}. \tag{83b}$$

These expressions show analytically the rate of growth of the total number of grid cells with the several parameters, for the local and the asymptotic geometry. In Fig. 44 we represent $\det \mathcal{M}$ as a function of X. We observe that it is monotonically increasing, evolving from a local to an asymptotic tangent, thereby implying a change in the rate of growth of M from X^6 to $\sqrt{X}$.

Figure 43c shows the evolution of $Pr(\epsilon)$ as we increase X, and for two regions of a priori interest in the parameter space. We take

$$\Omega_1 = \Omega$$

and

$$\Omega' = \Omega_2 = \begin{cases} \Delta_M R_o = 6 \times 10^5 \text{ ft} \\ \Delta_M v = 1.5 \text{ ft/sec} \\ \Delta_M \theta = 1^\circ \end{cases}$$

i.e., $V_{\Omega_2} = V_{\Omega_1}/10$. We note first the concave behavior of $Pr(\epsilon)$ with X. For small X the GAF main lobe is spread all over Ω and so $M = 1$, implying $Pr(\epsilon) = 0$. As X increases, the variation in M dominates over the signal energy-to-noise ratio variation, until a maximum is reached which could be arrived at analytically. Afterward $Pr(\epsilon)$ decreases

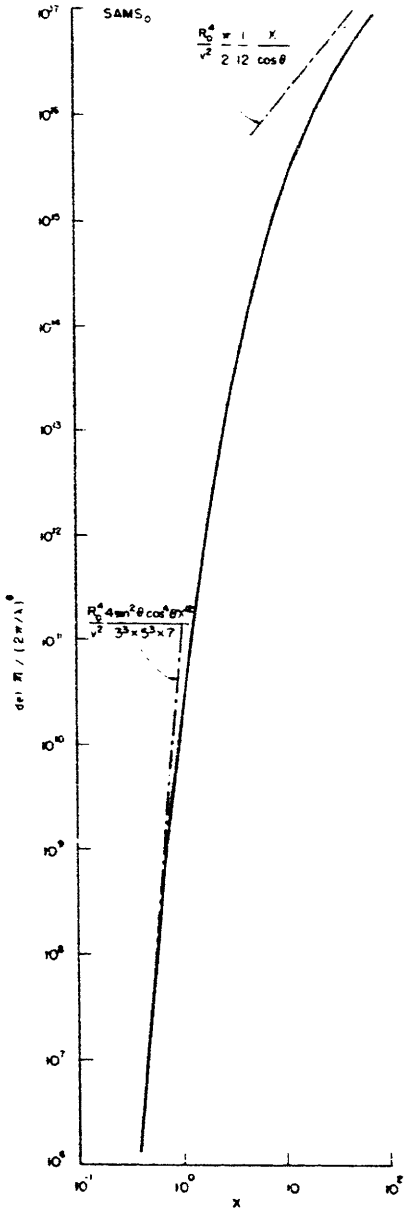

Fig. 44.
Determinant of $\mathcal{H}$ vs X.

monotonically, following a $\frac{1}{T}$ ln T law. The effect of changing V_Ω is more marked for small X, essentially pushing the point for which the GAF main lobe is smaller than the a priori region of interest to a larger value of X, and hence leading to M > 1. For large X this has a vanishing effect because of the ln T/T law.

Finally, we note that when X is small, so that the local analysis holds, and whenever all other parameters are kept identical, $M = M^r\left(R_o/R_o^r\right)^2$ where M^r corresponds to R_o^r (reference range). This expression says that the total number of grid cells increases with the square of the source/receiver separation, and it underlines the vast amount of computation time that may be required for very distant targets. When similar conditions hold

$$Pr(\epsilon) = \frac{R_o}{R_o^r}\left[1 + 2\,\frac{\ln\left(R_o/R_o^r\right)}{\ln M^r}\right][Pr(\epsilon)]^r,$$

where $[Pr(\epsilon)]^r$ is the probability of error under reference conditions. This equation displays the rate of growth of $Pr(\epsilon)$, as the source/receiver separation gets bigger. We note that the first factor, $\delta = R_o/R_o^r$, accounts for the normalization of the received power (spherical propagation), while the bracketed factor reflects the change in the total number of grid points with the source/receiver separation.

b. Graphical Analysis of the Total Performance Bounds

In Fig. 45 we represent as a function of X the total mean-square error $\sigma^2_{tot_j}$, and its global and local components, for the two different a priori regions of interest, Ω_1, Ω_2. We note first that for small X the local component dominates the performance, since the $Pr(\epsilon)$ is zero for small X. After a transition region where both components are of the same order, the global errors dominate the performance. We observe that, under the numerical conditions and the assumed a priori region, this transitional region occurs first for the range parameter, then for the sin θ parameter, and finally for the velocity parameter. We also note that it occurs for values of $X \in [.1,1]$, which is a region of interest in many applications.

The effect of reducing the a priori region of interest is twofold. One effect that is noted is the change of $Pr(\epsilon)$ which is purely reflected in Fig. 45a. The second results from the change in the a priori uncertainty of the parameters. Since in Ω_2 we have reduced $\Delta_M v$ and $\Delta_M \theta$, the changes in Fig. 45b and 45c reflect the coupling of both effects.

3.4.5 Asymptotic Behavior of the ML Algorithm

We have analyzed how the performance of the estimation algorithm depends on the geometric parameter X. We have seen that for X smaller than a transitional value X_{tran} the performance is well predicted by the Cramer-Rao bounds. Improvements can

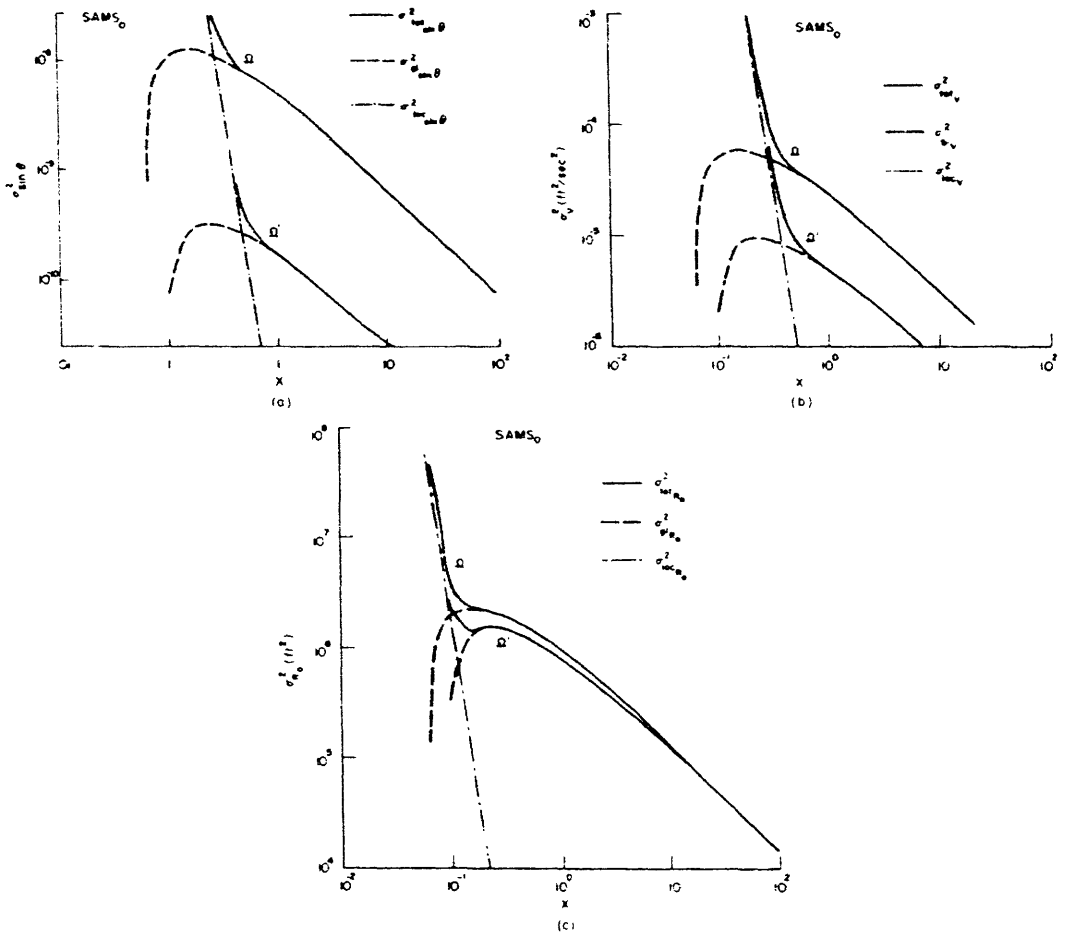

Fig. 45. (a) Speed total ML performance vs X.
(b) Angle total ML performance vs X.
(c) Range total ML performance vs X.

only be achieved by increasing the effective signal energy-to-noise ratio, for example, by using better sensors. For X larger than the transitional value a threshold phenomenon occurs with the receiver performance departing from the Cramer-Rao bound, because of the dominance of the (large) global errors.

The issues of asymptotic behavior as the SNR and/or N (total number of independent measurements) become large can be pursued. The conclusions are essentially equivalent to those in Section II. The relation between $\sigma^2_{gl_j}$ and $\sigma^2_{loc_j}$ for N = 1 and high signal energy-to-noise ratio is essentially independent of the SNR. This says that, under these conditions, for a given geometry, because of diversions, we cannot make the mean-square error term arbitrarily small with respect to the local mean-square error just by increasing the SNR; the receiver presents threshold effects, with its performance departing significantly from the one predicted by the Cramer-Rao bounds.

This suboptimal behavior is inherent in the two-step implementation of the ML

receiver, and not intrinsic to the ML parameter estimation with signals propagating through a Rayleigh channel. In fact, it can be proved that the ML parameter estimation problem with signals over a Rayleigh channel is asymptotically efficient in the signal-to-noise ratio sense, as we let SNR $\rightarrow \infty$. The proof follows essentially the arguments of Kelly, Reed, and Root[38] for the equivalent problem of asymptotic efficiency in the SNR sense, in the ML estimation of parameters embedded in signals multiplied by a channel characteristic of constant unknown but nonrandom, with amplitude b and uniform phase ψ. We merely have to be careful to further restrict their bounding argument to the sample functions with unknown nonzero amplitude b. But since the set of sample functions for which $b = 0$ is a set of measure zero, no essential modification of their argument leading to the efficiency of the ML estimate in the SNR sense is introduced in the more general context of signals over Rayleigh channels.

Finally, if we assume that we have N independent measurements, and if we let

$$\Delta_j^N = \frac{\sigma^2_{gl_j}}{\sigma^2_{loc_j}}, \tag{84}$$

we can prove the asymptotic efficiency in the classical sense:

$$\lim_{N\rightarrow\infty} \Delta_j^N = 0 \tag{85a}$$

and also if $N \geq 2$,

$$\lim_{SNR\rightarrow\infty} \Delta_j^N = 0, \tag{85b}$$

i.e., the suboptimality of the two-step mechanization disappears, and the estimates are also efficient in the SNR sense.

IV. SYNTHETIC ARRAY WITH MOVING SOURCE (SAMS)

We have carried out the analysis for the equivalent positioning and navigation problems for moving platforms when the receiving aperture is omnidirectional (short baseline) or the navigational station reduces to a fixed point source. These twin applications were cast in terms of a stationary array/moving source model with omnidirectional sensor ($SAMS_o$), thereby reducing passive position navigation to estimation of three parameters: source/receiver separation R_o, relative speed v, and a suitably defined angle θ_t (Fig. 46). The temporal modulations induced by the relative dynamics convey no information on the bearing angle θ_ℓ which is unidentifiable with the $SAMS_o$ model.

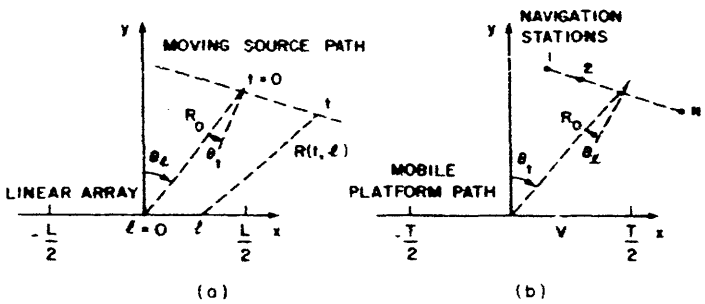

Fig. 46. Stationary Array/Moving Source.
(a) Positioning. (b) Navigation.

We shall consider now the class of position/navigation problems illustrated in Fig. 46 where a spatial and temporal nonnegligible baseline inducing both spatial and temporal diversity on the signal structure is generated. Keeping the tracking or positioning terminology, we refer to this class as a stationary array/moving source (SAMS) problem. We put the analysis of SAMS in the perspective of the results from Sections II and III and pursue the study of the optimal ML receiver structure, and of the processor performance, for two configurations arising in most applications of practical interest. We discuss in detail the space/time factorability of the ambiguity function, and the fundamental implications, in terms of parameter identifiability, introduced by the spatial/temporal coupling.

4.1 MODEL

Our assumptions on the planar geometry, narrow-band radiated signals, linear array structures, and deterministic constant-speed linear path are kept. In particular, see Eqs. 1-3, and section 2.1 on the geometric model signal and noise structures.

We make use of two geometric parameters:

$$\text{Spatial geometric parameter } X_\ell = \frac{L}{2R_o} \tag{86a}$$

Temporal geometric parameter $X_t = \frac{vT}{2R_o}$. (86b)

These parameters normalize the linear dimensions (half of the array length, or half of the distance traveled by the moving source during the observation interval) with respect to the source/receiver separation.

The range function $R(t,\ell)$ is the distance between the source at time t and the point at location ℓ in the linear array, which may be completely described by four parameters

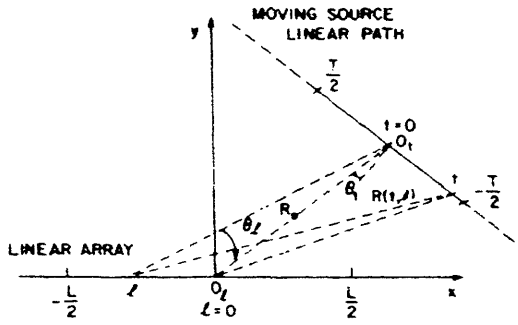

Fig. 47. SAMS planar geometry.

because of the deterministic assumption on the motions. Centering with respect to the array geometric center and the midpoint of the observation interval, we define the parameter vector as

$$A = \begin{bmatrix} R_o \\ v \\ \sin\theta_t \\ \sin\theta_\ell \end{bmatrix}$$

where R_o is the source/receiver separation at $t = 0$, $\ell = 0$, angles $\sin\theta_i$, $i = \ell, t$ are indicated in Fig. 47, and v is the source speed. By solving triangles ℓ-0_ℓ-t and $\hat{}_t$-t-0_ℓ successively, we obtain

$$R(t,\ell,A) \underline{\Delta} R(t,\ell) = \left\{R_o^2 + \ell^2 + (vt)^2 - 2R_o(\ell\sin\theta_\ell + vt\sin\theta_t) + 2\ell\, vt\cos(\theta_\ell - \theta_t)\right\}^{1/2} \tag{87a}$$

which equivalently can be expressed as

$$R(t,\ell,A) = \left\{\left[R_o - \ell\sin\theta_\ell - vt\sin\theta_t\right]^2 + \left[\ell\cos\theta_\ell + vt\cos\theta_t\right]^2\right\}^{1/2}. \tag{87b}$$

As discussed previously, we work with $\sin\theta_i$, $i = \ell, t$ and not with the angles themselves. This wave number dependence does not uniquely specify the relative source/receiver geometry but removes the known ambiguity introduced by the linear constraints

from the model. To illustrate this point, consider a ship navigation problem. Then either we know the side where the source center is (e.g., on port) or we repeat the experiment with a different line course.

The measurement of the bearing angle θ_ℓ resolves the indetermination of the signs of each individual factor in the product v sin θ_t that was observed in Section III. For, as we see in Fig. 48, the two geometric configurations I and II are clearly distinguishable.

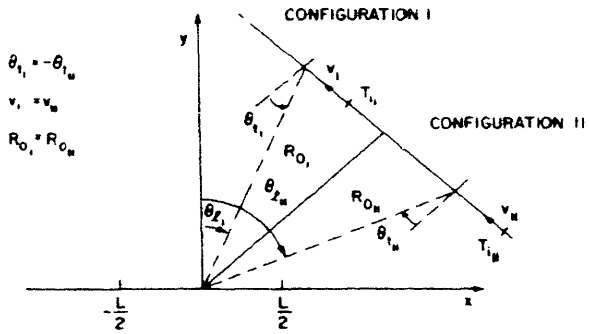

Fig. 48.
Ambiguity resolution of the signs of v and sin θ_t in SAMS.

4.2 RECEIVER STRUCTURE

The positioning/navigation problem with spatial and temporal diversity has been cast in the context of an estimation problem with a finite number of nonrandom unknown parameters imbedded nonlinearly on signals corrupted by additive temporally white, spatially homogeneous, Gaussian noise. The maximum-likelihood (ML) receiver is asymptotically efficient, and is composed of a matched filter followed by a square law envelope detector. The receiver structure is determined by the signal correlation function and by the generalized ambiguity function (GAF) given by Eqs. 13 and 14, and $R(t, \ell, A)$ is given by Eqs. 87.

The ML receiver specified by Eqs. 13d and 87 represents a processing over two dimensions, space and time. With the SASS and $SAMS_o$ of Sections II and III, the homogeneity introduced in one of these domains (the time stationarity of the relative dynamics in SASS or the omnidirectional sensor with $SAMS_o$) leads to a simpler one-dimensional processor. This can be viewed as a special case of a more general situation, where the receiver's two-dimensional structure is decoupled on its spatial and temporal dimensions; that is, the signal autocorrelation function factors as the product of a time integral and a space integral

$$\psi(A, \bar{A}) = \psi(A, \bar{A}, T)\, \psi(A, \bar{A}, L), \tag{88}$$

where $\psi(A, \bar{A}, Z) = \frac{1}{Z} \int_{-Z/2}^{Z/2} dz \exp j\Delta R(z, A, \bar{A})$, $z = \ell$ or t.

The importance of this factorability or separability is twofold. First, it expresses the processor in terms of two independent blocks, each representing a processing in one of the domains. If there are changes in one of these that do not affect the underlying

assumptions leading to the factorability of Eq. 88, they only affect the design of one block, and leave the other unaltered. Second, this factorability may lead to a separability of the signal autocorrelation, and hence of the generalized ambiguity function over the parameter space, which gives rise to considerable saving in the processing load work.

In the detection context a different concept of factorization of the optimal processor's structure has been considered by Middleton and Groginsky[39] who found conditions for the factorability of the optimal detector in two operations. The first condition depends only on the geometry of the array, the second on the statistics of the noise processes. They point out that in general factorability in this sense is not possible in optimal systems. For active systems, and for detection and estimation problems, some conditions on the signal structure that ensure the factorability of the processor have been found by Urkowitz et al.,[40] and have been generalized to the case of reverberation and colored noise by Pasupathy and Venetsanopoulos.[41]

With the present SAMS model the received random form exhibits a nonhomogeneous spatial and nonstationary temporal structure, which leads to a complex receiver whose analysis is not conducive to intuitive closed-form expressions. To understand the structure of SAMS and the theoretical limitations of performance, we pursue the questions of factorability in the sense defined by Eq. 88 and spatial/temporal coupling, by developing the analysis of SAMS for two specific configurations. In the first it is assumed that the temporal diversity dominates the spatial diversity. This leads to a decoupling of the spatial and temporal operations of the receiver, which are reflected in a separability of the ambiguity function as the product of two reduced-dimension (on the parameter space Ω) ambiguity structures. For this configuration, the passive ranging is essentially accomplished by using the temporal modulations. SAMS is put in the perspective of Sections II and III, decoupling into a $SAMS_o$ and a passive bearing problem, with a Rayleigh model. The second configuration considers the problem where the spatial and temporal baselines are comparable, and investigates the effects induced on the receiver structure and performance by the coupling.

For both we pursue a least-order analysis, based on truncated Taylor's series approximations to the range function, and compute the ambiguity function, as well as bounds on the mean-square performance.

4.3 DECOUPLED SPATIAL/TEMPORAL SAMS STRUCTURE

We make two hypotheses concerning the geometric configuration of SAMS:

H1: $X_\ell = \frac{L}{2R_o} \ll 1.$

H2: $X_\ell \ll X_t = \frac{vT}{2R_o}.$

These assumptions justify a linearized Taylor's series analysis on the spatial

variable. The range function becomes

$$R(t,\ell) \approx R(t,0) + \frac{\cos(\theta_t - \theta_\ell)\, vt - R_o \sin\theta_\ell}{R(t,0)}\,\ell \tag{89a}$$

$$= R(t,0) - \sin\theta_\ell\,(t,0)\,\ell, \tag{89b}$$

where $\theta_\ell\,(t,0)$ is the bearing angle at time t with respect to the center of the reference frame (Fig. 49). This linearized structure in the space variable simply states that, at each particular instant of time, the wave field across the receiver's array is planar, and that, as the source moves along its linear track, the spatial structure of the received signals changes (Fig. 49).

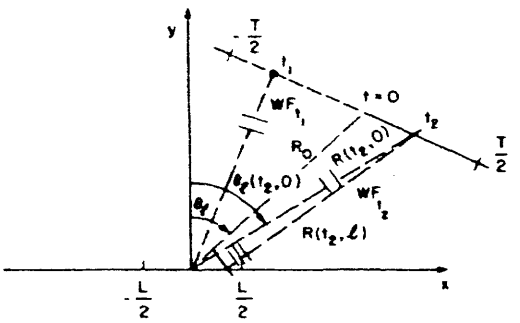

Fig. 49. Time-variant spatial structure.

We note that $R(t,0) = \{R_o^2 + (vt)^2 - 2(vt)\,R_o \sin\theta_t\}^{1/2}$ depends only on the reduced dimension vector

$$A_o = \begin{bmatrix} R_o \\ v \\ \sin\theta_t \end{bmatrix} \tag{89c}$$

of the source parameters associated with the $SAMS_o$ model in Section III, while $\theta_\ell\,(t,0)$ depends on the full parameter vector A.

4.3.1 Ambiguity Structure

The signal autocorrelation function can be rewritten

$$\psi(A,\bar{A}) \cong \frac{1}{T}\int_{-T/2}^{T/2} dt\, \exp\left[j\frac{2\pi}{\lambda}\Delta R(t,0,A_o,\bar{A}_o)\right]\left\{\frac{1}{L}\int_{-L/2}^{L/2} d\ell \times \exp\left[-j\frac{2\pi}{\lambda}\Delta \sin\theta_\ell\,(t,0,A,\bar{A})\right]\right\} \tag{90a}$$

or

$$\psi(A,\bar{A}) \cong \frac{1}{T}\int_{-T/2}^{T/2} dt \exp\left[j\frac{2\pi}{\lambda}\Delta R(t,0,A_o,\bar{A}_o)\right]\psi_\ell(\Delta \sin\theta_\ell(t,0,A,\bar{A})), \tag{90b}$$

where

$$\psi_\ell(\Delta \sin\theta_\ell(t,0,A,\bar{A})) = \operatorname{sinc}\left[\frac{2\pi}{\lambda}\Delta \sin\theta_\ell(t,0,A,\bar{A})\frac{L}{2}\right]. \tag{90c}$$

Since the wave fronts are planar across the array, we assume that spatial diversity techniques (array processing with beam forming) are used to match the bearing angle, so that as the source sweeps the horizon the receiver updates the bearing estimate. The function $\psi_\ell(\Delta \sin\theta_\ell(t,0,A,\bar{A}))$ is kept practically constant across the source travel (approximately tuned to 1), with the array sequentially steered to the source varying bearing, as illustrated in Fig. 50.

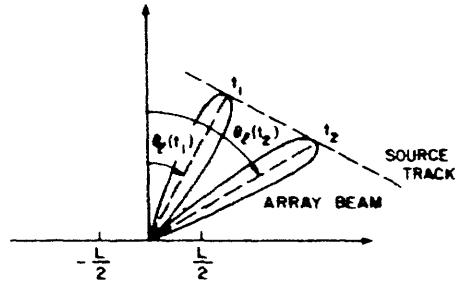

Fig. 50.
Sequential beam steering.

To compute the number of updates, we define the array bearing resolution[28] by

$$\psi_\ell(\sin\theta_\ell(t_1,0) - \sin\theta_\ell(t_2,0)) > \frac{1}{\sqrt{2}}. \tag{91}$$

That is, under the assumption that the aperture is steered at $\theta_\ell(t_1,0)$, the resolution is given by the bearing interval over which the (spatial) aperture response does not drop below the 3 dB cutoff. Since ψ_ℓ is the sinc function of Eq. 90c, we obtain

$$\sin\theta_\ell(t_1,0) - \sin\theta_\ell(t_2,0) < \frac{2.78}{\frac{2\pi}{\lambda}L}.$$

By taking $t_1 = 0$, the resolution is given by

$$\Delta \sin\theta_\ell = \sin\theta_\ell - \sin\theta_\ell(t_2,0) < \frac{2.78}{\frac{2\pi}{\lambda}L}.$$

The total bearing variation across the source travel is approximately

$$\sin\theta_\ell\left(\frac{T}{2},0\right) - \sin\theta_\ell\left(-\frac{T}{2},0\right) = \cos(\theta_\ell-\theta_t)\,X_t\left[1+\left(1-\frac{4\,\frac{vT}{2}\,R_o\sin\theta_t}{R\left(-\frac{T}{2},0\right)}\right)^{1/2}\right]$$

$$\approx 2\cos(\theta_\ell-\theta_t)X_t$$

so that the number of updates is

$$N_u \cong \left\lfloor 4.5\cos(\theta_\ell-\theta_t)\,\frac{LX_t}{\lambda}\right\rfloor, \tag{92a}$$

where $\lfloor(\cdot)\rfloor$ stands for the largest integer contained in $(\cdot)$. In the sequel we omit the bars.

For $\theta_\ell = \theta_t$

$$N_u \cong 4.5\,\frac{LX_t}{\lambda}$$

$$= 2.25\,\frac{L}{\lambda}\,\frac{(vT)}{R_o}. \tag{92b}$$

Returning to the ambiguity structure, if $N_u = 1$, we have

$$\psi_\ell(\Delta\sin\theta_\ell\,(t,0,A,\bar{A})) \cong \operatorname{sinc}\left[\frac{2\pi}{\lambda}\,(\Delta\sin\theta_\ell)\,\frac{L}{2}\right]$$

and

$$\psi(A,\bar{A}) = \psi_o(A_o,\bar{A}_o)\,\operatorname{sinc}\left[\frac{2\pi}{\lambda}\,(\Delta\sin\theta_\ell)\,\frac{L}{2}\right], \tag{93}$$

where $\psi_o(A_o,\bar{A}_o)$ is the signal autocorrelation function associated with the $SAMS_o$ model.

This says that when the angle spanned by the source travel is smaller than the receiver's aperture beamwidth (Fig. 51) the SAMS signal autocorrelation decouples in its spatial and temporal aspects, with a corresponding factorization over the parameter

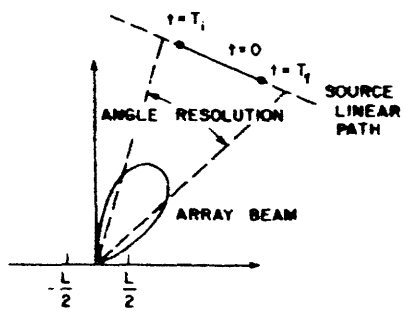

Fig. 51.
Source dynamics within a resolution cell of the linear array.

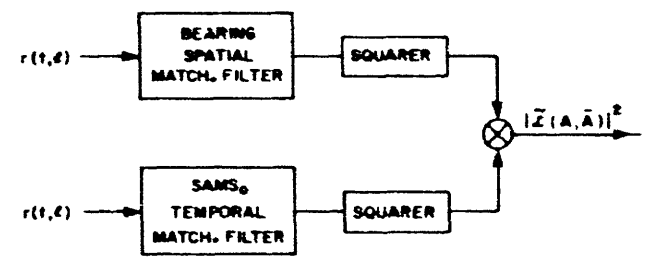

Fig. 52.
Decoupled receiver structure.

space Ω. The range, speed, and angle $\sin\theta_t$ are estimated from the temporal diversity, and the bearing from the spatial diversity. If $N_u > 1$, and the sequential beam steering shown in Fig. 50 is assumed, the receiver's structure is still practically decoupled:

$$\psi(A,\bar{A}) \cong \psi_o(A_o,\bar{A}_o)\,\psi_\ell(\Delta \sin\theta_\ell(t,0,A,\bar{A})). \tag{94}$$

The important difference between Eqs. 94 and 93 is in the time updating of Eq. 94, which yields a sequence of bearing measurements instead of a single bearing. The receiver structure is mathematically equivalent to the block diagram in Fig. 52.

We now study the mean-square performance of the decoupled structure. We concentrate on the analysis of the mean-square spread matrix $\mathcal{M}$ and its inverse.

4.3.2 Computation of the Inverse of the Mean-Square Spread Matrix

The mean-square spread matrix (MSSM), given in Appendix B by Eqs. B.6 and B.7, requires the computation of the gradient of the range phase with respect to the source parameters. The spatially linearized range function (see Eqs. 89) is

$$R(t,\ell,A) \approx R(t,0,A_o) - \sin\theta_\ell(t,0,A)\ell. \tag{95}$$

Here we explicitly exhibited as arguments the vectors A_o and A, to show on which source parameters each term depends. The gradient is

$$\nabla_A R(t,\ell,A) = \begin{bmatrix} \nabla_{A_o} R(t,0,A_o) \\ 0 \end{bmatrix} - \nabla_A \sin\theta_\ell(t,0,A)\ell.$$

We note that the first term does not depend on ℓ, in the second term this dependence is linear, and by using the assumed symmetry of the array geometry, it follows that the MSSM can be written

$$\mathcal{M} \cong \mathcal{M}_R + \mathcal{M}_{\theta_\ell}\frac{X_\ell^2}{3}, \tag{96a}$$

where

$$\mathcal{M}_R = \begin{bmatrix} \mathcal{M}_o & \vdots & o \\ \cdots & \vdots & \cdots \\ o & \vdots & 0 \end{bmatrix} \tag{96b}$$

$$\mathcal{M}_{\theta_\ell} = \begin{bmatrix} \mathcal{M}^3_{\theta_\ell} & \vdots & m \\ \cdots & \vdots & \cdots \\ m^T & \vdots & \mathcal{M}_{44_{\theta_\ell}} \end{bmatrix}. \tag{96c}$$

$\mathcal{M}_o$ is the MSSM associated with the $SAMS_o$ model in Section III,

$$\mathcal{M}_{44_{\theta_\ell}} = \left(\frac{2\pi}{\lambda}\right)^2 \left[\frac{\sin^2(\theta_t - \theta_\ell)}{\cos^2\theta_\ell} H_2 + H_o\right] R_o^2. \tag{96d}$$

In Appendix B, H_2 is given by Eq. B.10b and H_o by Eq. B.10a. The exact expression for the matrix $\mathcal{M}^3_{\theta_\ell}$ and the vector m does not concern us.

In order to compute the inversion of $\mathcal{M}$, we rearrange the terms in Eq. 96a. We define

$$\underset{\sim}{\mathcal{M}}_R = \begin{bmatrix} \mathcal{M}_o & \vdots & o \\ \cdots & \cdots & \cdots \\ o & \vdots & \mathcal{M}_{44_{\theta_\ell}} \frac{X_\ell^2}{3} \end{bmatrix}$$

$$\underset{\sim}{\mathcal{M}}_{\theta_\ell} = \begin{bmatrix} \mathcal{M}^3_{\theta_\ell} & \vdots & m \\ \cdots & \cdots & \cdots \\ m^T & \vdots & 0 \end{bmatrix} \frac{X_\ell^2}{3}$$

Since $\underset{\sim}{\mathcal{M}}_R > 0$, we can define a suitable unique square root matrix such that $\underset{\sim}{\mathcal{M}}_R = \underset{\sim}{\mathcal{M}}_R^{1/2} \underset{\sim}{\mathcal{M}}_R^{1/2}$, where

$$\underset{\sim}{\mathcal{M}}_R^{1/2} = \begin{bmatrix} \mathcal{M}_o^{1/2} & & o \\ & & \\ o & & \left[\mathcal{M}_{44_{\theta_\ell}} \frac{X_\ell^2}{3}\right]^{1/2} \end{bmatrix}.$$

The inverse of $\mathcal{M}$ leads to

$$\mathcal{M}^{-1} = \underset{\sim}{\mathcal{M}}_R^{-1/2} \left[I + \underset{\sim}{\mathcal{M}}_R^{-1/2} \underset{\sim}{\mathcal{M}}_{\theta_\ell} \underset{\sim}{\mathcal{M}}_R^{-1/2} \frac{X_\ell^2}{3}\right]^{-1} \underset{\sim}{\mathcal{M}}_R^{-1/2}. \tag{97}$$

For a valid mean square expansion of the inverse of the bracketed matrix in Eq. 97, we need to satisfy[39]

$$\max \lambda_i(\Delta) < 1, \tag{98}$$

where the $\lambda_i(\Delta)$ are the eigenvalues of

$$\Delta = \underset{\sim}{\mathcal{M}}_R^{-1/2}\,\underset{\sim}{\mathcal{M}}_{\theta_\ell}\,\underset{\sim}{\mathcal{M}}_R^{-1/2}\,\frac{X_\ell^2}{3} = \left[\begin{array}{c|c} \underset{\sim}{\mathcal{M}}_o^{-1/2}\,\underset{\sim}{\mathcal{M}}_{\theta_\ell}^{3}\,\underset{\sim}{\mathcal{M}}_o^{-1/2}X_\ell & m_\Delta \\ \hline m_\Delta^T & 0 \end{array}\right]$$

$$m_\Delta = \left[\frac{\mathcal{M}_{44_{\theta_\ell}}}{3}\right]^{-1/2}\mathcal{M}_o^{-1/2}m.$$

By a continuity argument, or by analyzing the trace and the determinant of Δ, we can show that $\lambda_1(\Delta) \sim 0(X_\ell)$, i.e., is at least of the order X_ℓ, or is zero and of the order $0\left(X_\ell^2\right)$. For sufficiently short baseline arrays, condition (98) will be satisfied. It follows that

$$\mathcal{M}^{-1} = \underset{\sim}{\mathcal{M}}_R^{-1/2}\left\{I + \sum_{n=1}^{\infty}(-1)^n\,\Delta^n\right\}\underset{\sim}{\mathcal{M}}_R^{-1/2} \tag{99}$$

which up to the least nonzero order in Δ is

$$\mathcal{M}^{-1} \approx \underset{\sim}{\mathcal{M}}_R^{-1/2}(I-\Delta)\,\underset{\sim}{\mathcal{M}}_R^{-1/2} \tag{100a}$$

$$= \left[\begin{array}{c|c} \mathcal{M}_o^{-1} & \underset{\sim}{m} \\ \hline \underset{\sim}{m}^T & \left(\mathcal{M}_{44_{\theta_\ell}}\frac{X_\ell^2}{3}\right)^{-1} \end{array}\right] - \left[\begin{array}{c|c} \mathcal{M}_o^{-1}\,\mathcal{M}_{\theta_\ell}^{3}\,\mathcal{M}_o^{-1}\frac{X_\ell^2}{3} & 0 \\ \hline 0 & 0 \end{array}\right] \tag{100b}$$

where $\underset{\sim}{m} = -\mathcal{M}_{44_{\theta_\ell}}^{-1}\,\mathcal{M}_o^{-1}m$.

A sufficient condition for Eq. 100a to be a reasonable approximation to Eq. 99 is[39] $\max\frac{X^T\Delta X}{X^TX} \ll 1$, which will certainly be the case for a sufficiently small array baseline, i.e., whenever $X_\ell \ll 1$.

Equation 100a represents the inverse of MSSM for SAMS when, because of the overall geometry, the signal wave field presents instantaneously a planar wave front across the array. The second term of the right-hand side of Eq. 100b represents the first-order correction, when the sequence of bearing measurements obtained by processing the time-variant spatial signal structure is coupled to the information conveyed in the temporal modulations, to lead to the estimates of the remaining source parameters, that is, the reduced parameter vector A_o.

When this coupling is neglected, as suggested by the decoupled receiver in Fig. 52,

the inverse MSSM is given by the first term of Eq. 100b and leads to a deterioration in the mean-square performance as seen from the oscillating character of the geometric series in Eq. 99.

The 3×3 minor $\mathcal{M}_o^{-1}$ in Eq. 100b is equivalent to the inverse of MSSM for the $SAMS_o$ model. The global and local results on the mean-square performance of the parameters in A_o are then equivalent to those derived for $SAMS_o$.

The crosscorrelations between the parameter errors, as computed from the inverse of MSSM, are $\rho_{ij} = \rho_{ij_o}$, for $i, j \leq 3$, and

$$\rho_{i4} = \frac{(\mathcal{M}^{-1})_{i4}}{\left[(\mathcal{M}^{-1})_{ii}(\mathcal{M}^{-1})_{44}\right]^{1/2}}$$

$$= \underset{\sim}{\rho}_{i4}(A, X_t)\, X_\ell .$$

That is, the crosscorrelation between the components of A_o is as in $SAMS_o$ but we note that a crosscorrelation of the order of X_ℓ is introduced by the weak coupling between the errors on the parameter estimates of A_o and the bearing angle θ_ℓ.

4.4 COUPLED SPATIAL/TEMPORAL SAMS STRUCTURE

We consider the problem where the spatial/temporal structures are coupled, because of the overall geometry and relative dimensions. The source travels in the near field of the array, and is observed by the receiver for a sufficiently large time interval. Significant (spatial) curvature and higher order (temporal) modulation effects are available, as illustrated in Fig. 53, to be jointly processed, and to yield the estimation of the four source parameters. The range function $R(t, \ell)$ exhibits a significant variation at each instant across the linear array, and at each array point across the source travel, as illustrated in Fig. 54 for a broadside ($\theta_\ell = 0$) and closest approach ($\theta_t = 0$) geometry.

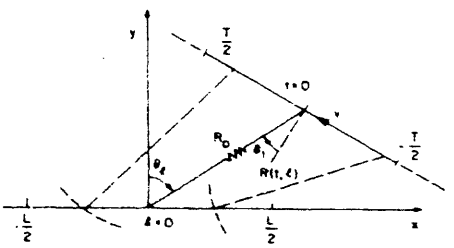

Fig. 53.
Spatial/temporal coupled curvature geometry.

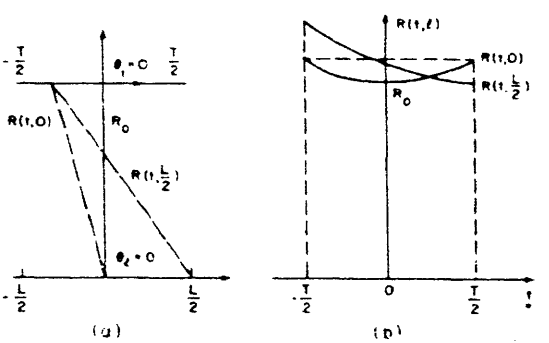

Fig. 54.
Spatial/temporal cross coupling ($X_\ell = X_t$). (a) Geometry. (b) Range function.

and for the special case where the array length equals the source travel.

To obtain closed-form expressions and an intuitive understanding of the coupling issues, we pursue in detail the analysis for the following case.

$$\text{H1:}\quad X_\ell = \frac{L}{2R_o} < 1$$

$$\text{H2:}\quad X_t = \frac{vT}{2R_o} < 1.$$

In H1 the range is larger than half the array length, and in H2 larger than half the source travel. These conditions justify a higher order truncated Taylor's series study in both space and time variables about the geometry center $t = 0$, $\ell = 0$.

In operator form the truncated Taylor's series is given by

$$R(t,\ell) \cong \sum_{n=0}^{N} \frac{1}{n!}\left(t\frac{\partial}{\partial t} + \ell\frac{\partial}{\partial \ell}\right)^n R(t,\ell)\Big|_{\substack{t=0\\ \ell=0}} . \tag{101}$$

The lower order terms lead to

$$R(t,\ell) \approx R_o - \sin\theta_t (vt) + \frac{\cos^2\theta_t (vt)^2}{2R_o} + \ldots$$

$$- \sin\theta_\ell \ell + \frac{\cos^2\theta_\ell \ell^2}{2R_o} - + \ldots$$

$$+ \frac{\cos\theta_\ell \cos\theta_t (vt)\ell}{R_o} + \ldots \tag{102}$$

In compact notation, letting $R_t \triangleq R(t,0)$ and $R_\ell \triangleq R(0,\ell)$, and recalling their Taylor's series expansion, we have

$$R(t,\ell) + R(0,0) \approx R_t + R_\ell + \frac{\cos\theta_\ell \cos\theta_t}{R_o}(vt)\ell + \text{higher order terms.} \tag{103}$$

Equation 103 represents the decomposition of the range function in terms of uncoupled terms (R_t and R_ℓ), and the cross coupling, which is approximated by a polynomial expression. Figure 55 illustrates several terms of the decomposition. We note that due to the incoherent model, the $R_o = R(0,0)$ term in Eq. 103 plays no essential role in the phase estimation process, and can be absorbed in the uniformly distributed random signal phase. Accordingly, it will be ignored in subsequent discussions.

First, we consider the structure of the ambiguity function on the parameter space Ω and second, the mean-square matrix $\mathcal{M}$, from which the performance bounds can be obtained.

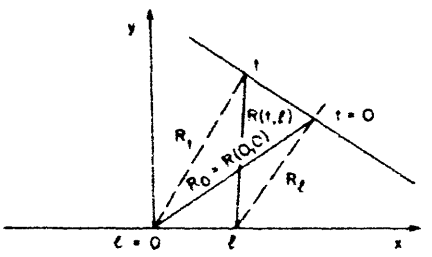

Fig. 55.
Range function decomposition.

4.4.1 Ambiguity Structure

In general, the signal autocorrelation and the ambiguity functions will be too complex to lend themselves to exact analysis, since they involve the double integration in time and space of a highly nonlinear function. We obtain a qualitative, as well as quantitative, description of their structure for SAMS, by exploiting the harmonic nature of the integrand, applying the method of stationary phase (MSP), and coupling the results for the $SAMS_o$ and SASS models.

First, we analyze the secondary structure by discussing the asymptotic behavior of the exact autocorrelation function for large parameter deviations in the parameter space Ω. Then, we use the Taylor's series approximation to the range phase, and investigate analytically the effects of the cross coupling on the ambiguity structure.

a. Asymptotic Behavior and Rate of Falloff of the Ambiguity Structure

The signal autocorrelation function is

$$\psi(A,\bar{A}) = \frac{1}{LT}\int_{-T/2}^{T/2} dt \int_{-L/2}^{L/2} d\ell \exp\left[j\frac{2\pi}{\lambda}\Delta R(t,\ell,A,\bar{A})\right]. \tag{104}$$

If large errors in one or more of the source parameters occur, we can apply the MSP to obtain the dominant term on the right-hand side of Eq. 104. It requires an extension of the MSP to two dimensions, which reduces to a sequential application of the one-dimensional MSP results to each one of the integrals of Eq. 104 (see, for example, Papoulis[42]).

For a phase stationary point (t^*, ℓ^*) in the domain of integration

$$\frac{\partial\Delta R_*}{\partial t} \triangleq \left.\frac{\partial\Delta R(t,\ell,A,\bar{A})}{\partial t}\right|_{\substack{t=t^*\\ \ell=\ell^*}} = 0, \qquad (t^*,\ell^*) \in \left[-\frac{T}{2},\frac{T}{2}\right]\times\left[-\frac{L}{2}\ \frac{L}{2}\right], \tag{105}$$

the signal autocorrelation function behaves asymptotically ($\|A-\bar{A}\|$ becomes large in Ω):

$$\psi(A,\bar{A}) \sim \frac{1}{\frac{2\pi}{\lambda} LT} \frac{2\pi j}{\left[\frac{\partial^2 \Delta R_*}{\partial \ell^2} \frac{\partial^2 \Delta R_*}{\partial t^2} - \left(\frac{\partial^2 \Delta R_*}{\partial \ell \partial t}\right)^2\right]^{1/2}} \exp\left[j \frac{2\pi}{\lambda} \Delta R_*\right], \tag{106}$$

where ΔR_*, $\partial^2 \Delta R_*/\partial \ell^2$, etc. stand for the evaluation of ΔR, $\partial^2 \Delta R/\partial \ell^2$, etc., at the point of stationary phase (t^*, ℓ^*). The denominator in Eq. 106 is assumed to be nonzero. If it vanishes, we obtain a bound involving higher order derivatives. Substituting in Eq. 106 the expression for the range phase $\Delta R(t, \ell, A, \bar{A})$, and computing the several derivatives, evaluated at the stationary phase, we obtain the asymptotic behavior of $\psi(A,\bar{A})$, and hence the rate of falloff of the ambiguity function for large parameter errors. These bounds are essentially inversely proportional to a certain combination of powers of the errors on the parameters. We refer to this as the hyperbolic decay of the secondary ambiguity structure (see section 3.3.2). We obtain similar bounds, if only one or neither of Eqs. 105 is satisfied. They express the dominant behavior of the signal autocorrelation for large parameter deviations, in terms of the first-order partial derivatives of the phase range difference evaluated at the extremes of the integration intervals.

Because of the unappealing analytical nature of these bounds, we do not write them explicitly but note that they can be computed in a straightforward way. They lead to a hyperbolic decay of the secondary ambiguity structure. Our previous experience has shown that these types of bounds are tight (see Fig. 15), and so for large parameter errors the ambiguity function is negligible in Ω.

b. Analytical Expression for the Coupled Ambiguity Structure

We proceed with the evaluation of the double integral defining the signal autocorrelation function $\psi(A,\bar{A})$ in Eq. 104. We use the polynomial approximation to the range function given in Eqs. 102 and 103. The range phase difference function is written

$$\frac{2\pi}{\lambda} \Delta R(t, \ell) \sim \Delta R_\ell + \Delta R_t + \Delta_{\ell t} \ell t, \tag{107a}$$

where

$$\Delta R_\ell \triangleq a_1 \ell + a_2 \ell^2 + \ldots = \frac{2\pi}{\lambda}\left[-\Delta(\sin\theta_\ell) + \Delta\left(\frac{\cos^2\theta_\ell}{2R_o}\right)\ell^2 + \ldots\right] \tag{107b}$$

$$\Delta R_t \triangleq \beta_1 t + \beta_2 t^2 + \ldots = \frac{2\pi}{\lambda}\left[-\Delta(v \sin\theta_t)\, t + \Delta\left(\frac{v \cos^2\theta_t}{2R_o}\right) t^2 + \ldots\right] \tag{107c}$$

$$\Delta_{\ell t} = \frac{2\pi}{\lambda} \Delta \left(\frac{\cos \theta_\ell \cos \theta_t \, v}{R_o} \right) = \frac{2\pi}{\lambda} \left(\frac{\cos \theta_\ell \cos \theta_t \, v}{R_o} - \frac{\overline{\cos \theta_\ell} \; \overline{\cos \theta_t} \; \overline{v}}{\overline{R}_o} \right). \quad (107d)$$

We make several remarks:

1. The $\Delta(\cdot)$ notation is explained in Eq. 107d. It represents the difference of the argument evaluated at the source parameter vector A and at the scanning value $\overline{A}$.

2. As noted below Eq. 103, due to the incoherent model, the constant phase factor R_o that should appear in Eqs. 107 contributes nothing to the GAF, and hence is ignored.

3. ΔR_ℓ depends only on the bearing angle $\sin \theta_\ell$ and the range R_o. In the sequel we let the two-dimensional parameter vector associated with the SASS model be

$$A_s = \begin{bmatrix} R_o \\ \sin \theta_\ell \end{bmatrix}. \quad (108)$$

ΔR_t depends only on the reduced three-dimensional vector (Eq. 89c) associated with $SAMS_o$. Only the cross coupling, reduced to its lowest order term $\Delta_{\ell t}$ in Eq. 107a, depends on the full parameter vector A. When a specific dependence is to be underlined, we explicitly exhibit as argument A_s, A_o or A, as the case might be.

The signal autocorrelation becomes

$$\psi(A, \overline{A}) \sim \frac{1}{LT} \int_{-T/2}^{T/2} dt \int_{-L/2}^{L/2} d\ell \, \exp[j(\Delta R_t + \Delta R_\ell + \Delta_{\ell t} \ell t)].$$

For example, we integrate over the space dimension and, after some algebraic manipulations,

$$\psi(A, \overline{A}) = \psi_s(A_s, \overline{A}_s) \, \psi_o(A_o, \overline{A}_o) + J_{\ell t}, \quad (109a)$$

where the signal autocorrelation associated with $SAMS_o$ is

$$\psi(A_o, \overline{A}_o) = \frac{1}{T} \int_{-T/2}^{T/2} dt \, \exp[j\Delta R_t], \quad (109b)$$

the signal autocorrelation associated with SASS is

$$\psi_s(A_s, \overline{A}_s) = \frac{1}{L} \int_{-L/2}^{L/2} d\ell \, \exp[j\Delta R_\ell], \quad (109c)$$

and the term exhibiting the coupled nature of the processor is

$$J_{\ell t} = \frac{1}{T} \int_{-T/2}^{T/2} dt \, \exp j[\Delta R_t] \left\{ \frac{1}{\Delta L_o} \int_0^{\gamma_t t} d\sigma \left[\exp j(\sigma + L_{f_o})^2 - \exp j(\sigma + L_{i_o})^2 \right] \right\}. \quad (109d)$$

The definitions of ΔL_o, L_{f_o}, etc. are as follows:

$$\Delta L_o = L_{f_o} - L_{i_o} = \sqrt{\frac{2}{\pi} a_2}\, L$$

$$L_{f_o} = \sqrt{\frac{2}{\pi} a_2}\left(\frac{L}{2} - \frac{a_1}{2a_2}\right)$$

$$L_{i_o} = \sqrt{\frac{2}{\pi} a_2}\left(-\frac{L}{2} - \frac{a_1}{2a_2}\right)$$

$$\gamma_t = \frac{\Delta_{\ell t}}{\sqrt{2a_2}}$$

$\mathcal{F}(\Sigma) = \int_0^{\Sigma} \exp j\sigma^2\, d\sigma$ (exponential Fresnel integral).

For a quadratic range phase expansion, for example, we recall that we can rewrite Eq. 109c:

$$\psi_s(A_s, \bar{A}_s) = \frac{1}{\Delta L_o}\left[\mathcal{F}(L_{f_c}) - \mathcal{F}(L_{i_o})\right]. \tag{110}$$

The quantities defined above have the physical interpretation presented in Appendix A below Eqs. A.11.

Equation 109a presents the coupled signal autocorrelation as given by two terms. The first represents the product of the ambiguity structures associated with each individual dimension of the problem (space and time). The second introduces the correction that is due to the coupling. We see that the ambiguity structure is not separable, unless $\gamma_t = 0$, or $\gamma_t T$ is large.

In order to interpret the cross-coupling term, we rewrite its expression. Let

$$f(t, \Sigma) = \frac{1}{\Delta\Sigma}\int_0^{\gamma_t t} d\sigma \exp j(\sigma + \Sigma)^2$$

$$F(t, \Sigma) = \frac{1}{T}\int_0^{t} f(t, \Sigma)\, dt$$

$$= \frac{t}{T} f(t, \Sigma) - \int_0^{t} t\, \frac{df(t, \Sigma)}{dt}\, dt$$

$$= \frac{1}{\gamma_t T}\,\frac{1}{\Delta\Sigma}\left\{(\gamma_t t + \Sigma)\left[\mathcal{F}(\gamma_t t + \Sigma) - \mathcal{F}(\Sigma)\right] - \frac{1}{2j}\left[\exp j(\gamma_t t + \Sigma)^2 - \exp(j\Sigma^2)\right]\right\}.$$

We then have

$$J_{\ell t} = J(T, L_{f_o}) - J(T, L_{i_o}), \tag{111a}$$

where

$$J(T,\Sigma) = F\left(\frac{T}{2},\Sigma\right)\exp\left[j\Delta R\left(\frac{T}{2}\right)\right] - F\left(-\frac{T}{2},\Sigma\right)\exp\left[j\Delta R\left(-\frac{T}{2}\right)\right]$$
$$- j\int_{-T/2}^{T/2} F(t,\Sigma)\frac{d\Delta R(t)}{dt}\exp[j\Delta R_t]\,dt. \qquad (111b)$$

For the quadratic expansion of ΔR_t

$$\left.\frac{d\Delta R(t)}{dt}\right|_{t=t_*} = \beta_1 + 2\beta_2 t_* = 0$$

$$\Longrightarrow t_* = -\frac{\beta_1}{2\beta_2}, \quad \beta_2 \neq 0.$$

For T sufficiently large, $t_* \in [-T/2, T/2]$, and by the MSP

$$j\int_{-T/2}^{T/2} F(t,\Sigma)\frac{d\Delta R(t)}{dt}\exp[j\Delta R_t]\,dt \approx 0.$$

For a large cross-coupling parameter γ_t, when the coupling is more evident, and for sufficiently large T

$$F\left(\pm\frac{T}{2},\Sigma\right) \xrightarrow[\text{large } \gamma_t T]{\sim} \frac{1}{2}\frac{1}{\Delta\Sigma}\left[\frac{1}{2} \mp \mathscr{F}(\Sigma)\right]. \qquad (112)$$

This leads to

$$J(T, L_{f_o}) - J(T, L_{i_o}) \xrightarrow[\text{large } \gamma_t T]{\sim} -\exp\left[j\beta_2\left(\frac{T}{2}\right)^2\right]\cos\left(\beta_1\frac{T}{2}\right)\psi_s(A_s, \bar{A}_s).$$

Here we use Eq. 112 in Eq. 111b, and assume a quadratic range approximation.

Finally,

$$\psi(A,\bar{A}) \approx \psi_s(A_s,\bar{A}_s)\left\{\left[\psi_o^r(A_o,\bar{A}_o) - \cos\left(\beta_1\frac{T}{2}\right)\cos\left[\beta_2\left(\frac{T}{2}\right)^2\right]\right]\right.$$
$$\left. + j\left[\psi_o^i(A_o,\bar{A}_o) - \cos\left(\beta_1\frac{T}{2}\right)\sin\left[\beta_2\left(\frac{T}{2}\right)^2\right]\right]\right\}, \qquad (113)$$

where $\psi_o = \psi_o^r + j\psi_o^i$.

Equation 113 shows that whenever T and $\gamma_t T$ are large, the signal autocorrelation is still separable in two parts, one dependent on the space domain and the other on the time domain but the latter factor is not simply the $SAMS_o$ signal autocorrelation. Similarly, we obtain equivalent results, if we start by integrating over time, and assume large L and $\gamma_\ell L$, where γ_ℓ has a definition equivalent to γ_t.

We now look at the coupled ambiguity structure along specific subspaces in Ω, that is, the coordinate axes or planes.

$(\Delta v, \Delta \sin\theta_t)$ Plane

Let $\pi_{v\theta_t}$ be the subspace (plane) in Ω given by $\Delta R_o = 0$ and $\Delta \sin\theta_\ell = 0$.

The signal autocorrelation function in $\pi_{v\theta_t}$ becomes

$$\psi(A, \bar{A}) \cong \frac{1}{T} \int dt \exp[j\Delta R_t] \operatorname{sinc}\left(\Delta_{\ell t} t \frac{L}{2}\right).$$

Consider the locus $\mathscr{L}$ on $\pi_{v\theta_t}$, where

$$\Delta_{\ell t} < \Delta_* = \frac{\pi}{\frac{L}{2}\frac{T}{2}}, \tag{114a}$$

or equivalently,

$$\Delta(v\cos\theta_t) < \delta = \frac{R}{\cos\theta_\ell} \frac{\pi}{\frac{L}{2}\frac{T}{2}}, \tag{114b}$$

as shown in Fig. 56.

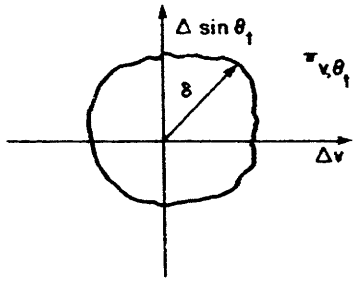

Fig. 56. Locus on $\pi_{v\theta_t}$.

For points in $\mathscr{L}$

$$0 < \operatorname{sinc}\left[\Delta_{\ell t} t \frac{L}{2}\right] < 1, \quad \text{for } vt \in \left[-\frac{T}{2}, \frac{T}{2}\right]$$

which leads to

$$\psi(A, \bar{A}) \sim \psi_o(A_o, \bar{A}_o) \operatorname{sinc}\left(\Delta_{\ell t} t^* \frac{L}{2}\right), \tag{115}$$

where $\operatorname{sinc}\left(\Delta_{\ell t} t^* \frac{L}{2}\right)$ is either computed at the stationary phase, if $t^* \in \left[-\frac{T}{2}, \frac{T}{2}\right]$, or is an average value.

Outside $\mathscr{L}$ the sinc is negligible whenever $t > t_o$, where $t_o = \frac{\pi}{\frac{L}{2}|\Delta_{\ell t}|}$, and hence

$$\psi(A, \bar{A}) \approx \frac{2t_o}{T}\left[\frac{1}{2t_o}\int_{-t_o}^{t_o} dt \exp[j\Delta R_t] \operatorname{sinc}\left(\Delta_{\ell t} t \frac{L}{2}\right)\right].$$

But, by the same argument,

$$\psi(A,\bar{A}) \sim \frac{2t_o}{T}\,\psi_{2t_o}(A_o,\bar{A}_o)\ \mathrm{sinc}\left(\Delta_{\ell t}\ell^*\,\frac{L}{2}\right). \tag{116}$$

In Eq. 116 the index $2t_o$ makes explicit the "modified" total observation interval.

The effect of coupling is to sharpen the ambiguity structure while maintaining its fundamental aspects, a main lobe and a secondary negligible structure. The quantitative analysis, in terms of the dimensions of the main lobe, will be pursued when we study the MSSM.

$\Delta \sin\theta_\ell$ Subspace

The analysis parallels the preceding one. We find

$$\psi(A,\bar{A}) \approx \frac{1}{L}\int_{-L/2}^{L/2} d\ell\ \exp[j\Delta R_\ell]\ \mathrm{sinc}\left(\Delta_{\ell t}\ell\,\frac{T}{2}\right).$$

Similarly, we define the locus $\mathscr{L}$ by Eq. 114a, which now implies

$$\Delta(\cos\theta_\ell) < \delta = \frac{R_o}{v\cos\theta_t}\,\frac{\pi}{\frac{L}{2}\,\frac{T}{2}}. \tag{117}$$

For points in the locus

$$\psi(A,\bar{A}) \sim \psi_s(A_s,\bar{A}_s)\ \mathrm{sinc}\left(\Delta_{\ell t}\ell^*\,\frac{T}{2}\right). \tag{118}$$

Outside $\mathscr{L}$ we define

$$\ell_o = \frac{R_o\pi}{\frac{vT}{2}\cos\theta_t\,|\Delta(\cos\theta_\ell)|}$$

to obtain

$$\psi(A,\bar{A}) \sim \frac{2\ell_o}{L}\,\psi_{2\ell_o}(A_s,\bar{A}_s)\ \mathrm{sinc}\left(\Delta_{\ell t}\ell^*\,\frac{T}{2}\right). \tag{119}$$

The conclusions are equivalent to the previous ones.

Radial Parameter

Along the radial parameter subspace

$$\psi(A,\bar{A}) \cong \frac{1}{LT}\int_{-T/2}^{T/2} dt \int_{-L/2}^{L/2} d\ell\ \exp\left[j\,\frac{2\pi}{\lambda}\,\frac{1}{2}\,(\cos\theta_\ell\ell + \cos\theta_t vt)^2\,\Delta\left(\frac{1}{R_o}\right)\right]. \tag{120}$$

Define the change of variables: $\sigma = \cos\theta_\ell\ell + \cos\theta_t vt$, and recall the definitions

$$X_{\ell c} = \frac{L}{2R_o}\cos\theta_\ell = \frac{L_{\ell c}}{R_o}$$

$$X_{t_c} = \frac{vT}{2R_o} \cos\theta_t = \frac{L_{tc}}{R_o}.$$

Performing the double integration in Eq. 120 along the dashed lines illustrated in Fig. 57, where the integrand is constant, we obtain

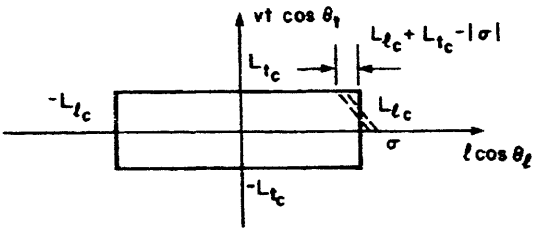

Fig. 57. Reduction of double integration to single integration.

$$\psi(A,\bar{A}) = \frac{(X_{\ell c} + X_{tc})^2}{X_{\ell c} X_{tc}} \psi'(A,\bar{A}) \tag{121a}$$

with

$$\psi'(A,\bar{A}) = \frac{1}{X_{\ell t_c}} \int_0^{X_{\ell t_c}} \left(1 - \frac{2\sigma}{X_{\ell t_c}}\right) \exp[j(\Delta K)\sigma^2]\, d\sigma, \tag{121b}$$

where we defined the wave number parameter $\Delta K = \frac{\pi}{\lambda} \Delta\left(\frac{1}{R_o}\right)$, and the equivalent total geometric parameter $X_{\ell t_c} = 2\left(X_{\ell_c} + X_{t_c}\right)$. Performing the integral in Eq. 121b, we have

$$\psi'(A,\bar{A}) = \frac{\mathcal{F}(\Delta K_{\ell t})}{\Delta K_{\ell t}} + \frac{1 - \exp\left[j\Delta K_{\ell t}^2\right]}{j(\Delta K_{\ell t})} \tag{122}$$

with $\Delta K_{\ell t} = \sqrt{\Delta K}\; X_{\ell t_c}$.

Equation 121b shows that the spatial/temporal coupled signal autocorrelation along the radial parameter subspace, apart from a normalizing factor, corresponds to the signal autocorrelation for a one-dimensional problem, with the source at broadside condition, where the equivalent total linear dimension (Fig. 58a) is $L_{tot} = L_{\cos\theta_\ell} + vT\cos\theta_t$, and the array shading is triangular and not uniform, as illustrated in Fig. 58b.

Finally, we comment that Eq. 121b generalizes the usual one-dimensional distribution of the (Fresnel zone) diffracted field for a plane wave in optics, to the case where the line source (equivalent in our problem to the temporal baseline) and the receiving aperture (spatial baseline) are not parallel ($\theta_\ell \neq \theta_t$), and there is a wide angle ($\theta_\ell \neq 0$) and oblique incidence ($\theta_t \neq 0$).

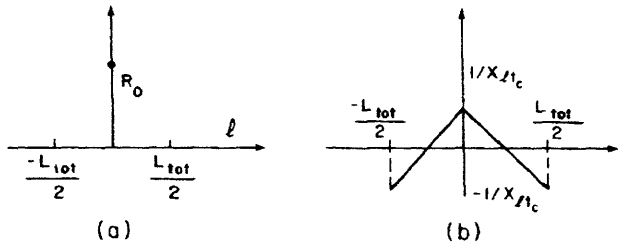

Fig. 58. (a) Equivalent SASS problem.
(b) Triangular shading.

4.4.2 Mean-Square Spread Matrix

We study the mean-square spread matrix (MSSM) $\mathcal{M}$ which exhibits the essential geometric aspects of the problem, and how they are reflected in the mean-square performance of the ML estimator.

In order to obtain intuitive closed-form expressions, we pursue a Taylor's series analysis in terms of the geometric parameters $X = \frac{L}{2R_o}$ and $X_t = \frac{vT}{2R_o}$. First, we consider a Taylor's series expansion of the range function in operator form given by Eq. 101. Although we restrict our attention to the lowest order term of det $\mathcal{M}$ that is needed to compute $\mathcal{M}^{-1}$ and the volume of the elementary grid cell, the dimensionality of $\mathcal{M}$ requires that we keep a relatively large number, N, of terms in expansion (101). The consequence is an extensive burden of algebraic manipulations leading to a not less extensive list of expressions. In Appendix D the results are given for the least order terms of $\mathcal{M}$, its classical adjoint $\mathcal{M}$, the inverse $\mathcal{M}^{-1}$, and det $\mathcal{M}$. Here we limit the analysis to det $\mathcal{M}$, the diagonal elements of $\mathcal{M}^{-1}$ from which the performance bounds can be obtained, and the parameter error crosscorrelations defined from the elements of $\mathcal{M}^{-1}$.

a. Determinant of $\mathcal{M}$

The determinant is given by

$$\det \mathcal{M} = \left(\frac{2\pi}{\lambda}\right)^8 \frac{1}{3^6 \cdot 5} \frac{\cos^2\theta_\ell}{\cos^2\theta_t} X_\ell^4 X_t^4 \left(X_{\ell_c}^4 + \frac{4}{5} X_{\ell_c}^2 X_{t_c}^2 + X_{t_c}^4\right) \frac{R_o^6}{v^2},$$

where

$$X_{\ell_c} = X_\ell \cos\theta_\ell = \frac{L \cos\theta_\ell}{2R_o}$$

$$X_{t_c} = X_t \cos\theta_t = \frac{vT \cos\theta_t}{2R_o}.$$

We make the following remarks:

1. The lowest order term in det $\mathcal{M}$ contains terms in

$$X_\ell^3 X_t^4,\ X_\ell^6 X_t^6,\ X_\ell^4 X_t^8$$

and is of order n_{SAMS} = order of least order term of det $\mathcal{M}$ = 12. In Section III we concluded that for the $SAMS_o$ problem n_{SAMS_o} = 12. On the other hand, the single-parameter bearing estimation leads to $n_{\sin\theta_\ell} = 2$.

We see, because of the coupling, that $n_{SAMS} < n_{SAMS_o} + n_{\sin\theta_\ell}$, while for the decoupled structure just discussed equality holds. The spatial/temporal cross coupling improves in a nontrivial way the joint estimation of all source parameters, thereby reducing the overall order of the problem. Intuitively speaking, with the decoupled problem at least third-order effects have to be measured from the temporal diversity, while only the linear delays can be estimated from the spatial curvature (bearing). The cross coupling reduces to second order the lowest order effects that have to be measured but now from both spatial and temporal diversity. Figure 54 shows that for the coupled geometry the range function depends significantly on both time and space, and this intuitively suggests an improvement in performance.

2. The terms in

$$X_\ell^{12},\ X_t^{12},\ X_\ell^{10} X_t^2,\ X_\ell^2 X_t^{10}$$

are absent. This follows from the fact that $\mathcal{M}_{22}$ and $\mathcal{M}_{33}$ depend on at least X_t^2, and $\mathcal{M}_{44}$ on X_ℓ^2. Finally, the last term has to be absent, since it would correspond to a decoupled structure, for which $n_{SAMS} = n_{SAMS_o} + n_{\sin\theta_\ell} = 14$ corresponding to lowest order terms $X_\ell^2 X_t^{12}$.

3. The matrix $\mathcal{M}$ is positive-definite, as can be concluded by direct application of Sylvester's rule.

4. We observed in section 4.4.1 that on the parameter subspace $\pi_{v\theta_t}$, the ambiguity structure, although separable, leads to a sharper lobe. Comparing the determinant for the v, $\sin\theta_t$ parameters for the SAMS

$$\det \mathcal{M}_{v,\sin\theta_t} = \mathcal{M}_{22}\mathcal{M}_{33} - \mathcal{M}_{23}^2$$

$$= \left(\frac{2\pi}{\lambda}\right)^4 \frac{R_o^4}{v^2}\,\frac{X_t^4}{3^3}\left[\frac{4}{5}X_t^2 + \frac{\cos^2\theta_\ell}{\cos^2\theta_t}X_\ell^2\right]$$

with Eq. 80c, we conclude that the last term, which reflects the cross coupling, quantifies the correction to the main lobe dimensions on $\pi_{v\theta_t}$.

5. If we let X_ℓ, $\cos\theta_\ell$, $X_{t_c} = X_t \cos\theta_t$ remain constant while increasing θ_t from 0° (closest approach) to $\frac{\pi}{2}$ (Fig. 59a), det $\mathcal{M}$ increases. This is a result of the cross

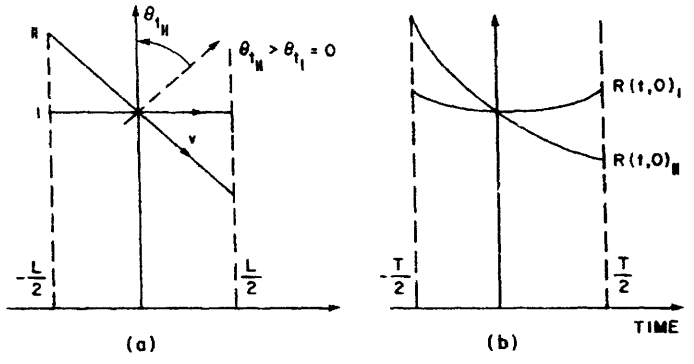

Fig. 59. Determinant of $\mathcal{M}$ dependence on angle θ_t as a result of cross coupling.

coupling observed in Fig. 59b. As θ_t increases but X_{t_c} is kept constant, the total source travel increases, with a larger variation of $R(t,\ell)$ over the total observation interval and across the array.

b. Mean-Square Parameter Spread

We discuss briefly the diagonal elements of the inverse matrix $\mathcal{M}^{-1}$, which measure the spread of the ambiguity structure along the different parameter axes.

Range Spread: From Appendix D we obtain

$$\mathcal{M}^{-1}_{R_o} = (\mathcal{M}^{-1})_{11} = \left(\frac{\lambda}{2\pi}\right)^2 \frac{3^2 \cdot 5}{X^4_{c_\ell}} \frac{1 + \frac{4}{5}\gamma^2}{1 + \frac{4}{5}\gamma^2 + \gamma^4},$$

where γ defines the relation between the temporal and spatial effective baselines

$$\gamma = \frac{X_{c_t}}{X_{c_\ell}} = \frac{vT \cos\theta_t}{L \cos\theta_\ell},$$

i.e., as seen from the oblique angle θ_t and bearing θ_ℓ.

We consider three cases.

1. Spatial baseline much larger than temporal baseline: If $\gamma \ll 1$, we obtain

$$\left(\mathcal{M}^{-1}_{R_o}\right)_I \approx \left(\frac{\lambda}{2\pi}\right)^2 \frac{3^2 \times 5}{X^4_{c_\ell}} \approx \left(\mathcal{M}^{-1}_{R_o}\right)_{SASS}.$$

This equation shows the range performance approaching the SASS result in Section II; the range parameter is essentially estimated from the spatial curvature effects observed across the array.

2. Comparable spatial and temporal baselines: If $\gamma \approx 1$, we have

$$\left(\mathcal{M}_{R_o}^{-1}\right)_{II} \approx \left(\frac{\lambda}{2\pi}\right)^2 \frac{3^2 \times 5}{7} \frac{1}{X_{c_\ell}^4} \left[\frac{9}{2} - 5(\gamma-1)\right].$$

Comparing this with Case 1 for $\gamma = 1$, we have

$$\frac{\left(\mathcal{M}_{R_o}^{-1}\right)_{II}}{\left(\mathcal{M}_{R_o}^{-1}\right)_{I}} \approx \frac{9}{14},$$

which shows that the cross coupling reduces the range standard deviation to approximately 80%.

3. Temporal baseline much larger than spatial baseline: If $\gamma \gg 1$, we get

$$\left(\mathcal{M}_{R_o}^{-1}\right)_{III} \approx \left(\frac{\lambda}{2\pi}\right)^2 \frac{2^2 \times 3^2}{X_{c_t}^2 X_{c_\ell}^2}.$$

Comparing this with the corresponding expression for the $SAMS_o$ problem in Section III, we have

$$\frac{\left(\mathcal{M}_{R_o}^{-1}\right)_{III}}{\left(\mathcal{M}_{R_o}^{-1}\right)_{SAMS_o}} \approx \frac{X_{t_s}^2 \gamma^2}{5}, \tag{123}$$

where $X_{t_s} = X_t \sin\theta_t = \frac{vT}{2R_o} \sin\theta_t$.

We recall that with the $SAMS_o$ model the range performance deteriorated sharply for $\theta_t \approx 0$, i.e., for broadside geometry. Equation 123 says when there is a small but nonzero cross coupling, that as long as

$$\frac{X_{t_s}^2 \gamma^2}{5} < 1,$$

the range performance is sharply improved.

Velocity and $\sin\theta_t$ Spread: From Appendix D we obtain

$$\mathcal{M}_v^{-1} = (\mathcal{M}^{-1})_{22} = \left(\frac{\lambda}{2\pi}\right)^2 \frac{v^2}{R_o^2} \frac{3^2 \times 5 \cos^2\theta_t}{\cos^2\theta_\ell X_\ell^2 X_t^2} \frac{1 + 5\gamma^2 + \gamma^4}{1 + 4\gamma^2 + 5\gamma^4} \tag{124}$$

and

$$\mathcal{M}^{-1}_{\sin\theta_t} = (\mathcal{M}^{-1})_{33} = \mathcal{M}^{-1}_{v} \left(\frac{\sin\theta_t}{v}\right)^2 . \tag{125}$$

These lowest order terms are in $X_t^{-2}X_\ell^{-2}$, representing an improvement of order two over the decoupled problem performance (recall that for the decoupled structure the speed and angle performance is essentially given by the $SAMS_o$ results, whose first non-zero term is of order X_t^{-6}). As in the discussion of point 1 for det $\mathcal{M}$, this represents the reduction on the order of the estimation problem introduced by the cross coupling. We note that the relation in Eq. 125 is only for the coefficients of the lowest order terms.

From Eq. 124 we can consider, as we did for the range spread, three cases.

1. Spatial baseline larger than the temporal baseline: We have $\gamma \ll 1$ and

$$\left(\mathcal{M}^{-1}_{v}\right)_I \approx \left(\frac{\lambda}{2\pi}\right)^2 \frac{v^2}{R_o^2} \frac{3^2 \times 5 \cos^2\theta_t}{\cos^2\theta_\ell \, X_\ell^2 X_t^2} .$$

2. Comparable spatial and temporal baselines: For $\gamma \approx 1$ we obtain

$$\frac{\left(\mathcal{M}^{-1}_{v}\right)_{II}}{\left(\mathcal{M}^{-1}_{v}\right)_I} \approx \frac{7}{10} \approx .83^2 .$$

3. Temporal baseline much larger than the spatial baseline: If $\gamma \gg 1$, we get

$$\frac{\left(\mathcal{M}^{-1}_{v}\right)_{III}}{\left(\mathcal{M}^{-1}_{v}\right)_I} \approx \frac{1}{5} \simeq .43^2 .$$

These results exhibit the improvement in the speed performance when the geometry changes from spatially dominant (Case I) to temporally dominant (Case II).

We can obtain similar relations for $\mathcal{M}^{-1}_{\sin\theta_t}$.

Bearing Spread: The lowest order term for the bearing mean-square spread, from Appendix D, is

$$\mathcal{M}^{-1}_{\sin\theta_\ell} = (\mathcal{M}^{-1})_{44} \approx \left(\frac{\lambda}{2\pi}\right)^2 \frac{1}{R_o^2} \frac{3}{X_\ell^2} = \left(\frac{\lambda}{2\pi}\right)^2 \frac{12}{L^2}, \tag{126}$$

which is exactly the expression obtained for the decoupled problem.

c. Parameter Error Crosscorrelations

The crosscorrelations between the several parameter errors, and as computed from

the elements of $\mathcal{M}^{-1}$, are algebraically complex expressions. We present below approximations obtained by Taylor's series expansions on both geometric parameters X_t^2 and X_ℓ^2 about $X_t = 0$ and $X_\ell = 0$.

Range/Speed Crosscorrelation: The first terms of the Taylor's series of the range/speed crosscorrelation lead to

$$\rho^2_{R_o,v} = \frac{\left(\mathcal{M}^{-1}_{R_o,v}\right)^2}{\left(\mathcal{M}^{-1}_{R_o}\right)^2 \left(\mathcal{M}^{-1}_{v}\right)^2} \approx 1 - \frac{5}{4}\frac{1}{\gamma^2} + \ldots \text{ (Taylor's series in } X_\ell^2) \tag{127}$$

$$\rho^2_{R_o,v} = 5\gamma^2 - 25\gamma^4 + \ldots \text{ (Taylor's series in } X_t^2), \tag{128}$$

where

$$\gamma = \frac{vT\cos\theta_t}{L\cos\theta_\ell}. \tag{129}$$

We note in Eq. 127 that for very large γ the range and the velocity parameters are perfectly correlated. This is in accordance with our previous results because for large γ the temporal diversity dominates the spatial diversity. Furthermore, for X_ℓ small the spatial curvature is negligible, and the SAMS problem is decoupled on its spatial and temporal aspects, having as net effect that the lowest order term in det $\mathcal{M}$ becomes of order 14 and not 12.

Equation 128 states that for a significant spatial diversity ($\gamma \ll 1$) the range and velocity parameter errors are relatively uncoupled, the range being estimated from the spatial diversity and the speed from the temporal modulations.

We now study the range/speed crosscorrelation for special configurations of practical interest.

1. Let the spatial/temporal geometry be symmetric and parallel as illustrated in Fig. 60.

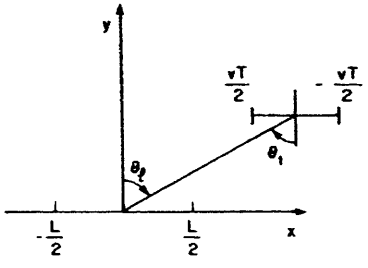

Fig. 60.
Spatial/temporal symmetric and parallel configuration.

Then $\cos\theta_\ell = \cos\theta_t$, $X_\ell = X_t$, and the range/speed crosscorrelation becomes $\rho^2_{R_o,v} = \frac{7}{9}$.

2. We study the crosscorrelation $\rho_{R_o,v}$ as a function of the bearing angle. We consider a specific geometric configuration, the symmetric closest approach with $\cos\theta_t = 1$ and $X_t = X_\ell$ (Fig. 61a), as it changes from broadside ($\theta_\ell = 0$) to end-fire $\left(\theta_t = \frac{\pi}{2}\right)$ configuration.

$$\rho_{R_o,v}(\cos\theta_\ell)\Big|_{\substack{\cos\theta_t=1 \\ X_\ell=X_t}} = \frac{4 + 20\cos\theta_\ell^2 + 25\cos\theta_\ell^4}{4 + 25\cos\theta_\ell^2 + 29\cos\theta_\ell^4 + 5\cos\theta_\ell^6}.$$

This function is represented graphically in Fig. 61b. We note that at end-fire ($\cos\theta_\ell = 0$) condition the errors on the range and the speed parameters are perfectly correlated, and

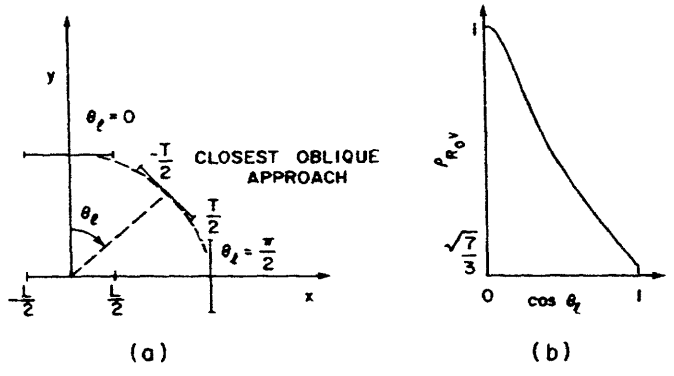

Fig. 61. (a) SAMS geometry (closest approach).
(b) Range/velocity crosscorrelation vs $\cos\theta_\ell$ (closest approach).

this correlation decreases monotonically to the minimum $\frac{\sqrt{7}}{3} \approx 0.88347583$ at the broadside ($\cos\theta_\ell = 0$) condition.

3. In Fig. 62b we study $\rho_{R_o,v}$ as a function of the spatial geometric parameter $X_\ell = \frac{L}{2R_o}$ for the parallel geometry $\cos\theta_\ell = \cos\theta_t$ displayed in Fig. 62a, when $X_t = .1$.

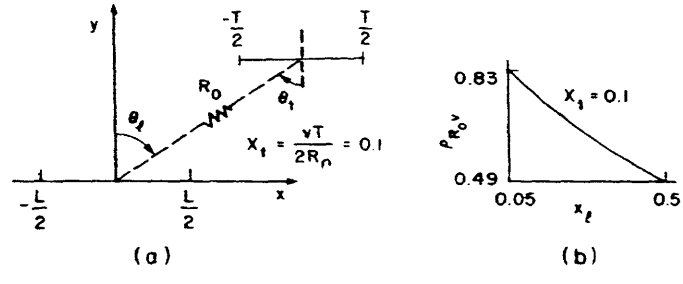

Fig. 62. (a) SAMS parallel geometry.
(b) Range/velocity crosscorrelation vs X_ℓ (parallel).

Under these conditions

$$\rho_{R_o,v} \cong \frac{2 + 100X_\ell^2 + 1250X_\ell^4}{2 + 125X_\ell^2 + 1450X_\ell^4 + 2500X_\ell^6}.$$

We note that this expression is valid for all θ_ℓ or θ_t, as long as the geometry remains parallel. From Fig. 62a we see that as X_ℓ increases the crosscorrelation error decreases monotonically.

Range sin θ_t Crosscorrelation: Remarks and results are equivalent to the preceding ones.

Range, Velocity, or sin θ_t, and sin θ_ℓ Crosscorrelation: For the crosscorrelation between R_o, v or sin θ_t, and sin θ_ℓ we obtain essentially $\rho_{i \sin \theta_\ell} \approx f(X_t) X_\ell^2$, where $f(X_t)$ is a certain function of X_t, cos θ_t, cos θ_ℓ. The important thing to note in this equation is the homogeneous behavior on X_ℓ^2 expressing the fact that for small X_ℓ the errors between sin θ_t and the remaining parameters are practically uncorrelated.

Velocity-sinθ_t Crosscorrelation: We have $\rho_{v, \sin \theta_t} \approx -1 + \alpha X_t^2$, i.e., in order to uncouple the estimates, we require some finite, nonzero, observation interval (equivalently, and more intuitively, in order to estimate speed v and sin θ_t, we need to observe these motions).

For the special case of a symmetric and parallel geometry, i.e., for $X_t = X_\ell$, cos θ_t = cos θ_ℓ, a Taylor's series expansion leads to

$$\rho_{v, \sin \theta_t} \approx -1 + \left[\frac{\sin^2 \theta_\ell + 28}{5} + 891 \sin \theta_\ell^4 - 465 \cos^2 \theta_\ell \sin^2 \theta_\ell \right] X_\ell^2.$$

We present this expression as an illustration of the complicated algebraic form that these crosscorrelations take.

4.5 SUMMARY

We have considered positioning/navigation problems, when both spatial and temporal diversity are present. After a brief description of the model and receiver, we pursued two main classes of problems. The first was characterized by the dominance of the temporal over the spatial baseline. It was shown that this dominance leads to a decoupled processing structure, with the receiver estimating the bearing angle from the spatial delays, and the remaining source/receiver parameters from the temporal diversity. The SAMS reduced to the "direct sum" of a $SAMS_o$, and a time-variant bearing angle estimation. We derived an expression for the required number of beam steering updates, and expressed the mean-square error performance in terms of the $SAMS_o$ results. In the second class we assumed a balanced geometry; that is, that the spatial and temporal

diversity parameters X_ℓ and X_t are of comparable size. This leads to a coupled receiving structure. The cross-coupling term was isolated and an expression was derived. Its effects were analyzed for several limiting geometries and along special subspaces of the parameter space Ω. We concluded that the cross coupling represented a nontrivial improvement, with a decrease of two on the order of the overall problem. Recall that this order is twice the sum of the lowest orders of the modulation effects that have to be measured in order to obtain a globally identifiable parameter estimation problem, and that it is also given by the order of the lowest order nonzero term of det $\mathcal{M}$.

For both problems we derived expressions for the ambiguity structure and for the mean-square spread matrix, from which the local and global performance bounds can be computed.

Part II. Applications to Positioning and Navigation

V. HYBRID ALGORITHM: A PRACTICAL SOLUTION TO PASSIVE TRACKING

We now explore important issues arising in the design of practical systems for passive tracking. There are three principal issues.

1. Global identifiability of the source/receiver relative parameters.
2. Minimization of the involved computational effort.
3. Sensitivity of the actual processing to model perturbations.

As we shall see, the first and second points motivate a practical integrated solution which is referred to as the hybrid algorithm having three steps.

1. Global acquisition via ML techniques.
2. Tracking of the local dynamics by a recursive linearized structure.
3. Reacquisition every T_i second.

We shall discuss the design and expected performance of each block of the hybrid algorithm, the sensitivity of the ML global acquisition to modeling assumptions, obtain the overall receiver mean-square performance, and finally, integrate the analysis in terms of four characteristic regions of behavior for the hybrid algorithm.

5.1 HYBRID ALGORITHM

The proposed procedure is illustrated in the context of the decoupled SAMS where the available spatial baseline is much smaller than the one synthesized by the source travel. The bearing angle is estimated from the spatial diversity and the remaining parameters are observed from the temporal diversity, with SAMS equivalent to a passive bearing measurement decoupled from a $SAMS_o$ problem. We concentrate on the latter where only the time dependence arises.

Under narrow-band and linear constraints, passive tracking reduces to a phase demodulation. The phase of the received waveform signal component is

$$2\pi ft + \phi(t) \cong 2\pi ft + \phi_o + 2\pi f\tau(t), \tag{130}$$

where $\tau(t) \approx \frac{R(t)}{c}$ is the observed delay and ϕ_o is the absolute phase reference for the incoherent model. Note that $\phi(t)$, as given by Eq. 130, represents the total phase modulation shown in Fig. 63 and not its modulo 2π version.

From either Eq. 130 or Fig. 63 we obtain

$$R(t) \approx \frac{\lambda}{2\pi}\Delta\phi(t) = \frac{\lambda}{2\pi}[\phi(t)-\phi_o],$$

where $\lambda f = c$, and $\Delta\phi(t)$ represents the total, integrated, absolute phase variation. From Fig. 63 we also write

$$R(t) = R(0) + \Delta R(t) \tag{131a}$$

with

$$R(0) \cong \frac{\lambda}{2\pi} \Delta\phi(0) \tag{131b}$$

and

$$\Delta R(t) = \int_0^t \dot{R}(u)\, du = \frac{\lambda}{2\pi} [\Delta\phi(t) - \Delta\phi(0)] = \frac{\lambda}{2\pi} [\phi(t) - \phi(0)]. \tag{132}$$

Equations 131b and 132 suggest that the range estimation be performed in two steps. The first acquires globally the source/receiver separation R(0) at a particular time

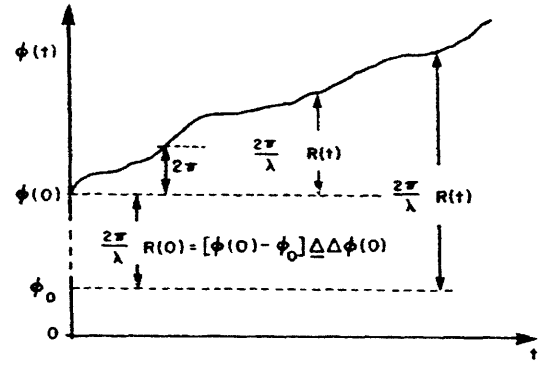

Fig. 63.
Absolute phase evolution.

reference t = 0; the second tracks the instantaneous phase variation, in order to obtain the range increment. The corresponding receiver structure is presented in Fig. 64, and is referred to as the hybrid algorithm.

The hybrid algorithm represents a compromise between two conflicting requirements, observability of the parameters and computational effort. The upper block in Fig. 64 accomplishes the global identifiability but is nonrecursive; the lower block is recursive but tracks only the local dynamics.

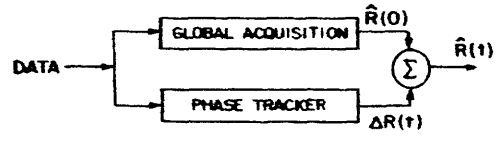

Fig. 64.
Global Acquisition/Tracking hybrid algorithm.

Subsequently we shall explore the design of both blocks, and their sensitivity to the geometry, to the statistical parameters, and to the model assumptions.

5.2. GLOBAL ACQUISITION

In active radar systems and in certain coherent and synchronized passive navigation systems ($\phi_o \approx 0$ in Eq. 131b) global ranging is achieved from a direct measurement of travel times. From Eq. 131b,

$$\hat{R}(0) = \frac{\lambda}{2\pi} \hat{\phi}(0) = \hat{\tau}(0)\, c, \tag{133}$$

where $\hat{\tau}(0)$ is the delay estimate. Equation 133 shows that ranging with coherent and synchronized clocks is based on absolute phase measurements. They may require, however, sophisticated and expensive equipment; and more important from a conceptual viewpoint, they assume an unrealistic model for many practical situations.

We have introduced an incoherent and asynchronous phase model. The absence of receiver/transmitter synchronism precludes global range estimation techniques based on absolute travel time measurements. By imposing motion constraints, we have been able to develop an inherently nonlinear receiver structure that achieves basically global acquisition, by estimating the higher order spatial/temporal modulations induced on the signal.

In this context the upper block of Fig. 64 is the nonlinear ML processor previously derived where the influence of the geometry and other statistical parameters on the receiver structure and performance have been analyzed.

There are two other points demanding further study.

1. The ML receiver requires a nonrecursive multidimensional stochastic maximization, which makes it impractical for tracking the changing geometry continuously. To alleviate the associated computational effort, we shall investigate recursive structures for the hybrid algorithm phase tracker block.

2. The ML receiver is sensitive to variations in the source travel, because of the underlying assumption of a deterministic constant speed path. We assume that the path perturbations are random accelerations. Because this more general model is used to design the phase tracker, we postpone discussion of the sensitivity issue.

5.3 PHASE TRACKER

Once the ML receiver has acquired the source, the range time update can be accomplished as given by Eq. 132, by measuring the range differences from the Doppler effects. This may be achieved with a digital Doppler counter,[3] or with any other phase-estimation structure. We have previously[20] used linearizing arguments to derive recursive filters based on extended Kalman-Bucy (EKB) techniques.

5.3.1 Model for Random Acceleration Motions

The model that we have used[20, 21] incorporates more realistic relative dynamic assumptions than those that we have assumed thus far. Specifically, they are described

by a set of finite-dimensional, nonlinear, stochastic differential equations, modeling a nominal constant-speed linear path perturbed by random accelerations. In the state-variable framework the model can be described as follows.

Dynamical System

$$dX(t) = f(X(t))\,dt + g(X(t))\,du(t) \tag{134a}$$

$$= \begin{bmatrix} F_R & o \\ o & F_\theta \end{bmatrix} X(t)\,dt + \begin{bmatrix} g_R \\ g_\theta \end{bmatrix} du(t) \tag{134b}$$

with

$$X = \begin{bmatrix} X_1 \\ \cdots \\ X_4 \end{bmatrix} = \begin{bmatrix} R \\ \dot{R} \\ \theta \\ \dot{\theta} \end{bmatrix}; \quad F_R = \begin{bmatrix} 0 & 1 \\ \dot{\theta}^2 & 0 \end{bmatrix}; \quad F_\theta = \begin{bmatrix} 0 & 1 \\ 0 & -\frac{2\dot{R}}{R} \end{bmatrix}; \tag{134c}$$

$$g_R = \begin{bmatrix} 0 & 0 \\ \sin\theta & \cos\theta \end{bmatrix}; \quad g_\theta = \frac{1}{R}\begin{bmatrix} 0 & 0 \\ \cos\theta & -\sin\theta \end{bmatrix}; \quad du(t) = \begin{bmatrix} du_x(t) \\ du_y(t) \end{bmatrix}. \tag{134d}$$

Equations 134 are to be interpreted in the Ito integral sense. We note, however, that the Wong-Zakai correction term[20] is zero for the specific g(X(t)) in Eq. 134d.

The observations are narrow-band and corrupted by an additive white Gaussian noise

$$dr(t) = h(X(t))\,dt + dw(t) \tag{135a}$$

with

$$h(X(t)) = \sqrt{2P}\begin{bmatrix} \sin\gamma(t,\ell) \\ \cos\gamma(t,\ell) \end{bmatrix}, \quad \ell \in \left[-\frac{L}{2}, \frac{L}{2}\right] \tag{135b}$$

$$\gamma(t,\ell) = \frac{2\pi}{\lambda}\left[R(t) - \ell\sin\theta(t)\right] + \xi(t). \tag{135c}$$

The phase drift process $\xi(t)$ is generated by a finite-dimensional system uncoupled from the state process, and it is independent of u(t) and w(t). The driving du(t) and the disturbance dw(t) are stochastic independent, Gaussian white noise with spectral matrices Q I and $\frac{N_o}{2}$ I, respectively, where I is the 2 × 2 identity matrix. We assume that the power level associated with the process $\xi(t)$ is much smaller than Q and $N_o/2$.

5.3.2 Linearized Mathematical Equivalent to the Extended Kalman-Bucy Filter (EKB)

Several linear approximations to the infinite-dimensional optimal filter have been

studied previously.[20] Under the assumptions on $\xi(t)$, since the portion of the linearized receiver associated with the phase drift $\xi(t)$ may be decoupled from the remaining part of the filter, we ignore it in the sequel.

We limit our attention to a brief discussion of the EKB. It can be shown[20] that the EKB is mathematically equivalent to two bearing beam form operations, which are the inputs to phase-locked loops tracking the bearing and range waveforms. Under linearizing assumptions on the receiver behavior, and for a centered geometry, these loops

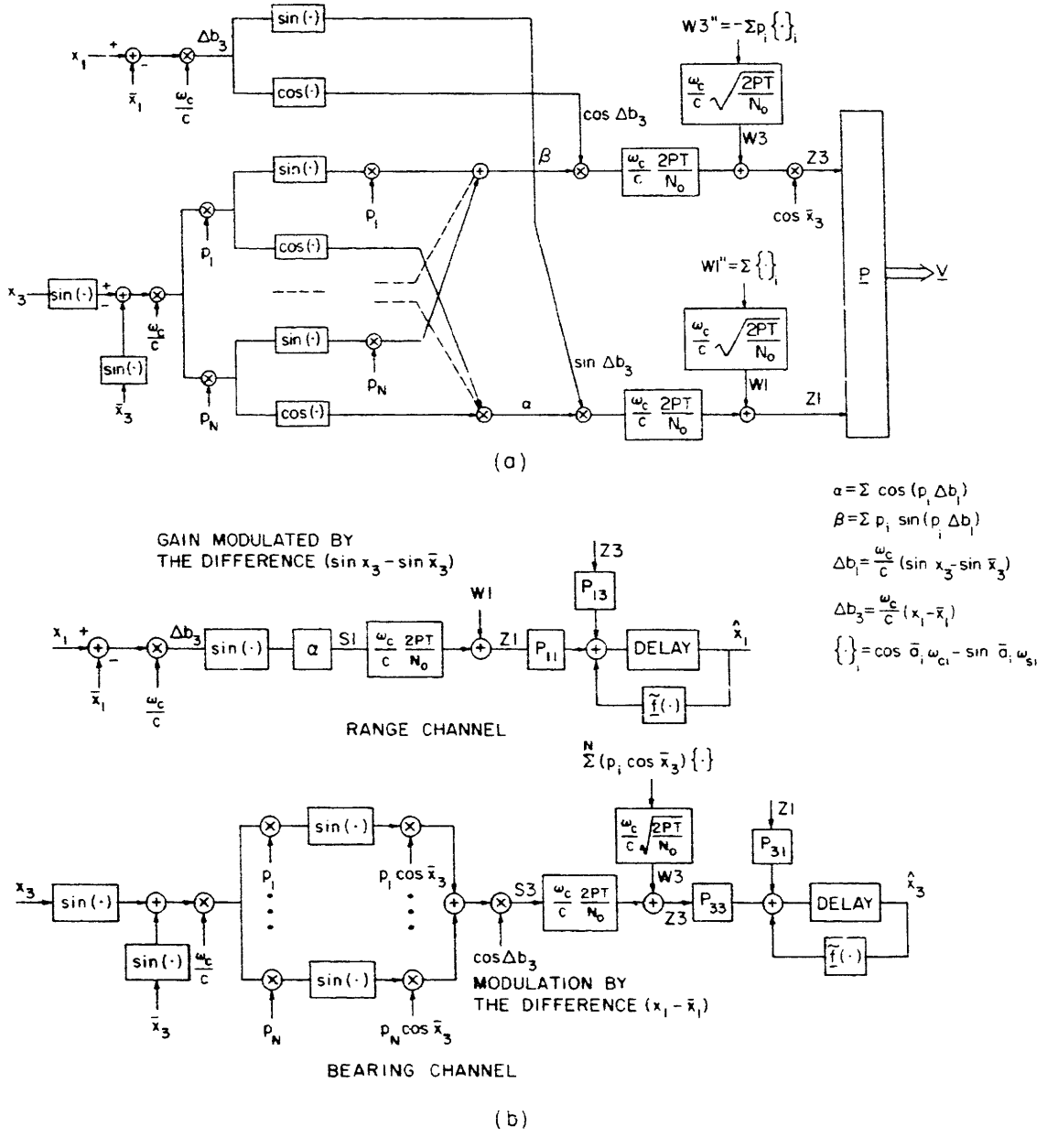

Fig. 65. (a) EKB mathematical model (polar coordinates).
(b) EKB decoupled structure.

are decoupled. The resulting receiver has the structure shown in Fig. 65a, which is rearranged in Fig. 65b.

REMARK. Figure 65 is taken from our previous work[20] where the discrete-time, discrete-array version of the continuous-time, continuous-array waveform tracking problem described above is implemented. The quantity T in the diagrams, which is associated with the (continuous-time, discrete-array) signal-to-noise ratio $2P/N_o$, is a normalizing factor relating it to the (discrete-time, discrete-array) signal-to-noise ratio. Other quantities in Fig. 65 are the following.

P_{ij} = error covariance elements, given by an EKB Riccati equation.

p_i, $i = 1, \ldots, N$, gives the location of the array elements.

W1, W3, = equivalent noise terms.

Z1, Z3 = range and bearing beams.

Under a small error assumption,

$$\cos\left[\frac{2\pi}{\lambda}\,\ell(\sin\theta(t) - \sin\hat{\theta}(t))\right] \approx 1,$$

and neglecting P_{13} as compared with P_{11} and P_{12} (as previously[20]), we can further rearrange the range channel of Fig. 65b in the decoupled loop shown in Fig. 66, with the gains

$$G' = \frac{2\pi}{\lambda}\,\mathrm{SNR}\;L \tag{136a}$$

$$a(t) = (\dot{\hat{\theta}}(t))^2. \tag{136b}$$

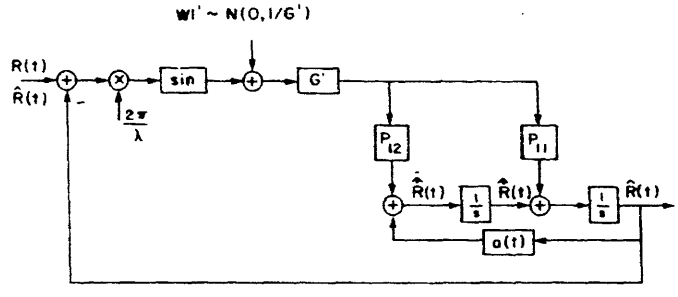

Fig. 66. Mathematical equivalent for signal source channel and EKB range loop.

5.3.3 Linearized Decoupled Range Loop

Under linearizing assumptions, the range phase tracking can be described by the following decoupled problem.

Dynamical System

$$dx(t) = F_R X(t)\, dt + g_R(X(t))\, du(t) \tag{137a}$$

with

$$F_R = \begin{bmatrix} 0 & 1 \\ a(t) & 0 \end{bmatrix}; \quad X(t) = \begin{bmatrix} R(t) \\ \dot{R}(t) \end{bmatrix}; \quad a(t) = \dot{\theta}^2(t) \tag{137b}$$

Observation Process

$$dr(t) = h(X(t))\, dt + dw(t) \tag{137c}$$

with

$$h(X(t)) = \sqrt{2PL} \begin{bmatrix} \sin\left[\frac{2\pi}{\lambda} R(t)\right] \\ \cos\left[\frac{2\pi}{\lambda} R(t)\right] \end{bmatrix} \tag{137d}$$

The "steady-state" solution for the EKB covariance Riccati equation applied to the decoupled problem given by Eqs. 137 leads to

$$P_{11} \cong \left(\frac{2P_{12}}{H_1}\right)^{1/2} \tag{138a}$$

$$P_{22} \cong (H_1 P_{12} - a) \left(\frac{2P_{12}}{H_1}\right)^{1/2} \tag{138b}$$

$$P_{12} \cong \frac{a}{H_1}\left[1 + \left(1 + \frac{QH_1}{a^2}\right)^{1/2}\right], \tag{138c}$$

where H_1 is an equivalent signal energy-to-noise ratio

$$H_1 = \left(\frac{2\pi}{\lambda}\right)^2 \frac{2P}{N_o} L. \tag{138d}$$

Note that in Eq. 138d the "modulation index"

$$\beta = \left(\frac{2\pi}{\lambda}\right)^2. \tag{138e}$$

Since

$$a(t) = \dot{\theta}^2(t) \leq \left|\frac{v}{R(T_c)}\right|^2 \ll 1, \tag{139a}$$

where v is the source nominal speed, and $R(T_o)$ is the source/receiver separation at the point of closest approach, for a strong signal energy-to-noise ratio assumption

$$\frac{QH_1}{a(t)^2} \gg 1. \tag{139b}$$

Equations 138 can be approximated by

$$P_{12} \cong \frac{1}{H_1} (QH_1)^{1/2} \tag{139c}$$

$$P_{11} \cong \frac{1}{H_1} (4QH_1)^{1/4} \tag{139d}$$

$$P_{22} = \frac{2Q}{(4QH_1)^{1/4}}. \tag{139e}$$

Equations 138 and 139 express the filter gains of Fig. 66 in terms of the nominal geometry and statistical parameters, and can be precomputed. In the subsequent analysis, for economy of notation, we shall work with Eqs. 139. If condition (139b) is not satisfied, the results remain valid, as long as we use the more correct Eqs. 138.

Figure 67 represents a rearrangement of Fig. 66 and shows a block diagram for the steady-state configuration of the EKB decoupled range loop.

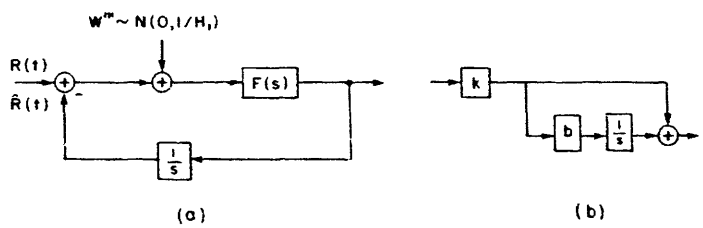

Fig. 67. EKB decoupled range loop.
(a) Phase-locked range loop.
(b) F(s) diagram.

a. Steady-State Loop Parameters

Figure 67 has the structure of a second-order phase-locked loop with filter

$$F(s) = k\left(1 + \frac{b}{s}\right), \tag{140a}$$

where

$$k = \left(\frac{2\pi}{\lambda}\right)^2 SNR\ L\ P_{11} \tag{140b}$$

$$b = \frac{P_{12}}{P_{11}}. \tag{140c}$$

The EKB range channel performs like a second-order phase-locked loop tracking the waveform $\phi(t) = \frac{2\pi}{\lambda} R(t)$.

Using the steady-state error covariance values (Eqs. 139) the filter gain is

$$k = (4QH_1)^{1/4} \tag{141a}$$

and

$$b = \left(\frac{QH_1}{4}\right)^{1/4}. \tag{141b}$$

Important parameters are the noise bandwidth B_L and the signal-to-noise ratio a in the bandwidth loop (see Van Trees[24]). For the second-order filter under consideration

$$B_L = \frac{k+b}{4} = \frac{3}{8}(4QH_1)^{1/4} \tag{141c}$$

$$a = \frac{(SNR)_{eq}}{B_L} = \frac{8}{3}\frac{H_1}{(4QH_1)^{1/4}}. \tag{141d}$$

In terms of the noise bandwidth loop we rewrite Eqs. 139:

$$P_{11} \cong \frac{8}{3}\frac{B_L}{H_1} \tag{141e}$$

$$P_{22} \cong \frac{3}{4}\frac{Q}{B_L}. \tag{141f}$$

Equations 141e and 141f are intuitively satisfying expressions. They say that in the steady state, the mean-square error on the range increment increases with the loop bandwidth (more noise is allowed in the system), and decreases with the equivalent signal energy-to-noise ratio H_1. Also, the mean-square error on the range phase rate decreases with the loop bandwidth B_L (for larger B_L the loop inertia decreases) and increases with the driving noise power level Q.

5.3.4 Extended Kalman-Bucy Filter (EKB) Linearized Performance vs Maximum-Likelihood (ML) Performance

Equation 141e contrasts with the Cramer-Rao performance bound derived in Section III for the incoherent parametrized model

$$\sigma^2_{R_{o_{loc}}} \approx \frac{1}{H_1 T} \frac{5^2 \times 7}{2 \sin^2\theta_t \cos^4\theta_t} \frac{1}{X_t^6}, \tag{142}$$

where the geometric parameter $X_t = \frac{vT}{2R_o}$. The conceptual difference is that the ML algorithm acquires the range estimation from the modulations induced on the signal structure, while the EKB achieves only the range local tuning. The EKB is not globally observable, exhibiting "lock-in" points separated by wavelength λ on the range parameter axis, as observed experimentally[20] and illustrated in Fig. 68. The EKB assumes

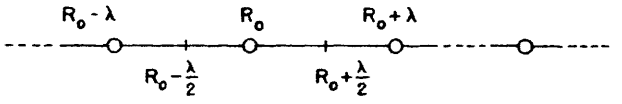

Fig. 68. EKB range "lock-in" points.

that its a priori range estimate $R(0)$ satisfies

$$R(0) - \frac{\lambda}{2} \leq \hat{R}(0) < R(0) + \frac{\lambda}{2}. \tag{143}$$

When

$$\left(N - \frac{1}{2}\right)\lambda \leq \hat{R}(0) - R(0) \leq \left(N + \frac{1}{2}\right)\lambda \tag{144}$$

for $N \neq 0$, the original global offset ($\approx N\lambda$) is not resolved by the EKB, which simply integrates the linear effects.

The global acquisition sensitivity to the random modulations and, in particular, the validity of Eq. 142 will be analyzed in section 5.4.

a. EKB Simulation Results

Simulation results[20] have shown that the error covariance propagated by the EKB Riccati equation predicts the filter performance correctly in the linear region. Figure 69 shows[21] representative runs for the four-dimensional problem of Eqs. 134. In particular, Fig. 69b illustrates the range and range rate standard deviations, indicated by s(1) and s(2), computed via Monte Carlo simulations. The curve for s(1) indicates that as long as the filter is started within the right range λ-cell, the filter range error standard deviation converges to the filter's predicted value. The curve for s(2) illustrates the filter's insensitivity to large initial errors on the range rate parameter.

5.3.5 Extended Kalman-Bucy Filter (EKB) Nonlinear Behavior

Because of the presence of noise, the actual range phase error at the output of the phase-locked loop (Fig. 67) undergoes diffusion that results in the so-called cycle skipping phenomena studied in conjunction with the nonlinear behavior of phase-locked loops.

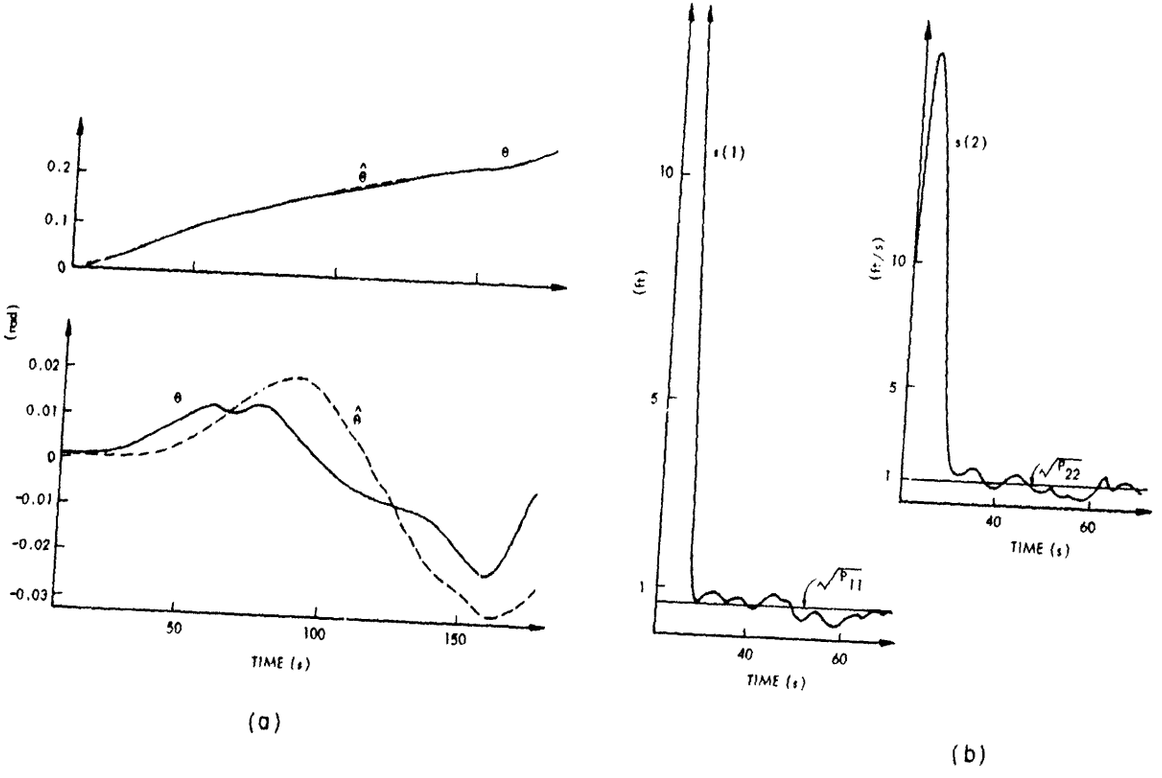

Fig. 69. EKB simulation results.

The range increment error process at the EKB output can be decomposed as

$$\mathbf{E}_R^{EKB}(t) \approx \tilde{\mathbf{E}}_R(t) + \lambda J_R(t), \tag{145}$$

where $\tilde{\mathbf{E}}_R(t) \approx \left(\mathbf{E}_R^{EKB}(t)\right) \pmod{\lambda}$ is the error associated with the EKB range loop, whenever the loop performs in its linear region; $J_R(t)$ is the counting process accumulating the number of cycles skipped by the loop in $[0, t]$. This error decomposition is illustrated in Fig. 70 where we assumed that the filter was originally started within the right λ-cell.

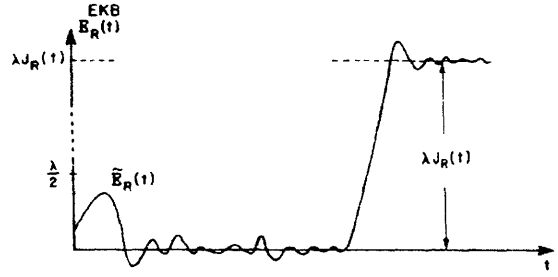

Fig. 70.
Cycle skipping phenomena.

$J_R(t)$ has been described by Lindsey and others,[43, 44] on the basis of experimental evidence,[45, 46] as a Poisson process, with the resulting approximate probabilistic structure for the range phase jumping

$$\Pr\{J_R(t) = j\} = \frac{(\bar{J}_R t)^j \exp(-\bar{J}_R t)}{j!}. \tag{146}$$

$\bar{J}_R$ represents the total average number of phase jumps per unit time, and is usually referred to as the frequency of skipping cycles. Exact analytical results for $\bar{J}_R$ are extremely hard to obtain for higher order loops, with or without modulation. A good approximation for the high SNR case, however, can be worked out.[47] The resulting expression is equivalent to that for the first-order loop, with the parameters depending on the system dynamics obtained with sufficient accuracy from the linearized model of the phase-locked loop structure. The analysis[47] has received good experimental confirmation for a second-order loop.[45]

For the loop shown in Fig. 67 we obtain

$$\bar{J}_R = \text{frequency of cycle skipping} \approx \frac{2B_L}{\pi^2 a I_0^2(a)}. \tag{147a}$$

For $a \gg 1$ it can be approximated by

$$\bar{J}_R \approx \frac{4B_L}{\pi} e^{-2a}. \tag{147b}$$

In Eqs. 147 $I_o(a)$ is a modified Bessel function of the first kind. Substituting Eqs. 141c and 141d in Eqs. 147a and 147b yields

$$\bar{J}_R = \frac{3}{16\pi^2}\left(\frac{Q}{H_1}\right)^{1/2}(I_o(a))^{-2} \underset{a \text{ large}}{\approx} \frac{3}{\pi\sqrt{2}}(QH_1)^{1/4}\exp(-2a). \tag{148a}$$

The average time between cycle skips is given by the inverse of the frequency to skip a cycle

$$T_{skp} = (\bar{J}_R)^{-1}. \tag{148b}$$

For the EKB range phase-locked loop with bandwidth and signal-to-noise ratio in the bandwidth loop given by Eqs. 141, in Fig. 71 we represent the average time between cycle skips T_{skp} as a function of SNR at the receiver site for several values of the spectral driving noise power level Q, and for wavelength λ = 50 ft and array length L = 250 ft.

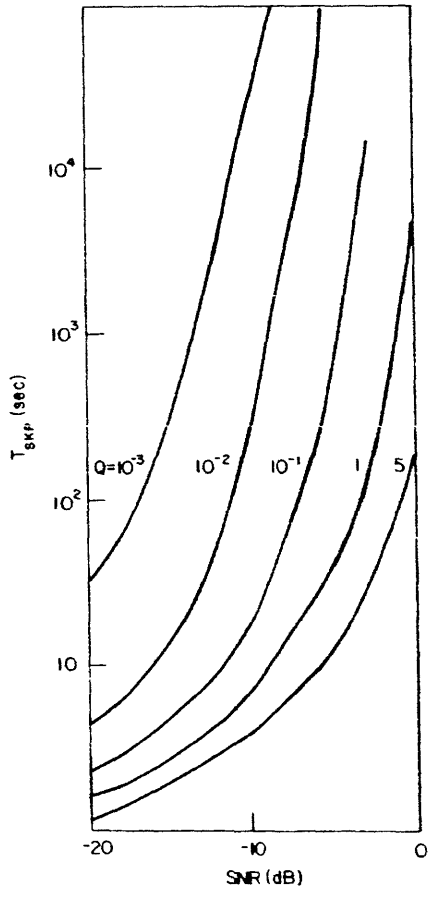

Fig 71.
Average cycle skipping time vs signal-to-noise ratio for several values of Q.

We note that for large SNR the curves approach an exponential behavior, and the cycle skipping phenomena will not be an issue in most applications. For smaller SNR, and as Q increases, the larger bandwidth causes the loop to skip cycles at a much higher

rate, with the curves approaching zero as SNR $\to$ 0 or Q $\to \infty$.

The mean-square error associated with the EKB phase tracker can be computed from Eq. 145. We assume

H1: In the steady state the two types of errors $\tilde{\mathbf{E}}_R$ and $\lambda J_R(t)$ in Eq. 145 are statistically independent. (This is a common assumption.[45]) We have in the steady state

$$E\left(\mathbf{E}_R^{EKB}(t)\right)^2 \approx P_{11} + \lambda^2(\bar{J}_R t). \tag{149}$$

Equation 149 shows that the EKB error variance grows without bound with t. It justifies the third step of the hybrid algorithm, reacquisition every T_i second.

Finally, the probability $\mathscr{P}_{skp}$ of the loop loosing lock in the interval [0, t] is

$$\mathscr{P}_{skp} \triangleq \Pr\,(J_R(t) \geq 1) \cong 1 - \exp(-\bar{J}_R t). \tag{150a}$$

For large signal-to-noise ratio and reasonable t, using Eq. 147b, we obtain

$$\ln \mathscr{P}_{skp} \approx -2a + \left[\ln \frac{4B_L t}{\pi} - \bar{J}_R t\right] \tag{150b}$$

$$\approx -2a. \tag{150c}$$

5.4. SENSITIVITY OF ML GLOBAL ACQUISITION TO PATH PERTURBATIONS

In the error performance analysis of the ML global acquisition algorithm a deterministic constant-speed linear path was assumed. We now investigate the sensitivity of this analysis to random path perturbations, by using the state-variable model.

The range function is decomposed as

$$R(t) = R_d(t) + R_n(t),$$

where

$R_d(t)$ = deterministic component, parametrized by the source parameter vector

$R_n(t)$ = noisy component, caused by random perturbations of the nominal source course.

Working with the decoupled description of Eqs. 137, we have

$$\ddot{R}_d(t) \cong a(t)\, R_d(t) + g u_d(t)$$

$$\ddot{R}_n(t) \cong a(t)\, R_n(t) + g u_n(t)$$

$$\ddot{R}(t) \cong a(t)\, R(t) + g u(t),$$

where $u(t) = u_d(t) + u_n(t) = u_n(t)$.

Under the assumption that at the starting point T_i the noisy component is zero, the second-order statistics of R(t) are $ER(t) = R_d(t)$ and $\text{Cov}(R(t)) = \Sigma_{11_R}(t)$. Defining $\Sigma_R(t) = \text{Cov}\left[\begin{pmatrix} R(t) \\ \dot{R}(t) \end{pmatrix}\right]$, we obtain the usual propagation equation

$$\frac{d}{dt}\,\Sigma_R(t) = \dot{\Sigma}_R(t) = F_R\Sigma_R(t) + \Sigma_R(t)\,F_R^T + g_R Q I g_R^T, \tag{151}$$

where F_R and g_R are given in Eqs. 134 and 137. Equation 151 can be integrated. Neglecting higher order terms in $a^2(t)$, which is consistent with a second-order approximation in X_t, we obtain

$$\Sigma_{11_R}(T) \cong \frac{T^3 Q}{3}\left[1 + \frac{aT^2}{5}\right], \tag{152}$$

where, for simplification, we assume at the starting point $t = T_i$ that $\Sigma_R(T_i) = \underline{0}$. Using the nominal bound on a(t) given by Eq. 139a, we have

$$\Sigma_{11_R}(T) \cong \frac{T^3 Q}{3}\left[1 + \frac{4X_t^2}{5}\right],$$

where, as before, $X_t = \frac{vT}{2R_o}$. We give the following definition.

Definition 5. Root-Mean-Square Range Error Caused by Path Variations

$$\Sigma_R^{1/2} = \left\{\frac{1}{T}\int_0^T \Sigma_{11_R}(t)\,dt\right\}^{1/2}.$$

To shorten the notation, we refer to $\Sigma_R^{1/2}$ more simply as the rms range path variation. After substitution

$$\Sigma_R^{1/2} \approx \sqrt{\frac{QT^3}{12}\left(1 + \frac{4^2X_t^2}{30}\right)}, \tag{153a}$$

and for small X_t this leads to

$$\Sigma_R^{1/2} \approx \left(\frac{QT}{3}\right)^{1/2}\frac{T}{2}. \tag{153b}$$

This quantity is represented in Fig. 72 as a function of the acquisition time T and for several values of Q.

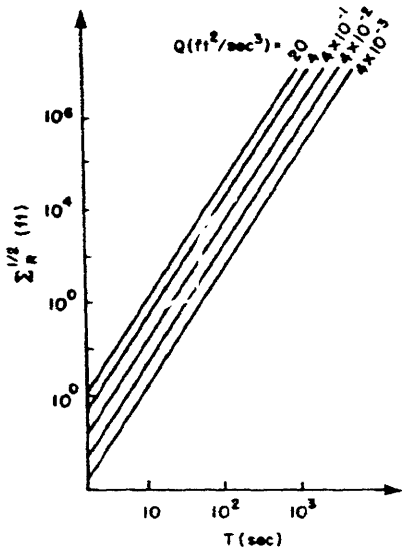

Fig. 72.

Root-mean-square range path variation vs acquisition time with Q as parameter.

Notation

In the sequel we let

$$\Sigma_R = \left(\Sigma_R^{1/2}\right)^2 \approx \frac{QT^3}{12} \tag{153c}$$

and refer to it as the mean-square range path variation.

The total range error at the output of the ML processor can be written

$$\mathbf{E}_R^{ML} \approx \mathbf{E}_R^d + \mathbf{E}_R^n,$$

where $\mathbf{E}_R^d \approx$ error induced on the ML algorithm by the additive measurement noise, after an acquisition time T_{acq}; $\mathbf{E}_R^n \approx$ error induced on the ML receiver by the path random perturbations. We assume

H2: The additive measurement noise and the path random accelerations are uncorrelated.

We have

$$\sigma_{R_o}^2 = E\left(\mathbf{E}_R^{ML}\right)^2 \approx E\left(\mathbf{E}_R^d\right)^2 + E\left(\mathbf{E}_R^n\right)^2 \tag{154a}$$

$$\approx \sigma_{R_{o_{tot}}}^2 + \Sigma_R, \tag{154b}$$

where $\sigma_{R_{o_{tot}}}^2$ is the mean-square error associated with the ML deterministic linear path analysis of the preceding sections, and Σ_R is the mean-square range path variation given by Eq. 153c.

In Fig. 73 we represent the range mean-square-error performance $\sigma^2_{R_o}$ at the output of the ML processor as a function of the total acquisition time T_{acq}. The

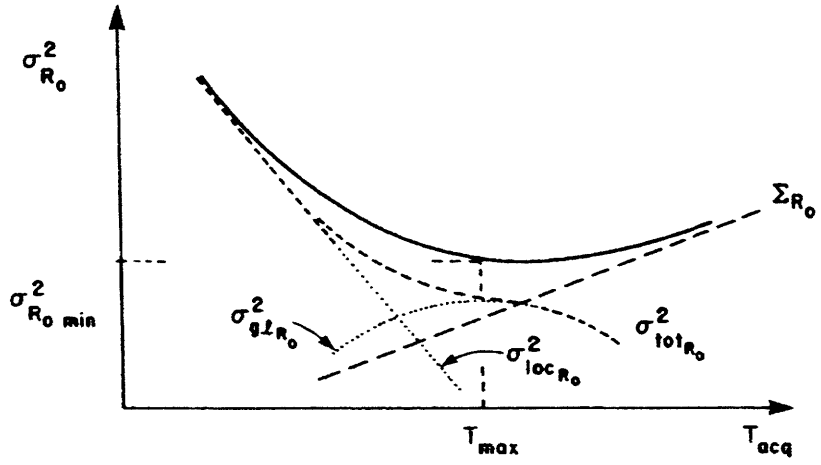

Fig. 73. Decomposition of the mean-square error at the ML processor output.

main consequence of the path perturbations, as illustrated by Fig. 73, is the existence of a maximum acquisition time T_{max}, or equivalently of a minimum mean-square error $\sigma^2_{R_{o\ min}}$; beyond T_{max} the path random acceleration effects dominate, and the ML performance deteriorates. We should note that $\sigma^2_{R_{o\ min}}$ decreases as the signal-to-noise ratio increases, while T_{max} decreases when either signal-to-noise ratio or the driving noise level, Q, increases.

5.5 HYBRID ALGORITHM ERROR ANALYSIS

Synthesizing our error analysis, we decompose the range error at the output of the hybrid algorithm as

$$\mathbf{E}_R(t) \approx R(t) - \hat{R}(t) \approx N^{ML}\lambda + \mathbf{E}_R^{EKB}(t), \tag{155}$$

where $N^{ML}\lambda = \left\lfloor \mathbf{E}_R^{ML} \right\rfloor$ = total error offset in integer number of wavelengths resulting from the global acquisition step of the hybrid algorithm, and $\mathbf{E}_R^{EKB}(t)$ = error associated with the EKB phase tracker. Besides hypotheses H1 and H2 we further assume

H3: The steady-state behavior of the EKB phase tracker is independent of the ML estimator output.

H3 formalizes in the model the phase-locked loop structure insensitivity to the absolute phase reference.

Under H1, H2, and H3, the mean-square error at the output of the hybrid algorithm, from Eq. 155, is

$$E\left(\mathbf{E}_R^2(t)\right) \approx P_{11} + \lambda^2(\bar{J}_R t), \qquad \text{if} \quad E\left(\mathbf{E}_R^{ML}\right)^2 < \left(\frac{\lambda}{2}\right)^2 \tag{156a}$$

$$E\left(\mathbf{E}_R^2(t)\right) \approx \left(N^{\overline{ML}}\lambda\right)^2 + P_{11} + \lambda^2(\bar{J}_R t), \qquad \text{if} \quad E\left(\mathbf{E}_R^{ML}\right)^2 > \left(\frac{\lambda}{2}\right)^2 \tag{156b}$$

$$E\left(\mathbf{E}_R^2(t)\right) \approx \sigma^2_{R_{o_{tot}}} + \Sigma_{R_o} + \lambda^2(\bar{J}_R t), \qquad \text{if} \quad E\left(\mathbf{E}_R^{ML}\right)^2 \gg \left(\frac{\lambda}{2}\right)^2. \tag{156c}$$

5.6 REGIONS OF BEHAVIOR FOR THE HYBRID ALGORITHM

We have now carried out in detail the error analysis at the output of the two blocks of the hybrid algorithm. Besides the error analysis associated independently with each one, the hybrid structure raised some additional points as follows.

1. A maximum acquisition time T_{max} determining the minimum attainable ML mean-square-error performance, as illustrated in Fig. 73, which is imposed by the errors induced on the global acquisition by the path variations.

2. A maximum usable time for the EKB recursive structure, determined by the average time T_{skp} for the occurrence of a cycle skip.

3. Suitable statistical independence assumptions on the errors, H1, H2, and H3, which lead to the mean-square-error approximation given by Eqs. 156.

Integrating, we distinguish 4 regions of behavior for the hybrid algorithm, which are summarized in Table 1. Figure 74 illustrates these regions for three signal-to-noise ratio parameter values, by sketching the range mean-square-error performance

Table 1. Regions of behavior for hybrid algorithm.

Region	T_{acq}	T_{skp}	$E\left(\mathbf{E}_R^{ML}\right)^2$	HA Mean-Square Error	Remarks
I. Tracking within Phase	$< T_{max}$	$> T_{acq}$	$< \left(\frac{\lambda}{2}\right)^2$	Eq. 156a	EKB saves computational effort and determines final HA mean-square error
II. Tracking within Geometry			$> \left(\frac{\lambda}{2}\right)^2$	Eq. 156b or 156c	EKB saves computational effort; ML determines final HA mean-square error
III. Acquisition		$\lesssim T_{acq}$		Eq. 156c	EKB not used for significant time
IV. Large Errors	$> T_{max}$				System has to be redesigned (e.g., larger SNR)

as a function of acquisition time. Later we shall quantify them exactly in the context of specific applications.

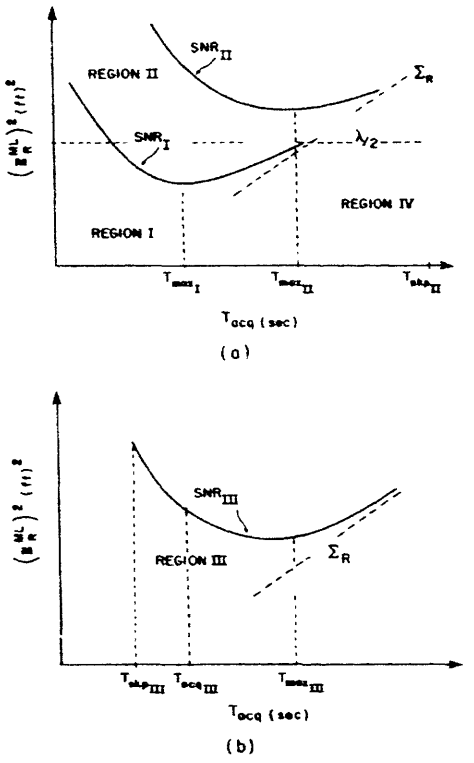

Fig. 74.
Typical regions of behavior for the hybrid algorithm: (a) Regions I, II, IV; (b) Region III.

Region IV, "Large Errors" (Fig. 74a), represents an underdesigned system, with the acquisition errors exceeding the required accuracy. In the other three regions, the path variations are not fundamental constraints. In Region III, "Acquisition" (Fig. 74b), the average time for cycle skip is smaller or of the order of the required acquisition time, so that no recursive tracking is accomplished, and the hybrid algorithm just achieves the global acquisition step. In Regions I and II, the phase, and thus the range increments, may be recursively tracked via the EKB, with a corresponding saving in the associated computational effort. But only in Region I, "Tracking within the Phase," curve SNR_I (Fig. 74a), does the hybrid algorithm performance attain the EKB accuracy. In Region II, "Tracking within the Geometry," curve SNR_{II} (Fig. 74a), the acquisition errors are larger than half the wavelength, so that the original offset in wavelengths acts as a bias at the output of the EKB and of the hybrid algorithm.

We do not want to accumulate range errors arising from cycle skipping phenomena; hence, a practical strategy for the hybrid algorithm in Regions I and II is indicated in Fig. 75. It has the following steps.

1. Global acquisition with the ML processor.

2. Initialize the linearized recursive structure with the estimates resulting from step 1.

3. Reacquisition every T_{skp} second with the nonlinear ML filter. At this stage the current EKB estimates and the associated variance errors are used to determine which parameter region of interest is to be scanned.

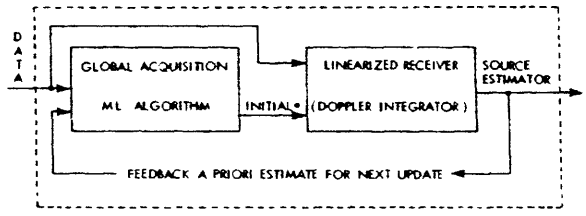

Fig. 75. Hybrid algorithm.

For Region III the hybrid algorithm reduces to the global acquisition step with the nonlinear ML algorithm.

VI. APPLICATIONS TO NAVIGATION AND POSITIONING

We shall now apply the passive tracking theory that we have developed to problems drawn from practical situations. We consider distinct underlying physical environments (underwater and free space), and illustrate the applicability of the theory to different geometric and statistical conditions.

For each application the fundamental phenomena are considered and cast in the framework of one of the passive tracking classes that we have considered. We choose a nominal range of values, based on physical considerations, and discuss the tradeoffs among the geometry, the statistical parameters, and the desirable accuracies.

First, we study two passive positioning problems, and then show how navigation can be cast in the context of passive tracking by exploiting its dualism to positioning. We discuss the significant novel issue of discretization arising in the latter application. Finally, we present Monte Carlo simulation results for the ML acquisition step of the hybrid algorithm.

6.1 AIR TRAFFIC CONTROL PRECISION LANDING

6.1.1 Problem Description

There is a need for improved accuracy in locating a plane in three-dimensional space as it approaches landing. The airport control tower must decide whether the plane is following a nominal path leading to a safe landing. If not, it declares a missed approach, and the plane is directed to circle the airport to prepare for a new approach. An important source of location error derives from altitude and speed measurements, which may be affected by large inaccuracies. Very high structures cannot be used on an airport surface, and active systems may produce unacceptable interference problems. We shall investigate the feasibility of a precision landing monitor involving passive measurements of aircraft position by ground sensors.

Figure 76 shows plan and side views for ideal landing geometry. At the left of both views is the runway, which is approached by the plane from the right. The aircraft

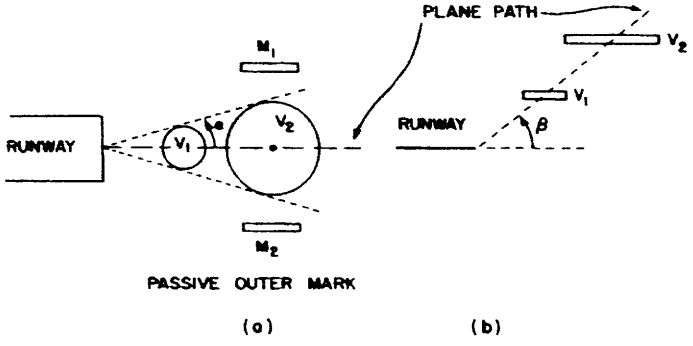

Fig. 76. Landing geometry: (a) plan view, (b) side view.

course may be given by an azimuth α and an elevation angle β, both usually between 3° and 6°. To make a safe landing, the plane must follow a certain nominal path, defined at different ranges by shrinking cylindrical volumes $V_1, V_2, \ldots$ (see circular sections on the plan view and vertical sections on the side view) that measure the allowable error in the aricraft position. At the threshold of the runway the plane's position should be known with a very small residual error.

It is assumed that there are passive antennas along the landing path monitoring narrow-band signals such as a single tone modulated by some coding for identification purposes transmitted from the aircraft. In order to avoid end-fire configurations, which lead to a considerable loss of performance, the passive structures are not placed at the end of the runway but are mounted along the approach path before the threshold of the runway, as indicated by outer marks M_1 and M_2 in Fig. 76a. The passive location problem is to position the plane with respect to these outriggers. In a particular application it may be necessary to have several pairs of marks, placed along the landing path.

Although in the half three-dimensional space a single passive receiving element, for example, M_1, locates the airplane only up to the intersection of a half cone and a half sphere (see Fig. 77), we shall consider only the simpler problem of a planar geometry.

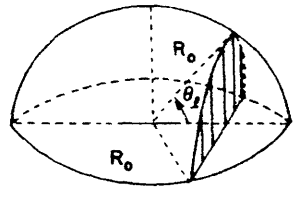

Fig. 77.
Three-dimensional ambiguity associated with single linear array.

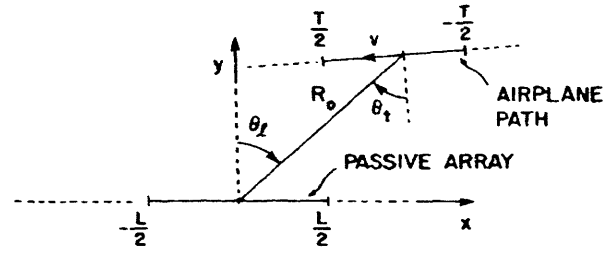

Fig. 78.
Precision landing geometry.

The idealized version of this precision landing problem is sketched in Fig. 78. The aircraft position and dynamics are parametrized by the range R_o, the speed v with respect to the ground, and the two viewing angles θ_ℓ and θ_t.

6.1.2 Hybrid Algorithm

a. Model

The hybrid algorithm achieves two main tasks, global acquisition, followed by local tracking and integration of the dynamics. For the global acquisition step we model the parameter vector $A = [R_o \; v \; \theta_t \; \theta_\ell]^T$ as nonrandom, unknown. For the linearized part of the hybrid algorithm, the dynamics is assumed to be described by a finite-dimensional system of stochastic differential equations (Eqs. 134).

Inside the plane, a crystal radiates a single tone at frequency f that is observed to be corrupted by additive, white, Gaussian noise. Because of the lack of synchronization, the phase of the received signal has a uniformly distributed random variable component. With these assumptions on the radiated signal and those on vector A, the global acquisition step of the hybrid algorithm fits the stationary array/moving source (SAMS) general model. Accordingly, we shall use the appropriate results on the ML receiver's structure and performance.

b. Nominal Parameter Values

For a jet plane in an airport traffic area, the altitude is below 10^4 ft, and the speed is required to be below maximum, taken here as approximately 200 knots. The speed measurement with respect to the ground may be in great error (depending on air circulation, wind speed, etc.); knowledge of the altitude may also be considerably inaccurate. In air traffic control the frequencies used are in the VHF or L-band. These considerations lead to the choice of numerical values indicated in Table 2.

Table 2. Numerical values for precision landing.

$f = 1$ GHz, $\lambda = 1$ ft
$R_o \lesssim 10^4$ ft (typically 6000 ft)
$v < 200$ knots = 337 ft/sec (typically 300 ft/sec)
$\theta_t = 15°$; $\theta_\ell \approx 15°$
$\Delta_M v \lesssim 80$ ft/sec
$\Delta_M \sin\theta_t = 1$
$\Delta_M R_o \lesssim \frac{R_o}{5}$
$L = 30$ ft, $T = 8$ sec (typical value), $X_t = .2$

In Table 2 we have used the notation in Sections II-IV. In particular, we recall that $\Delta_M A_i$ stands for the a priori uncertainty on the parameter A_i.

c. Review of ML Performance Results

For an aircraft speed of 300 ft/sec and an observation interval larger than 1 sec, the temporal baseline is much larger than the spatial baseline. That is,

$$\gamma = \frac{vT}{L} > 10 \gg 1.$$

In accordance with Section IV, the spatial/temporal ML receiver is practically decoupled,

with the reduced parameter $A_o = [R_o \; v \sin\theta_t]^T$ being estimated from the temporal diversity and the bearing $\sin\theta_\ell$ from the spatial diversity. The performance analysis reduces to the corresponding analysis for $SAMS_o$ and bearing estimation.

In order to concentrate on the basic aspects of the problem, we restrict the discussion mainly to tradeoffs and demands imposed by the range accuracy requirements on the geometric and statistical parameters. In particular, for the resulting signal-to-noise ratio values the attainable accuracies on the speed v, the bearing θ_ℓ, and the inclination θ_t are well within the desirable limits.

The mean-square performance at the output of the ML processing block of the hybrid algorithm (Eqs. 52) for parameter A_j is

$$\sigma^2_{tot_{A_j}} = \sigma^2_{loc_{A_j}} + \sigma^2_{gl_{A_j}} \tag{157a}$$

with

$$\sigma^2_{loc_{A_j}} = \sigma^2_{CR_{A_j}} [1 - Pr(\epsilon)] \tag{157b}$$

and

$$\sigma^2_{gl_{A_j}} = \frac{(\Delta_M A_j)^2}{6} Pr(\epsilon), \tag{157c}$$

where σ^2_{CR} is the Cramer-Rao bound, and Pr (ϵ) is the probability of a decision error. For the large signal energy-to-noise ratio case (Eq. 50)

$$Pr(\epsilon) \approx \frac{1}{E_r/N_o} \left[\ln M - \frac{1}{2M} + \gamma \right],$$

where M is the total number of grid cells in the first step of the ML algorithm.

For the decoupled SAMS problem, and whenever $X_t = vT/2R_o < 1$ we have the analytical expressions

$$M = \frac{V_\Omega}{k} (\det \mathcal{M})^{1/2} \simeq \frac{\Delta_M R_o \Delta_M v \Delta_M \sin\theta_t}{8} \left(\frac{2\pi}{\lambda}\right)^3 \frac{R_o^2}{v} \frac{2 \sin\theta_t \cos^2\theta_t X_t^6}{3 \times 5 \times \sqrt{105}} \tag{158a}$$

$$\sigma_{R_{o_{CR}}} = \text{Gain} \frac{\lambda}{2\pi} \frac{5\sqrt{7}}{\sin\theta_t \cos^2\theta_t} \frac{1}{X_t^3} \tag{158b}$$

$$\sigma_{v_{CR}} = \text{Gain} \frac{\lambda}{2\pi} \frac{5\sqrt{7}}{2} \frac{v}{R_o \sin\theta_t} \frac{1}{X_t^3} \tag{158c}$$

$$\sigma_{\sin\theta_{t_{CR}}} = \text{Gain} \frac{\lambda}{2\pi} \frac{5\sqrt{7}}{2} \frac{1}{R_o} \frac{1}{X_t^3}, \tag{158d}$$

where

$$\text{Gain} = \left[1 + \frac{N_o}{2P_n\sigma_b^2}\,\frac{1}{LT}\right]^{1/2} \frac{1}{\left(\frac{2P_n 2\sigma_b^2}{N_o}\,LT\right)^{1/2}}. \tag{158e}$$

For the high signal energy-to-noise ratio

$$\text{Gain} \approx \frac{1}{\sqrt{2\ \text{SNR}\ LT}}, \tag{158f}$$

where SNR represents the effective signal-to-noise ratio at the receiver site, i.e.,

$$\text{SNR} = \frac{P_n}{N_o}\,2\sigma_b^2. \tag{158g}$$

6.1.3 ML System Curves

Unless otherwise stated, in the subsequent set of figures, we assume the nominal values listed in Table 2.

Figure 79: Study of range accuracy vs SNR for two values of the geometric parameter $X_t = \frac{vT}{2R_o} = .1; .2$, and the a priori range uncertainty $\Delta_M R_o$ = 500 ft; 10^3 ft.

NOTE.

1. The curves for the local (Cramer-Rao bounds) $\sigma_{loc_{R_o}}$, global $\sigma_{gl_{R_o}}$, and total $\sigma_{tot_{R_o}}$ errors are linear, and thus reflect the modeling assumptions on the SNR dependence.

2. For $X_t = .1$ and $\Delta_M R_o \leq 10^3$ ft, the performance is well predicted by the Cramer-Rao bound.

3. For $X_t = .2$ and for $\Delta_M R_o$ in the range of values indicated, both the local and global errors contribute significantly to the mean-square performance (transitional region, referred to in sec. 3.4.4b).

4. We indicate in Fig. 79 the $\lambda/2$ threshold separating the tracking within the phase (Region I) from the tracking within the geometry (Region II) (see sec. 5.6). The tracking within the phase requires ~50 dB for $X_t = .2$, and 60 dB for $X_t = .1$.

Figure 80: Tradeoff between required SNR and actual aircraft passive receiver separation, for two typical accuracy requirements:

$\sigma_{R_o} = \frac{\lambda}{2}$ ft (Region I, upper curve)

= 50 ft (Region II, lower curve)

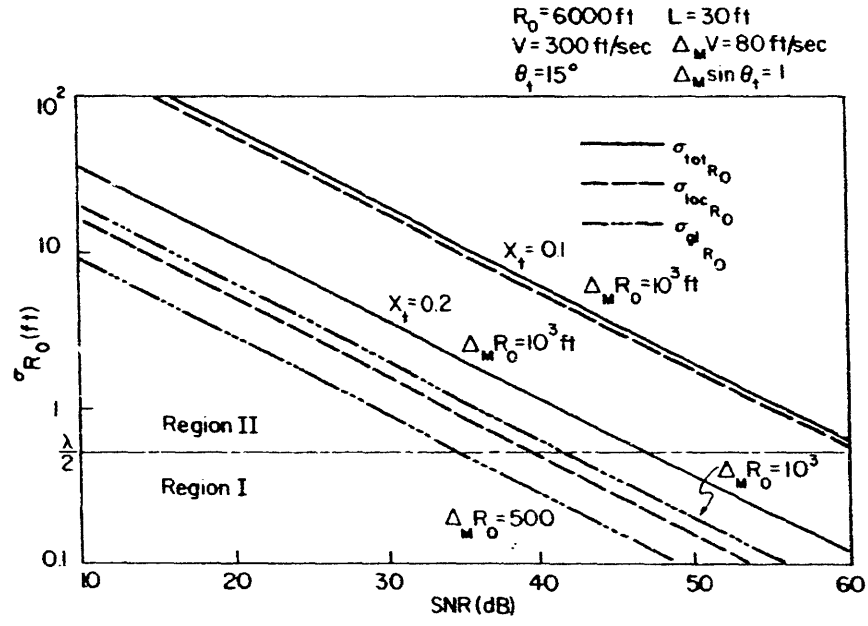

Fig. 79. Range accuracy vs SNR.

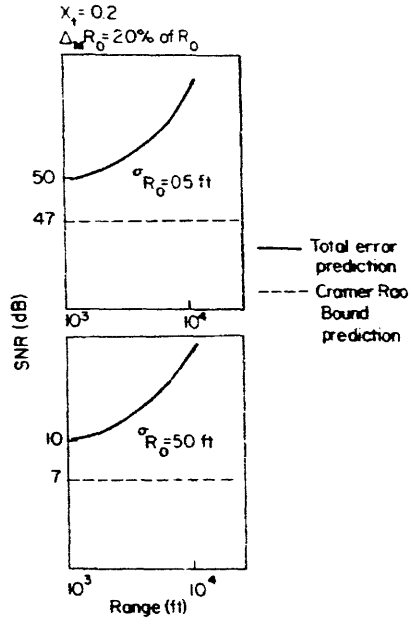

Fig. 80. SNR vs range.

NOTE.

1. The extra 40 dB required to go from Region II (tracking within geometry) to Region I (tracking within phase).

2. The additional SNR required with respect to the value predicted by the CR bound, which is due to the global errors induced by the large a priori uncertainty.

Figure 80 suggests an iterative global acquisition scheme, where several pairs of receiving elements are placed along the airplane landing path, with increasingly greater accuracy requirements. This strategy is in accordance with the vanishing sequence of uncertainty cylinders in Fig. 76. As the plane travels through, $\Delta_M R_o$ is reduced from one iteration to the next, with the net effect of diminishing $\sigma_{gl_{R_o}}$ and of the performance approaching the Cramer-Rao bounds.

Figure 81: Study of total acquisition time T_{acq} required by the ML receiver as the actual range changes for an SNR = 40 dB, and two accuracy requirements

$$\sigma_{R_o} = \frac{\lambda}{2} \text{ ft (Region I)}, \qquad \sigma_{R_o} = 50 \text{ ft (Region II)}.$$

NOTE.

1. The tracking within the geometry (lower curve) is linear, thereby reflecting the Cramer-Rao dependence on T_{acq}.

2. The tracking within phase (upper curve) changes from the Cramer-Rao dependence to a global dependence, with a sharper slope.

Since we cannot arbitrarily increase the acquisition interval, because of the limitations imposed by the path random perturbations (recall Fig. 73), Fig. 81 says that if the overall geometry does not lead to a Cramer-Rao dependence, it is unrealistic to expect to improve the estimation accuracy significantly by increasing the acquisition time; any significantly higher performance standard has to be met with enough SNR.

Figure 82: Speed accuracy vs SNR, for two different mean-square speed accuracies.

NOTE.

1. For slower avionics the total temporal baseline is shorter, and hence leads to a deterioration of performance (left end of both curves). This can be partly compensated by increasing T_{acq}, depending on the path perturbation.

2. The change in the curve slope as the speed increases from Cramer-Rao to global (ln v) dependence.

3. Even for σ_v = .1 ft/sec, which may be thought of as an upper bound on the desired speed accuracy in most practical situations, the necessary SNR is less than 50 dB, which is below the SNR demanded by the tracking within the phase acquisition mode.

6.1.4 Related Hybrid Algorithm Issues

In the context of the precision landing scheme, we consider the issues of sensitivity of the ML algorithm to path disturbances, linear performance of the extended

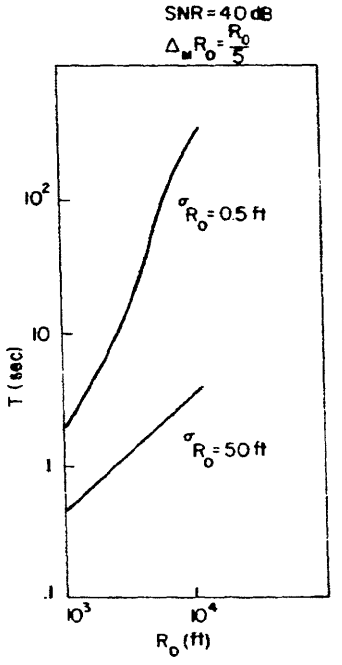

Fig. 81. Acquisition time vs range for two range accuracy requirements.

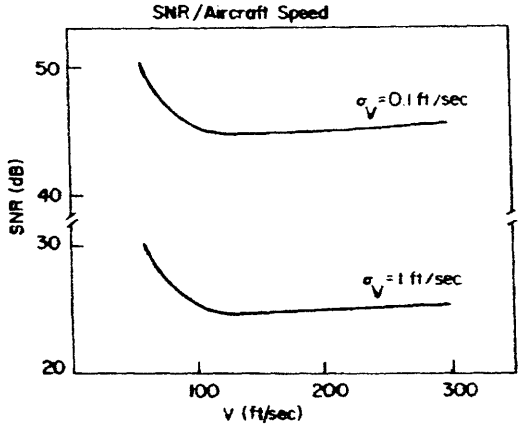

Fig. 82. Speed accuracy vs SNR.

Kalman-Bucy filter (EKB), and average time to skip a cycle.

a. Sensitivity of the ML Receiver to Path Perturbations

As a function of the acquisition time the mean-square range path variation is given by Eqs. 153:

$$\Sigma_R(T) \cong \frac{QT^3}{12}\left[1 + \frac{4^2 X_t^2}{30}\right].$$

Table 3 summarizes the values of $\Sigma_R^{1/2}$ for several Q and T, extracted from Fig. 72. It shows that the effects of the path variation may be a limiting factor on the final attainable range accuracy.

Table 3. Root-mean-square path variation.

$\Sigma_R^{1/2}$ (ft)	4	8	T_{acq} (sec)
4×10^{-3}	.15	.35	
4×10^{-2}	.46	1.3	
4×10^{-1}	1.45	4.12	
4	4.6	13	
20	10	30	
Q (ft^2/sec^3)			

b. Extended Kalman-Bucy Linearized Performance

The source parameter estimates returned by the ML processor initialize an extended Kalman-Bucy filter (EKB) as discussed in Section V. A simple calculation using Eqs. 138 and 139 shows that for the SNR values required by the global range acquisition, the EKB linearized mean-square performance is well within most actual practical requirements. In particular, for a low SNR (in terms of the precision landing application), SNR = 10 dB and Q = 1, from Eq. 139c, we have

$$P_{11} \cong \left(\frac{4Q}{H_1}\right)^{1/4} \cong .367 \text{ ft}^2$$

and for the steady-state range rate mean-square performance

$$P_{22} \cong \frac{2Q}{(4QH_1)^{1/4}} \approx .365^2 \text{ (ft/sec)}^2.$$

c. Average Time for Cycle Skipping

From Eqs. 148, we have

$$T_{skp} = \bar{J}_R^{-1} \approx \frac{\pi\sqrt{2}}{3} (QH_1)^{-1/4} \exp 2a.$$

For an SNR ≈ 10 dB, we obtain $a \approx 12 \times 10^3$ which leads to $\ln T_{skp} \approx 12 \times 10^3$. The probability of a cycle skip is extremely low ($\ln P_{skp} \approx -2a$).

6.1.5 Conclusion

The preceding analysis shows that the range global acquisition is the determining factor of the hybrid algorithm performance in the passive precision landing. There are two main sources of inaccuracy: errors incurred by the ML receiver, because of the additive noise disturbances, and errors induced by flight turbulence.

A practical solution to the passive precision landing, with two sets of passive outriggers, is illustrated in Fig. 83. Relatively early in the approach path we place the passive receiving element (Set 1) designed for tracking planes at 10^4 ft range with 300 ft/sec speed. Between Set 1 and Set 2 the plane is recursively tracked by the EKB. Set 2 is placed deeper in the landing path, and is designed for tracking planes at

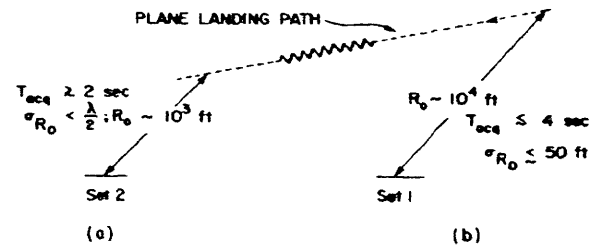

Fig. 83. Practical solution to passive landing. (a) Tracking within phase. (b) Tracking within geometry.

10^3 ft range, with nominal speed of 150 ft/sec. From then on the plane is tracked by the EKB. We assume that the passive receiver elements in each set have L = 50 ft, and the SNR level at the receiver site is SNR = 50 dB. The rest of the nominal values are listed in Table 2. With this choice of parameters, we study in Fig. 84 the attainable range accuracies for light ($\sqrt{Q_2} = g/10$) and medium ($\sqrt{Q_1} = g/2$) turbulence flight conditions, where $g \cong 32$ ft/sec^2 is the gravitational constant.

The upper curves in Fig. 84 correspond to the expected performance at Set 1 of the outriggers in Fig. 83, and the lower curves to Set 2. For the indicated turbulence conditions, the range acquisition accuracy depends on both the ML receiver performance $\sigma^{ML}_{tot_{R_o}}$ and the rms path variance, which limits the maximum acquisition time and attainable accuracy.

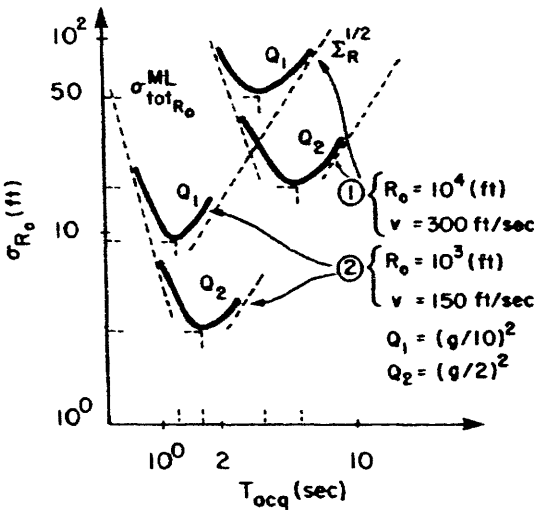

Fig. 84. Range accuracy for two different flight turbulence conditions vs acquisition time.

As a final remark we note that, by working with higher carrier frequencies, we can obtain improvement in range accuracy.

6.2 PASSIVE POSITIONING via UNDERWATER ACOUSTICS

We analyze the problem of locating an undersea platform in time and space by passive acoustic techniques. We utilize the radiated signature of the platform source to determine a collection of parameters, called a fix, from which the source/receiver geometry can be reconstructed.

We explore two different configurations of important practical implication. With one we study the issues involved with passive ranging by measuring curvature with a large array; with the other we concentrate on the tradeoffs and limitations of passive tracking of the modulations induced by the relative source/receiver dynamics on the temporal signal structure.

We assume a planar geometry and linear structures. As before, we work with the narrow-band assumption on the radiated signals (single tone). Generalizations of this model, to which the analysis can be straightforwardly extended, will be discussed in Section VII.

6.2.1 Underwater Acoustic Model

We consider two nominal geometries, sketched in Fig. 85. In Fig. 85a a large array observes the spatial diversity of the source signature, with the source considered practically at rest during each observation interval. In Fig. 85b a short array observes the temporal modulations induced on the signal structure and tracks the source motion. We model the platform relative dynamics as a nominal constant-speed linear path.

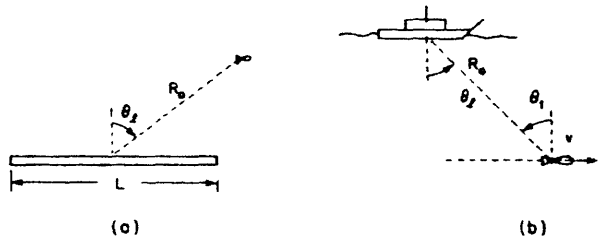

Fig. 85. Underwater acoustic geometry.
(a) SASS. (b) SAMS.

We study the applicability of the hybrid algorithm to both problems. For the global acquisition step we assume

H1: The problem of Fig. 85a fits the SASS model in Section II; $A_s = [R_o \sin \theta_\ell]^T$ is a nonrandom, unknown parameter vector. Furthermore, the source is at rest and the measurement noise is temporally white and spatially homogeneous.

H2: The problem of Fig. 85b fits the decoupled SAMS model in Section IV; $A = [A_o \vdots \sin \theta_\ell]^T$, with $A_o = [R_o \; v \sin \theta_t]^T$, is a nonrandom, unknown parameter vector. Also, the source follows a deterministic constant-speed linear path, and the measurement noise is temporally white and spatially homogeneous.

For the phase tracker of the hybrid algorithm we assume that the nominal dynamics is disturbed by random accelerations, as described by the finite-dimensional stochastic differential equations (134).

We explore subsequently the tradeoffs among the geometry, the statistical parameters, and the attainable accuracies for the global acquisition and the linearized tracking, the issues of global step sensitivity to path variations and of linearized Kalman-Bucy filter cycle skipping.

Because of the dualism of the two problems illustrated in Fig. 85, and in order to avoid repetition, we discuss both in parallel.

6.2.2 Nominal Parameter Values

Table 4 summarizes typical values for the several parameters. Unless otherwise stated these are the assumed conditions. We recall the notation $\Delta_M A_i = A_{i_{max}} - A_{i_{min}} =$ the a priori region of uncertainty for parameter A_i in the parameter space Ω.

For the values in the right column of Table 4 the ratio between the spatial and the temporal geometric parameters is $\gamma = \frac{X_\ell}{X_t} = \frac{L}{vT} = \frac{1}{48} \ll 1$, and according to the analysis in Section IV, SAMS decouples in $SAMS_o$ and becomes a bearing angle estimation problem. In the sequel we concentrate on the novel $SAMS_o$ aspects, since the passive bearing estimation has been widely documented.

Table 4. Nominal values for passive acoustic positioning.

$\lambda = 50$ ft	$\Delta_M R_o = 2 \times R_o = 12 \times 10^4$ ft
$\sigma_b^2 = 1$	$\Delta_M \theta_\ell = 5°$
$R_o = 6 \times 10^4$ ft	
SASS	SAMS
$\theta_\ell = 0°$; $T = 250$ sec	$\theta_\ell = 0°$; $\theta_t = 15°$
$L = 12 \times 10^3$ ft; $X_\ell = \frac{L}{2R_o} = .1$	$v = 30$ ft/sec; $\Delta_M v = 3$ ft/sec
	$L = 250$ ft; $T = 400$ sec; $X_t = \frac{vT}{2R_o} = .1$

6.2.3 Review of ML Mean-Square Performance

In the following equations subscripts s and o refer to SASS and SAMS$_o$, respectively. The global acquisition ML mean-square performance (Eq. 52a) is given by

$$\sigma^2_{tot_{A_j}} \cong \sigma^2_{loc_{A_j}} + \sigma^2_{gl_{A_j}}, \tag{159}$$

where $\sigma^2_{loc_{A_j}}$, $\sigma^2_{gl_{A_j}}$, and Pr (ϵ) have been reviewed by Eqs. 157. For SASS we recall from Section II the Taylor's series results:

$$M_s \approx \frac{V_{\Omega_s}}{k_s} (\det \mathcal{M}_s)^{1/2} \cong \frac{(\Delta_M R_o)(\Delta_M \sin\theta)}{4} \left(\frac{2\pi}{\lambda}\right)^2 \frac{R_o \cos^2\theta\, X^3}{3\sqrt{15}} \tag{160a}$$

$$\sigma_{R_{o_{CR_s}}} \approx G_s^{-1/2} \frac{3\sqrt{5}}{\cos^2\theta\, X^2} \tag{160b}$$

$$\sigma_{\sin\theta_{CR_s}} \approx G_s^{-1/2} \frac{\sqrt{3}}{R_o X} \tag{160c}$$

$$G_s^{-1/2} = \left[\frac{2\bar{E}_r}{N_o} \frac{\bar{E}_r}{N_o + \bar{E}_r} \left(\frac{2\pi}{\lambda}\right)^2\right]^{-1/2} \approx \left[\frac{2\bar{E}_r}{N_o} \left(\frac{2\pi}{\lambda}\right)^2\right]^{-1/2} \tag{160d}$$

$$\bar{E}_r = (SNR)\left(2\sigma_b^2\right) LT, \tag{160e}$$

where SNR represents the signal-to-noise ratio at the receiver site.

For $SAMS_o$, the corresponding results have been cited in Eqs. 158.

REMARK.

Since the discussion here is intended as an exploration of the fundamental design aspects, we concentrate on the range. With respect to the other parameters, the reader is referred to the performance curves in Sections II and III where they are drawn for a 50 ft wavelength. As before, the higher SNR demands are placed upon the system by the range accuracy requirements.

6.2.4 ML System Curves

We now present several system curves for the global acquisition step of the hybrid algorithm. First, we discuss the $SAMS_o$ aspects of the problem illustrated in Fig. 85b, and then the SASS problem of Fig. 85a. The sensitivity issues of $SAMS_o$ to path variations will be dealt with in section 6.2.6.

$SAMS_o$

Figure 86: Mean-square range performance vs available SNR at the receiver site, for several regions of a priori indetermination $\Delta_M R_o = R_o (=6\times 10^4$ ft); $2R_o$; $5R_o$; $10R_o$; $20R_o$ $(=12 \times 10^5$ ft), which are indicated as parameters on the curves.

NOTE.

1. We have only one curve for $\sigma^2_{loc_{R_o}}$, since the Cramer-Rao bound depends only on the actual source/receiver separation but not on the a priori length, $\Delta_M R_o$, of the associated region of indetermination.

2. We observe that for an a priori indetermination, $\Delta_M R_o \lesssim 2R_o = 12 \times 10^4$ ft, the global errors $\sigma^2_{gl_{R_o}}$ are negligible compared with the $\sigma^2_{loc_{R_o}}$, and the Cramer-Rao bound predicts well the system performance (local region). For $\Delta_M R_o \gtrsim 20R_o = 12 \times 10^5$ ft exactly the opposite is true (global region). For 12×10^4 ft $= 2R_o \lesssim \Delta_M R_o \lesssim 20R_o = 12\times 10^5$ ft both errors affect significantly the total performance (transitional region). As we have observed, this transitional region is determined by the problem geometry $(X_t, \Delta_M R_o)$ but is independent of the statistical parameters.

3. The tracking within the phase requires SNR above 60 dB which is not available in most practical situations. This can be improved either by enlarging X_t (increasing the observation interval) or having a larger receiving array (larger array gain).

Figure 87: Mean-square range performance vs the length of the range region $\Delta_M R_o$ of a priori uncertainty. There are two sets, each of which has three curves. The three upper curves correspond to $X_t = \frac{vT}{2R_o} = .1$ and the three lower curves to $X_t = .25$. For each value of X_t we considered three distinct SNR values: SNR = 1 (0 dB); 10 (10 dB); 100 (20 dB). The curves are essentially translations of each other. The σ^2_{loc} are

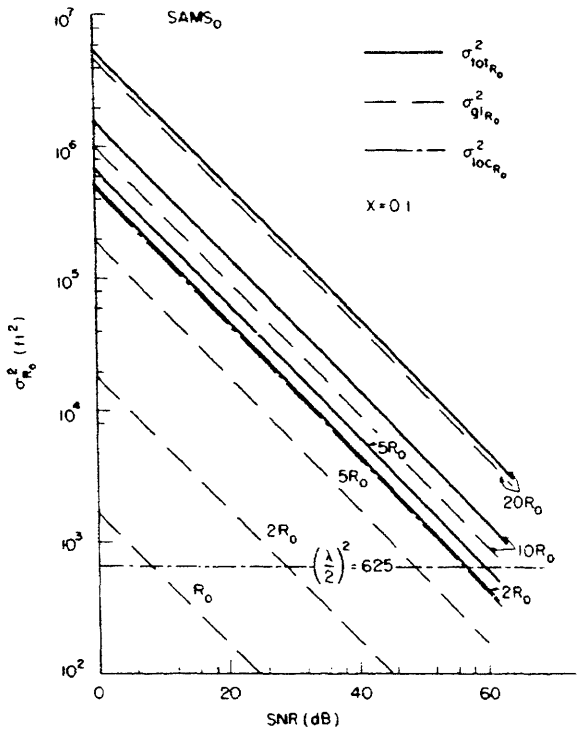

Fig. 86. Mean-square performance vs SNR (SAMS$_0$).

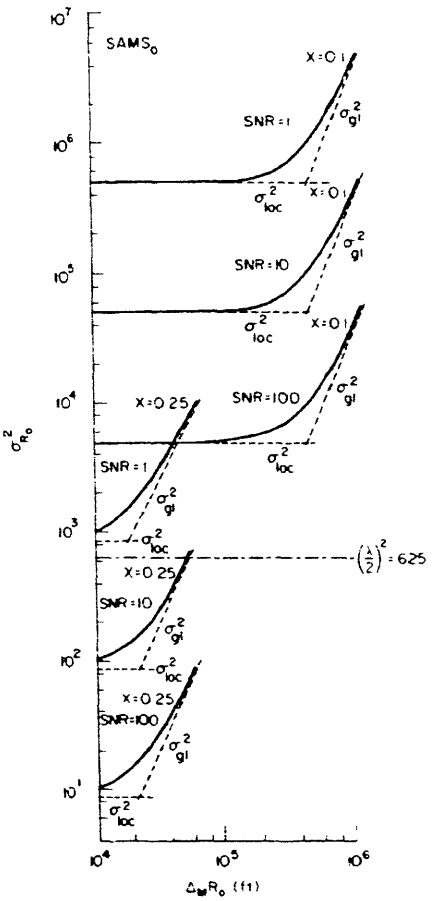

Fig. 87. Mean-square performance vs a priori range uncertainty.

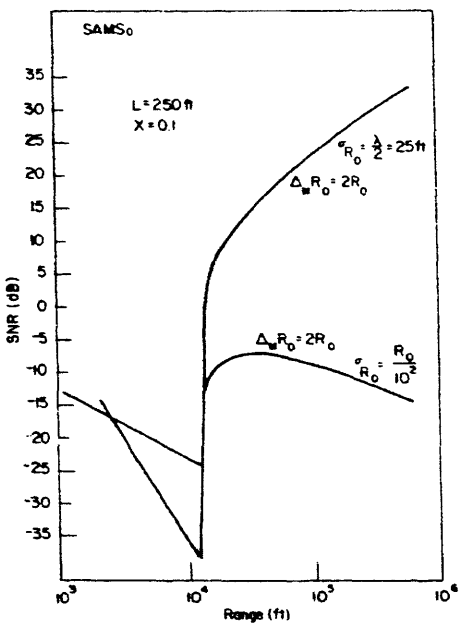

Fig. 88. SNR vs range.

practically horizontal (independent of $\Delta_M R_o$). The transitional region, as we have noted, is independent of SNR but does depend on the diversity geometric parameter X.

Figure 88: SNR vs actual range of operation, for two values of the desired rms performance:

$$\sigma_{R_o} = \frac{\lambda}{2} = 25 \text{ ft (tracking within phase)}$$

$$\sigma_{R_o} = \frac{R_o}{10} \text{ ft (tracking within geometry).}$$

NOTE.

1. The sharp threshold exhibited by both curves at $R_o = R_{o_{th}} = 12.5 \times 10^3$ ft, which is practically determined by the geometric parameter $X_t = .1$ and the a priori uncertainty $\Delta_M R_o = 2R_o$. This threshold corresponds to the sudden transition from a local to a global region. For $R_o < R_{o_{th}}$, $\Delta_M R_o$ is small, and the main lobe of the ambiguity function structure spreads all over the region of interest in the parameter space Ω. As R_o increases, so does $\Delta_M R_o$, and at $R_{o_{th}}$ we have M = 2, and hence a nonzero probability of decision errors, which coupled to $\Delta_M R_o$ leads to a nonzero, large $\sigma_{gl_{R_o}}$.

2. Because the curves are drawn for a constant diversity geometric parameter $X_t = \frac{vT}{2R_o} = .1$, for larger range the acquisition time is increased, and as a consequence the curves decrease at their right ends.

SASS

Figure 89: $\sigma^2_{R_o}$ vs SNR. The discussion is similar to that for Fig. 86. Note that the transitional region occurs for $\frac{R_o}{5} \lesssim \Delta_M R_o \lesssim 2R_o$.

Figure 90: $\sigma^2_{R_o}$ as a function of $\Delta_M R_o$ for two values of the diversity parameter $X_\ell = .1, .25$, and for two values of SNR. The discussion follows that for Fig. 87. Note that the curves shown are below the $\lambda/2$ threshold line. In comparison with Fig. 86, we see that for equivalent SASS and $SAMS_o$ geometry, the same range performance requires an excess of approximately 40 dB in $SAMS_o$. The alternative for an equivalent performance at the same SNR levels is to increase the $SAMS_o$ diversity parameter X_t to approximately three times the SASS diversity parameter X_ℓ. In practice, however, there exists an upper bound T_{max} on the acquisition time because of path variations, as we shall see in section 6.2.6.

Figure 91: SNR vs actual range for two different range accuracy requirements $\sigma_{R_o} = \frac{\lambda}{2}$ ft and $\sigma_{R_o} = \frac{R_o}{10^2}$ ft. The discussion is similar to that for Fig. 88. Note, however, the

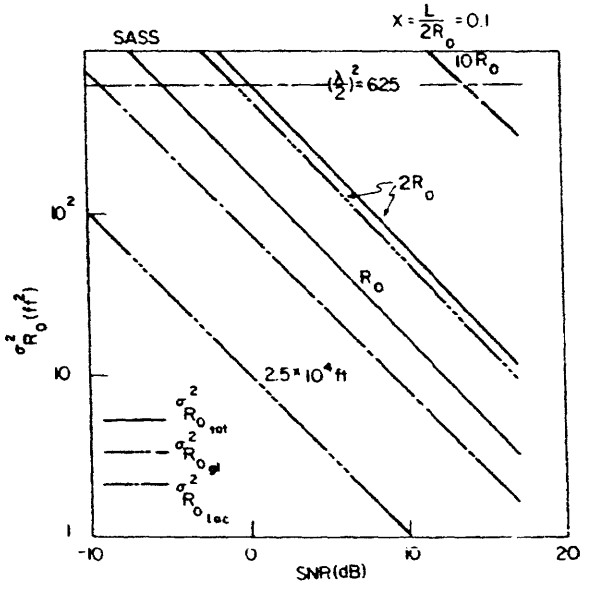

Fig. 89. Range performance vs SNR.

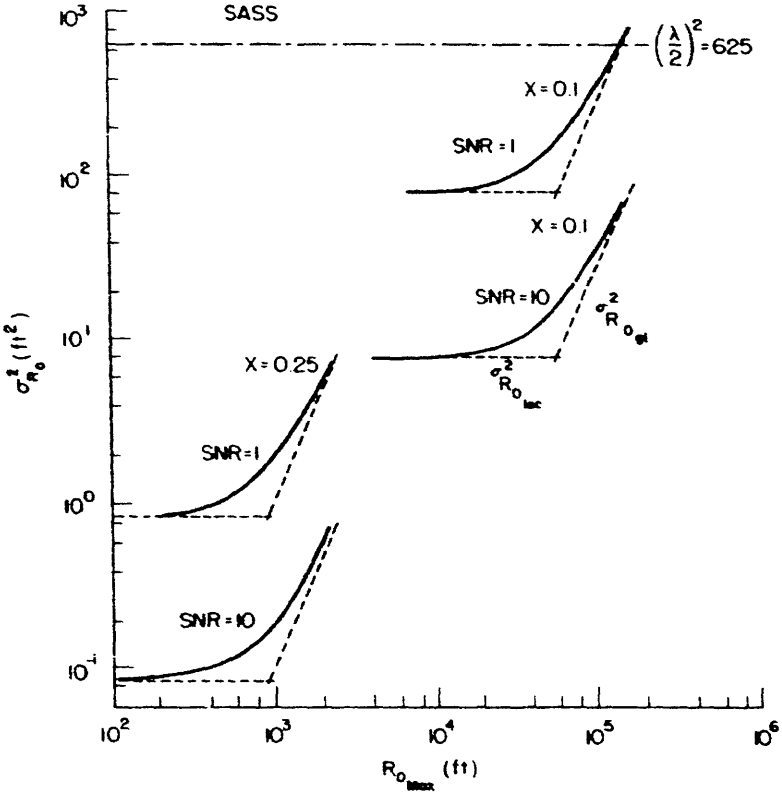

Fig. 90. Range performance vs a priori range uncertainty.

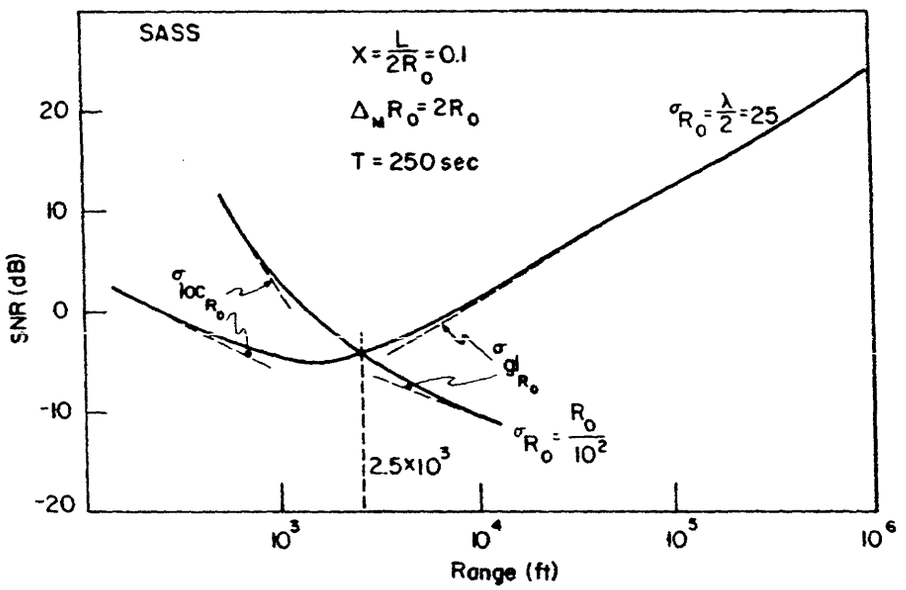

Fig. 91. SNR vs range.

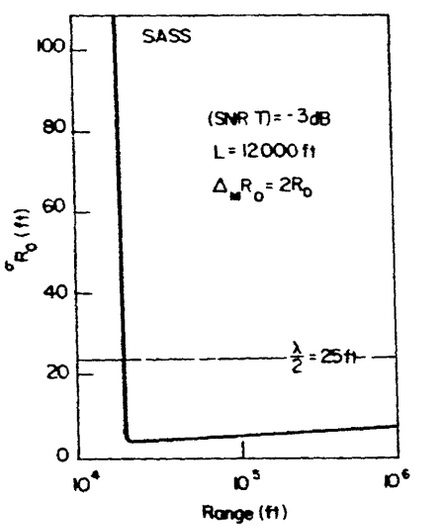

Fig. 92. Range performance vs range.

much smoother transition.

Figure 92: We explore the performance deterioration experienced by a fixed system ($L = 12 \times 10^3$ ft) as the actual range increases. We adjust the observation interval so that SNR T = −3 dB = constant. After a sudden transition from a global region (left end of the curve) to a local one (right part), the receiver's range performance changes very slowly over a wide range interval. It suggests, as a practical rule, that we over-dimension the system slightly, by increasing the SNR level at the receiver (e.g., with improved sensor quality), to achieve the required accuracy at the nominal source/receiver separation. For more distant platforms the system accuracy can be readjusted by augmenting the duration of the observation interval.

6.2.5 Linearized Performance of the Extended Kalman-Bucy Filter

The linearized block (phase tracker) of the hybrid algorithm has been analyzed and simulated in the context of undersea acoustics,[20] and the results have been reported.[21] The motions are modeled by a finite-dimensional, stochastic, dynamical system (see Eqs. 134). For representative runs, see Fig. 69. We limit ourselves here to a brief discussion of the EKB linearized range and range rate performance. For $\lambda = 50$ ft and $L = 250$ ft, in the steady state, from Eqs. 139d and 139e, we obtain

$$P_{11} \approx \frac{1}{2\ \mathrm{SNR}} (Q\ \mathrm{SNR})^{1/4}$$

$$P_{22} \approx \frac{Q}{(Q\ \mathrm{SNR})^{1/4}}.$$

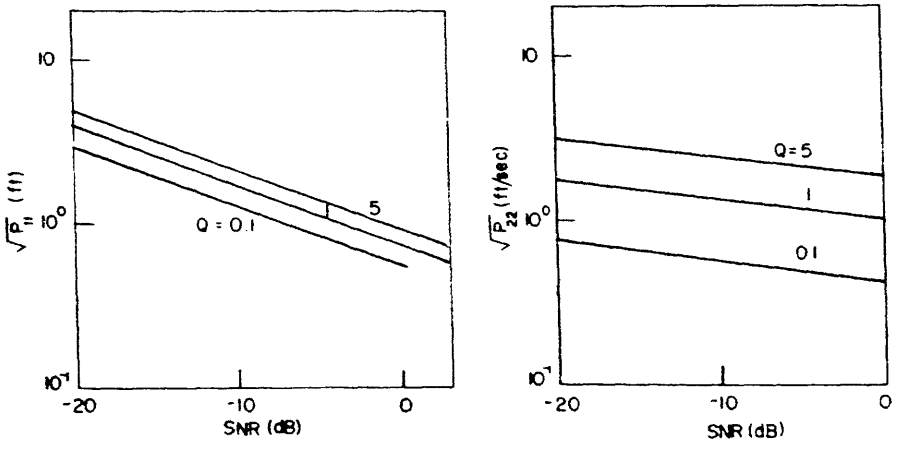

Fig. 93. EKB mean-square performance vs SNR.

Figure 93: We show the expected EKB steady-state linearized mean-square performance as a function of SNR for several values of Q. Comparing these curves with the range performance curves for the ML acquisition step, we conclude that for underwater

acoustic tracking the linearized performance of the EKB filter is well within the required accuracy.

6.2.6 Root-Mean-Square Variation and Cycle Skipping

The EKB loop cycle skipping phenomena and the effects of the rms phase variations on the ML receiver may introduce important limitations on the hybrid algorithm performance.

The average time for the loop to skip a cycle, from Eqs. 148, is

$$T_{skp} \approx \bar{J}_R^{-1} \approx \frac{32\pi^2}{3}\left(\frac{SNR}{Q}\right)^{1/2} I_o(a)^2 \approx \frac{\pi}{3}\frac{\exp 2a}{\sqrt{Q\ SNR}}.$$

As the driving noise power level Q increases, the larger loop bandwidth required for tracking the dynamics causes the loop to skip a cycle at a higher rate. For large values of SNR, T_{skp} grows exponentially. But for SNR equal to or smaller than 0 dB the cycle skipping phenomena may cause the loop behavior to depart significantly from the linearized prediction.

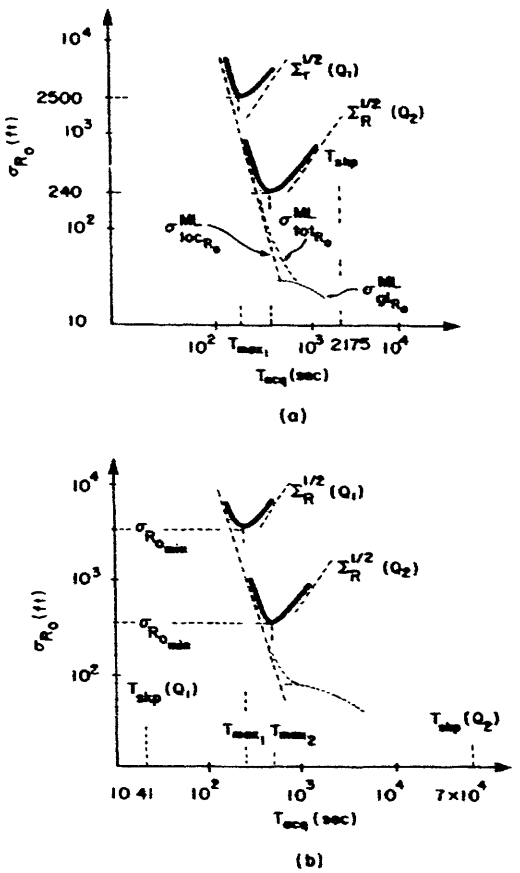

Fig. 94.
Underwater acoustic positioning modes of behavior. $Q_1 = 4$, $Q_2 = 4 \times 10^{-3}$ (ft^2/sec^3).

The rms range phase variation, given by Eq. 153b, is

$$\Sigma_R^{1/2} \simeq \left(\frac{QT^3}{12}\right)^{1/2}.$$

In Fig. 94 we show the effects of the path variations on σ_{R_o} for two different random acceleration levels. In Fig. 94a SNR = 0 dB is assumed, and in Fig. 91b, SNR = −10 dB. The other nominal parameter values are indicated in Table 4. For small acquisition times T_{acq}, the contribution of $\Sigma_R^{1/2}$ is negligible. But for larger T_{acq} it may become the limiting factor on the attainable accuracy, and hence determine the maximum acquisition time T_{max} and the maximum range performance $\sigma_{R_{o_{min}}}$.

We have indicated the corresponding T_{skp} values in both parts of Fig. 94. For an undisturbed path ($Q_2 = 4 \times 10^{-3}$ ft^2/sec^3) cycle skipping phenomena is not a

problem, even for SNR = -10 dB. For larger $Q_1 = 4\ ft^2/sec^3$, T_{skp} may significantly determine the hybrid algorithm performance. In Fig. 94a for SNR = 0 dB, $Q = Q_1$ we have $T_{skp} \approx 32$ min, $T_{max} \approx 3$ min and the EKB has to be reacquired every half hour. In Fig. 94b for SNR = -10 dB, $Q = Q_1$ we have $T_{skp} = 21$ sec, $T_{max} \cong 4$ min and the hybrid algorithm is in the acquisition mode, with no tracking by the EKB possible for a practically significant time interval.

6.2.7 Summary

We have analyzed the hybrid algorithm mean-square performance and operation modes for the passive underwater acoustic position problem for both SASS and $SAMS_o$ configurations.

Because of the small geometry diversity that is synthesized, the problems usually fall near the boundary of transition and threshold regions where the predicted performance changes from a local to a global bound; because of the low SNR available at the receiver site and the path disturbances, the rms range phase variation and the cycle skipping phenomena determine significantly the performance and the behavior mode of the hybrid algorithm.

6.3 PRECISION NAVIGATION via SATELLITES AND OTHER NAVIGATIONAL AIDS

Many radio navigation aids serving a wide variety of purposes are available, for example, for guidance of ships on the high seas, surveillance of intercontinental commercial air traffic, radio tracking of ocean drifting buoys or of free-sounding balloons, location of speeding trucks on highways, etc.

These navigational aids (navaids) are based on measurement of frequency Doppler shifts and/or of travel time delays of signals transmitted from a station (passive navigation), or signals initiated or transponded at the user's platform (active navigation). The measurements are converted to platform geometric parameters (e.g., range) and coupled to the known geographical location of the navigational station to provide for a platform fix.

Basically, we group the navigational systems into earth- and satellite-based. Earth-based systems include the low- and very low-frequency navaids. Usually, these are chains of a centrally located master, and several slave transmitters, such as Omega, Loran C, or Decca. Surveys of these have been made.[8,48]

The only satellite-based system now available for general use is the Navy Navigational Satellite System (NNSS) also referred to as TRANSIT.[49,50] Several programs have been implemented for restricted purposes and integrated into specific missions, such as EOLE (monitoring meteorological collecting data balloons),[6] TWERLE (Tropical Wind, Energy Conversion and Reference Level Experiment),[6] etc. Numerous experiments have been proposed for navigation, collision avoidance, and traffic control, such as the NASA Position Location and Communication Equipment (PLACE), the Department

of Transportation's (DOT) Advanced Air Traffic Management Systems concepts, the Federal Aeronautics Administration (FAA) Astro-Dabs, the DOT/FAA Aerosat experiment, etc.[10]

Two important desirable characteristics are accuracy and global coverage. The coverage of Omega with eight sparsely located stations is worldwide, and its accuracy for ship navigation is 1 mile at 1500 mile range. Decca is a coastal navaid with 200-300 meter accuracy at 100 mile range.[8] The satellites represent the trend for future navigation systems, since they may provide global worldwide coverage with very significant improvement in accuracy.

In the sequel we concentrate on satellites. They are either orbiting (low altitude, 1000 km for NNSS, or medium altitude, up to 20×10^3 km) or geostationary (at $\sim 40 \times 10^3$ km). Table 5 summarizes pertinent data.

Table 5. Navigational satellite data.

Satellite	Altitude (km)	Transit Time	Coverage	Carrier Frequency (MHz)
Orbiting	Low $\sim 10^3$ - 7000	15 min	Global	VHF (150, 400)
Orbiting	Medium $\sim 20 \times 10^3$	2.5-4 h	Global	VHF, L-band
Geostationary	High $\sim 40 \times 10^3$	Permanent	$\frac{1}{3}$ Earth	VHF, L-band

First, we shall discuss orbiting satellites, applying straightforwardly the theory that we have developed. Then we shall discuss navigation with geostationary (also called geosynchronous) satellites, after we extend the continuous space passive tracking results of Sections II and IV to the case of a discrete space domain.

6.3.1 Orbiting Satellites

Figure 95a illustrates a navigation configuration with an orbiting satellite. The moving platform monitors the signals radiated by the satellite as it passes overhead. Figure 95b casts this navigation problem in the $SAMS_o$ context of Section III.

The identifiable source/receiver parameter vector is $[R_o \; v \; \sin\theta_t]^T$, where

$$v = \{v_s^2 + v_p^2 + 2v_s v_p \cos(\theta_s - \theta_p)\}^{1/2}$$

$$\tan\theta_t = \frac{v_s \sin\theta_s + v_p \sin\theta_p}{v_s \cos\theta_s + v_p \cos\theta_p}.$$

The satellite speed v_s is usually predicted accurately and radioed to the passive user, and the satellite bearing $\sin\theta_s$ can be measured by auxiliary means, for example,

optically, so that from these equations the platform speed v_p and bearing $\sin\theta_p$ are determined. In any case, we work with the parameter vector $A = [R_o \; v \sin\theta_t]^T$.

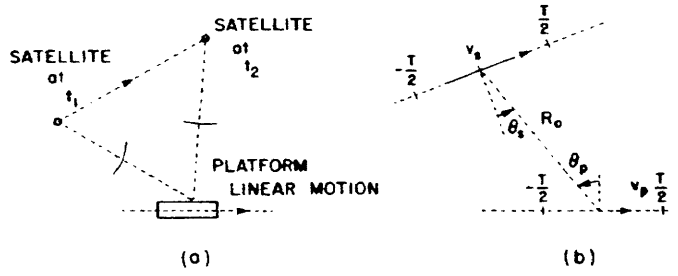

Fig. 95. (a) Moving platform orbiting satellite configuration.
(b) $SAMS_o$ navigation problem.

To illustrate the application of the results of Sections III and V, we consider a ship navigating the high seas. A reasonable choice of parameters is v = 7 km/sec ($\approx v_s$, since $v_p \ll v_s$), R_o = 5000 km, θ_t = 30°, SNR = 3 dB (at the user's site), L = 250 ft, f = 400 MHz ($\lambda \cong 2.46$ ft). We also assume a path disturbance level Q = 1 ft^2/sec^3, and an a priori range uncertainty of approximately 20 miles. Figure 96 shows the range

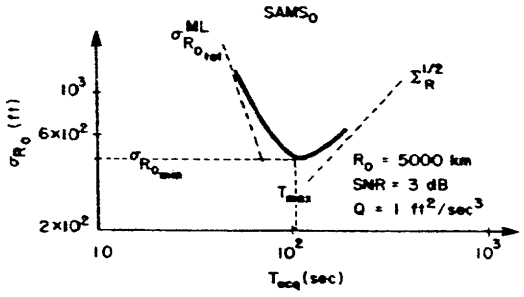

Fig. 96. Range accuracy vs acquisition time for ship navigation satellite problem.

accuracy as a function of the acquisition time. For smaller T_{acq} the performance is essentially predicted by the Cramer-Rao bound (Eq. 69a):

$$\sigma_{R_{o_{tot}}} \approx \sigma_{R_{o_{loc}}} = \frac{1}{(2\,SNR\,LT)^{1/2}} \frac{5\sqrt{7}}{\sin\theta_t \cos^2\theta_t} \frac{\lambda}{2\pi} \frac{1}{X^3}.$$

For large T_{acq} the rms range phase variations dominate (Eq. 153b):

$$\Sigma_R^{1/2} \approx \left(\frac{QT^3}{12}\right)^{1/2}.$$

For the maximum T_{acq}, $T_{max} \approx 120$ sec the minimum rms error $\sigma_{R_o} \approx 450$ ft, which

is below the .1-.5 mile accuracy set as a goal for merchant ship high seas navigation in the post-1985 year period.[10]

For this choice of parameters the EKB exhibits a linearized performance well within the required accuracy, and leads to a very large value for T_{skp}. We conclude that the basic limitations are imposed by the global acquisition step.

6.3.2 Geostationary Satellites

Figure 97 illustrates a navigational problem with geosynchronous satellites. We assume that the passive user recognizes the signals originating at N different satellites (by coding a common subcarrier on distinct carrier frequencies). The navigational problem with N spatial point sources is then the dual of a positioning problem with N sensors. Accordingly, we do not make a distinction and we keep the positioning nomenclature (SASS, SAMS, etc.).

The satellite constellation may be viewed as an ensemble resulting from the spatial sampling of a continuous source. Two questions arise as to the applicability of the passive tracking theory developed previously:

1. What are the effects of sampling on the sidelobe structure of the ambiguity function?

2. How does discretization affect the ML receiver resolution, i.e., the mean-square-error performance?

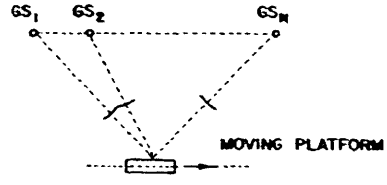

Fig. 97.
Moving Platform/Geostationary satellites.

Because of the modulation nonlinearities of passive tracking, the answers to both questions are nontrivial. We consider them briefly for a stationary array/stationary source configuration, and for a second-order approximation (Fresnel zone) to the range phase function.

a. Discrete Ambiguity Function in the Fresnel Zone

Figure 98 illustrates a centered geometry with an array of N equally spaced elements. The range phase difference for the Fresnel zone is

$$\frac{2\pi}{\lambda}\left[\Delta R(t,\ell,A,\bar{A})-\Delta R_o\right] \cong \frac{2\pi}{\lambda}\left[-(\Delta \sin\theta)\,\ell + \Delta\left(\frac{\cos^2\theta}{2R_o}\right)\ell^2\right] \tag{161a}$$

$$\triangleq k_1\ell + k_2\ell^2. \tag{161b}$$

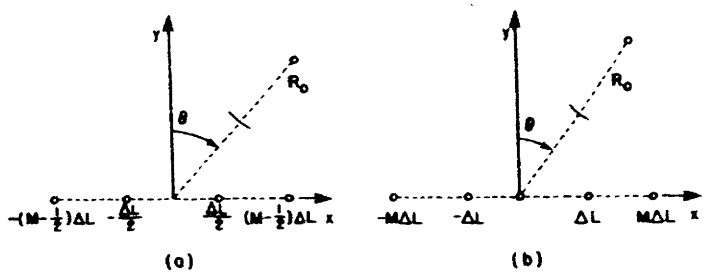

Fig. 98. Discrete SASS geometry. (a) N = 2M. (b) N = 2M + 1.

For the equally spaced geometries of Fig. 98, the discrete generalized ambiguity function (DGAF)

$$\phi(k_1, k_2) = \left| \frac{1}{N} \sum_{i=1}^{N} \exp j\left(k_1 \ell_i + k_2 \ell_i^2\right) \right|^2 \tag{162a}$$

becomes

1. N = 2M + 1 = odd

$$\phi(k_1, k_2) = \frac{1}{N^2} \left\{ N + \frac{2 \cos\left[(M+1)k_1 \Delta L\right] \sin\left[M k_1 \Delta L\right]}{\sin\left(k_1 \Delta L\right)} \right.$$

$$+ 4 \sum_{1}^{M} \cos\left(k_1 m \Delta L\right) \cos\left(k_2 m^2 \Delta L^2\right)$$

$$\left. + 8 \sum_{m>n}^{M} \sum_{n=1}^{M-1} \cos\left(k_1 m \Delta L\right) \cos\left(k_1 n \Delta L\right) \cos\left[k_2 (m^2 - n^2)\, \Delta L^2\right] \right\}. \tag{162b}$$

2. N = 2M = even

$$\phi(k_1, k_2) = \left(\frac{2}{N}\right)^2 \left\{ \sum_{1}^{M} \cos^2\left[k_1 \left(m - \frac{1}{2}\right) \Delta L\right] \right.$$

$$+ 2 \sum_{m>n}^{M} \sum_{n=1}^{M-1} \cos\left[k_1 \left(m - \frac{1}{2}\right) \Delta L\right] \cos\left[k_1 \left(n - \frac{1}{2}\right) \Delta L\right]$$

$$\left. \cos\left[k_2 \Delta L^2 ((m^2 - m) - (n^2 - n))\right] \right\}. \tag{162c}$$

We see that for

$$k_{1_s} = m_1 \frac{2\pi}{\Delta L} \qquad \left(\Delta \sin\theta = -\Delta \dot{R}_o = m_1 \frac{\lambda}{\Delta L}\right) \tag{163a}$$

$$k_{2_s} = m_2 \frac{2\pi}{\Delta L^2}, \quad \text{for N odd} \left(\Delta\vec{\vec{R}}_o = m_2 \frac{2\lambda}{\Delta L^2}\right) \tag{163b}$$

$$= m_2 \frac{\pi}{\Delta L^2}, \quad \text{for N even} \left(\Delta\vec{\vec{R}}_o = m_2 \frac{\lambda}{\Delta L^2}\right) \tag{163c}$$

the discrete ambiguity is

$$\phi(k_1, k_2) = 1. \tag{163d}$$

In the (k_1, k_2) space, let

$$\Omega_1 = \left[-\frac{\pi}{\Delta L}, \frac{\pi}{\Delta L}\right] \times \left[-\frac{\pi}{\Delta L^2}, \frac{\pi}{\Delta L^2}\right], \quad \text{for N odd} \tag{164a}$$

$$= \left[-\frac{\pi}{\Delta L}, \frac{\pi}{\Delta L}\right] \times \left[-\frac{\pi}{2\Delta L^2}, \frac{\pi}{2\Delta L^2}\right], \quad \text{for N even.} \tag{164b}$$

The structure of the DGAF within Ω_1, referred to as primary cell, depends on the sampling rate and, as in the linear theory, important distortion may result. For an oversampled array

$$\frac{\Delta L}{\lambda} \ll 1, \quad \frac{\Delta L^2}{\lambda} \ll 1 \tag{165a}$$

we expect that the DGAF approaches the continuous GAF. The intuitive reason is reminiscent of the method of stationary phase, since a large number of sinusoidals with large and slightly different frequencies tends to cancel their mutual effects. In Ω_1 the DGAF will present a quadratic main lobe and a negligible secondary structure. In Fig. 99 (see Van Trees[24] for the Siebert plot) the dashed areas indicate the regions where the DGAF is significant (main lobe and its equally spaced repetitions), and the unshaded areas indicate where the DGAF is negligible (secondary structure).

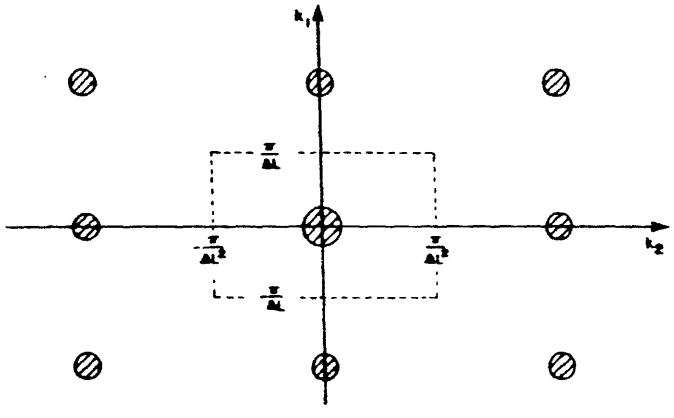

Fig. 99. Discrete ambiguity function for an oversampled array.

For an undersampled array

$$\frac{\Delta L}{\lambda} \gg 1 \quad \text{or} \quad \frac{\Delta L^2}{\lambda} \gg 1 \tag{165b}$$

aliasing results, and the DGAF exhibits important secondary structure within Ω_1, and hence a detailed study is required for each application.

b. Discrete Mean-Square (Local) Performance in the Fresnel Zone

For the Rayleigh signal model the discrete mean-square spread matrix (DMSSM) $\mathcal{M}_d$ is obtained by substituting sums for integrals in Eqs. B.3 and B.4 in Appendix B.

We define the n^{th} geometric moment associated with the linear array of N sensors as

$$L_n = \frac{1}{N} \sum_{i=1}^{N} \ell_i^n, \tag{166}$$

where ℓ_i is the i^{th} array element location.

In the Fresnel zone and for a centered geometry

$$\mathcal{M}_d = \left(\frac{2\pi}{\lambda}\right)^2 \begin{bmatrix} \dfrac{\cos^4\theta}{4R_o^4}\left(L_4 - L_2^2\right) & 0 \\ 0 & L_2 \end{bmatrix} \tag{167}$$

The Cramer-Rao bounds are obtained by normalizing the elements of $\mathcal{M}_d^{-1}$ by

$$G_d^{-1} = \frac{1}{2\bar{E}_r/N_o}\left[1 + \frac{N_o}{\bar{E}_r}\right], \tag{168a}$$

where

$$\bar{E}_r = \left(\frac{2P}{N_o}\right)_d \left(2\sigma_b^2\right) NT, \tag{168b}$$

with

$$\left(\frac{2P}{N_o}\right)_d = \text{(spatially discrete) SNR level at the receiver site.} \tag{168c}$$

6.3.3 Discrete Ambiguity and Performance for Geostationary Satellites

For economic reasons the number of satellites simultaneously available at each location[10] is usually ≤ 4. It is easy to see that a centered geometry (with source parameters defined with respect to the array geometric center) requires at least three satellites to

measure the apparent curvature from which range is inferred. The results for a four-satellite constellation may be summarized as follows.

The DGAF is

$$\phi(k_1, k_2) = \sin^2(k_1 \Delta L) \sin^2\left(\frac{k_1}{2} \Delta L\right) + \cos\left(\frac{3}{2} \Delta L k_1\right) \cos\left(\frac{k_1}{2} \Delta L\right) \cos\left(k_2 \Delta L^2\right), \tag{169a}$$

with the primary cell

$$\Omega_1 = \left[-\frac{\pi}{\Delta L}, \frac{\pi}{\Delta L}\right] \times \left[-\frac{\pi}{2\Delta L^2}, \frac{\pi}{2\Delta L^2}\right]. \tag{169b}$$

Study of Eq. 169a shows that the main lobe is limited to

$$\Delta\Omega = \left[-\frac{\pi}{3\Delta L}, \frac{\pi}{3\Delta L}\right] \times \left[-\frac{\pi}{2\Delta L^2}, \frac{\pi}{2\Delta L^2}\right] \tag{170}$$

and important secondary maxima exist in Ω_1 such as

$$\phi\left(\pm\frac{2}{3}\frac{\pi}{\Delta L}, \pm\frac{\pi}{2\Delta L^2}\right) = \left(\frac{3}{4}\right)^2. \tag{171}$$

We shall refer to $\Delta\Omega$ as the discrete resolution cell for the four-satellite constellation problem.

The spread of the DGAF main lobe may also be quantified by using the quadratic local approximation in terms of $\mathcal{M}_d$ and its inverse. For the four-satellite problem, from Eq. 167,

$$\mathcal{M}_d^{-1} = \left(\frac{\lambda}{2\pi}\right)^2 \left[\begin{array}{c|c} \dfrac{4R_o^4}{\cos^4\theta} \dfrac{1}{L_4 - L_2^2} & 0 \\ \hline 0 & \dfrac{1}{L_2} \end{array}\right] \tag{172a}$$

where

$$L_2 = \frac{5}{4}\Delta L^2, \quad L_4 = \frac{41}{16}\Delta L^4, \quad L_4 - L_2^2 = \Delta L^4. \tag{172b}$$

Substituting Eq. 172b in Eq. 172a and normalizing by means of the signal energy-to-noise ratio leads to the Cramer-Rao performance bounds for the discrete SASS with a four-satellite constellation.

$$\sigma_{R_o} \approx G_d^{-1/2}\left(\mathcal{M}_d^{-1}\right)_{R_o}^{1/2} \approx G_d^{-1/2} \frac{\lambda}{2\pi} \frac{9}{2} \frac{1}{(X\cos\theta)^2} \tag{173a}$$

$$\sigma_{\sin\theta} \approx G_d^{-1/2} \left(\mathcal{M}_d^{-1}\right)^{1/2}_{\sin\theta} \approx G_d^{-1/2} \frac{3}{\pi\sqrt{5}} \frac{1}{L_\lambda}, \tag{173b}$$

where X = geometric spatial diversity parameter $= \frac{L}{2R_o} = \frac{3\Delta L}{2R_o}$, $L_\lambda = \frac{L}{\lambda} = \frac{3\Delta L}{\lambda}$.

6.3.4 Global Acquisition Strategy for a Constellation of Geostationary Satellites

The discrete ambiguity function exhibits a structure, reproduced in the parameter space Ω at equally spaced intervals. To avoid global ambiguities, the important sidelobes (peaks in Ω_1) must be shifted beyond the a priori region of uncertainty $\Delta_M\Omega$. In (k_1, k_2) space

$$\Delta_M\Omega = \left[k_{1_{min}}, k_{1_{max}}\right] \times \left[k_{2_{min}}, k_{2_{max}}\right]. \tag{174a}$$

In the passive user parameter space

$$\Delta_M\Omega = \underset{i}{\times} \left[A_{i_{min}}, A_{i_{max}}\right] \tag{174b}$$

which for the discrete SASS simply reduces to

$$\Delta_M\Omega = \left[\sin\theta_{min}, \sin\theta_{max}\right] \times \left[R_{o_{min}}, R_{o_{max}}\right]. \tag{174c}$$

This may be achieved by matching the resolution cell $\Delta\Omega$ to $\Delta_M\Omega$, for example, through proper choice of wavelength. For the four-satellite constellation, from Eqs. 170 and 174a, we have

$$\lambda > \max\left((\Delta_M \sin\theta)\Delta L, (\Delta_M \ddot{R}_o)\Delta L^2\right), \tag{175a}$$

where

$$\Delta_M \sin\theta = \frac{\lambda}{2\pi}\Delta_M k_1 = \frac{\lambda}{2\pi}\left(k_{1_{max}} - k_{1_{min}}\right) = \sin\theta_{max} - \sin\theta_{min} \tag{175b}$$

$$\Delta_M \ddot{R}_o = \frac{\lambda}{2\pi}\Delta_M k_2 = \frac{\lambda}{\pi}\left(k_{2_{max}} - k_{2_{min}}\right). \tag{175c}$$

Alternatively, when using the quadratic representation for the main lobe given by the mean-square spread matrix we want the diagonal elements of the inverse discrete spread matrix to satisfy

$$\left(\mathcal{M}_d^{-1}\right)^{1/2}_{A_i} \geq \Delta_M A_i = A_{i_{max}} - A_{i_{min}}, \quad \text{for every } i. \tag{176}$$

This leads to the condition for λ:

$$\lambda \geq \max_i \left(\left(\underset{\sim}{\mathcal{A}}_d^{-1} \right)_{A_i}^{-1/2} \Delta_M A_i \right), \tag{177a}$$

where

$$\left(\underset{\sim}{\mathcal{A}}_d^{-1} \right)_{A_i} = \frac{\left(\underset{\sim}{\mathcal{A}}_d^{-1} \right)_{A_i}}{\lambda}. \tag{177b}$$

Equations 175 or 177 may lead, however, to unacceptable resolution, that is, to large Cramer-Rao bounds. A practical strategy, which can be implemented whenever

$$G_d = 2 \frac{\left(\bar{E}_r / N_o \right)^2}{1 + \frac{\bar{E}_r}{N_o}} > 1, \tag{178a}$$

is a sequential procedure with the global ML acquisition repeated with decreasing wavelengths

$$\lambda_{j+1} \cong \frac{\lambda_j}{G_d^{1/2}} = \frac{\lambda_1}{\left(G_d^{1/2} \right)^j} \tag{178b}$$

with λ_1 given by Eqs. 175 or 177. Since the approach behind Eqs. 177 generalizes in a straightforward way to arbitrary N and to other classes of problems such as discrete-space, continuous-time SAMS, and is also consistent with the quadratic (local) analysis for GAF and DGAF, we assume that λ_1 has been determined by Eqs. 177.

The sequential procedure stops with the smallest order step

$$j = J \tag{179a}$$

for which the corresponding mean-square performance

$$\sigma_{A_i}^J < \sigma_{A_i}, \quad \text{for every } i, \tag{179b}$$

where σ_{A_i} is the desired rms performance. The corresponding wavelength is

$$\lambda_J = \frac{\max_i \left(\Delta_M A_i \left(\underset{\sim}{\mathcal{A}}_d^{-1} \right)_{A_i}^{-1/2} \right)}{\left(G_d^{1/2} \right)^{J-1}} \tag{180a}$$

and

$$\sigma_{A_i}^J = \frac{\max_m \left(\Delta_M A_m \left(\underset{\sim}{\mathcal{A}}_d^{-1} \right)_{A_m}^{-1/2} \right)}{\left(G_d^{1/2} \right)^J} \left(\underset{\sim}{\mathcal{A}}_d^{-1} \right)_{A_i}. \tag{180b}$$

Let

$$\left(\Delta_M A_{m_{max}}\right)\left(\underset{\sim}{\mathcal{M}}_d^{-1}\right)^{-1/2}_{A_{m_{max}}} = \max_m \left(\left(\Delta_M A_m\right)\left(\underset{\sim}{\mathcal{M}}_d^{-1}\right)^{-1/2}_{A_m} \right). \tag{181a}$$

If $m_{max} = i$ in Eq. 181a, we obtain

$$\sigma^J_{A_{m_{max}}} = \frac{\left(\Delta_M A_{m_{max}}\right)}{\left(G^{1/2}\right)^J}. \tag{181b}$$

Finally, the number J is the smallest integer containing all J^i, where

$$J^i = \frac{\ln \left\{ \left[\left(\Delta_M A_{m_{max}}\right)\left(\underset{\sim}{\mathcal{M}}_d^{-1}\right)^{-1/2}_{A_{m_{max}}} \right] \left(\underset{\sim}{\mathcal{M}}_d^{-1}\right)^{1/2}_{A_i} \right\} - \ln \sigma_{A_i}}{\ln \left(G_d^{1/2}\right)}. \tag{181c}$$

6.3.5 Commercial Avionics Surveillance with Geostationary Satellites

The preceding considerations are applied to the air traffic control situation illustrated in Fig. 100. The signals radiated by each geosynchronous satellite are coded for identification purposes and for relaying to the passive users the satellite ephemeris, which is necessary for the ultimate geographic position determination. The signals are also modulated by a common set of subcarriers that is available for refinement of the relative position estimates.

We summarize in Table 6 the nominal relative parameter values for the configuration of Fig. 100.

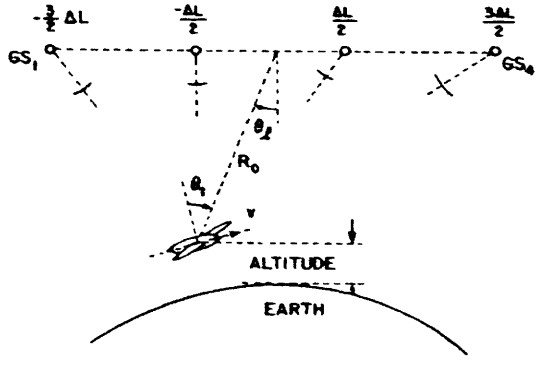

Fig. 100. Commercial avionics surveillance with geostationary satellites.

Table 6. Nominal values for commercial avionics surveillance.

$R_o \approx 4 \times 10^4$ km
$\theta_t \cong 30°$
$\theta_\ell \cong 15°$
$V \approx 2000$ knots $= 10^3$ m/sec (SST)
Elementary Observation Time $= \Delta T \approx .5$ sec
Surveillance Update Cycle $T \approx 30$ sec (SST)
$T \approx 90$ sec (subsonic)
$\sigma_v \approx 5$ ft/sec, $\sigma_{R_o} \approx 250$ ft
Carrier Frequency $\approx f \sim 1.5$ GHz (L-band)
Satellites Interspacing $\Delta L \approx \frac{6000}{3}$ km

Again, we stress that Eqs. 177-181 not only apply to the SASS context but also to $SAMS_o$ or SAMS.

REMARKS

1. For $N \neq 4$ the rationale behind this sequential global acquisition procedure remains, but the values of λ and λ_{i+1} are not simply determined by Eqs. 177a and 178. If the problem geometry leads to a local type of configuration where the global errors are negligible and the mean-square-error performance is correctly predicted by the Cramer-Rao bounds, Eq. 178 is still valid. When $\sigma_{tot_{A_i}} > \sigma_{CR_{A_i}}$ the sequence of λ_j can be determined graphically from both the local and global error components. For large N, when no significant secondary lobes arise in the primary cell Ω_1, λ_1 should be determined from the dimensions of Ω_1 (see Eqs. 164).

2. To avoid ionospheric propagation losses and simplify the implementation, we assume that each satellite radiates a carrier modulated by a set of common subcarriers with decreasing wavelengths. The passive user refines its resolution by sequentially processing these subcarriers.

a. Model Considerations

In order to apply the hybrid algorithm concept to this navigation problem, we make the following assumption for the global acquisition step.

H ML 1: The problem fits a discrete-space, continuous-time SAMS model. That is,

1. The source/receiver parameter vector (see Fig. 100) $A = [R_o \; v \sin\theta_t \; \sin\theta_\ell]^T$ is nonrandom, unknown.

2. The plane follows a constant-speed linear path.

3. The additive measurement noise is white.

4. The narrow-band signals originating at the point sources (discrete space) are continuously available in time.

For the linearized phase tracker this model is generalized by substituting the following for points 1 and 2.

H EKB 1:

1. The plane follows a nominal constant-speed linear path disturbed by random accelerations (Eqs. 134).

b. ML Mean-Square Performance

For the nominal parameter values in Table 6 the ratio between the temporal and the spatial diversity

$$\gamma = \frac{X_t}{X_\ell} = \frac{vT/R_o}{L/2R_o} \ll 1,$$

and the rms performance for range R_o and spatial bearing $\sin\theta_\ell$ are given by Eq. 167. The cross coupling plays an important role in the estimation of aircraft speed v and temporal bearing $\sin\theta_t$. Adapting the results of Eqs. 124 and 125 for the coupled SAMS to the discrete spatial baseline satellite configuration of Fig. 100, for the Cramer-Rao performance we obtain

$$\sigma_v \approx G_d^{-1/2}\left(\mathcal{M}_d^{-1}\right)_v^{1/2} \approx G_d^{-1/2}\,\frac{\lambda}{2\pi}\,\frac{v}{R_o}\,\frac{3\sqrt{3}\cos\theta_t}{\cos\theta_\ell}\,\frac{1}{X_\ell X_t} \tag{182a}$$

$$\sigma_{\sin\theta_t} \approx G_d^{-1/2}\left(\mathcal{M}_d^{-1}\right)_{\sin\theta_t}^{1/2} \approx \sigma_v\,\frac{\sin\theta_t}{v}, \tag{182b}$$

where G_d is given by Eq. 168a.

c. ML System Discussion

We assume the values in Table 6 unless otherwise specified. For the signal-to-noise ratio (SNR) at the user site we consider as a nominal value SNR = 0 dB, and as comparison value SNR = 6 dB. The total time interval for the range global acquisition is the elementary observation interval ΔT in Table 6, $\Delta T = \frac{1}{2}$ s.

Range Accuracy. Figure 101 studies the total number of steps given by Eq. 181c,

$$J \geq J^{R_o} = \frac{\ln (\Delta_M R_o) - \ln \sigma_{R_o}}{\ln \left(G_d^{1/2}\right)},$$

that are necessary to achieve a desired accuracy σ_{R_o}, when the a priori uncertainty is

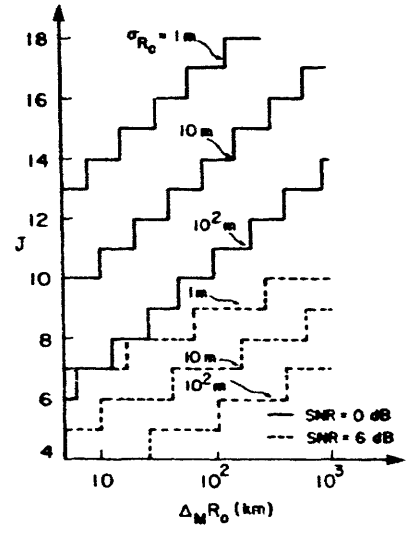

Fig. 101. Number of updates vs a priori range uncertainty.

$\Delta_M R_o$. We considered three values for σ_{R_o}: σ_{R_o} = 1 m, 10 m, 10^2 m, and the two indicated SNR values. As an example, we read from the curve that to go from a relatively large uncertainty $\Delta_M R_o = 10^2$ km to a very small final rms error σ_{R_o} = 10 m with SNR = 0 dB, requires 14 sequential updates. If the SNR level is increased to 6 dB, only 7 steps are necessary. The starting value for λ, from Eq. 177a, is

$$\lambda^1_{R_o} = \Delta_M R_o \left(\underset{\sim}{\mathcal{A}}_d^{-1}\right)^{-1/2}_{R_o} \approx 1315 \text{ m} \tag{183}$$

and the final value, from Eq. 178b, is

$$\lambda^{14}_{R_o} \approx \frac{\lambda^1_{R_o}}{\left(G_d^{1/2}\right)^{13}} \approx \frac{\lambda^1}{2^{13}} \approx .17 \text{ m}.$$

Speed Accuracy. For the example described above, we let the a priori speed uncertainty $\Delta_M v = 10^2$ m/sec. From Eq. 182a we obtain

$$\left(\underset{\sim}{\mathcal{M}}_d^{-1}\right)_v^{1/2} = \frac{\left(\mathcal{M}_d^{-1}\right)_v^{1/2}}{\lambda} = \frac{22.83}{T}.$$

To solve the original uncertainty given by $\Delta_M v = 10^2$ m/sec, the wavelength must be greater than

$$\lambda_v^1 \approx (\Delta_M v)\left(\underset{\sim}{\mathcal{M}}_d^{-1}\right)_v^{-1/2} \approx 4.38T.$$

For any reasonable T this is much smaller than $\lambda_{R_o}^1$ given by Eq. 183. The final accuracy is

$$\sigma_v \approx \frac{\lambda}{\sqrt{SNR}}\left(\underset{\sim}{\mathcal{M}}_d^{-1}\right)_v^{1/2} \approx 8.071\,\frac{\lambda}{\sqrt{SNR}}\,T^{-3/2}.$$

For $\lambda = 1$ m Fig. 102 studies the speed accuracy as a function of the acquisition time T_{acq} for two levels of SNR.

If we take $T_{acq} = \Delta T = .5$ sec $\overset{\text{SNR = 0 dB}}{\Longrightarrow}$ $\sigma_v \approx 22.83$ m/sec. If $T_{acq} = 3\Delta T$ $\overset{\text{SNR = 0 dB}}{\Longrightarrow}$ $\sigma_v \approx 4.5$ m/sec. Since the EKB is insensitive to large a priori inaccuracies on the velocity measurements, the range of σ_v in Fig. 102 is acceptable for starting the linearized EKB.

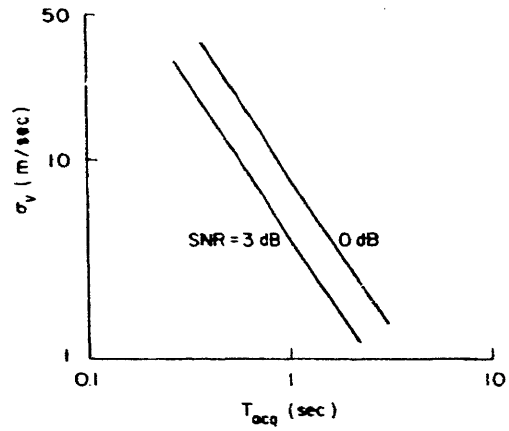

Fig. 102. Speed accuracy vs acquisition time.

Similar considerations could be pursued for the other two parameters.

d. Extended Kalman-Bucy Filter

Concentrating the discussion on the range and range rate parameters, for the linearized phase tracker we find that the steady-state covariance values, from Eqs. 139d and 139e, are

$$P_{11} \approx \frac{1}{H_1}(4QH_1)^{1/4}$$

$$P_{22} \approx \frac{2Q}{(4QH_1)^{1/4}}.$$

For moderate turbulence flight conditions $Q \approx \left(\frac{g}{2}\right)^2 \approx 5\ m^2/sec^3$, and for $\lambda \approx 1$ m, SNR = 0 dB, we obtain $P_{11} \approx .1182$ m, $P_{22} = 5.286$ m/sec. The loop bandwidth and the equivalent signal-to-noise ratio in the bandwidth loop $B_L = \frac{3}{8}(4QH_1)^{1/4} \approx 3.546$, and $c \approx \frac{8}{3}\frac{H_1}{(4QH_1)}\ 1/4 \approx 22.55$. The average time between cycle skips is

$$T_{skp} \approx \frac{\pi}{4B_L} e^{2c} \approx 1.4 \times 10^9 \text{ sec.}$$

The results for P_{11}, P_{22}, and T_{skp} show that the EKB loop performs well within the limitations imposed by the global ML processor.

6.3.6 Conclusion

We have considered two typical navigation problems involving satellites. With orbiting satellites the continuous-time formulation of $SAMS_o$ is particularly suitable.

With geosynchronous satellites we had to adapt the passive tracking results to a discrete-space formulation. Although the general principles extend in a straightforward way, the details of the resulting structure depend largely on the number of available satellites, and on ratios of powers of the satellites interspacing ΔL and wavelength λ. The main issue deals with the ambiguity function periodic structure and, within each primary cell Ω_1 with the important secondary lobes that may arise from aliasing effects.

We have presented a sequential updating algorithm where the wavelength is reduced by a factor equal to the square root of the available signal energy-to-noise ratio which achieves both the global acquisition and the desired resolution.

We have studied the tradeoffs between the necessary number of updates, the a priori uncertainty, the available signal-to-noise ratio at the user site, and the desired accuracy in the context of an SST commercial avionics surveillance application by using a constellation of four geosynchronous satellites.

The large spatial baseline available allows very accurate final estimates. Starting with a large range a priori uncertainty (100 km), we saw that an accurate estimate ($\sigma_{R_o} \approx$ 10 m) could be achieved in 14 steps, with a final wavelength of approximately 1 m. Here there is a tradeoff between computation time and complexity, in that these 14 steps can be processed sequentially in time by a single processor unit or simultaneously by 14 processor units. We analyzed the EKB performance, and concluded that the linearized performance was within the required accuracy, and that the cycle skip phenomena will not be an issue unless the EKB is used with larger wavelengths.

6.4 MONTE CARLO SIMULATION RESULTS

We report the results of simulating the ML processor in the context of the passive positioning with underwater acoustics discussed in section 6.2. The linearized EKB structures have been previously analyzed,[20] and the results reported.[21] See Fig. 69 for some illustrative runs.

There are three main points concerning the Monte Carlo simulations. The first is the actual implementation on a discrete environment (computer) of the simulation of a stochastic problem, with the "discretized" version of a white noise process and the design of (stochastic) maximization routines. The second relates to the statistical confidence associated with the simulation results themselves, with a tradeoff between the finiteness of the computation time available and the number of samples taken in the ensemble average. The third relates to the closeness of the simulation results to those predicted by the theoretical analysis, with the determination of regions where both converge (in a statistical sense).

We shall now discuss these points briefly.

6.4.1 Algorithm Implementation

We implemented the two-step algorithm mechanizing the ML estimation receiver for both SASS and $SAMS_o$ contexts.

Because of the discrete environment, the noise levels were normalized by the (space and time) sampling intervals.[20] If ΔL = array sampling interval and ΔT = time sampling interval, we obtain

$$(SNR)_d = \frac{2P}{\frac{N_o}{\Delta L \Delta T}} = (SNR)_c \, \Delta L \, \Delta T,$$

where the index d stands for discrete, and c for continuous environment. The maximization algorithm was essentially a search procedure, superimposing grids of varying overall and elementary cell size. This technique bounds the accuracy to the size of the smallest elementary cell used (quantization errors) but avoids the implementation of costlier maximization routines.

Because of limited computer time availability, we restricted ourselves to testing the local results on the mean-square performance, i.e., to the statistical test of the Cramer-Rao bounds by bounding the a priori region of uncertainty so that

$$\sigma^2_{gl} \ll \sigma^2_{loc} \rightarrow \sigma^2_{tot} \approx \sigma^2_{loc}.$$

6.4.2 Confidence Intervals Associated with Statistical Averages

The simulation results had as the main objective to compare the performance predicted by the analysis with that computed by statistically averaging the simulated runs.

Because of the stochastic nature of the problem, the performance measures computed by the Monte Carlo runs are themselves random variables. For example, for a random variable with known mean and variance σ_x^2 the variance computed from the ensemble averaging,

$$\hat{\sigma}_x^2 = \frac{1}{N} \sum_{i=1}^{N} (x_i - \bar{x})^2,$$

for all practical purposes, is an unbiased estimate of σ_x^2, normally distributed with mean σ_x^2 and variance $2\sigma_x^2/N$. We have then $\Pr\{(1-\alpha)\sigma_x^2 < \hat{\sigma}_x^2 < (1+\alpha)\sigma_x^2\} \approx \text{erf}\left(\frac{\alpha}{2}\sqrt{N}\right)$, where

$$\text{erf}(X) = \frac{2}{\sqrt{\pi}} \int_0^X \exp(-y^2)\, dy,$$

with α a positive constant. We are particularly interested in the 3σ confidence interval (α=2).

6.4.3 Simulation Results

We simulated one geometry for each problem, for several values of the signal-to-noise ratio. Table 7 summarizes the important data.

Table 7. Simulated configuration parameters.

λ = 50 ft; $R_o = 6 \times 10^3$ ft

$\sigma_b^2 = 1$; $\vartheta_\ell = 0$

SASS	$SAMS_o$
$\Delta L = \frac{\lambda}{2}$ = 25 ft	v = 30 ft/sec
L = 3980 ft	$\theta_t = -15°$
ΔT = T = 1 sec	ΔL = L = 50 ft
X_ℓ = .331	ΔT = 5 s, NT = 24
	X_t = .287

Figure 103 represents the SASS simulation results for 15 Monte Carlo runs. We distinguish a threshold region below SNR = −30 dB. Above this value the statistical results are within a 3σ confidence interval I (3σ) of the Cramer-Rao bounds. The point for SNR = −34 dB is approximately one order of magnitude apart from the Cramer-Rao curve.

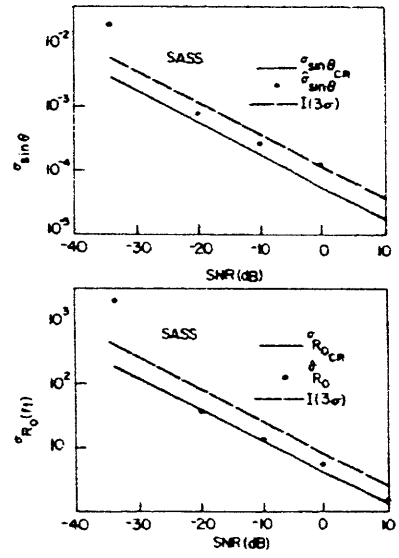

Fig. 103. SASS simulation results.

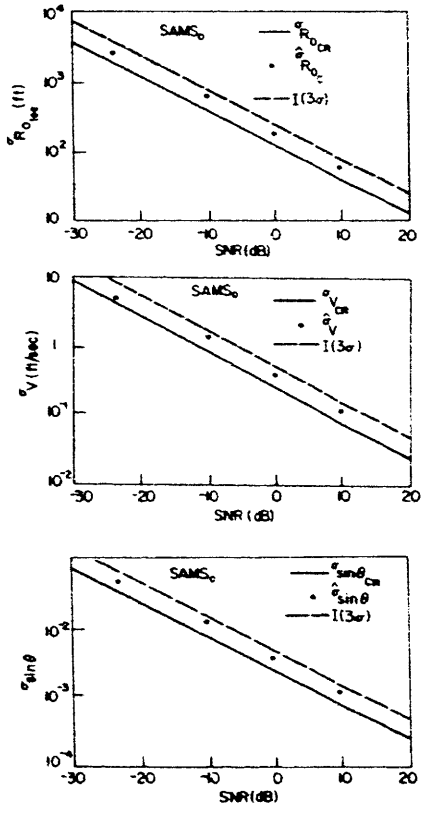

Fig. 104. $SAMS_o$ simulation results.

Figure 104 presents the $SAMS_o$ simulation results, averaged over 15 runs, for varying SNR. The curves show that all statistically computed standard deviations are within the 3σ confidence interval I (3σ) of the theoretically computed Cramer-Rao standard deviation.

As a final comment on these simulation results, we note that when the Rayleigh amplitude $|\tilde{b}|$ of the complex multiplicative Rayleigh parameter $\tilde{b}$ is kept constant (unknown) and equal to $|\tilde{b}|^2 = 2\sigma_b^2$ the agreement between the theoretical and practical results is even closer than that indicated by Figs. 103 and 104. The reason is that for $\tilde{b}$ a zero-mean complex Gaussian random variable there are runs for which $|\tilde{b}|$ is very small, and regardless of SNR, this deteriorates the statistical performance computed via the Monte Carlo simulations.

VII. CONCLUSIONS AND EXTENSIONS

7.1 CONCLUSIONS

We have considered the passive tracking problem with narrow-band and linear constraints.

In Part I, Sections I-IV, we developed a simple model, designed optimal and suboptimal receivers, and analyzed their structure and associated errors. The main contributions of this research are the following.

1. A simple model that encompasses the fundamental global and local characteristics of the passive tracking problem and exhibits explicitly the symmetry between the space and time aspects.

2. A systematic treatment of the passive global identifiability of the parameters defining the relative source/receiver geometry. We emphasized the passive global range observability, as obtained from the higher order phase modulations induced on the radiated signal structure by the spatial and/or temporal diversity.

3. Analysis of the global ambiguity structure associated with nonhomogeneous passive narrow-band tracking, with bounds on its asymptotic behavior.

The ambiguity structure for the distant observer was considered extensively. The range phase was approximated by a truncated n^{th}-order Taylor's series, and the resulting ambiguity function associated with generalized n^{th}-order sinc functions (secs. 2.3, 3.3, and Appendix A). We bounded the asymptotic behavior of these approximate structures; for example, for the generalized third-order sinc the bound was related to an Airy function.

By application of the method of stationary phase (MSP), we have shown that the general ambiguity function is negligible for large parameter errors. Coupling the analytical studies to graphical displays, we concluded that the generalized ambiguity function (GAF) presents a quadratic ellipsoidal main lobe, with negligible secondary structure (see end of sec. 3.3.3).

4. Global and local mean-square error bounds. Graphical displays exploring the effects of the geometry and of the statistical parameters on the mean-square performance, were presented. We considered the distant and close observer situations and, by means of Taylor's series, we derived simple, intuitively pleasing, approximate expressions, showing how they compare with the exact bounds.

Depending solely on the geometry, we concluded that independent of the signal-to-noise ratio the two-step practical implementation of the ML receiver exhibits two distinct performance behaviors: a local region where the mean-square performance is well approximated by the local bounds and determined by the sharpness and dimensions of the ambiguity structure main lobe; and a global region where decision errors induce large inaccuracies on the average and the performance is given by the global bounds. In practice, the global bounds may be circumvented by means of independent

measurements (see secs. 2.4.3 and 3.4.5).

5. Study of the space/time factorability and coupling issues in passive tracking. We analyzed in detail the distant observer situation, and reached the following conclusions:

(a) When the temporal diversity (source travel) dominates the spatial baseline, the ambiguity structure factors. The spatial bearing angle is observed from the available spatial diversity, and the rest of the parameters from the temporally induced modulations. Intuitively, the decoupled receiver incorporates beam steering (spatial operation), and a bank of matched filters, over a three-dimensional parameter space (temporal processing). We derived an expression for the total number of steering operations and, by putting the problem in the perspective of previously obtained results, analyzed its mean-square performance (sec. 4.1).

(b) When the temporal and spatial baselines are comparable, the receiver is not separable. This coupling, although it results in more complex receivers, represents a nontrivial improvement on the global identifiability of the source parameters. The order of the estimation problem is reduced with respect to the decoupled situation, and hence only requires measurements of second-order effects in both space and time domains (Fresnel zone). Again, by using Taylor's series techniques, we arrived at intuitively satisfying analytical expressions quantifying the mean-square spread of the main lobe and the (local and global) mean-square performance bounds (sec. 4.2 and Appendix D).

In Part 2, Sections V and VI, we presented a practical hybrid receiver for passive tracking, and applied the preceding theory and results to positioning and navigation problems. The main results are as follows.

1. A practical hybrid algorithm achieving a compromise between the continuous global estimation of the relative source/receiver geometry and the complexity of implementation.

Global acquisition is accomplished by an ML processor requiring a multidimensional stochastic maximization. The local dynamics is recursively tracked by a linearized filter, an extended Kalman-Bucy filter (EKB).

2. Sensitivity analysis of each receiver block to the geometry, statistical parameters, and modeling assumptions, leading to four characteristic modes for the hybrid algorithm's behavior:

(a) For high signal-to-noise (SNR) applications, the errors associated with global acquisition dominate the hybrid algorithm's behavior, and the results of Part 1 predict well the overall performance. In practice, because of random perturbations, the source deviates from the assumed nominal linear constant path, and imposes a maximum acquisition time, after which the induced errors are larger than those arising from additive measurement noise (sec. 5.4).

(b) For low SNR (the breakdown occurring approximately at 0 dB noise ratio), the errors associated with the EKB nonlinear behavior (cycle skipping phenomena) may significantly deteriorate the EKB performance, and tracking is impossible.

3. An illustrative design of practical passive systems for use in precision landing

air traffic control, underwater acoustic positioning, and navigation with orbiting and geostationary satellites. The precision landing problem (sec. 6.1) is typically a high SNR application (approximately 40 dB is available at the receiver site), with the global acquisition imposing the harder limitations on the hybrid algorithm performance. Flight turbulence conditions determine the maximum acquisition time, and the corresponding ML mean-square error.

The underwater acoustic problem (sec. 6.2) is highly sensitive to the geometry and statistical parameters. For higher SNR and certain geometry tracking is possible, with the rms path variations determining the maximum allowable performance. For lower SNR the hybrid algorithm reduces to the acquisition step, with the time updating accomplished nonrecursively by the ML processor.

Passive navigation with satellites (sec. 6.3) presents practical situations, with a large baseline synthesized by either orbiting or geostationary satellites, leading to geometry that yields accurate ranging. Examples are given of tradeoffs and attainable accuracy for ship navigation and SST commercial avionics surveillance (secs. 6.3.2 and 6.3.5).

4. Analysis of the sampling effects on the nonhomogeneous second-order (Fresnel zone) ambiguity structure.

5. A sequential procedure for resolving the ambiguities resulting from discretization effects associated with the geostationary satellite passive navigation.

6. Monte Carlo simulation studies (secs. 5.3 and 6.4) demonstrating the existence of regions of statistical convergence between the theoretical and the simulated results.

7.2 EXTENSIONS

The generalizations and extensions of the present work relate basically to the modeling assumptions and to the receiver complexity. A selected list includes the following points.

1. Signal Assumptions. A narrow-band source signature was assumed. In many practical situations a better model would be a combination of broadband and narrow-band components,[51] while in others the signals would be broadband. A forthcoming thesis[52] deals with the last situation. Our results may be extended in a straightforward manner to the case of a long observation interval, compared with the signal and noise correlation times, and to the travel time of the wave field across the array. These processes admit a Fourier representation with uncorrelated coefficients, and the problem reduces to a multitone problem where the relative source/receiver geometric parameters enter through phase modulations, as in the single-tone model.

Using the results of Bangs,[14] we find that the Fisher information matrix for the multitone problem is given by

$$J = G \underset{\sim}{\mathcal{A}}, \tag{184a}$$

with

$$G = \left\{ \sum_{k=1}^{K} \frac{[S_s(w_k)/S_n(w_k)]^2}{1 + G(w_k) \dfrac{S_s(w_k)}{S_n(w_k)}} \left(\frac{2\pi}{\lambda_k}\right)^2 \right\}. \tag{184b}$$

Here $S_s(w_k)$, $S_n(w_k)$ are the power spectra of the signal and noise processes at w_k, $G(w_k)$ is the array gain, $\underset{\sim}{\mathcal{M}}$ is the mean-square spread matrix normalized by $(2\pi/\lambda_k)^2$, as defined in Appendix B. The matrix J, given by Eqs. 184, is the product of a gain G that incorporates the new signal modeling assumptions (multitone) and of the mean-square spread matrix reflecting the geometric aspects, which remains the same as in the single-tone situation studied in this report.

2. Noise Assumptions. We considered unstructured additive measurement noises, spatially and temporally white Gaussian. When the measurement exhibits a significant structure it may be combated by high-resolution array processing methods.[28] But this involves a generalization of these procedures to nonhomogeneous wave fields.

3. Dynamics and Geometry. We assumed nominal linear motions and linear array structures. The effects of nonlinear motions and/or nonlinear receiving structures can be analyzed by using the approach considered here, by incorporating the new geometry on the range phase function.

4. Higher Order Receivers. The hybrid algorithm developed in Section V is decoupled in two blocks. From the illustrative studies carried out in Section VI, we anticipate that in many practical applications the sensitivity of the global step to the path perturbations constitutes a limiting factor on the mean-square performance of the hybrid algorithm. Higher order receivers, designed along the lines of the more sophisticated techniques of nonlinear waveform estimation theory,[53] may then be necessary. The problems with these techniques relate not only to added conceptual difficulties but mainly to a large associated computational effort.[53]

APPENDIX A

Generalized Ambiguity Function

A.1 INTRODUCTION

The generalized ambiguity function (GAF) for the narrow-band passive problem is given by $\phi(A, \bar{A}) = |\psi(A, \bar{A})|^2$, where $\psi(A, \bar{A})$ is the signal autocorrelation function:

$$\psi(A, \bar{A}) = \frac{1}{2Z} \int_{-Z}^{Z} dx \exp\left[j \frac{2\pi}{\lambda} \Delta R(x, A, \bar{A}) \right]. \tag{A.1}$$

With SASS or MASS the parameter vector $[R_o \sin\theta]^T$ is two-dimensional, while for $SAMS_o$ the parameter vector $[R_o \; v \sin\theta]^T$ is three-dimensional, since we estimate further the relative source/observer speed v.

The analysis for the two-dimensional SASS or MASS parallels that for $SAMS_o$ and can be obtained as a special case by assuming in the final results that $v = \bar{v}$. In order to reduce the unnecessary details to a minimum, we concentrate the discussion on the more general $SAMS_o$ configurations of Section III. The implications of the results of this appendix have been discussed in Sections II and III.

Since we are dealing with $SAMS_o$ the spatial domain is $x = vt$ and we rewrite the signal autocorrelation function as

$$\psi(A, \bar{A}) = \frac{1}{T} \int_{-T/2}^{T/2} dt \exp\left[j \frac{2\pi}{\lambda} \Delta R(t, A, \bar{A}) \right] \tag{A.2}$$

with the phase difference

$$\Delta R(t, A, \bar{A}) = \left[R_o^2 + (vt)^2 - 2(vt) R_o \sin\theta \right]^{1/2} - \left[\bar{R}_o^2 + (\bar{v}t)^2 - 2(\bar{v}t) \bar{R}_o \overline{\sin\theta} \right]^{1/2}. \tag{A.3}$$

The analysis of the GAF is carried out in steps. First, we consider polynomial approximations to the phase difference and study the approximate structure of the GAF so obtained. Second, we return to the general expression of the GAF and concentrate on presenting bounds on the asymptotic behavior of the function.

A.2 POLYNOMIAL APPROXIMATION

The range phase difference is approximated by finite-degree polynomials, obtained by truncation of Taylor's series expansions. We have

$$\frac{2\pi}{\lambda} \Delta R(t, A, \bar{A}) \approx \sum_{i=0}^{n} \Delta_i t^i, \qquad t \in \left[-\frac{T}{2}, \frac{T}{2} \right],$$

where

$$\Delta_i \triangleq \frac{1}{i!}\frac{2\pi}{\lambda}\overset{(i)}{\Delta R_o} = \frac{1}{i!}\frac{2\pi}{\lambda}\frac{d^i}{dt^i}\left[R(t, A) - R(t, \bar{A})\right]\Big|_{t=0}.$$

Subsequently we study linearized, second-order and third-order polynomial expansions.

A.2.1 Linearized Analysis

By linearizing the phase difference,

$$\Delta R(t, A, \bar{A}) \approx \Delta R_o - \Delta(v \sin\theta)\, t, \tag{A.4}$$

where $\Delta R_o = R_o - \bar{R}_o$, and $\Delta(v \sin\theta) = v \sin\theta - \bar{v}\,\overline{\sin}\,\theta$. This approximation is valid whenever

$$\frac{\Delta\dot{R}_o}{\Delta\ddot{R}_o} = \frac{\Delta(v \sin\theta)}{\Delta\left(\frac{v^2\cos^2\theta}{R_o}\right)} \gg \frac{T}{2}, \tag{A.5}$$

that is, when the Doppler mismatch $\Delta\dot{R}_o$ is much greater than the error $\Delta\ddot{R}_o \frac{T}{2}$ induced in the Doppler by the range acceleration mismatch. This may happen because either T is small (short observation interval) or $\Delta\ddot{R}_o$ is small; that is, we are analyzing the ambiguity structure in the neighborhood of the Doppler parameter axis.

The ambiguity function is given approximately by

$$\phi(A, \bar{A}) \cong \operatorname{sinc}^2\left[\frac{2\pi}{\lambda}\Delta(v \sin\theta)\frac{T}{2}\right] = \left(\frac{\sin\left[\frac{2\pi}{\lambda}\Delta(v \sin\theta)\frac{T}{2}\right]}{\frac{2\pi}{\lambda}\Delta(v \sin\theta)\frac{T}{2}}\right)^2. \tag{A.6}$$

See Fig. 13 for the graphical representation of this function. The zeros occur at $\Delta(v \sin\theta) = k\frac{\lambda}{T}$, $k = \pm1, \pm2, \ldots$, and the maxima at $\Delta(v \sin\theta) = 0$ and $\Delta(v \sin\theta) = \pm\left(k + \frac{1}{2}\right)\frac{\lambda}{T}$, $k = 1, 2, 3, \ldots$. The maxima of sinc^2 decrease monotonically as we depart from the origin. The relation between absolute maximum (at the origin) and the second relative maximum is

$$\frac{1}{\left(\frac{2}{3\pi}\right)^2} \approx 22.5;$$

that is, the second maximum is reduced to approximately 4.5% of the value at the origin. This relation is independent of the specific values of the parameters and, in fact, is an intrinsic relation of the sinc function.

A.2.2 Quadratic Analysis

The phase variation is approximated by the quadratic expansion

$$\Delta R(t, A, \bar{A}) \approx \Delta R_o - \Delta(v \sin\theta)\, t + \Delta\left(\frac{v^2 \cos^2\theta}{R_o}\right)\frac{t^2}{2} \qquad (A.7)$$

where we also have

$$\Delta\left(\frac{v^2 \cos^2\theta}{R_o}\right) = \frac{v^2 \cos^2\theta}{R_o} - \frac{\bar{v}^2(1 - \overline{\sin}^2\theta)}{\bar{R}_o}.$$

This approximation is valid in the region

$$\frac{\Delta\ddot{R}_o}{\Delta\dddot{R}_o} = \frac{\Delta\left(\frac{v^2 \cos^2\theta}{R_o}\right)}{\Delta\left(\frac{3v^2 \cos^2\theta}{R_o}\frac{v \sin\theta}{R_o}\right)} \gg \frac{T}{3},$$

that is, whenever T is small but not so small that relation (A.5) holds, or $\Delta\dddot{R}_o$ is small (the ambiguity structure is analyzed in a neighborhood of the $\Delta\dot{R}_o$, $\Delta\ddot{R}_o$ plane). For economy of notation we define

$$\Delta_o = \frac{2\pi}{\lambda}\Delta R_o$$

$$\Delta_1 = \frac{2\pi}{\lambda}\Delta(v \sin\theta)$$

$$\Delta_2 = \frac{1}{2}\frac{2\pi}{\lambda}\Delta\left(\frac{v^2 \cos^2\theta}{R_o}\right),$$

so that

$$\frac{2\pi}{\lambda}\Delta R(t, A, \bar{A}) \approx \Delta_o + \Delta_1 t + \Delta_2 t^2. \qquad (A.8)$$

The GAF is approximately

$$\phi(A, \bar{A}) \approx \left|\frac{1}{T}\int_{-T/2}^{T/2} \exp\left[j(\Delta_1 t + \Delta_2 t^2)\right]dt\right|^2. \qquad (A.9)$$

When $\Delta_2 = 0$, the GAF has approximately the sinc^2 structure that we have just discussed. We assume therefore $\Delta_2 \neq 0$, and rewrite the right-hand side of Eq. A.8 as

$$\alpha(t-\beta)^2 + \gamma^2 = \Delta_o + \Delta_1 t + \Delta_2 t^2, \qquad (A.10)$$

where

$$\alpha = \Delta_2 = \frac{\pi}{\lambda}\Delta\left(\frac{v^2\cos^2\theta}{R_o}\right) \tag{A.11a}$$

$$\beta = -\frac{\Delta_1}{2\Delta_2} = -\frac{\Delta(v\sin\theta)}{\Delta\left(\frac{v^2\cos^2\theta}{R_o}\right)} \tag{A.11b}$$

$$\gamma = \left[\Delta_o - \frac{\Delta_1^2}{4\Delta_2}\right]^{1/2} \tag{A.11c}$$

We note that α corresponds to a normalized version of the error on the range acceleration parameter, while β is a shift on the observation interval caused by the nonzero mismatch on the Doppler parameter and the radial acceleration parameter. Given that we assume an incoherent phase model, γ which corresponds to a normalization of the phase reference is ignored in the sequel. We change variables

$$\frac{\pi}{2}t = \sqrt{\alpha}\ (t-\beta) \tag{A.12a}$$

and define

$$\Sigma_f = \sqrt{\alpha}\left(\frac{T}{2} - \beta\right) \tag{A.12b}$$

$$\Sigma_i = \sqrt{\alpha}\left(-\frac{T}{2} - \beta\right) \tag{A.12c}$$

$$\Delta\Sigma = \Sigma_f - \Sigma_i = \sqrt{\alpha}\ T \tag{A.12d}$$

$$C = \frac{1}{\Delta\Sigma}\int_{\Sigma_i}^{\Sigma_f}\cos\left(\frac{\pi}{2}t^2\right)dt \tag{A.12e}$$

$$S = \frac{1}{\Delta\Sigma}\int_{\Sigma_i}^{\Sigma_f}\sin\left(\frac{\pi}{2}t^2\right)dt. \tag{A.12f}$$

Tabulated Fresnel integrals[30] are

$$\mathcal{F}_c(\Sigma) = \int_0^{\Sigma}\cos\left(\frac{\pi}{2}t^2\right)dt \tag{A.13a}$$

$$\mathcal{F}_s(\Sigma) = \int_0^{\Sigma}\sin\left(\frac{\pi}{2}t^2\right)dt \tag{A.13b}$$

with symmetry relations $\mathcal{F}_c(\Sigma) = -\mathcal{F}_c(-\Sigma)$, $\mathcal{F}_s(\Sigma) = -\mathcal{F}_s(-\Sigma)$. We define the complex

Fresnel integral as

$$\mathcal{F}(\Sigma) = \mathcal{F}_c(\Sigma) + j\mathcal{F}_s(\Sigma) = \int_0^{\Sigma} \exp j\left(\frac{\pi}{2} t^2\right) dt. \tag{A. 14}$$

Then the signal autocorrelation function is simply

$$\psi(A, \bar{A}) = \frac{1}{\Delta\Sigma} \left[\mathcal{F}(\Sigma_f) - \mathcal{F}(\Sigma_i)\right], \tag{A. 15}$$

with the ambiguity function given by its amplitude squared. We now analyze the behavior of these functions.

a. GAF Radial Acceleration

For $\Delta_1 = 0$ we obtain

$$\psi(A, \bar{A}) = \frac{1}{\Sigma} \mathcal{F}(\Sigma) \tag{A. 16}$$

and

$$\phi(A, \bar{A}) = \left|\frac{1}{\Sigma} \mathcal{F}(\Sigma)\right|^2, \tag{A. 17}$$

where

$$\Sigma = \sqrt{a}\, \frac{T}{2} = \sqrt{\frac{\pi}{\lambda} \Delta \left(\frac{v^2 \cos^2\theta}{R_o}\right)}\, \frac{T}{2}.$$

The graph of $\mathcal{F}(\Sigma)$ in the complex plane is given by the cornu spiral.[42, 54] In Fig. 15 we represent Eq. A. 17. The first minimum is at $\Sigma_m \cong 1.9$, and the second local maximum at $\Sigma_{2_m} = 2.26$ where the ambiguity function $\phi(A. \bar{A}) = .132$; that is, the GAF is reduced approximately to 13% of its maximum value 1, which occurs at $\Sigma = 0$.

We proceed with local and asymptotic analyses of expressions (A. 16) and (A. 17). From Abramowitz and Stegun[55] we find that the complex Fresnel integral is equivalent to $\mathcal{F}(\Sigma) = \Sigma M\left(\frac{1}{2}, \frac{3}{2}, j\frac{\pi}{2}\Sigma^2\right)$, where M(a, b, z) is a confluent hypergeometric function defined by the series

$$M(a, b, z) = 1 + \frac{az}{b} + \ldots + \frac{(a)_n z^n}{(b)_n n!},$$

with

$$(a)_n = a(a+1) \ldots (a+n-1), (a)_o = 1.$$

Then letting $\xi = \frac{\pi}{2}\Sigma^2$, we obtain

$$\psi(A, \bar{A}) = M\left(\frac{1}{2}, \frac{3}{2}, j\xi\right)$$

$$= 1 + \sum_{n=1}^{\infty} \frac{1}{1+2n} \frac{\xi^n}{n!}.$$

This can be rearranged in real and imaginary components as

$$\psi(A, \bar{A}) = \left\{1 - \frac{\xi^2}{5 \cdot (2)!} + \sum_{k=2}^{\infty} (-1)^k \frac{1}{1+4k} \frac{\xi^{2k}}{(2k)!}\right\}$$

$$+ j\left\{\frac{\xi^2}{3} - \frac{\xi^3}{7 \cdot (3)!} + \sum_{k=2}^{\infty} (-1)^k \frac{1}{3+4k} \frac{\xi^{2k+1}}{(2k+1)!}\right\}. \qquad \text{(A. 18)}$$

In the neighborhood of $\Sigma = 0$ we have the local approximation for the ambiguity function

$$\phi(A, \bar{A}) \tilde{=} 1 - \frac{4\xi^2}{45} + \frac{2^4}{3^3 \times 5^2 \times 7} \xi^4 + \text{higher order terms.} \qquad \text{(A. 19)}$$

From the asymptotic expansion of the confluent hypergeometric function,[56] for large Σ we obtain

$$\psi(A, \bar{A}) = \Gamma\left(\frac{3}{2}\right) e^{j\frac{\pi}{2}} (j\xi)^{-1/2}$$

$$+ \frac{\Gamma\left(\frac{3}{2}\right)}{\Gamma\left(\frac{1}{2}\right)} \frac{e^{j\xi}}{j\xi}\left\{1 + \frac{1}{2}(j\xi)^{-1} - \frac{3}{2^2}\xi^{-2} + \frac{3 \cdot 5}{2^3}(j\xi)^{-3}\right.$$

$$\left. + \sum_{n=4}^{s} \frac{1 \cdot 3 \cdot 5 \ldots (2n-1)}{2^n} (j\xi)^{-n} + 0(\xi^{-s})\right\}, \qquad \text{(A. 20)}$$

where the remainder converges to zero as

$$0(|\xi|^{-s}) = \frac{1 \cdot 3 \ldots (2s-1)}{2^s} (j\xi)^{-s}\left[\frac{1}{6} - s + (j\xi) + 0(|\xi|^{-1},\right].$$

Up to least order we have

$$\psi(A, \bar{A}) \sim \Gamma\left(\frac{3}{2}\right) e^{j\frac{\pi}{2}} \frac{1}{(j\xi)^{1/2}} \qquad \text{(A. 21a)}$$

and so

$$\phi(A, \bar{A}) \sim \left|\Gamma\left(\frac{3}{2}\right)\right|^2 \frac{1}{\xi} = \frac{1}{2\Sigma^2}. \qquad \text{(A. 21b)}$$

b. General Quadratic GAF

We examine directly the quadratic GAF structure as given by Eq. A. 15. The asymptotic behavior of the GAF as the parameter errors become large is studied by means of the method of stationary phase (MSP).[42] The MSP analysis is applied to the integral form

$$N(k) = \int_a^b \exp[j\, k\mu(x)]\, dx \qquad \text{(A. 22)}$$

based on the fact that for large k the exponential term varies rapidly and the integral tends to zero. The asymptotic analysis quantifies how fast it converges and follows from a Taylor's series expansion of the integral (A. 22). As it turns out, the MSP result depends on the particular behavior of the phase $\mu(x)$ in the observation interval, that is, on its stationary points in $[-X,X]$, i.e., on $x \in [-X, X]$ where $\mu'(x) = 0$.

The MSP analysis can be applied to other integral forms where large parameter values are involved (e.g., large observation interval) when with a suitable change of variables the form can be reduced to (A. 22).

To show that the Fresnel integral defined by Eq. A. 17 can be written equivalently as Eq. A. 22, let ζ be a fixed constant and define $\Sigma = \sqrt{k}\ \zeta$ and $\tau = \sqrt{k}\ \xi$. We have

$$\mathcal{F}(\Sigma) = \sqrt{k}\ \int_0^{\zeta} \exp(jk\xi^2)\, d\xi$$

which has the form of (A. 22). Clearly $k \to \infty$ as $\Sigma \to \infty$. But[42]

$$\mathcal{F}(x) = \sqrt{k} \int_0^x \exp(jk\xi^2)\, d\xi \sim \sqrt{\pi/2} \left[\frac{e^{j\pi/4}}{\sqrt{2}} + \frac{e^{j\frac{\pi}{2}x^2}}{j\pi x} + 0(x^{-1})\right], \qquad \text{(A. 23)}$$

where $0(x^{-1})$ is a function such that

$$x\, 0(x^{-1}) \xrightarrow[x\to\infty]{} 0.$$

Substituting in Eq. A. 15, we have

$$\psi(A, \bar{A}) \sim \frac{\sqrt{\pi/2}}{(\Sigma_f - \Sigma_i) j\pi \Sigma_f \Sigma_i} \left[\Sigma_i \exp j\left(\frac{\pi}{2}\Sigma_f^2\right) - \Sigma_f \exp\left(j\frac{\pi}{2}\Sigma_i^2\right)\right], \qquad \text{(A. 24a)}$$

and recalling the definitions in Eqs. A. 11 and A. 12, we obtain

and so

$$\phi(A, \bar{A}) \sim \left|\Gamma\left(\frac{3}{2}\right)\right|^2 \frac{1}{\xi} = \frac{1}{2\Sigma^2}. \tag{A.21b}$$

b. General Quadratic GAF

We examine directly the quadratic GAF structure as given by Eq. A.15. The asymptotic behavior of the GAF as the parameter errors become large is studied by means of the method of stationary phase (MSP).[42] The MSP analysis is applied to the integral form

$$N(k) = \int_a^b \exp[j\, k\mu(x)]\, dx \tag{A.22}$$

based on the fact that for large k the exponential term varies rapidly and the integral tends to zero. The asymptotic analysis quantifies how fast it converges and follows from a Taylor's series expansion of the integral (A.22). As it turns out, the MSP result depends on the particular behavior of the phase $\mu(x)$ in the observation interval, that is, on its stationary points in $[-X,X]$, i.e., on $x \in [-X, X]$ where $\mu'(x) = 0$.

The MSP analysis can be applied to other integral forms where large parameter values are involved (e.g., large observation interval) when with a suitable change of variables the form can be reduced to (A.22).

To show that the Fresnel integral defined by Eq. A.17 can be written equivalently as Eq. A.22, let ζ be a fixed constant and define $\Sigma = \sqrt{k}\ \zeta$ and $\tau = \sqrt{k}\ \xi$. We have

$$\mathcal{F}(\Sigma) = \sqrt{k}\ \int_0^{\zeta} \exp(jk\xi^2)\, d\xi$$

which has the form of (A.22). Clearly $k \to \infty$ as $\Sigma \to \infty$. But[42]

$$\mathcal{F}(x) = \sqrt{k} \int_0^x \exp(jk\xi^2)\, d\xi \sim \sqrt{\pi/2} \left[\frac{e^{j\pi/4}}{\sqrt{2}} + \frac{e^{j\frac{\pi}{2}x^2}}{j\pi x} + 0(x^{-1})\right], \tag{A.23}$$

where $0(x^{-1})$ is a function such that

$$x\, 0(x^{-1}) \xrightarrow[x\to\infty]{} 0.$$

Substituting in Eq. A.15, we have

$$\psi(A, \bar{A}) \sim \frac{\sqrt{\pi/2}}{(\Sigma_f - \Sigma_i) j\pi \Sigma_f \Sigma_i} \left[\Sigma_i \exp j\left(\frac{\pi}{2}\Sigma_f^2\right) - \Sigma_f \exp\left(j\frac{\pi}{2}\Sigma_i^2\right)\right], \tag{A.24a}$$

and recalling the definitions in Eqs. A.11 and A.12, we obtain

$$\phi(A, \bar{A}) \sim \frac{1}{\left(\frac{T}{2}\right)^2 \left(2\Delta_2 \frac{T}{2}\right)^2}$$

which decays hyperbolically with Δ_2^2, as concluded from Eqs. A.21.

From (A.25) and when (A.26) does not hold, we obtain

$$\phi(A, \bar{A}) \sim < \frac{\pi/2}{\left(\frac{T}{2}\right)^2 \left[\Delta_1 + 2\Delta_2 \frac{T}{2}\right] \left[1 - \frac{2\left(2\Delta_2 \frac{T}{2}\right) \Delta_1}{\left(2\Delta_2 \frac{T}{2}\right)^2 + \Delta_1^2}\right]} . \tag{A.29}$$

A.2.3 Third-Order Approximation

We pursue the approximation analysis a step further, since for SAMS$_o$ third-order effects are required for global identifiability of the three source parameters, as discussed in Section III.

The signal autocorrelation function is simply

$$\psi(A, \bar{A}) \cong \frac{1}{T} \int_{-T/2}^{T/2} \exp j\left(\Delta_1 t + \Delta_2 t^2 + \Delta_3 t^3\right) dt, \tag{A.30}$$

where, as before, we have ignored the contribution of the phase reference Δ_o. By a change of variables, we obtain

$$\psi(A, \bar{A}) \cong \frac{1}{\Delta\Sigma} \int_{\Sigma_i}^{\Sigma_f} \exp j\omega\tau \exp j\ ^3\ d\tau, \tag{A.31a}$$

where

$$\omega = \frac{1}{\Delta_3^{1/3}} \left(\Delta_1 - \frac{\Delta_2^2}{3\Delta_3}\right) \tag{A.31b}$$

$$\Sigma_f = \Delta_3^{1/3} \left(\frac{T}{2} + \frac{1}{3} \frac{\Delta_2}{\Delta_3}\right) \tag{A.31c}$$

$$\Sigma_i = \Delta_3^{1/3} \left(-\frac{T}{2} + \frac{1}{3} \frac{\Delta_2}{\Delta_3}\right) \tag{A.31d}$$

$$\Delta\Sigma = \Sigma_f - \Sigma_i = \Delta_3^{1/3}\, T. \tag{A.31e}$$

Along the Δ_3 axis, i.e., whenever $\Delta_1 = 0$ and $\Delta_2 = 0$ the GAF is simply

$$\phi(A, \bar{A}) = |\psi(A, \bar{A})|^2 = \left| \frac{1}{\Sigma} \int_0^{\Sigma} \cos \tau^3 \, d\tau \right|^2 \tag{A.32}$$

where $\Sigma = \Delta_3^{1/3} \frac{T}{2}$. This function is represented in Fig. 31b. Returning to the general third-order polynomial GAF structure (Eqs. A.31) and assuming that the observation interval goes to infinity ($\Sigma_i \to -\infty$, $\Sigma_f \to +\infty$), we can rewrite the asymptotic ambiguity function structure as

$$\psi(A, \bar{A}) \sim \frac{1}{\Sigma} \int_0^{\infty} \cos(\pm \omega\tau + \tau^3) \, d\tau. \tag{A.33}$$

From Abramowitz and Stegun[57] the integral representation of one of the Airy functions

$$\mathrm{Ai}\left(\pm \frac{x}{(3a)^{1/3}} \right) = \frac{(3a)^{1/3}}{\pi} \int_0^{\infty} \cos(at^3 \pm xt) \, dt;$$

hence, we see that the signal correlation function goes asymptotically as

$$\psi(A, \bar{A}) \sim \frac{\pi}{3^{1/3}} \frac{1}{\Sigma} \mathrm{Ai}\left(\frac{\pm \omega}{3^{1/3}} \right). \tag{A.34a}$$

For the Airy functions we have the following asymptotic expansions:

$$\mathrm{Ai}(z) \sim \frac{1}{2} (\pi^2 z)^{-1/4} \, e^{-\xi} \sum_0^{\infty} (-1)^k \, c_k \xi^{-k}$$

$$\mathrm{Ai}(-z) \sim (\pi^2 z)^{-1/4} \left[\sin\left(\xi + \frac{\pi}{4}\right) \sum_0^{\infty} (-1)^k \, c_{2k} \xi^{-2k} - \cos\left(\xi + \frac{\pi}{4}\right) \sum_0^{\infty} (-1)^k \, c_{2k+1} \xi^{-(2k+1)} \right],$$

where

$$\xi = \frac{2}{3} z^{3/2}$$

$$c_o = 1$$

$$c_k = \frac{\Gamma\left(3k + \frac{1}{2}\right)}{54^k \, k! \, \Gamma\left(k + \frac{1}{2}\right)} = \frac{(2k+1)(2k+3) \ldots (6k-1)}{216^k \, k!}.$$

In particular, the first few terms lead to

$$\mathrm{Ai}(z) \sim \frac{1}{2} (\pi^2 z)^{-1/4} \, e^{-\xi} \left[1 - \frac{5}{72} \xi^{-1} \right]$$

$$\mathrm{Ai}(-z) \sim (\pi^2 z)^{-1/4}\left[\sin\left(\xi+\frac{\pi}{4}\right)-\cos\left(\xi+\frac{\pi}{4}\right)\frac{5}{72}\xi^{-1}\right].$$

Substitution in Eq. A.34a yields for $\omega > 0$

$$\psi(A,\bar{A}) \sim \frac{\pi}{3^{1/3}}\frac{1}{\Sigma}\frac{1}{2}\left(\pi^2\frac{\omega}{3^{1/3}}\right)^{-1/4} e^{-\xi}\left[1-\frac{5}{72}\xi^{-1}\right] \tag{A.34b}$$

and for $\omega < 0$

$$\psi(A,\bar{A}) \sim \frac{\pi}{3^{1/3}}\frac{1}{\Sigma}\frac{1}{2}\left(\pi^2\frac{\omega}{3^{1/3}}\right)^{-1/4}\left[\sin\left(\xi+\frac{\pi}{4}\right)-\cos\left(\xi+\frac{\pi}{4}\right)\frac{5}{72}\xi^{-1}\right], \tag{A.34c}$$

where now

$$\xi = \frac{2}{3}\left(\frac{\omega}{3^{1/3}}\right)^{3/2},$$

with

$$\omega = \frac{1}{\Delta_3^{1/3}}\left(\Delta_1 - \frac{\Delta_2^2}{3\Delta_3}\right).$$

Along the Δ_3 axis (i.e., whenever Eq. A.32 holds),

$$\int_0^{\Sigma}\cos\tau^3\,d\tau - \int_0^{\infty}\cos\tau^3\,d\tau = \frac{\pi\mathrm{Ai}(0)}{3^{1/3}} = \frac{\pi}{3\Gamma(2/3)}. \tag{A.34d}$$

Along this line, and asymptotically,

$$\phi(A,\bar{A}) \sim \left|\frac{1}{\Sigma}\frac{\pi}{3\Gamma(2/3)}\right|^2. \tag{A.34e}$$

A.2.4 General Expression of the GAF

Finally, we consider briefly the asymptotic behavior of the GAF as given by its general expression. We apply the method of stationary phase (MSP). Let n be the first positive integer for which

$$\overset{(n)}{\Delta R}(x_o) \triangleq \left.\frac{d^n \Delta R(x,A,\bar{A})}{dx^n}\right|_{x=x_o} \neq 0 \qquad x_o \in \left[-\frac{T}{2},\frac{T}{2}\right].$$

As the observation interval increases we have the following behavior:

$$\int_{-T/2}^{T/2} \cdot \approx 2f_n(x_o, A, \bar{A}) \exp j\pi/2n, \quad n \text{ even} \tag{A.35}$$

$$\int_{-T/2}^{T/2} \cdot \approx f_n(x_o, A, \bar{A})\, 2 \cos \frac{\pi}{2n}, \quad n \text{ odd} > 1 \tag{A.36}$$

where

$$f_n(x_o, A, \bar{A}) = \exp\left[j \frac{2\pi}{\lambda} \Delta R(x_o, A, \bar{A})\right] \frac{\Gamma(1/n)}{n \sqrt[n]{\frac{2\pi}{\lambda} \frac{d^n \Delta R}{dx^n}\Big|_{x_o}} \Big/ n!}$$

For n = 1, we obtain

$$\int_{-T/2}^{T/2} dx \exp\left[j \frac{2\pi}{\lambda} \Delta R(x, A, \bar{A})\right] \sim \frac{1}{j \frac{2\pi}{\lambda}} \left[\frac{\exp\left[j \frac{2\pi}{\lambda} \Delta R\left(\frac{T}{2}, A, \bar{A}\right)\right]}{\frac{d\Delta R}{dx}\Big|_{T/2}} - \frac{\exp\left[j \frac{2\pi}{\lambda} \Delta R\left(-\frac{T}{2}, A, \bar{A}\right)\right]}{\frac{d\Delta R}{dx}\Big|_{-T/2}} \right]. \tag{A.37}$$

The asymptotic behavior of the GAF is as follows.

If Eq. A.37 holds,

$$\phi(A, \bar{A}) \sim \frac{1}{\left(\frac{2\pi}{\lambda} T\right)^2} \left| \frac{\exp\left[j \frac{2\pi}{\lambda} \Delta R\left(\frac{T}{2}\right)\right]}{\Delta \dot{R}\left(\frac{T}{2}\right)} - \frac{\exp\left[j \frac{2\pi}{\lambda} \Delta R\left(-\frac{T}{2}\right)\right]}{\Delta \dot{R}\left(-\frac{T}{2}\right)} \right|^2. \tag{A.38}$$

which by algebraic manipulation leads to

$$\phi(A, \bar{A}) \sim \frac{1}{\left(\frac{2\pi}{\lambda} \frac{T}{2}\right)^2} \frac{1}{\Delta \dot{R}_+^2} \frac{1}{\Delta \dot{R}_-^2} \left\{\Delta \dot{R}_+^2 + \Delta \dot{R}_-^2 - 2\Delta \dot{R}_+ \Delta \dot{R}_- \cos \frac{2\pi}{\lambda} (\Delta R_+ - \Delta R_-)\right\}, \tag{A.39}$$

$$\sim < \frac{1}{\left(\frac{2\pi}{\lambda} T\right)^2} \left\{ \frac{1}{|\Delta \dot{R}_+|} + \frac{1}{|\Delta \dot{R}_-|} \right\}^2, \tag{A.40}$$

where $\Delta \dot{R}_\pm = \Delta \dot{R}\left(\pm \frac{T}{2}, A, \bar{A}\right)$.

If Eq. A.35 holds, we obtain

$$\phi(A, \bar{A}) \sim \left\{ \frac{1}{T/2} \frac{\Gamma(1/n)}{n \sqrt[n]{\frac{2\pi}{\lambda} \Delta R^{(n)}(x_o)/n!}} \right\}^2. \tag{A.41}$$

If Eq. A.36 holds, the bound (A.41) is multiplied by $\cos^2\left(\frac{\pi}{2n}\right)$.

APPENDIX B

Mean-Square Spread Matrix Computation

The mean-square spread matrix (MSSM) $\mathcal{M}$ has been defined (sec. 2.4) as

$$\mathcal{M} = -\frac{1}{2}\left[\left.\frac{\partial^2 \phi(A, A_a)}{\partial A_i \partial A_j}\right|_{A=A_a}\right]_{i,j}$$

This matrix is a measure of how flat the GAF main lobe is, and it reflects the effects of the geometry on its structure and on the receiver performance. The Cramer-Rao bounds are obtained by scaling $\mathcal{M}$ with a signal energy-to-noise ratio-dependent factor, and the total number of grid cells in the "largest of" step of the estimation algorithm is directly related to the eigenvalues and eigenvectors of $\mathcal{M}$, in particular, to det $\mathcal{M}$.

We shall compute the spread matrix expression and work in general with the $SAMS_o$ problem. We write

$$\phi(A, A_a) = |\psi(A, A_a)|^2 = \psi(A, A_a)\, \psi^*(A, A_a),$$

where A_a is the actual source parameter vector, and $\psi(A, A_a)$ is the signal correlation function defined by Eqs. 13. Differentiating with respect to A_j, we obtain

$$\frac{\partial \phi}{\partial A_j} = 2\ \mathrm{Re}\left\{\psi \frac{\partial \psi^*}{\partial A_j}\right\}.$$

Then differentiating with respect to A_i, we have

$$\frac{\partial^2 \phi}{\partial A_i \partial A_j} = 2\ \mathrm{Re}\left\{\frac{\partial \psi}{\partial A_i}\frac{\partial \psi^*}{\partial A_j} + \frac{\partial^2 \psi^*}{\partial A_i \partial A_j}\right\}. \tag{B.1}$$

Because of the total signal energy normalization,

$$\int_{-X}^{X} |\tilde{s}_n(A)|\,|\tilde{s}_n(A_a)|\,dx = 1.$$

Differentiating this equation twice, we can obtain

$$\left.\frac{\partial^2 \psi^*}{\partial A_i \partial A_j}\right|_{A=A_a} = -\left.\left\langle \frac{\partial \tilde{s}_n}{\partial A_i}, \frac{\partial \tilde{s}_n}{\partial A_j}\right\rangle\right|_{A=A_a},$$

where the inner product notation introduced in Eq. 10c has been used. The first term

in Eq. B.1 is

$$\left.\frac{\partial\psi}{\partial A_i}\,\frac{\partial\psi^*}{\partial A_j}\right|_{A=A_a} = \left\langle \frac{\partial\tilde{s}_n}{\partial A_i},\ \tilde{s}_n \right\rangle \left\langle \frac{\partial\tilde{s}_n}{\partial A_j},\ \tilde{s}_n \right\rangle^*$$

where * stands for complex conjugation. The matrix $\mathcal{M}$ is then given by

$$\mathcal{M} = \mathcal{M}_o - \mathcal{M}_1, \tag{B.2}$$

where

$$\mathcal{M}_{o_{ij}} = \mathrm{Re}\left\{\left\langle \frac{\partial\tilde{s}_n}{\partial A_i},\ \frac{\partial\tilde{s}_n}{\partial A_j} \right\rangle\right\} \tag{B.3}$$

$$\mathcal{M}_{1_{ij}} = \mathrm{Re}\left\{\left\langle \frac{\partial\tilde{s}_n}{\partial A_i},\ \tilde{s}_n \right\rangle \left\langle \frac{\partial\tilde{s}_n}{\partial A_j},\ \tilde{s}_n \right\rangle^*\right\}. \tag{B.4}$$

All quantities are evaluated at the source location parameters, and $\tilde{s}_n$ is defined by expression (13b). The Fisher information matrix (FIM) is given by

$$J = G'(\mathcal{M}_o - \mathcal{M}_1), \tag{B.5}$$

where the gain G' is defined in Eq. 27b.

By direct substitution of the signal expression

$$\left\langle \frac{\partial\tilde{s}_n}{\partial A_i},\ \frac{\partial\tilde{s}_n}{\partial A_j} \right\rangle = \left(\frac{2\pi}{\lambda}\right)^2 \frac{1}{2X}\int_{-X}^{X} \frac{\partial R(x, A)}{\partial A_i}\,\frac{\partial R(x, A)}{\partial A_j}\,dx$$

$$\left\langle \frac{\partial\tilde{s}_n}{\partial A_i},\ \tilde{s}_n \right\rangle = j\,\frac{2\pi}{\lambda}\,\frac{1}{2X}\int_{-X}^{X} \frac{\partial R(x, A)}{\partial A_i}\,dx.$$

The matrices $\mathcal{M}_o$ and $\mathcal{M}_1$ are then

$$\mathcal{M}_o = \left(\frac{2\pi}{\lambda}\right)^2 \frac{1}{2X}\int_{-X}^{X} [\nabla_A R(x, A)][\nabla_A R(x, A)]^T\,dx \tag{B.6}$$

$$\mathcal{M}_1 = \left(\frac{2\pi}{\lambda}\right)^2 \left[\frac{1}{2X}\int_{-X}^{X} \nabla_A R(x, A)\,dx\right]\left[\frac{1}{2X}\int_{-X}^{X} \nabla_A R(x, A)\,dx\right]^T, \tag{B.7}$$

where ∇_A • is the gradient column vector operator with respect to the parameter vector A, and $X = Z/R_o$. Computing the integrands and defining

$$f_1(x,\theta) = \frac{1}{\sqrt{2X}} \frac{1 - x\sin\theta}{\left((1-x\sin\theta)^2 + x^2\cos^2\theta\right)^{1/2}}$$

$$f_2(x,\theta) = \frac{R_o}{v}\frac{1}{\sqrt{2X}} \frac{x - \sin\theta}{\left((1-x\sin\theta)^2 + x^2\cos^2\theta\right)^{1/2}} x$$

$$f_3(x,\theta) = R_o \frac{1}{\sqrt{2X}} \frac{x}{\left((1-x\sin\theta)^2 + x^2\cos^2\theta\right)^{1/2}},$$

we obtain

$$\mathcal{M}_{o_{ij}} = \left(\frac{2\pi}{\lambda}\right)^2 \int_{-X}^{X} f_i f_j \, dx$$

$$\mathcal{M}_{1_{ij}} = \left(\frac{2\pi}{\lambda}\right)^2 \left[\int_{-X}^{X} f_i \, dx\right]\left[\int_{-X}^{X} f_j \, dx\right].$$

By application of the Schwarz inequality, we can see that $\mathcal{M}_{o_{ii}} \geq \mathcal{M}_{1_{ii}}$, $i = 1, 2, 3$, except for the degenerate conditions $X = 0$ (no observer) or $\theta = \pi/2$ (end-fire geometry). Performing the computations, we obtain

$$\mathcal{M}_o = \left(\frac{2\pi}{\lambda}\right)^2 \begin{bmatrix} 1 - \cos^2\theta H_2 & = & = \\ \hline \frac{R_o}{v}(-\sin\theta H_1 + \cos^2\theta H_2) & \left(\frac{R_o}{v}\right)^2\left(\frac{X^2}{3} - \cos^2\theta H_2\right) & = \\ \hline -R_o(H_1 - \sin\theta H_2) & \frac{R_o^2}{v}(-\sin\theta H_2 + H_3) & R_o^2 H_2 \end{bmatrix} \tag{B.8}$$

$$\mathcal{M}_1 = \left(\frac{2\pi}{\lambda}\right)^2 \begin{bmatrix} (F_o - \sin\theta F_1)^2 & = & = \\ \hline \frac{R_o}{v}(F_o - \sin\theta F_1)(F_2 - \sin\theta F_1) & \left(\frac{R_o}{v}\right)^2 (F_2 - \sin\theta F_1)^2 & = \\ \hline -R_o(F_o - \sin\theta F_1) F_1 & \frac{R_o^2}{v}(F_2 - \sin\theta F_1) F_1 & R_o^2 F_1^2 \end{bmatrix} \tag{B.9}$$

where

$$X = \frac{Z}{R_o} = \frac{L/2}{R_o} \text{ for SASS or } \frac{vT}{2R_o} \text{ for MASS and SAMS}$$

$$R = 1 + x^2 - 2x \sin\theta_o$$

$$H_o = \frac{1}{2X}\int_{-X}^{X} \frac{1}{R}\,dx = \frac{1}{\cos\theta}\,\Delta \arctan \qquad \text{(B. 10a)}$$

$$H_1 = \frac{1}{2X}\int_{-X}^{X} \frac{x}{R}\,dx = \frac{1}{2}\,\Delta \ln + \tan\theta\,\Delta \arctan$$

$$H_2 = \frac{1}{2X}\int_{-X}^{X} \frac{x^2}{R}\,dx = 1 + \sin\theta\,\Delta \ln - \frac{\cos 2\theta}{\cos\theta}\,\Delta \arctan \qquad \text{(B. 10b)}$$

$$H_3 = \frac{1}{2X}\int_{-X}^{X} \frac{x^3}{R}\,dx = 2\sin\theta + \frac{1 - 2\cos 2\theta}{2}\,\Delta \ln - \tan\theta(1 + 2\cos 2\theta)\,\Delta \arctan$$

$$F_o = \frac{1}{2X}\int_{-X}^{X} \frac{1}{\sqrt{R}}\,dx = \Delta \text{ arsh}$$

$$F_1 = \frac{1}{2X}\int_{-X}^{X} \frac{x}{\sqrt{R}}\,dx = \Delta\sqrt{R} + \sin\theta\,\Delta \text{ arsh}$$

$$F_2 = \frac{1}{2X}\int_{-X}^{X} \frac{x^2}{\sqrt{R}}\,dx = \frac{1}{2}\left[\frac{1}{2}(1+X^2+2X\sin\theta)^{1/2} + (1+X^2-2X\sin\theta)^{1/2} + 3\sin\theta\,\Delta\sqrt{R} + (3\sin^2\theta - 1)\,\Delta \text{ arsh}\right],$$

where

$$\Delta \arctan = \frac{1}{2X}\left[\text{arsh}\left(-\tan\theta + \frac{x}{\cos\theta}\right)\right]\Bigg|_{-X}^{X} = \frac{1}{2X}\left[\arctan\left(\tan\theta + \frac{X}{\cos\theta}\right) - \arctan\left(\tan\theta - \frac{X}{\cos\theta}\right)\right] \qquad \text{(B. 11)}$$

$$\Delta \text{ arsh} = \frac{1}{2X}\left[\text{arsh}\left(-\tan\theta + \frac{x}{\cos\theta}\right)\right]\Bigg|_{-X}^{X} \qquad \text{(B. 12)}$$

$$\Delta\sqrt{R} = \frac{1}{2X}\left[\sqrt{R}\right]\Big|_{-X}^{X} \qquad \text{(B. 13)}$$

$$\Delta \ln = \frac{1}{2X}\left[\ln R\right]\Big|_{-X}^{X} \qquad \text{(B. 14)}$$

REMARK. With the SASS or MASS problems the second line and column of $\mathcal{M}$ are deleted.

Analyzing the elements of $\mathcal{M}_o$ and $\mathcal{M}_1$ in Eqs. B.8 and B.9, we note that we can rewrite the spread matrix as

$$\mathcal{M} = S\,\mathcal{M}'S, \tag{B.15}$$

where S is the scaling diagonal matrix

$$S = \begin{bmatrix} \frac{1}{R_c} & 0 & \\ 0 & \frac{1}{v} & \\ & & 1 \end{bmatrix} \tag{B.16}$$

and $\mathcal{M}'$ is the spread matrix for the normalized estimation problem, where the parameter vector is

$$A_n = \begin{bmatrix} \frac{R_o}{R_{o_a}} & \frac{v}{v_a} & \sin\vartheta \end{bmatrix}^T. \tag{B.17}$$

The elements of $\mathcal{M}'$ depend only on the source bearing angle and on the geometric parameter $X = Z/R_o$.

APPENDIX C

Asymptotic Behavior of the Mean-Square Spread Matrix

C.1 GENERAL DERIVATION

As discussed in Sections II and III, the mean-square spread matrix (MSSM) $\mathcal{M}$ reflects the effects of the geometry on the receiver performance. We shall study its asymptotic behavior for large values of the geometric parameter, i.e., as $X = \frac{Z}{R_o} \to \infty$, or equivalently as $Y = \frac{1}{X} \to 0$.

We start with Eqs. B.8 to B.14 and make the change of variables $y = x^{-1}$. We define the trinomial $R_{\pm}(x) = 1 + x^2 \pm 2x \sin\theta$, which is abbreviated R_+ or R_- when the variable is understood from the context.

We perform one of the integrations in detail.

$$F_1 = \frac{1}{2X}\int_{-X}^{X} \frac{x}{\sqrt{R_-}}\,dx = -\frac{Y}{2}\left\{\int_{-Y}^{-\infty} \frac{-1}{y^2\sqrt{R_-}}\,dy + \int_{\infty}^{Y} \frac{1}{y^2\sqrt{R_+}}\,dy\right\}$$

$$= \frac{Y}{2}\int_{Y}^{\infty}\left[\frac{1}{y^2\sqrt{R_-}} - \frac{1}{y^2\sqrt{R_+}}\right]dy.$$

These integrals have been tabulated by Gradshteyn and Ryzhik.[58] The final results for all quantities of interest are given below. Set

$$\mathcal{K}_{i_\pm} = \frac{Y}{2}\int_{Y}^{\infty} \frac{1}{y^i R_\pm}\,dy$$

$$\mathcal{F}_{i_\pm} = \frac{Y}{2}\int_{Y}^{\infty} \frac{1}{y^i\sqrt{R_\pm}}\,dy.$$

From Gradshteyn and Ryzhik[59] we have

$$\operatorname{arsh} z = \ln 2z - \sum_{k=1}^{\infty} \frac{(2k)!}{2^{2k}(k!)^2\,2k} z^{-2k}.$$

With

$$|z|^2 = \left|\frac{1 \pm Y\sin\theta}{Y\cos\theta}\right|^2 > 1$$

which is satisfied when $\frac{1}{Y} > 1 + \sin\theta$, or equivalently when $Y < 2$, we obtain $Y[\Delta_+ \operatorname{arsh}]$ of the order $Y\operatorname{Ln} Y + 0(Y^{-3})$ as $Y \to 0$. But $\lim_{Y\to 0} Y^{\epsilon}\operatorname{Ln} Y = 0$ for any $\epsilon > 0$.

The Taylor's series expansions of Eqs. B.11-B.14 lead to

$$\Delta \text{ atan} \cong 2 \cos \theta Y + 0(Y^3)$$

$$\ln \frac{R_-}{R_+} \cong -4 \sin \theta Y + 0(Y^3)$$

$$\Delta_- \text{arsh} \cong -2 \sin \theta Y + 0(Y^3)$$

$$\Delta \sqrt{R} \cong -2 \sin \theta Y + 0(Y^3)$$

$$\sqrt{R_-} + \sqrt{R_+} \cong 2 + \cos^2 \theta Y^2.$$

Substituting in the expressions of H_i and F_i, we obtain

$$H_1 = \mathcal{H}_{1_-} - \mathcal{H}_{1_+} = \frac{\pi}{2} \tan \theta Y + \frac{1}{4} \left[\ln \frac{R_-}{R_+} \right] Y - \frac{\tan \theta}{2} [\Delta \text{ atan}] Y \tag{C.1}$$

$$H_2 = \mathcal{H}_{2_-} + \mathcal{H}_{2_+} = 1 - \frac{\cos 2\theta}{\cos \theta} \frac{\pi}{2} Y + \frac{\sin \theta}{2} \left[\ln \frac{R_-}{R_+} \right] Y + \frac{\cos 2\theta}{2 \cos \theta} [\Delta \text{ atan}] Y \tag{C.2}$$

$$H_3 = \mathcal{H}_{3_-} - \mathcal{H}_{3_+} = \sin \theta - \frac{1 - 4 \sin^2 \theta}{2} \frac{Y}{2} \left[\ln \frac{R_-}{R_+} \right] - \tan \theta (3 - 4 \sin^2 \theta) \frac{Y}{2} [\pi - \Delta \text{ atan}] \tag{C.3}$$

$$F_o = \mathcal{F}_{1_-} - \mathcal{F}_{1_+} = [\text{arsh}(\tan \theta)] Y + \frac{1}{2} [\Delta_- \text{arsh}] Y \tag{C.4}$$

$$F_1 = \mathcal{F}_{2_-} - \mathcal{F}_{2_+} = \frac{1}{2} \Delta \sqrt{R} + \frac{\sin \theta}{2} [\Delta_+ \text{arsh}] Y \tag{C.5}$$

$$F_2 = \mathcal{F}_{3_-} + \mathcal{F}_{3_+} = \frac{1}{4Y} (\sqrt{R_-} + \sqrt{R_+}) + \frac{3}{4} \sin \theta \Delta \sqrt{R} + \frac{Y}{4} (3 \sin^2 \theta - 1) [\Delta_+ \text{arsh}], \tag{C.6}$$

where

$$\nabla \text{atan} = \text{atan} \left(-\tan \theta + \frac{Y}{\cos \theta} \right) + \text{atan} \left(\tan \theta + \frac{Y}{\cos \theta} \right) \tag{C.7}$$

$$\nabla \sqrt{R} = \sqrt{R_-} - \sqrt{R_+} = (1 + Y^2 - 2Y \sin \theta)^{1/2} - (1 + Y^2 + 2Y \sin \theta)^{1/2} \tag{C.8}$$

$$\nabla_\pm \text{arsh} = \text{arsh} \left(\frac{1}{Y \cos \theta} - \tan \theta \right) \pm \text{arsh} \left(\frac{1}{Y \cos \theta} + \tan \theta \right). \tag{C.9}$$

These expressions can be expanded in a Taylor's series about Y = 0, except for $\Delta_+ \text{arsh}$. But we note that $\lim_{Y \to 0} Y[\Delta_+ \text{arsh}] = 0$.

$$H_1 \cong \frac{\pi}{2} \tan \theta Y - 2 \sin^2 \theta Y^2 \tag{C.10}$$

$$H_2 \cong 1 - \frac{\cos 2\theta}{\cos\theta}\frac{\pi}{2}Y + (\cos^2\theta - 3\sin^2\theta)\,Y^2 \tag{C.11}$$

$$H_3 \cong \sin\theta\left[1 - (3 - 4\sin^2\theta)\frac{\pi Y}{2\cos\theta} + 4\cos(2\theta)\,Y^2\right] \tag{C.12}$$

$$F_o \cong Y[\operatorname{arsh}(\tan\theta) - \sin\theta Y] \tag{C.13}$$

$$F_1 \cong -\sin\theta Y + \frac{\sin\theta}{2}[\Delta_+\operatorname{arsh}]\,Y \tag{C.14}$$

$$F_2 \cong \frac{1}{2Y} + \frac{Y}{4}\left[(\cos^2\theta - 6\sin^2\theta) + (3\sin^2\theta - 1)[\Delta_+\operatorname{arsh}]\right]. \tag{C.15}$$

The asymptotic behavior of the MSSM up to first order in $Y = \frac{1}{X} = \frac{R_o}{Z}$ is given by

$$\mathcal{M} \sim \left(\frac{2\pi}{\lambda}\right)^2 \begin{bmatrix} \sin^2\theta + \cos\theta\cos(2\theta)\frac{\pi}{2}Y & \frac{R_o}{v}\left[\cos^2\theta - \frac{1}{2}\left[\operatorname{arsh}(\tan\theta) - \frac{\sin^2\theta}{2}\Delta_+\operatorname{arsh}\right] - \frac{\pi}{2}\frac{Y}{\cos\theta}(\cos^4\theta + \sin^4\theta)\right] & = \\ = & \left(\frac{R_o}{v}\right)^2\left[\frac{1}{12Y^2} - \frac{3\cos^2\theta + 2\cos 2\theta}{4} + \frac{\cos^2\theta}{4}\Delta_+\operatorname{arsh} + \cos\theta\cos(2\theta)\frac{\pi}{2}Y\right] & = \\ R_o\left(-\sin\theta + \frac{\pi}{2}\sin(2\theta)Y\right) & \frac{R_o^2}{v}\left[\frac{\sin\theta}{2}\left(1 - \frac{1}{2}\Delta_+\operatorname{arsh}\right) - \frac{\pi}{2}Y\sin 2\theta\right] & R_o^2\left(1 - \frac{\cos 2\theta}{\cos\theta}\frac{\pi}{2}Y\right) \end{bmatrix} \tag{C.16}$$

Before tackling the inversion of this three-dimensional matrix, we shall first consider the diagonal elements, then the principal minors, and finally return to the full three-dimensional matrix.

C.2 LIMITING BEHAVIOR OF DIAGONAL ELEMENTS

This analysis provides the asymptotic behavior when only one parameter is to be estimated, and the other two are assumed known a priori. We obtain

$$\lim_{Y\to 0} \mathcal{M}_R^{-1} = \lim_{Y\to 0} \frac{\left(\frac{\lambda}{2\pi}\right)^2}{\sin^2\theta + \cos\theta\cos(2\theta)\frac{\pi}{2}Y} = \left(\frac{\lambda}{2\pi}\right)^2 \frac{1}{\sin^2\theta} \tag{C.17}$$

$$\lim_{Y\to 0} \mathcal{M}_v^{-1} = \lim_{Y\to 0} \frac{1}{\mathcal{M}_{22}} \sim \left(\frac{\lambda}{2\pi}\right)^2 \left(\frac{v}{R_o}\right)^2 12Y^2 \tag{C.18}$$

$$\lim_{Y\to 0} \mathcal{M}_{\sin\theta}^{-1} = \lim_{Y\to 0} \frac{\left(\frac{\lambda}{2\pi}\right)^2}{R_o^2\left(1 - \frac{\cos 2\theta}{\cos\theta}\frac{\pi}{2}Y\right)} = \left(\frac{\lambda}{2\pi}\right)^2 \frac{1}{R_o^2}. \tag{C.19}$$

C.3 LIMITING BEHAVIOR OF PRINCIPAL MINORS

C.3.1 Range/Angle Estimation

$$\mathcal{M}_{R_o,\sin\theta} \approx \left(\frac{2\pi}{\lambda}\right)^2 \left[\begin{array}{c|c} \sin^2\theta + \cos\theta\cos(2\theta)\,\frac{\pi}{2}\,Y & R_o\left[-\sin\theta + \frac{\pi}{2}\sin(2\theta)\,Y\right] \\ \hline = & R_o^2\left[1 - \frac{\cos 2\theta}{\cos\theta}\,\frac{\pi}{2}\,Y\right] \end{array}\right]. \tag{C.20}$$

The determinant is

$$\det \mathcal{M}_{R_o,\sin\theta} \sim \left(\frac{2\pi}{\lambda}\right)^4 R_o^2\,\frac{\pi}{2}\,\frac{Y}{\cos\theta}. \tag{C.21}$$

The inverse is

$$\mathcal{M}^{-1}_{R_o,\sin\theta} \approx \left(\frac{\lambda}{2\pi}\right)^2 \left[\begin{array}{c|c} \frac{2}{\pi}\,\frac{\cos\theta}{Y} - \cos 2\theta & \frac{\sin 2\theta}{R_o}\left[\frac{1}{\pi Y} - \cos\theta\right] \\ \hline = & \frac{1}{R_o^2}\left[\frac{2}{\pi}\,\frac{\cos\theta\sin^2\theta}{Y} + \cos^2\theta\cos 2\theta\right] \end{array}\right] \tag{C.22}$$

We study briefly the normalized spread function

$$f_R(\theta, Y) = \frac{2}{\pi}\,\frac{\cos\theta}{Y} - \cos 2\theta \tag{C.23}$$

$$f_\theta(\theta, Y) = \frac{1}{R_o^2}\left[\frac{2}{\pi}\,\frac{\cos\theta\sin^2\theta}{Y} + \cos^2\theta\cos 2\theta\right] \tag{C.24}$$

$$f_{R\theta}(\theta, Y) = \frac{\sin 2\theta}{R_o}\left[\frac{1}{\pi Y} - \cos\theta\right]. \tag{C.25}$$

Note that f_R and f_θ are even functions of θ and $f_{R\theta}$ is odd.

a. Mean-Square Range Spread. From Eq. C.23 we obtain

$$\frac{d^{2n+1}}{d\theta^{2n+1}} f_R(\theta, Y) = (-1)^n\left[-\frac{2\sin\theta}{\pi Y} + 2^{2n+1}\sin 2\theta\right], \quad n = 0, 1, 2, \ldots$$

$$\frac{d^{2n}}{d\theta^{2n}} f_R(\theta, Y) = (-1)^{n+1}\left[-\frac{2\cos\theta}{\pi Y} + 2^{2n}\cos 2\theta\right], \quad n = 1, 2, \ldots$$

In particular, the zeros of the first derivative for $\theta \in \left[0, \frac{\pi}{2}\right]$ are

$$\frac{df_R(\theta, Y)}{d\theta} = 0 \rightarrow \begin{cases} \theta = 0 \\ \text{or} \\ \cos\theta = \frac{1}{2\pi Y} \end{cases}$$

$$\text{At } \theta = 0 \quad \ddot{f}_R = 2\left(-\frac{1}{\pi Y} + 2\right) \rightarrow \begin{cases} \ddot{f}_R < 0 & \text{if } Y < \frac{1}{2} \\ =0 & \text{if } Y = \frac{1}{2} \\ >0 & \text{if } Y > \frac{1}{2} \end{cases}$$

$$\text{At } \cos\theta = \frac{1}{2\pi Y} \rightarrow \ddot{f}_R = -4\sin^2\theta < 0 \quad \text{for } \theta \neq 0$$

$$\text{For } \theta = 0,\ Y = \frac{1}{2\pi} \rightarrow \ddot{f}_R = 0 \text{ but } f_R^{(iv)} = -12 < 0.$$

Conclusions:

For (a) $Y > \frac{1}{2\pi}$, $\theta = 0$ is a local minimum.

For (b) $Y \leq \frac{1}{2\pi}$, $\theta = 0$ is a local maximum

In case (a) a local maximum occurs at $\cos\theta = \frac{1}{2\pi Y}$, while in case (b) the function decreases monotonically to 1 at $\theta = \pi/2$.

b. Mean-Square Bearing Spread. We observe that $f_\theta(0) = 1$, $f_\theta\left(\frac{\pi}{2}\right) = 0$ and $\dot{f}_\theta = 0$ for $\theta = 0$, which is a stationary point. For $Y \ll \frac{1}{\pi}$ a second stationary point, which is a maximum, occurs at approximately $\cos\theta \approx \frac{1}{\sqrt{3}} \rightarrow \theta \approx 55°$.

A pictorial representation of these functions is given in Section II, Figs. 22 and 23.

C.3.2 Range/Velocity Estimation

We obtain from Eq. C.16 the inverse range/velocity minor

$$\mathcal{M}^{-1}_{R_o,v} \sim \left(\frac{\lambda}{2\pi}\right)^2 \left[\begin{array}{c|c} \frac{1}{\sin^2\theta} & -\frac{v}{R_o} 12Y^2 \frac{1}{\sin^2\theta}\left[\cos^2\theta - \frac{1}{2}\left[\text{arsh}(\tan\theta) - \frac{\sin^2\theta}{2}\Delta_+\text{arsh}\right]\right] \\ \hline = & \left(\frac{v}{R_o}\right)^2 12Y^2 \end{array}\right] \tag{C.26}$$

where the determinant

$$\det \mathcal{M}_{R_o,v} \sim \left(\frac{2\pi}{\lambda}\right)^2 \left(\frac{R_o}{v}\right)^2 \frac{\sin^2\theta}{12Y^2}. \tag{C.27}$$

Up to lowest order

$$\left(\mathcal{M}^{-1}_{R_o,v}\right)_{R_o} \sim \left(\frac{\lambda}{2\pi}\right)^2 \frac{1}{\sin^2\theta} \tag{C.28}$$

$$\left(\mathcal{M}^{-1}_{R_o,v}\right)_{v} \sim \left(\frac{\lambda}{2\pi}\right)^2 \left(\frac{v}{R_o}\right)^2 12Y^2. \tag{C.29}$$

C.3.3 Velocity/Bearing Estimation

Again, from Eq. C.16, for the inverse of the velocity/bearing minor we obtain

$$\mathcal{M}^{-1}_{v,\sin\theta} \sim \left(\frac{\lambda}{2\pi}\right)^2 \left[\begin{array}{c|c} \left(\frac{v}{R_o}\right)^2 12Y^2 & \frac{v}{R_o^2}\frac{\sin\theta}{2}\left[1-\frac{1}{2}\Delta_+ \operatorname{arsh}\right]12Y^2 \\ \hline = & \frac{1}{R_o^2} \end{array}\right] \tag{C.30}$$

$$\det \mathcal{M}_{v,\sin\theta} \sim \left(\frac{2\pi}{\lambda}\right)^4 \frac{R_o^4}{v^2}\frac{1}{12Y^2}. \tag{C.31}$$

Finally, we consider the full three-dimensional problem.

C.4 SAMS MEAN-SQUARE SPREAD MATRIX

The determinant and $\mathcal{M}^{-1}$ are computed directly from Eq. C.16.

$$\det \mathcal{M} \sim \left(\frac{2\pi}{\lambda}\right)^6 \frac{R_o^4}{v^2}\frac{\pi}{2}\frac{1}{12}\frac{1}{\cos\theta}\frac{1}{Y}. \tag{C.32}$$

$$\mathcal{M}^{-1} \sim \left(\frac{\lambda}{2\pi}\right)^2 \left[\begin{array}{c|c|c} \frac{2\cos\theta}{\pi Y} - \cos 2\theta & -\frac{v}{R_o}\left[1-\frac{\sin^2\theta}{2}-\frac{1}{2}\operatorname{arsh}(\tan\theta)\right]\frac{2}{\pi}12\cos\theta Y & -\frac{1}{R_o}\frac{\sin 2\theta}{\pi Y} \\ \hline = & \left(\frac{v}{R_o}\right)^2 12Y^2 & -\frac{v}{R_o^2}\sin\theta\left[1-\frac{\sin^2\theta}{2}-\frac{1}{2}\operatorname{arsh}(\tan\theta)\right]\frac{2}{\pi}12\cos\theta Y \\ \hline = & = & \left[\frac{2\cos\theta\sin^2\theta}{\pi Y}+\cos^2\theta\cos 2\theta\right]\frac{1}{R_o^2} \end{array}\right] \tag{C.33}$$

C.5 VERY LONG BASELINE INTERFEROMETRY (RANGE/BEARING)

In Fig. 25 we illustrated a linear observer composed of three widely separated short collinear arrays. We shall derive the Cramer-Rao performance bounds for the range

and bearing parameters, under the following assumptions.

H1: $R_o \gg \Delta L$, i.e., the source/observer center separation is much larger than the physical dimensions of the individual linear sensors.

H2: $R_o \ll L$, i.e., the source/receiver center separation is much smaller than the total observer system dimension.

Under H1 we linearize the range phase function across each individual stave about its geometric center. We obtain

$$R(x) = (r_o + x^2 - 2xr_o \sin\theta)^{1/2} \approx r_o - \sin\theta x \quad \text{for } x \in (-\epsilon, \epsilon)$$

$$\approx R(1) - \sin\theta_{L/2}(x-1) \quad \text{for } x \in ((1-\epsilon),(1+\epsilon))$$

$$\approx R(-1) - \sin\theta_{-L/2}(x+1) \quad \text{for } x \in (-(1+\epsilon),-(1-\epsilon)).$$

But

$$\sin\theta_{\pm L/2} = \cos\left(\frac{\pi}{2} - \theta_{\pm L/2}\right) = -\cos\left(\frac{\pi}{2} - |\theta_{\pm L/2}|\right).$$

Under H2

$$\theta_{L/2} \cong -\theta_{-L/2} = \theta_L,$$

and we can approximate

$$\cos\left(\frac{\pi}{2} - |\theta_{\pm L/2}|\right) \approx 1 - \left(\frac{\pi}{2} - \theta_L\right)^2 \frac{1}{2}.$$

Also

$$\frac{\pi}{2} - \theta_L \approx \sin\left(\frac{\pi}{2} - \theta_L\right) \approx \tan\left(\frac{\pi}{2} - \theta_L\right) = \frac{R_o \cos\theta}{\frac{L}{2} - R_o \sin\theta} \cong r_o \cos\theta,$$

so that

$$\sin\theta_{\pm L/2} \approx \mp\left[1 - \frac{r_o^2 \cos^2\theta}{2}\right].$$

We then have

$$R(x) \approx \begin{cases} r_o - \sin\theta x \quad \text{for } x \in [-\epsilon, \epsilon] & \text{(C.34)} \\ R(1) + \left(1 - \dfrac{r_o^2 \cos^2\theta}{2}\right)(x-1) \quad \text{for } x \in [1-\epsilon, 1+\epsilon] & \text{(C.35)} \\ R(-1) - \left(1 - \dfrac{r_o^2 \cos^2\theta}{2}\right)(x+1) \quad \text{for } x \in [-(1+\epsilon), -(1-\epsilon)] & \text{(C.36)} \end{cases}$$

To compute the spread matrix, we need the gradient of R(x) with respect to the

parameter vector $[R_o \sin\theta]^T$. Because of the Rayleigh model, in subsequent computations we ignore the presence of the zeroth-order term in the phase approximations Eqs. C.34-C.36. We arrive at

$$\mathcal{M} = \left(2\pi \frac{L/2}{\lambda}\right)^2 \frac{1}{3}\epsilon^3 r_o^2 \left[\begin{array}{c|c} \dfrac{\cos^4\theta}{(L/2)^2} & -\dfrac{\cos^2\theta}{(L/2)} \sin\theta r_o \\ \hline = & \dfrac{1}{r_o^2} + \sin^2\theta r_o^2 \end{array}\right] \tag{C.37}$$

$$\det \mathcal{M} = \left[\left(2\pi \frac{L/2}{\lambda}\right)^2 \frac{1}{3}\epsilon^3 r_o^2\right]^2 \frac{\cos^4\theta}{(L/2)^2 r_o^2} \tag{C.38}$$

$$\mathcal{M}^{-1} \approx \frac{1}{m}\left[\begin{array}{c|c} \left(\dfrac{L/2}{\cos^2\theta}\right)^2 + \left(\dfrac{L/2 \sin\theta r_o^2}{\cos^2\theta}\right)^2 & \dfrac{L/2 \sin\theta r_o^3}{\cos^2\theta} \\ \hline = & r_o^2 \end{array}\right] \tag{C.39}$$

where

$$m = \left(2\pi \frac{L/2}{\lambda}\right)^2 \frac{1}{3}\epsilon^3 r_o^2. \tag{C.40}$$

The Cramer-Rao bounds are given by

$$\sigma_{R_o} \approx G^{-1/2}\left(\mathcal{M}^{-1}\right)_{11}^{1/2} \approx G^{-1/2}\ \sqrt{3}\ \frac{1}{\pi}\left(\frac{L/2}{\Delta L}\right)^{1/2}\left(\frac{L/2}{R_o \cos\theta}\right)^2 \frac{1}{\Delta L/\lambda} R_o \left[1 + \frac{r_o^4 \sin^2\theta}{2}\right] \tag{C.41}$$

$$\sigma_{\sin\theta} \approx G^{-1/2}\left(\mathcal{M}^{-1}\right)_{22}^{1/2} \approx G^{-1/2}\ \sqrt{3}\ \frac{1}{\pi}\left(\frac{L/2}{\Delta L}\right)^{1/2}\left(\frac{1}{\Delta L/\lambda}\right). \tag{C.42}$$

But from Eq. 27c

$$G^{-1/2} = \frac{\alpha}{(SNR_{eff})^{1/2}} \frac{1}{\sqrt{LT}}. \tag{C.43}$$

We obtain

$$\sigma_{\sin\theta} \approx \frac{\alpha}{(SNR_{eff})^{1/2}} \frac{1}{(\Delta LT)^{1/2}} \sqrt{\frac{3}{2}} \frac{1}{\pi} \left(\frac{1}{\Delta L/\lambda}\right) \tag{C.44}$$

and

$$\sigma_{R_o} \approx \sigma_{\sin\theta} \tan^2\theta_L R_o. \tag{C.45}$$

APPENDIX D

Taylor's Series Approximation to Four-Dimensional SAMS Mean-Square Spread Matrix

We present the local analysis expressions for the mean-square spread matrix $\mathcal{M}$, its classical adjoint $\tilde{\mathcal{M}}$, the inverse $\mathcal{M}^{-1}$, and the determinant det $\mathcal{M}$. The results are so extensive that most of the time we restrict ourselves to the last-order terms. In actual computations we have used the required higher order terms to obtain the exact coefficients for the terms of interest in det $\mathcal{M}$, and also to preserve the positive-definite character of $\mathcal{M}$. In particular, we stress that when certain equalities between elements of $\mathcal{M}$ or $\mathcal{M}^{-1}$ occur such as $\tilde{\mathcal{M}}_{33} = \frac{\tilde{\mathcal{M}}_{22}}{v^2} \sin\theta_t^2$ they are intended only as an economy in notation, and it is to be understood that the equality holds only for the least order terms exhibited in this appendix and not for the higher order terms that have to be considered when manipulating the matrices. We use the notation

$$X_{\ell_c} = X_\ell \cos\theta_\ell = \frac{L}{2R_o}\cos\theta_\ell$$

$$X_{t_c} = X_t \cos\theta_t = \frac{vT}{2R_o}\cos\theta_t$$

$$X_{i_s} = X_i \sin\theta_i, \quad i = \ell, t.$$

Mean-Square Spread Matrix

$$\mathcal{M}_{11} = \left(\frac{2\pi}{\lambda}\right)^2 \frac{1}{9}\left(X_{c_\ell}^4 + 5X_{c_\ell}^2 X_{c_t}^2 + X_{c_t}^4\right)$$

$$\mathcal{M}_{22} = \left(\frac{2\pi}{\lambda}\right)^2 \left(\frac{R_o}{v}\right)^2 X_t^2 \left[\frac{\sin\theta_t^2}{3} + \frac{X_\ell^2}{9}\cos\theta_\ell\cos(\theta_\ell + 2\theta_t) + \frac{(\cos\theta_t X_t)^2}{5}\left(\frac{4\cos\theta_t^2}{9} - 3\sin^2\theta_t\right)\right]$$

$$\mathcal{M}_{ii} = \left(\frac{2\pi}{\lambda}\right)^2 R_o^2 X_{a_i}^2 \left[\frac{1}{3} - \frac{\cos\theta_{a_j}}{9\cos\theta_i^2} X_{a_j}^2 \cos\left(\theta_{a_j} + 2\theta_{a_i}\right) + \frac{X_{a_i}^2}{5}\left(\frac{31\sin^2\theta_{a_i}}{9} - 1\right)\right].$$

For $i = 3$, $a_i = t$, $a_j = \ell$; for $i = 4$, $a_i = \ell$, $a_j = t$.

$$\mathcal{M}_{12} = \left(\frac{2\pi}{\lambda}\right)^2 \frac{R_o}{v} X_t^2 \left[\frac{X_{tc}^2}{5}\left(\sin^2\theta_t - \frac{2\cos^2\theta_t}{9}\right) - \frac{X_\ell^2\cos\theta_\ell}{9}\cos(2\theta_t + \theta_\ell)\right]$$

$$\mathcal{M}_{1i} = \left(\frac{2\pi}{\lambda}\right)^2 R_o \frac{X_{\alpha_i}^2}{9}\left[\frac{11\cos\theta_{\alpha_i}^2 \sin\theta_{\alpha_i}}{5} X_{\alpha_i}^2 + 2\cos\theta_{\alpha_j}\cos(\theta_{\alpha_i} - \theta_{\alpha_j})\right].$$

The same convention applies for i, α_i, α_j.

$$\mathcal{M}_{23} = \left(\frac{2\pi}{\lambda}\right)^2 \frac{R_o^2}{v} X_t^2\left[\frac{\sin\theta_t}{3} + \frac{\sin\theta_t}{2} X_t^2\left(\frac{3\sin^2\theta_t}{5} - \frac{7\cos\theta_t^2}{9} - \frac{1}{5}\right) - \frac{\cos\theta_\ell}{9\cos\theta_t} X_\ell^2 \sin(\theta_\ell + 2\theta_t)\right]$$

$$\mathcal{M}_{24} = \left(\frac{2\pi}{\lambda}\right)^2 \frac{R_o^2}{v} \frac{X_\ell^2 X_t^4}{9\cos\theta_\ell}\left[-\sin(2\theta_\ell + 2\theta_t) - \cos\theta_t \sin\theta_t - \sin\theta_\ell \cos\theta_\ell \sin^2\theta_t\right]$$

$$\mathcal{M}_{34} = \left(\frac{2\pi}{\lambda}\right)^2 R_o^2 \frac{X_\ell^2 X_t^2}{3}\left[\frac{\cos\theta_\ell \sin\theta_t^2}{3\cos\theta_t} + \frac{\cos\theta_t \sin\theta_\ell^2}{3\cos\theta_\ell} + \sin\theta_\ell \sin\theta_t - \frac{2\cos\theta_\ell \cos\theta_t}{3}\right].$$

Classical Adjoint Matrix M

$$\tilde{\mathcal{M}}_{11} = \left(\frac{2\pi}{\lambda}\right)^6 \frac{R_o^6}{v^2} \frac{X_\ell^2 X_t^4}{3^4 \cos\theta_t^2}\left[\frac{4}{5} X_{t_c}^2 + X_{\ell_c}^2\right]$$

$$\tilde{\mathcal{M}}_{22} = \left(\frac{2\pi}{\lambda}\right)^6 R_o^4 \frac{X_\ell^2 X_t^2}{3^4}\left[\frac{X_{t_c}^4}{5} + X_{\ell_c}^2 X_{t_c}^2 + \frac{X_{\ell_c}^4}{5}\right]$$

$$\tilde{\mathcal{M}}_{33} = \frac{\tilde{\mathcal{M}}_{22}}{v^2} \sin\theta_t^2$$

$$\tilde{\mathcal{M}}_{44} = \left(\frac{2\pi}{\lambda}\right)^6 R_o^4 \frac{1}{3^5 \times 5} \frac{\cos^2\theta_\ell}{\cos\theta_t^2} X_\ell^2 X_t^2\left[X_{t_c}^4 + \frac{4}{5} X_{\ell_c}^2 X_{t_c}^2 + X_{\ell_c}^4\right]$$

$$\tilde{\mathcal{M}}_{12} = \left(\frac{2\pi}{\lambda}\right)^6 \frac{R_o^5}{v} \frac{X_\ell^2 X_t^4}{3^4}\left[\frac{2}{5} X_{t_c}^2 + X_{\ell_c}^2\right]$$

$$\tilde{\mathcal{M}}_{13} = -\frac{\tilde{\mathcal{M}}_{12}}{v} \sin\theta_t$$

$$\tilde{\mathcal{M}}_{23} = -\frac{\tilde{\mathcal{M}}_{22}}{v} \sin\theta_t$$

$$\tilde{\mathcal{M}}_{14} = -\left(\frac{2\pi}{\lambda}\right)^6 \frac{R_o^5}{v^2} \frac{X_\ell^2 X_t^2}{3^5 \times 5} \left[2\cos\theta_t (3\cos\theta_\ell \sin\theta_t + 2\cos\theta_t \sin\theta_\ell) X_t^4 \right.$$

$$\left. + \frac{\cos^2\theta_\ell (25\cos\theta_\ell \sin\theta_t + 44\cos\theta_t \sin\theta_\ell)}{5\cos\theta_t} X_\ell^2 X_t^2 + \frac{11\cos\theta_\ell^4 \sin\theta_\ell X_\ell^4}{\cos\theta_t^2} \right]$$

$$\tilde{\mathcal{M}}_{24} = -\left(\frac{2\pi}{\lambda}\right)^6 \frac{R_o^4}{v} \frac{X_\ell^2 X_t^4}{3^5 \times 5} \left\{ \cos\theta_t^3 (3\cos\theta_\ell \sin\theta_t + 2\cos\theta_t \sin\theta_\ell) X_t^4 \right.$$

$$+ \frac{\cos\theta_\ell^2 \cos\theta_t (25\cos\theta_\ell \sin\theta_t + 22\cos\theta_t \sin\theta_\ell)}{5} X_\ell^2 X_t^2$$

$$\left. - \frac{\cos\theta_\ell^4 (\cos\theta_\ell \sin\theta_t - 9\cos\theta_t \sin\theta_\ell)}{\cos\theta_t} X_\ell^4 \right\}$$

$$\tilde{\mathcal{M}}_{34} = -\tilde{\mathcal{M}}_{24} \sin\theta_t .$$

Inverse Matrix

We present explicitly only the diagonal elements.

$$(\mathcal{M}^{-1})_{11} = \left(\frac{\lambda}{2\pi}\right)^2 \frac{3^2 \cdot 5}{X_{c_\ell}^4} \left[1 - \frac{X_{t_c}^4}{X_{\ell_c}^4 + \frac{4}{5} X_{\ell_c}^2 X_{t_c}^2 + X_{t_c}^4} \right]$$

$$(\mathcal{M}^{-1})_{22} = \left(\frac{\lambda}{2\pi}\right)^2 \frac{v^2}{R_o^2} \frac{3^2 \cdot 5\cos^2\theta_t}{\cos^2\theta_\ell} \frac{1}{X_\ell^2 X_t^2} \left[1 - \frac{4}{5} \frac{1 - \frac{1}{4} X_{p_{eq_c}}^2}{1 + \frac{4}{5} X_{p_{eq_c}}^2} \right]$$

$$(\mathcal{M}_{33})^{-1} = \frac{(\mathcal{M}^{-1})_{22}}{v^2} \sin^2\theta_t$$

$$(\mathcal{M}^{-1})_{44} = \left(\frac{\lambda}{2\pi}\right)^2 \frac{3}{X_\ell^2}$$

where

$$X_{p_{eq_c}}^2 = \frac{1}{\frac{1}{X_{\ell_c}^2} + \frac{1}{X_{t_c}^2}}$$

Determinant of $\mathcal{M}$

$$\det \mathcal{M} = \left(\frac{2\pi}{\lambda}\right)^8 \frac{R_c^6}{v^2} \frac{1}{3^6 \cdot 5} \frac{\cos^2\theta_\ell}{\cos^2\theta_t} X_\ell^4 X_t^4 \left[X_{\ell_c}^4 + \frac{4}{5} X_{\ell_c}^4 X_{t_c}^2 + X_{t_c}^4 \right].$$

Acknowledgement

There are several people to whom I would like to express my gratitude.

Professor Arthur B. Baggeroer gave me his advice and support throughout my stay at M.I.T. The numerous technical discussions that we had contributed greatly toward shaping and developing this work.

Dr. Kenneth D. Senne, one of the readers of my thesis, met with me frequently during the last two and a half years. His knowledge and advice had a direct influence in the evolution of my thesis research.

Professor Harry L. Van Trees provided the original interest that introduced me to the subject.

Professor Alan S. Willsky willingly served as a thesis reader, and made many useful comments.

The companionship of my former officemate, Professor José P. Albuquerque of Pontificia Universidade Católica, Brasil, made my first three years at M.I.T. easier in all respects.

My officemates, Kenneth B. Theriault, whom I bothered with all sorts of questions and who read part of the manuscript, Leroy C. Pusey, Louis S. Metzger, and Stanley R. Robinson, with whom I had many interesting discussions, deserve my thanks.

I also want to acknowledge assistance from the following organizations: Information Processing Center and Project MAC, especially for its MACSYMA program, at M.I.T. and Instituto de Alta Cultura, and Instituto Superior Técnico, Universidade Técnica de Lisboa, Portugal, for supporting my graduate education at M.I.T.

References

1. E. E. Westerfield, "Determination of Position of a Drifting Buoy by Means of the Navy Navigation Satellite System," IEEE International Conference on Engineering in the Ocean Environment, Ocean 72, pp. 443-446.

2. R P. Porter, R. C. Spindel, and R. J. Jaffee, "CW Beacon System for Hydrophone Motion Determination," J. Acoust. Soc. Am. 53, 1691-1699 (1973).

3. R. C. Spindel and R. P. Porter, "Precision Tracking Systems for Sonobuoys," IEEE International Conference on Engineering in the Ocean Environment, Ocean 74, Vol. II.

4. D. T. Acheson, "Radiosonde Tracking with Loran C, Omega and Other Transmitters," Second Symposium on Meteorological Observations and Instrumentation, American Meteorological Society, San Diego, California, March 27-30, 1972.

5. J. M. Beukers, "Integrated Upper and Meteorological Sounding Systems," Second Symposium on Meteorological Observations and Instrumentation, American Meteorological Society, San Diego, California, March 27-30, 1972.

6. IEEE Transactions on Geoscience Electronics, Special Issue on Data Collection from Multiple Earth Platforms, Vol. GE-13, No. 1, January 1975.

7. R. W. Bass, R. E. Mortensen, V. D. Norum, B. Shawaf, and H. W. Sorensen, "ASW Target Motion and Measurement Models," Technical Report 72-024-01, Computer Software Analysts, Inc., Los Angeles, California, September 1972.

8. J. M. Beukers, "A Review and Applications of VLF and LF Transmissions for Navigation and Tracking," Navigation: Journal of the Institute of Navigation, Vol. 21, No. 2, pp. 117-133, Summer 1974.

9. A. E. Fiore and P. Rosenberg, "Earth Satellite Systems for Marine and Transoceanic Air Navigation and Traffic Control," Navigation: Journal of the Institute of Navigation, Vol. 17, No. 3, pp. 234-245, Fall 1970.

10. K. D. McDonald, "A Survey of Satellite-Based Systems for Navigation, Position Surveillance, Traffic Control and Collision Avoidance," Navigation: Journal of the Institute of Navigation, Vol. 20, No. 4, pp. 301-320, Winter 1973-1974.

11. C. Counselman, "Radio Interferometry Course Notes," Department of Earth Sciences, M.I.T., Fall Term 1973.

12. R. C. Kolb and F. H. Hollister, "Bearings Only Target Motion Estimates," U.S. Naval Electronics Laboratory Center, San Diego, California, 1968.

13. V. H. MacDonald and P. M. Schultheiss, "Optimum Passive Bearing Measurement in a Spatially Incoherent Noise Environment," J. Acoust Soc. Am. 46, 37-43 (1969).

14. W. J. Bangs, "Array Processing with Generalized Beam-Formers," Ph.D. Thesis, Yale University, New Haven, Connecticut, September 1971.

15. W. J. Bangs and P. M. Schultheiss, "Space-Time Processing for Optimal Parameter Estimation," in J. W. R. Griffiths, P. L. Stocklin, and C. van Schooneveld (Eds.), Signal Processing (Academic Press, Inc., New York, 1973).

16. Proc. IEEE, Special Issue on Rays and Beams, Vol. 62, pp. 1409-1618, 1974.

17. A. B. Baggeroer, "High Resolution Velocity/Depth Spectra Estimation for Seismic Profiling," IEEE International Conference on Engineering in the Ocean Environment, Ocean 74, Vol. II, pp. 201-211.

18. M. T. Taner and F. Koehler, "Velocity Spectra-Digital Computer Derivation and Applications of Velocity Function," Geophys., Vol. 34, No. 6, pp. 859-881, December 1969.

19. P. Beckmann and A. Spizzichino, Scattering of Electromagnetic Waves from Rough Surfaces (Pergamon Press, New York, 1963).

20. J. M. F. Moura, "Estimation of the Dynamics of a Moving Source by an Integrated Spatial and Temporal Processing," S. M. Thesis, Department of Electrical Engineering, M. I. T., 1973.

21. J. M. F. Moura, H. L. Van Trees, and A. B. Baggeroer, "Space/Time Tracking by a Passive Observer," Proc. Fourth Symposium on Nonlinear Estimation Theory and Its Applications, San Diego, California, September 10-12, 1973.

22. R. O. Harger, Synthetic Aperture Radar Systems. Theory and Design (Academic Press, Inc., New York, 1970).

23. H. L. Van Trees, Detection, Estimation, and Modulation Theory: Part 2. Nonlinear Modulation Theory (John Wiley and Sons, Inc., New York, 1971).

24. H. L. Van Trees, Detection, Estimation, and Modulation Theory: Part 3. Radar-Sonar Signal Processing and Gaussian Signals in Noise (John Wiley and Sons, Inc., New York, 1971).

25. Ibid., Chap. 10.

26. P. M. Woodward, Probability and Information Theory, with Applications to Radar (McGraw-Hill Book Company, New York, 1955).

27. E. J. Kelly, "The Radar Measurement of Range, Velocity, and Acceleration," IRE Trans. on Military Electronics, Vol. MIL-5, No. 2, pp. 51-57, April 1961; E. J. Kelly and R. P. Wishner, "Matched-Filter Theory for High-Velocity Targets," IEEE Trans. on Military Electronics, Vol. MIL-9, No. 1, pp. 56-64, January 1965.

28. A. B. Baggeroer, "Space/Time Random Processes and Optimum Array Processing," U.S. Naval and Undersea Center Report, 1973 (preliminary copy).

29. H. L. Van Trees and A. B. Baggeroer, Multidimensional and Multivariable Processes (John Wiley and Sons, Inc., New York, 1975).

30. M. Abramowitz and Irene A. Stegun, Handbook of Mathematical Functions (Dover Publications, New York, 1965).

31. H. L. Van Trees, Detection, Estimation, and Modulation Theory: Part 1. Detection, Estimation, and Linear Modulation Theory (John Wiley and Sons, Inc., New York, 1968).

32. H. L. Van Trees, Detection, Estimation, and Modulation Theory: Part 3, op. cit., see Appendix.

33. Proc. IEEE, Special Issue on Radio and Radar Astronomy, Vol. 61, No. 9, pp. 1164-1376, September 1973.

34. H. F. Hinteregger, "Geodetic and Astronometric Applications of Very Long Baseline Interferometry," Ph.D. Thesis, Department of Electrical Engineering, M. I. T., June 1972.

35. A. E. E. Rogers, "Very Long Baseline-Interferometry with Large Effective Bandwidth for Phase-Delay Measurements," Radio Sci. 5, 1239-1248 (1970).

36. J. N. Pierce, "Theoretical Diversity Improvement in Frequency-Shift Keying," Proc. IRE 46, 903-910 (1958).

37. S. M. Sussman, "Simplified Relations for Bit and Character Error Probabilities for M-ary Transmission over Rayleigh Fading Channels," IEEE Trans. on Communication Technology, Vol. COM-12, No. 4, pp. 207-209, December 1964.

38. E. J. Kelly, I. S. Reed, and W. L. Root, "The Detection of Radar Echoes in Noise," Parts I and II, J. SIAM 8, 309-341 (1960).

39. D. Middleton and H. L. Groginsky, "Detection of Random Signals by Receivers with Distributed Elements: Optimum Receiver Structures for Normal Signals and Noise Fields," J. Acoust. Soc. Am. 38, 727-737 (1965).

40. H. Urkowitz, C. A. Hauer, and J. F. Koval, "Generalized Resolution in Radar Systems," Proc. IRE 50, 2093-2105 (1962).

41. S. Pasupathy and A. N. Venetsanopoulos, "Optimum Active Array Processing Structure and Space/Time Factorability," IEEE Trans. on Aerospace and Electronics Systems, Vol. AES-10, No. 6, pp. 770-778, November 1974.

42. A. Papoulis, Systems and Transforms with Applications in Optics (McGraw-Hill Book Company, New York, 1968).

43. W. C. Lindsey, Synchronization Systems in Communication and Control (Prentice-Hall, Inc., Englewood Cliffs, N. J., 1972).

44. W. C. Lindsey and M. K. Simon, Telecommunication Systems Engineering (Prentice-Hall, Inc., Englewood Cliffs, N. J., 1973).

45. F. J. Charles and W. C. Lindsey, "Some Analytical and Experimental Phase-Locked Loop Results for Low Signal-to-Noise Ratios," Proc. IEEE 54, 1152-1166 (1966).

46. J. R. Rowbotham and R. W. Sanneman, "Random Characteristics of the Type II Phase-Locked Loop," IEEE Trans. on Aerospace and Electronics Systems, Vol. AES-3, No. 4, pp. 604-612, July 1967.

47. A. J. Viterbi, Principles of Coherent Communication (McGraw-Hill Book Company, New York, 1966).

48. M. Kayton and W. R. Fried (Eds.), Avionics Navigation Systems (John Wiley and Sons, Inc., New York, 1969).

49. R. L. Easton, "The Role of Time/Frequency in Navy Navigation Satellites," Proc. IEEE 60, 557-563 (1972).

50. E. Ehrlich, "The Role of Time/Frequency in Satellite Position Determination Systems," Proc. IEEE 60, 564-571 (1972).

51. S. Pasupathy and P. M. Schultheiss, "Passive Detection of Gaussian Signals with Narrow-Band and Broad-Band Components," J. Acoust. Soc. Am. 56, 917-921 (1974).

52. L. Metzger, Ph.D. Thesis, Department of Electrical Engineering and Computer Science, M. I. T., October 1, 1975.

53. R. S. Bucy, "Building and Evaluating Nonlinear Filters," in J. B. Keller and H. P. McKean (Eds.), Stochastic Differential Equations (American Mathematical Society, Providence, R. I., 1973), pp. 189-190; R. S. Bucy, C. Hecht, and K. D. Senne, "An Engineer's Guide to Building Nonlinear Filters," Technical Report SRL-TR-72-0004 (Vol. 1, 2), Frank J. Seiler Research Laboratory, Air Force Systems Command, U.S. Air Force Academy, Colorado, May 1972.

54. J. W. Goodman, Introduction to Fourier Optics (McGraw-Hill Book Company, San Francisco, 1968).

55. M. Abramowitz and Irene A. Stegun, op. cit., p. 301.

56. Ibid., expansion 13.5.1, p. 508.

57. Ibid., integral representation 10.4.32, p. 447.

58. I. S. Gradshteyn and I. M. Ryzhik, Table of Integrals, Series and Products (Academic Press, Inc., New York, 1965), see 2.269.

59. Ibid., see 1.642.

JOINT SERVICES ELECTRONICS PROGRAM
REPORTS DISTRIBUTION LIST

Department of Defense

Defense Documentation Center
Attn: DDC-TCA (Mrs. V. Caponio)
Cameron Station
Alexandria, Virginia 22314

Assistant Director, Electronics and Computer Sciences
Office of Director of Defense Research and Engineering
The Pentagon
Washington, D.C. 20315

Office of the Director of Defense Research and Engineering
Information Office Library Branch
The Pentagon
Washington, D.C. 20301

ODDR&E Advisory Group on Electron Devices
201 Varick Street
New York, New York 10014

Chief, R&D Division (340)
Defense Communications Agency
Washington, D.C. 20301

Director, National Security Agency
Fort George G. Meade, Maryland 20755
Attn: Dr. T. J. Beahn

Institute for Defense Analysis
Science and Technology Division
400 Army-Navy Drive
Arlington, Virginia 22202

Dr. Stickley
Defense Advanced Research Projects Agency
Attn: Technical Library
1400 Wilson Boulevard
Arlington, Virginia 22209

Dr. R. Reynolds
Defense Advanced Research Projects Agency
Attn: Technical Library
1400 Wilson Boulevard
Arlington, Virginia 22209

Department of the Air Force

AF/RDPS
The Pentagon
Washington, D.C. 20330

AFSC (LJ/Mr. Irving R. Mirman)
Andrews AFB
Washington, D.C. 20334

Directorate of Electronics and Weapons
HQ AFSC/DLC
Andrews AFB, Maryland 20334

Directorate of Science
HQ AFSC/DLS
Andrews AFB
Washington, D.C. 20334

LTC J. W. Gregory
AF Member, TAC
Air Force Office of Scientific Research
(AFSC) AFSOR/NE
Bolling Air Force Base, D.C. 20332

Mr. Carl Sletten
RADC/ETE
Hanscom AFB, Massachusetts 01731

Dr. Richard Picard
RADC/ETSL
Hanscom AFB, Massachusetts 01731

Mr. Robert Barrett
RADC/ETS
Hanscom AFB, Massachusetts 01731

Dr. John N. Howard
AFGL/CA
Hanscom AFB, Massachusetts 01731

Dr. Richard B. Mack
RADC/ETER
Hanscom AFB, Massachusetts 01731

Documents Library (TILD)
Rome Air Development Center
Griffiss AFB, New York 13441

Mr. H. E. Webb, Jr. (ISCP)
Rome Air Development Center
Griffiss AFB, New York 13441

Mr. Murray Kesselman (ESCA)
Rome Air Development Center
Griffiss AFB, New York 13441

Mr. W. Edwards
AFAL/TE
Wright-Patterson AFB, Ohio 45433

Mr. R. D. Larson
AFAL/DHR
Wright-Patterson AFB, Ohio 45433

Howard H. Steenbergen
AFAL/DHE
Wright-Patterson AFB, Ohio 45433

Chief Scientist
AFAL/CA
Wright-Patterson AFB, Ohio 45433

HQ ESD (DRI/Stop 22)
Hanscom AFB, MA 01731

Professor R. E. Fontana
Head Dept. of Electrical Engineering
AFIT/ENE
Wright-Patterson AFB, Ohio 45433

Mr. John C. Mott-Smith (MCIT)
HQ ESD (AFSC)
Hanscom AFB, MA 01731

LTC Richard J. Gowen
Professor
Dept of Electrical Engineering
USAF Academy, Colorado 80840

AUL/LSE-9663
Maxwell AFB, Alabama 36112

AFETR Technical Library
P.O. Box 4608, MU 5650
Patrick AFB, Florida 32925

ADTC (DLOSL)
Eglin AFB, Florida 32542

HQ AMD (RDR/Col. Godden)
Brooks AFB, Texas 78235

USAF European Office of Aerospace
Research
Technical Information Office
Box 14, FPO, New York 09510

Dr. Carl E. Baum
AFWL (ES)
Kirtland AFB, New Mexico 87117

USAFSAM/RAL
Brooks AFB, Texas 78235

Department of the Army

HQDA (DAMA-ARZ-A)
Washington, D.C. 20310

Commander
US Army Security Agency
Attn: IARD-T
Arlington Hall Station
Arlington, Virginia 22212

Commander
US Army Materiel Development and
Readiness Command
Attn: Technical Library Rm 7S 35
5001 Eisenhower Avenue
Alexandria, Virginia 22333

Commander
US Army Ballistics Research Laboratory
Attn: DRXRD-BAD
Aberdeen Proving Ground
Aberdeen, Maryland 21005

Commander
Picatinny Arsenal
Attn: SMUPA-TS-T-S
Dover, New Jersey 07801

US Army Research Office
Attn: Dr. Hermann Robl
P.O. Box 12211
Research Triangle Park, NC 27709

US Army Research Office
Attn: Mr. Richard O. Ulsh
P.O. Box 12211
Research Triangle Park, NC 27709

US Army Research Office
Attn: Dr. Jimmie R. Suttle
P. O. Box 12211
Research Triangle Park, NC 27709

US Army Research Office
Attn: Dr. Horst Wittmann
P.O. Box 12211
Research Triangle Park, NC 27709

Commander
Frankford Arsenal
Attn: Mr. George C. White, Jr.
Deputy Director, Pitman-Dunn Laboratory
Philadelphia, Pennsylvania 19137

JOINT SERVICES REPORTS DISTRIBUTION LIST (continued)

Commander
US Army Missile Command
Attn: Chief, Document Section
Redstone Arsenal, Alabama 35809

Commander
US Army Missile Command
Attn: DRSMI-RR
Redstone Arsenal, Alabama 35809

Commander
US Army Materials and Mechanics
Research Center
Attn: Chief, Materials Sciences Division
Watertown, Massachusetts 02172

Commander
Harry Diamond Laboratories
Attn: Mr. John E. Rosenberg
2800 Powder Mill Road
Adelphi, Maryland 20783

Commandant
US Army Air Defense School
Attn: ATSAD-T-CMS
Fort Bliss, Texas 79916

Commandant
US Army Command and General Staff
College
Attn: Acquisitions, Lib Div
Fort Leavenworth, Kansas 66027

Dr. Hans K. Ziegler
Army Member, TAC/JSEP
US Army Electronics Command
(DRSEL-TL-D)
Fort Monmouth, New Jersey 07703

Mr. J. E. Teti
Executive Secretary, TAC/JSEP
US Army Electronics Command
(DRSEL-TL-DT)
Fort Monmouth, New Jersey 07703

Director
Night Vision Laboratory, ECOM
Attn: DRSEL-NV-D
Fort Belvoir, Virginia 22060

Commander/Director
Atmospheric Sciences Laboratory (ECOM)
Attn: DRSEL-BL-DD
White Sands Missile Range, NM 88002

Director
Electronic Warfare Laboratory (ECOM)
Attn: DRSEL-WL-MY
White Sands Missile Range, NM 88002

Commander
US Army Armament Command
Attn: DRSAR-RD
Rock Island, Illinois 61201

Director, Division of Neuropsychiatry
Walter Reed Army Institute of Research
Washington, D.C. 20012

Commander
USASATCOM
Fort Monmouth, New Jersey 07703

Commander
US Army R&D Group (Far East)
APO San Francisco, California 96343

Commander
US Army Communications Command
Attn: Director, Advanced Concepts
Office
Fort Huachuca, Arizona 85613

Project Manager
AFTADS
EAI Building
West Long Branch, New Jersey 07764

Commander
US Army White Sands Missile Range
Attn: STEWS-ID-R
White Sands Missile Range, NM 88002

Director, TRI-TAC
Attn: TT-AD (Mrs. Briller)
Fort Monmouth, New Jersey 07703

Commander
US Army Communication Command
Attn: CC-OPS-PD
Fort Huachuca, Arizona 85613

COL Robert Noce
Senior Standardization Representative
US Army Standardization Group, Canada
Canadian Force Headquarters
Ottawa, Ontario, Canada K1A 0K2

Commander
US Army Electronics Command
Attn: DRSEL-RD-O (Dr. W. S. McAfee)
CT-L (Dr. R. Buser)
NL-O (Dr. H. S. Bennett)
NL-T (Mr. R. Kulinyi)
TL-B
VL-D
WL-D
TL-MM (Mr. N. Lipetz)
NL-H (Dr. F. Schwering)
TL-E (Dr. S. Kronenberg)
TL-E (Dr. J. Kohn)
TL-I (Dr. C. Thornton)
NL-B (Dr. S. Amoroso)
Fort Monmouth, New Jersey 07703

Project Manager
Ballistic Missile Defense Program
Office
Attn: DACS-BMP (Mr. A. Gold)
1300 Wilson Boulevard
Washington, D.C. 22209

Department of the Navy

Office of Naval Research
Electronic and Solid State Sciences
Program (Code 427)
800 N. Quincy
Arlington, Virginia 22217

Office of Naval Research
Code 200
Assistant Chief for Technology
800 N. Quincy
Arlington, Virginia 22217

Office of Naval Research
Information Sciences Program (Code 437)
800 N. Quincy
Arlington, Virginia 22217

Naval Research Laboratory
4555 Overlook Avenue, S.W.
Washington, D.C. 20375
Attn: Codes 2627
4000
4105
5000
5700
5203
5210
5270
5300
5400
5460
5464
5500
5510
6400

Director
Office of Naval Research Branch Office
536 South Clark Street
Chicago, Illinois 60605

San Francisco Area Office
Office of Naval Research
760 Market Street, Room 447
San Francisco, California 94102

Dr. A. Laufer
Chief Scientist
Office of Naval Research Branch Office
1030 East Green Street
Pasadena, California 91101

Director
Office of Naval Research Branch Office
715 Broadway, 5th Floor
New York, New York 10003

New York Area Office
Office of Naval Research
715 Broadway, 5th Floor
New York, New York 10003

Mr. L. W. Sumney
Naval Electronics Systems Command
NC #1
2511 Jefferson Davis Highway
Arlington, Virginia 20360

Mr. R. Fratila
Naval Electronics Systems Command
NC #1
2511 Jefferson Davis Highway
Arlington, Virginia 20360

Mr. N. Butler
Naval Electronics Systems Command
NC #1
2511 Jefferson Davis Highway
Arlington, Virginia 20360

Dr. H. J. Meuller
Naval Air Systems Command
JP #1
1411 Jefferson Davis Highway
Arlington, Virginia 20360

Capt. R. B. Meeks
Naval Sea Systems Command
NC #3
2531 Jefferson Davis Highway
Arlington, Virginia 20362

Commander
Naval Surface Weapons Center
Attn: Technical Library
Silver Spring, Maryland 29010

Naval Surface Weapons Center
Attn: Code 212
Silver Spring, Maryland 29010

Officer-in-Charge
Naval Surface Weapons Center
Dahlgren Laboratory
Dahlgren, Virginia 22448

Naval Air Development Center
Attn: Technical Library
Johnsville
Warminster, Pennsylvania 18974

Commander
Naval Avionics Facility
Indianapolis, Indiana 46241
Attn: D/035 Technical Library

Naval Missile Center
Technical Library
Code 5632.2
Point Mugu, California 93042

Naval Weapons Center
Attn: Technical Library, Code 533
China Lake, California 93555

Naval Weapons Center
Attn: Code 6010
China Lake, California 93555

Naval Weapons Center
Mathematics Division
China Lake, California 93555

Naval Training Equipment Center
Technical Library
Orlando, Florida 32813

Naval Research Laboratory
Underwater Sound Reference Division
Technical Library
P.O. Box 8337
Orlando, Florida 32806

Naval Underwater Sound Center
Technical Library
New London, Connecticut 06320

U.S. Naval Oceanographic Office
Library - Code 1600
Washington, D.C. 20373

Commandant, Marine Corps
Scientific Advisor (Code AX)
Washington, D.C. 20380

Dr. Gernot M. R. Winkler
Director, Time Service
US Naval Observatory
Mass. Ave. at 34th St. N.W.
Washington, D.C. 20390

Naval Postgraduate School
Technical Library
Monterey, California 93940

Naval Electronics Laboratory Center
Technical Library
San Diego, California 92152

Naval Electronics Laboratory Center
Attn: Code 2600
San Diego, California 92152

Naval Electronics Laboratory Center
San Diego, California 92152
Attn: Codes 2000
2200
2300
3000
3200
3300
4800
5000
5200
5300

Naval Undersea Center
Technical Library
San Diego, California 92152

Naval Ship Research and Development Center
David W. Taylor
Code 522.1
Bethesda, Maryland 20084

Office of Chief of Naval Operations
NAICOM/MIS Planning Branch
NOP-916D, Pentagon
Washington, D.C. 20350

Technical Information Officer
Office of Naval Research
Boston Branch Office
495 Summer Street
Boston, Massachusetts 02210

Other Government Agencies

Mr. F. C. Schwenk, RD-T
National Aeronautics and Space Administration
Washington, D.C. 20546

Los Alamos Scientific Laboratory
Attn: Reports Library
P.O. Box 1663
Los Alamos, New Mexico 87544

M. Zane Thornton
Deputy Director Institute for Computer Sciences and Technology
National Bureau of Standards
Washington, D.C. 20234

Director, Office of Postal Technology (R&D)
US Postal Service
11711 Parklawn Drive
Rockville, Maryland 20852

NASA Lewis Research Center
Attn: Library
21000 Brookpark Road
Cleveland, Ohio 44135

Library -R51
Bureau of Standards - Acquisition
Boulder, Colorado 80302

MIT Lincoln Laboratory
Attn: Library A-082
P. O. Box 73
Lexington, Massachusetts 02173

Dr. Jay Harris
Program Director, Devices and Waves Program
NSF
1800 G Street
Washington, D.C. 20550

Dr. Howard W. Etzel
Deputy Director, Division of Materials Research
NSF
1800 G Street
Washington, D.C. 20550

Dr. Dean Mitchell
Program Director, Solid-State Physics
Division of Materials Research
National Science Foundation
1800 G Street
Washington, D.C. 20550

Non-Government Agencies

Director
Research Laboratory of Electronics
Massachusetts Institute of Technology
Cambridge, Massachusetts 02139

Director
Microwave Research Institute
Polytechnic Institute of New York
Long Island Graduate Center, Route 110
Farmingdale, New York 11735

Asst. Director, Microwave Research Institute
Polytechnic Institute of New York
333 Jay Street
Brooklyn, New York 11201

Director
Columbia Radiation Laboratory
Department of Physics
Columbia University
538 West 120th Street
New York, New York 10027

Director
Coordinated Science Laboratory
University of Illinois
Urbana, Illinois 61801

Director
Stanford Electronics Laboratory
Stanford University
Stanford, California 94305

Director
Microwave Laboratory
Stanford University
Stanford, California 94305

Director
Electronics Research Laboratory
University of California
Berkeley, California 94720

Director
Electronics Sciences Laboratory
University of Southern California
Los Angeles, California 90007

Director
Electronics Research Center
The University of Texas at Austin
Engineering-Science Bldg 112
Austin, Texas 87812

Director of Laboratories
Division of Engineering and Applied Physics
Harvard University
Pierce Hall
Cambridge, Massachusetts 02138